NATIONAL TECHNICAL UNIVERSITY OF ATHENS

SCHOOL OF CIVIL ENGINEERING

DEPARTMENT OF GEOTECHNICAL ENGINEERING

D O C T O R A L D I S S E R T A T I O N

Macroelement modelling for the mechanical response of granular soil and layered sites improved with granular columns

Anthi Maria

Diploma in Civil Engineering, N.T.U.A.

Master of Science in Civil Engineering, N.T.U.A.

Supervised by: Associate Professor Nikos Gerolymos

September 2021

ΕΘΝΙΚΟ ΜΕΤΣΟΒΙΟ ΠΟΛΥΤΕΧΝΕΙΟ

ΣΧΟΛΗ ΠΟΛΙΤΙΚΩΝ ΜΗΧΑΝΙΚΩΝ

ΤΟΜΕΑΣ ΓΕΩΤΕΧΝΙΚΗΣ

Δ Ι Δ Α Κ Τ Ο Ρ Ι Κ Η Δ Ι Α Τ Ρ Ι Β Η

Ανάπτυξη μακροστοιχείων για την ανάλυση της μηχανικής συμπεριφοράς κοκκωδών εδαφών και σύμμικτων σχηματισμών

Άνθη Μαρία

Διπλωματούχος Πολιτικός Μηχανικός, Ε.Μ.Π.

Κάτοχος Μεταπτυχιακού Διπλώματος, Ε.Μ.Π.

Επιβλέπων: Αναπλ. Καθηγητής Νίκος Γερόλυμος

Σεπτέμβριος 2021

NATIONAL TECHNICAL UNIVERSITY OF ATHENS

SCHOOL OF CIVIL ENGINEERING

DEPARTMENT OF GEOTECHNICAL ENGINEERING

MACROELEMENT MODELLING FOR THE MECHANICAL RESPONSE OF GRANULAR SOIL AND LAYERED SITES IMPROVED WITH GRANULAR COLUMNS

DOCTORAL THESIS

Of

Maria S. Anthi

Diploma (M.Eng.) in Civil Engineering, NTUA

M.Sc., NTUA

The thesis is submitted to the School of Civil Engineering of the National Technical University of Athens in fulfilment of the requirements for the Degree of Doctor of Philosophy

ADVISORY COMMITTEE

1. N. Gerolymos, Assoc. Professor NTUA (Supervisor)
2. G. Gazetas, Professor Emeritus NTUA
3. I. Anastasopoulos, Professor ETH Zurich

EXAMINATION COMMITTEE

1. N. Gerolymos, Assoc. Professor NTUA (Supervisor)
2. G. Gazetas, Professor Emeritus NTUA
3. I. Anastasopoulos, Professor ETH Zurich
4. G. Bouckovalas, Professor NTUA
5. V. Georgiannou, Professor NTUA
6. A. Papadimitriou, Assoc. Professor NTUA
7. P. Dakoulas, Professor UTH

Athens, September 2021

ΕΘΝΙΚΟ ΜΕΤΣΟΒΙΟ ΠΟΛΥΤΕΧΝΕΙΟ

ΣΧΟΛΗ ΠΟΛΙΤΙΚΩΝ ΜΗΧΑΝΙΚΩΝ

ΤΟΜΕΑΣ ΓΕΩΤΕΧΝΙΚΗΣ

ΑΝΑΠΤΥΞΗ ΜΑΚΡΟΣΤΟΙΧΕΙΩΝ ΓΙΑ ΤΗΝ ΑΝΑΛΥΣΗ ΤΗΣ ΜΗΧΑΝΙΚΗΣ ΣΥΜΠΕΡΙΦΟΡΑΣ ΚΟΚΚΩΔΩΝ ΕΔΑΦΩΝ ΚΑΙ ΣΥΜΜΙΚΤΩΝ ΣΧΗΜΑΤΙΣΜΩΝ

ΔΙΔΑΚΤΟΡΙΚΗ ΔΙΑΤΡΙΒΗ

της

Μαρίας Σ. Άνθη

Διπλωμα Πολιτικού Μηχανικού, ΕΜΠ

Μ.Δ.Ε., ΕΜΠ

Η διατριβή υποβάλλεται στη Σχολή Πολιτικών Μηχανικών του Εθνικού Μετσόβιου Πολυτεχνείου προς εκπλήρωση των προϋποθέσεων του τίτλου του Διδάκτορος Μηχανικού

ΤΡΙΜΕΛΗΣ ΣΥΜΒΟΥΛΕΥΤΙΚΗ ΕΠΙΤΡΟΠΗ

1. Ν. Γερόλυμος, Αν. Καθηγητής ΕΜΠ (Επιβλέπων)
2. Γ. Γκαζέτας, Ομότιμος Καθηγητής ΕΜΠ
3. Ι. Αναστασόπουλος, Καθηγητής ΕΤΗ Zurich

ΕΠΤΑΜΕΛΗΣ ΕΞΕΤΑΣΤΙΚΗ ΕΠΙΤΡΟΠΗ

1. Ν. Γερόλυμος, Αν. Καθηγητής ΕΜΠ (Επιβλέπων)
2. Γ. Γκαζέτας, Ομότιμος Καθηγητής ΕΜΠ
3. Ι. Αναστασόπουλος, Καθηγητής ΕΤΗ Zurich
4. Γ. Μπουκοβάλας, Καθηγητής ΕΜΠ
5. Β. Γεωργιάννου, Καθηγήτρια ΕΜΠ
6. Α. Παπαδημητρίου, Αν. Καθηγητής ΕΜΠ
7. Π. Ντακούλας, Καθηγητής ΠΘ

Αθήνα, Σεπτέμβριος 2021

Προλεγόμενα

Με την ολοκλήρωση της διδακτορικής διατριβής μου, θα ήθελα να εκφράσω τις ειλικρινείς μου ευχαριστίες, σε όλους όσους συνέβαλλαν στην προσπάθεια μου αυτή.

Πρώτα απ' όλα, θα ήθελα να ευχαριστήσω τον Αναπλ. Καθ. κ. Νίκο Γερόλυμο, επιβλέποντα της διατριβής, για τη διαρκή επιστημονική καθοδήγηση και την ανυπολόγιστη συνεισφορά του, την ακέραια εμπιστοσύνη που μου έδειξε σε κάθε πτυχή της πολυετούς συνεργασίας μας, για την ελευθερία και το σεβασμό που επέδειξε στις ερευνητικές επιλογές μου και για τη γενναιόδωρη διάθεση του χρόνου του, που αφειδώς μου παρείχε.

Επίσης, θερμές ευχαριστίες οφείλω στον Ομότιμο Καθ. κ. Γ. Γκαζέτα και τον Καθ. κ. Ι. Αναστασόπουλο, ως μέλη της τριμελούς επιτροπής, για τις πολύτιμες συμβουλές, την εμπιστοσύνη και την άμεση ανταπόκριση κάθε φορά που χρειαζόμουν τη βοήθεια τους.

Τις ιδιαίτερες ευχαριστίες μου θα ήθελα να απευθύνω στα μέλη της επταμελούς εξεταστικής επιτροπής· τον Καθ. κ. Γ. Μπουκοβάλα, την Καθ. κα. Β. Γεωργιάννου, τον Καθ. κ. Π. Ντακούλα και τον Αναπλ. Καθ. κ. Α. Παπαδημητρίου, για την τιμή που μου έκαναν να συμμετέχουν στην επιτροπή εξέτασης της διδακτορικής διατριβής. Οι εποικοδομητικές υποδείξεις και οι εύστοχες παρατηρήσεις τους υπήρξαν πολύτιμες για το βέλτιστο αποτέλεσμα της διατριβής.

Θα ήθελα ακόμη να εκφράσω τις ευχαριστίες μου προς τους Συναδέλφους του Τομέα Γεωτεχνικής· τους Γιάννη Τσιάπα, Κωνσταντίνο Μπαζαίο, Ταξιαρχούλα Λημναίου, Ελένη Παυλοπούλου, Φίλιππο Χόρτη και Δημήτρη Γεωργίου, με τους οποίους υπήρξαμε συνοδοιπόροι και συμπαραστάτες, σε αυτήν την επίπονη προσπάθεια.

Ευχαριστώ τις αγαπημένες μου φίλες και συναδέλφους Κέλλυ Κουνιάκη και Βάλια Ζωντανού, που πάντοτε απλόχερα μου χάριζαν τη στήριξη, την ενθάρρυνση και την ηθική τόνωση, για να ολοκληρώσω το εγχείρημα μου.

Ένα βαθύτατο ευχαριστώ θα ήθελα να εκφράσω στον Άγγελο Τσάτση για την έμπρακτη συμβολή του στην πραγματοποίηση αυτού του σκοπού, την ανιδιοτελή και ανυπολόγιστη υποστήριξη, τη στωικότητα που επιδείκνυε σε δύσκολες στιγμές και τη δύναμη που καθημερινά μου ενέπνεε να συνεχίσω την προσπάθεια ως το τέλος.

Τέλος, θα ήθελα να ευχαριστήσω την οικογένεια μου για την αμέριστη υποστήριξη και ενθάρρυνση τους σε κάθε μου βήμα και ιδιαίτερα τους γονείς μου, Σπύρο και Ζαφειρία, για την ανεκτικότητα, την υπομονή, την αδιαπραγμάτευτη αγάπη και τη βαθιά πίστη τους σε μένα, χωρίς την οποία θα ήταν εξαιρετικά δύσκολο να φτάσω ως εδώ. Το ευχαριστήριο αυτό σημείωμα εκφράζει ένα ελάχιστο μέρος της ευγνωμοσύνης που αισθάνομαι για εκείνους…

ΕΘΝΙΚΟ ΜΕΤΣΟΒΙΟ ΠΟΛΥΤΕΧΝΕΙΟ
ΣΧΟΛΗ ΠΟΛΙΤΙΚΩΝ ΜΗΧΑΝΙΚΩΝ – ΤΟΜΕΑΣ ΓΕΩΤΕΧΝΙΚΗΣ

ΠΕΡΙΛΗΨΗ

της Διδακτορικής Διατριβής

της Άνθη Μαρίας

Στόχος της Διδακτορικής Διατριβής είναι η ανάπτυξη ενός ολοκληρωμένου μαθηματικού πλαισίου για την ανάλυση της συμπεριφοράς κοκκωδών εδαφών και σύμμικτων εδαφικών σχηματισμών, αποτελούμενων από κοκκώδη και αργιλικά εδάφη, ενισχυμένα με εδαφικά στραγγιστήρια / χαλικοπασσάλους. Για το σκοπό αυτό, αξιοποιήθηκε το καταστατικό προσομοίωμα Ta-Ger για αμμώδη εδάφη, το οποίο εκφράστηκε στο δισδιάστατο χώρο των τάσεων *p-q*, ε_{vol}-ε_q και τροποποιήθηκε μαθηματικά ώστε να εξυπηρετήσει τη μεθοδολογία βαθμονόμησης. Εξέχοντα χαρακτηριστικά του μοντέλου αποτελούν η συμβατότητα με την θεωρία κρίσιμης κατάστασης για μονοτονική και ανακυκλική φόρτιση, ο ανισοτροπικός πλαστικός νόμος ροής και ο εμπνευσμένος από τους Bouc – Wen νόμος κράτυνσης, προσφέροντας αξιοσημείωτη ευελιξία στην αναπαράσταση σύνθετων μηχανισμών ανακυκλικής συμπεριφοράς της άμμου, όπως η μείωση της δυσκαμψίας και η απώλεια της αντοχής λόγω ανάπτυξης υπερπιέσεων πόρων.

Η βαθμονόμηση των παραμέτρων του προσομοιώματος πραγματοποιήθηκε με στόχο την ταυτόχρονη αναπαραγωγή πειραματικών καμπυλών για το τέμνον μέτρο διάτμησης (*G-γ*) και την υστερητική απόσβεση (*ξ-γ*), συναρτήσει της διατμητικής παραμόρφωσης, και των ημιεμπειρικών καμπυλών αντίστασης σε ρευστοποίηση κατά NCEER. Η βαθμονόμηση πραγματοποιήθηκε για εύρος σχετικών πυκνοτήτων και στάθμεων φόρτισης. Υπό στραγγιζόμενες συνθήκες φόρτισης, αξιοποιήθηκαν οι ακόλουθες ομάδες καμπυλών *(G-γ)*, *(ξ-γ)* από την βιβλιογραφία: i) Ishibashi και Zhang (1993), ii) Vucetic και Dobry (1991) και iii) Darendeli et al. (2001). Κατά τη διαδικασία βαθμονόμησης υπό αστράγγιστες συνθήκες φόρτισης, η συσχέτιση για την αντοχή σε ρευστοποίηση αναφοράς $CRR_{M_w=7.5\,\sigma'_{v_0}=1atm}$ με δεδομένα από δοκιμές SPT που προτάθηκε από τους Idriss & Boulanger (2004, 2008) συνδυάστηκε με: (α) την εμπειρική φόρμουλα των Seed & Idriss (1982), που συσχετίζει το σεισμικό μέγεθος με τον ισοδύναμο αριθμό ομοιόμορφων κύκλων φόρτισης, (β) τον συντελεστή διόρθωσης λόγω μεγέθους σεισμικής έντασης (*MSF*) που προτάθηκε από τους i) Idriss (1995) και ii) Andrus και Stokoe (1997) και (γ) τον συντελεστή διόρθωσης λόγω πίεσης υπερκειμένων K_σ κατά NCEER (1996, 1998). Επιπλέον, αναπτύχθηκε μία απλοποιημένη εκδοχή του καταστατικού προσομοιώματος, για την αναπαραγωγή της συμπεριφοράς αργιλώδους εδάφους υπό ανακυκλική φόρτιση, με βάση την παραδοχή μηδενικής επαυξητικής ογκομετρικής παραμόρφωσης και συσχετίζοντας την παράμετρο αντοχής M_s του μοντέλου με την αστράγγιστη διατμητική αντοχή S_u της αργίλου. Η βαθμονόμηση του καταστατικού προσομοιώματος για αργιλικά υλικά πραγματοποιήθηκε βάσει καμπυλών *(G-γ)* , *(ξ-γ)* της βιβλιογραφίας κατά: i) Ishibashi και Zhang (1993) και ii) Vucetic και Dobry (1991).

Το προσομοίωμα αξιοποιήθηκε για την ανάπτυξη αριθμητικού αλγορίθμου επίλυσης άμεσης μεθόδου πεπερασμένων διαφορών, στη γλώσσα προγραμματισμού MATLAB, με στόχο την ανάλυση της κυματικής απόκρισης πολύστρωτου εδαφικού σχηματισμού τόσο για συνθήκες πλήρους στράγγισης όσο και για αστράγγιστες συνθήκες φόρτισης. Η επίλυση της διαφορικής εξίσωσης της μονοδιάστατης διάδοσης σεισμικού κύματος επαληθεύτηκε μέσω σύγκρισης με την αναλυτική λύση (Gazetas, 1982), για διάφορες γραμμικές κατανομές διατμητικής ταχύτητας με το βάθος. Το μοντέλο επαληθεύτηκε μέσω σύγκρισης με πειραματικά αποτελέσματα φυγοκεντριστή (Hashash et al., 2015), σε εδαφικό προφίλ ύψους 26m (σε πρωτότυπη κλίμακα) αποτελούμενο από ξηρή άμμο (Nevada sand) σχετικής πυκνότητας D_r=60%, που υποβλήθηκε σε δύο στάθμες σεισμικής διέγερσης στη βάση του. Η σύγκριση της υπολογισθείσας με τη μετρηθείσα συμπεριφορά κρίθηκε ικανοποιητική. Επιπλέον, για την επικύρωση του αλγορίθμου αξιοποιήθηκαν οι καταγραφές στο Port Island, του σεισμού του 1995 στο Kobe της Ιαπωνίας. Χρησιμοποιήθηκε η καταγραφή των επιταχύνσεων σε βάθος 83m και το προφίλ των διατμητικών ταχυτήτων του εδάφους της περιοχής, δεδομένα που αντλήθηκαν από τη διεθνή βιβλιογραφία. Για τις λοιπές εδαφικές παραμέτρους, χρησιμοποιήθηκε η βαθμονόμηση που προτάθηκε. Εκτελώντας ανάλυση υπό αστράγγιστες συνθήκες φόρτισης, παρήχθησαν οι χρονοϊστορίες των επιταχύνσεων σε βάθος 32m, 16m και στην επιφάνεια του σχηματισμού. Η σύγκλιση με τις καταγεγραμμένες στα ίδια βάθη επιταχύνσεις, κρίθηκε αρκετά ικανοποιητική. Ακόμα, σημειώθηκε ρευστοποίηση στο ασθενές στρώμα της άμμου, σε συμφωνία με τις επιτόπου παρατηρήσεις.

Ο αλγόριθμος σεισμικής απόκρισης εδαφικού σχηματισμού επεκτάθηκε, ώστε να ληφθεί υπόψη η ταυτόχρονη αποτόνωση των υπερπιέσεων των πόρων που αναπτύσσονται κατά την σεισμική διέγερση κορεσμένου μη συνεκτικού εδάφους, μέσω της κατακόρυφης στερεοποίησης του. Η επίλυση της διαφορικής εξίσωσης της κατακόρυφης στερεοποίησης εδαφικού σχηματισμού επαληθεύτηκε μέσω σύγκρισης με την αναλυτική λύση κατά Terzaghi. Η επικύρωση του μοντέλου, μέσω αναπαραγωγής του ιστορικού περιστατικού του σεισμού του Kobe 1995, επαναλήφθηκε λαμβάνοντας υπόψιν την ταυτόχρονη στερεοποίηση των σχηματισμών.

Στη συνέχεια, το μοντέλο εφαρμόστηκε, με στόχο τη σύνθεση ελαστικών φασμάτων απόκρισης κατάλληλων για τον αντισεισμικό σχεδιασμό κατασκευών σε ρευστοποιήσιμο έδαφος κατηγορίας S_2 κατά EC8. Αξιοποιώντας τη βάση δεδομένων PEER Ground motion database, επιλέχθηκαν 63 επιταχυνσιογραφήματα, για διάφορες τιμές μεγέθους M_w και απόστασης από το ρήγμα R_{JB} (9 συνδυασμοί M_w, R_{JB} και 7 επιταχυνσιογραφήματα για τον κάθε συνδυασμό) και φάσμα απόκρισης συμβατό με το φάσμα απόκρισης που προκύπτει από διαθέσιμες στη βιβλιογραφία σχέσεις εξασθένησης για ίδιο μέγεθος σεισμού και απόσταση από το ρήγμα. Τα επιταχυνσιογραφήματα χρησιμοποιήθηκαν για τη διέγερση της βάσης 10 εδαφικών κατατομών ευπαθών σε ρευστοποίηση και υπολογίστηκαν τα ελαστικά φάσματα στην επιφάνεια των σχηματισμών, σε 3 συνθήκες στράγγισης: στραγγιζόμενες, αστράγγιστες και λαμβάνοντας υπόψη την κατακόρυφη στερεοποίηση των σχηματισμών, ήτοι 1890 σεισμικές αναλύσεις. Για κάθε κατηγορία M_w, R_{JB} παρήχθη ένα φάσμα απόκρισης, ως μέσος όρος όλων των φασμάτων της κατηγορίας αυτής. Το μέσο κανονικοποιημένο ελαστικό φάσμα επιφανείας που παρήχθη γραμμικοποιήθηκε σύμφωνα με την προσέγγιση του EC8, σε φάσμα αποτελούμενο από 4 κλάδους και προτάθηκαν τιμές για τις χαρακτηριστικές παραμέτρους που καθορίζουν το σχήμα του εν λόγω φάσματος σχεδιασμού, για εδαφικούς τύπους S_2 και A.

Τέλος, το μοντέλο αξιοποιήθηκε για την προσομοίωση της σεισμικής απόκρισης εδαφικού σχηματισμού ενισχυμένου με κατακόρυφα στραγγιστήρια / χαλικοπασσάλους, με σκοπό την αποτόνωση των υπερπιέσεων των πόρων του εδάφους. Η διαφορική εξίσωση της εδαφικής στερεοποίησης επαναδιατυπώθηκε ώστε να ληφθεί υπόψη και η οριζόντια υδατική ροή σε αξονοσυμμετρικό μοντέλο, θεωρώντας τον γεωμετρικό μέσο όρο της πίεσης πόρων στην ακτίνα επιρροής του στραγγιστηρίου, ως αντιπροσωπευτική τιμή για την μονοδιάστατη κατακόρυφη διάδοση του διατμητικού κύματος. Το μοντέλο επαληθεύτηκε μέσω σύγκρισης με τρισδιάστατες αριθμητικές αναλύσεις (FLAC3D, Itasca 2006) λεπτής στρώσης ρευστοποιήσιμης άμμου, περιβαλλόμενης από αργιλικές στρώσεις ώστε να αποτρέπεται η κατακόρυφη στράγγιση, με ακτίνα επιρροής εδάφους R_e=1.4m και χαλικοπάσσαλο ακτίνας R_d=0.5m, υποβαλλόμενης σε ημιτονοειδή διέγερση 12 κύκλων (Bouckovalas et al., 2011). Η σύγκριση των αποτελεσμάτων κρίθηκε ικανοποιητική.

NATIONAL TECHNICAL UNIVERSITY OF ATHENS
SCHOOL OF CIVIL ENGINEERING – GEOTECHNICAL DEPARTMENT

ABSTRACT

of the Doctoral Dissertation

of Anthi Maria

The scope of the doctoral dissertation is the development of a macro-element model for the mechanical response of granular soil and layered sites improved with granular columns.The model is based on the plasticity constitutive model for sand Ta-Ger expressed in a one dimensional *p*-*q*, ε_{vol}-ε_q space form, slightly revised from its initial formulation, which exhibits remarkable versatility in representing complex patterns of sand cyclic behavior, such as stiffness decay and decrease in strength due to build-up of pore-water pressure.

The calibration of the model parameters was based on a procedure that targeted to the optimum performance in both drained and undrained load conditions by simultaneously matching the response in terms of: (a) the cyclic resistance ratio curves as per the NCEER/NSF methodology, and (b) widely-used experimental shear modulus and damping ratio curves available in the literature. The calibration was executed for various sand relative densities and under various levels of effective stress. The methodology under drained loading conditions was based on matching model response with the *(G-γ), (ξ-γ)* curves suggested by: i) Ishibashi and Zhang (1993), ii) Vucetic and Dobry (1991) and iii) Darendeli et al. (2001). Under undrained loading conditions, the correlation for the reference cyclic resistance ratio $CRR_{M_w=7.5\ \sigma'_{v_0=1atm}}$ from SPT data by Idriss & Boulanger (2004, 2008) was combined with (a) the empirical formula of Seed & Idriss 1982), that relates the earthquake magnitude to the equivalent number of uniform cycles of the seismic motion, (b) the magnitude scaling factors (*MSFs*) proposed by i) Idriss (1995) and ii) Andrus and Stokoe (1997), that associates the reference cyclic resistance ratio with the actual one and (c) the correction factor for overburden stress K_σ suggested by the NCEER (1996, 1998) workshops. A simplified version of the developed *p*-*q* version of Ta-Ger model was used to represent the behavior of clay in cyclic loading, based on the assumption of zero incremental volumetric strains and relating M_s with the undrained strength S_u. The calibration procedure was based on matching two families of *(G-γ), (ξ-γ)* curves: i) the Ishibashi and Zhang (1993) and ii) the Vucetic και Dobry (1991).

The model was then implemented through an explicit finite difference algorithm into an in-house computer code which performs integration of the wave equations to obtain the non-linear response of the soil, under both drained and undrained conditions of loading. The accuracy of the algorithm was verified through comparison with analytical solutions for the amplification function of soil deposits with linearly increasing V_s (Gazetas, 1982), subjected to vertically propagating shear waves. The capability of the model in simulating the seismic

response of horizontally layered deposits was validated against two centrifuge experiments (Hashash et al, 2015). The tests involved a 26m thick profile of dry stiff Nevada sand with D_r=60%, subjected to two levels of seismic excitation at its base. The computed response was reasonably compared to the measured one. The case history of Port Island vertical array records in the 1995 Kobe earthquake was then employed to verify the versatility of the model to predict the dynamic response of saturated soil. The accordance of the model response and the in situ records in terms of acceleration time histories at 0m, -16m, -32m and -83m and surface spectrum was quite satisfactory. Field investigations along with previous simulations of the seismic response of the site indicated that liquefaction must have occurred at the gravelly sand layer above the shallow alluvial clay and the sandy layer below it. This was confirmed by the present analysis, where pore water pressure generation took place at the specific layers. Thus, it can be inferred that the developed model was satisfactory in reproducing the observed response.

The developed numerical non-linear ground response analysis algorithm was then reformulated in order to take into consideration the simultaneous dissipation of the excess pore water pressure through soil grains. The differential equation that describes the one-dimensional, vertical, soil consolidation was approached with the finite differences technique and its solution was verified against Terzaghi's analytical solution. The model validation against the case history of the Port Island array from the Kobe 1995 earthquake was repeated, considering the simultaneous vertical soil consolidation.

The model was then applied to estimate the elastic response spectra at the surface of soil profiles with liquefiable layers (ground type S_2) as per EC8:2004. The investigation study involved the ground response analysis of diverse soil profiles, all including a liquefiable zone, excited with a suite of earthquake motions at their base. The acceleration time histories were extracted from the PEER Ground Motion Database having characteristics compatible with the NGA-estimated response spectrum at the bedrock and with key seismological parameters such as the earthquake magnitude M_w and horizontal distance from the fault R_{JB}. Two different methods were applied regarding the selection of base excitations: amplitude scaled records (to match a target response spectrum) and spectral matched records. From the results an idealized response spectrum was deduced in terms of the design spectrum parameters S, η, T_B and T_C. It was shown that the idealized ground surface response spectrum was marginally sensitive to the method of base excitation selection.

Finally, the developed numerical algorithm was applied for the simulation of the seismic response of liquefiable sandy sites improved with vertical drains. The differential equation of soil consolidation was reformulated to account not only for the vertical water flow up to the ground surface, but also for the axisymmetric water flow, through the ground towards the drain. The mechanical interaction between the drain material and the surrounding soil in case of stone columns / gravel piles, is possible to be taken into consideration, by increasing the overall strength of the composite gravel pile-surrounding soil material. The proposed numerical algorithm was validated against a set of non-linear, dynamic, three dimensional, numerical analyses that were carried out in the finite differences program FLAC3D (Itasca, 2006) and concerned a thin liquefiable sand layer of D_r=60% encased between clayey layers, in order to establish purely horizontal flow towards the drains, improved with drains of radius R_d=0.5m and a center-to-center distance (2 R_e) equal to 2.8m (Bouckovalas et al., 2011). The comparison of the results was satisfactory.

ΕΘΝΙΚΟ ΜΕΤΣΟΒΙΟ ΠΟΛΥΤΕΧΝΕΙΟ
ΣΧΟΛΗ ΠΟΛΙΤΙΚΩΝ ΜΗΧΑΝΙΚΩΝ – ΤΟΜΕΑΣ ΓΕΩΤΕΧΝΙΚΗΣ

ΕΚΤΕΝΗΣ ΠΕΡΙΛΗΨΗ

της Διδακτορικής Διατριβής

της Άνθη Μαρίας

επιβλέπων: Αναπληρωτής Καθηγητής Ν. Γερόλυμος

***Θέμα*: «Ανάπτυξη μακροστοιχείων για την ανάλυση της μηχανικής συμπεριφοράς κοκκωδών εδαφών και σύμμικτων σχηματισμών»**

Εισαγωγή

Η εκτίμηση της σεισμικής εδαφικής απόκρισης κατέχει εξέχουσα σημασία στη σεισμική μηχανική, καθώς αποτελεί συνήθως το πρώτο βήμα για την εκτίμηση της συμπεριφοράς των κατασκευών σε προβλήματα αλληλεπίδρασης εδάφους – κατασκευής. Στο πλαίσιο αυτό, η παγκόσμια βιβλιογραφία έχει αφιερώσει σημαντική προσπάθεια τις τελευταίες δεκαετίες στην ανάπτυξη αναλυτικών μεθόδων και αριθμητικών εργαλείων για την πρόβλεψη της εδαφικής συμπεριφοράς υπό ισχυρές σεισμικές διεγέρσεις. Τα καταστατικά μοντέλα και οι αριθμητικοί κώδικες που έχουν προταθεί για τη μονοδιάστατη ανάλυση πολύστρωτων εδαφικών σχηματισμών επιβαλλόμενων σε κατακορύφως διαδιδόμενα διατμητικά *S* κύματα, μπορούν να διαιρεθούν στις εξής κατηγορίες: (α) ισοδύναμα ιξωδοελαστικά μοντέλα, (β) μη γραμμικά υστερητικά (ή φαινομενολογικά) μοντέλα και (γ) μοντέλα πλασιμότητας.

Στην παρούσα εργασία το καταστατικό προσομοίωμα Ta-Ger για αμμώδη εδάφη (Tasiopoulou and Gerolymos, 2016 a & b) διατυπώνεται στο δισδιάστατο χώρο των τάσεων p-q, ε_{vol}-ε_q, με σκοπό την εισαγωγή του σε αριθμητικό κώδικα πεπερασμένων διαφορών που εκτελεί δυναμική, μη γραμμική ανάλυση εδαφικού σχηματισμού οριζόντιας στρωματογραφίας που υποβάλλεται σε κατακόρυφη διάδοση διατμητικών *S* κυμάτων. Η

μαθηματική δομή του προσομοιώματος τροποποιείται ώστε: (i) να εξυπηρετήσει την προτεινόμενη ενοποιημένη διαδικασία βαθμονόμησης για αστράγγιστες και στραγγιζόμενες συνθήκες φόρτισης με έμφαση στο φαινόμενο της ρευστοποίησης και (ii) να περιγράψει την υστερητική συμπεριφορά της αργίλου σε ανακυκλική φόρτιση, υπό πλήρως αστράγγιστες συνθήκες. Εξέχοντα χαρακτηριστικά του μοντέλου αποτελούν η συμβατότητα με τη θεωρία κρίσιμης κατάστασης για μονοτονική και ανακυκλική φόρτιση, ο ανισοτροπικός πλαστικός νόμος ροής και ο εμπνευσμένος από τους Bouc – Wen νόμος κράτυνσης, προσφέροντας αξιοσημείωτη ευελιξία στην αναπαραγωγή σύνθετων μηχανισμών ανακυκλικής συμπεριφοράς όπως η μείωση της δυσκαμψίας και η απώλεια της αντοχής λόγω ανάπτυξης υπερπιέσεων πόρων.

Το καταστατικό προσομοίωμα Ta-Ger

Το καταστατικό προσομοίωμα Ta-Ger για άμμους έχει θεμελιωδώς εκφραστεί στον εξαδιάστατο χώρο των τάσεων. Σε όρους μέσης ενεργού τάσης p – αποκλίνουσας τάσης q, το μοντέλο διατυπώνεται ως προς τις επαυξητικές τιμές τάσεων – παραμορφώσεων ως ακολούθως :

$$\begin{bmatrix} dp \\ dq \end{bmatrix} = \eta \begin{bmatrix} K - \frac{-K^2 M_s d}{-K M_s d + 3G} \zeta_a{}^n & \frac{3KGd}{-KM_s d + 3G} \zeta_a{}^n \\ \frac{-3KGM_s}{-KM_s d + 3G} \zeta_a{}^n & 3G - \frac{9G^2}{-KM_s d + 3G} \zeta_a{}^n \end{bmatrix} \begin{bmatrix} d\varepsilon_p \\ d\varepsilon_q \end{bmatrix} \quad [1]$$

, όπου K και G είναι τα ελαστικά (μικρών παραμορφώσεων) μέτρα συμπίεσης και διάτμησης αντίστοιχα, d είναι ο λόγος της επαυξητικής πλαστικής ογκομετρικής παραμόρφωσης $d\varepsilon_p{}^p$ προς την επαυξητική πλαστική αποκλίνουσα παραμόρφωση $d\varepsilon_q{}^p$ και βασίζεται στη θεωρία διαστολικότητας του Rowe καθώς εξαρτάται από την απόσταση του τρέχοντος λόγου τάσεων q/p από τη γραμμή αλλαγής φάσης. Το M_{pt} and M_s είναι οι παράμετροι αλλαγής φάσης και αντοχής. Το ζ_α (Tasiopoulou and Gerolymos, 2016a) είναι μια υστερητική αδιάστατη παράμετρος που παρέχει το νόμο φόρτισης – αποφόρτισης και είναι συνάρτηση της παραμέτρου ζ του Bouc–Wen (Gerolymos and Gazetas 2005, Gerolymos et al. 2007), ενώ ο εκθέτης n ελέγχει το ρυθμό μετάβασης από την ελαστική κατάσταση στην πλήρως πλαστική. Τέλος, ο παράγοντας η που πολλαπλασιάζει το ελαστο-πλαστικό μητρώο κράτυνσης εκφράζει την απολεσθείσα υστερητική ενέργεια. Για το ελαστικό μέτρο διάτμησης G_{max} υιοθετείται η ακόλουθη έκφραση:

$$G_{max} = 1592.6\, p_a\, {D_r}^{0.6464} \left(\frac{p\prime}{p_a}\right)^m \quad [2]$$

, όπου p_a είναι η ατμοσφαιρική πίεση, D_r είναι η σχετική πυκνότητα της άμμου και p' είναι η μέση ενεργός τάσης συμπίεσης. Το μέτρο συμπίεσης δίνεται από:

$$K = \frac{2(1+\nu)}{3(1-2\nu)} G \quad [3]$$

, όπου ν είναι ο λόγος του Poisson. Ο εκθέτης n εκφράζεται ως άθροισμα των συνιστωσών του υπό αστράγγιστες και υπό στραγγιζόμενες συνθήκες φόρτισης, n_u και n_d αντίστοιχα, ως ακολούθως:

$$n = n_u e^{-A\frac{D_r - D_{r0}}{1-D_{r0}}} + n_d \left(1 - e^{-A\frac{D_r - D_{r0}}{1-D_{r0}}}\right) \quad [4]$$

, όπου D_{r0} είναι η αρχική τιμή της σχετικής πυκνότητας και A ένας μεγάλος αριθμός (π.χ. $A \approx 100$). Η συνιστώσα υπό αστράγγιστες συνθήκες n_u είναι συνάρτηση της αθροιστικής επαυξητικής αποκλίνουσας παραμόρφωσης, σύμφωνα με την ακόλουθη σχέση:

$$n_u = n_f + \left[n_{peak} + \left(n_0 - n_{peak}\right) e^{-b \sum de_q} - n_f\right] e^{-g \sum de_q} \quad [5]$$

, όπου n_o είναι η αρχική τιμή του n, n_{peak} είναι η ασυμπτωτικά μέγιστη τιμή, n_f είναι η τελική τιμή του n και $\Sigma d\varepsilon_q$ είναι η αθροιστική επαυξητική αποκλίνουσα παραμόρφωση. Η συνιστώσα n_d είναι σταθερή και ουσιαστικά ενεργοποιείται με την εξέλιξη της σχετικής πυκνότητας (στραγγιζόμενες συνθήκες). Τέλος, η παράμετρος απολεσθείσας υστερητικής ενέργειας η, που ενεργοποιείται αποκλειστικά υπό στραγγιζόμενες συνθήκες φόρτισης και είχε αρχικά προταθεί από τους Gerolymos and Gazetas (2005) και Drosos et al. (2012), διατυπώνεται ως:

$$\eta = \frac{s_1}{s_1 + \mu^{s_2}} \quad [6]$$

, όπου το μ εκφράζει την πλασιμότητα αναφοράς σε όρους διατμητικής παραμόρφωσης και τα s_1, s_2 αποτελούν συναρτήσεις της μέσης ενεργού τάσης συμπίεσης p'.

Μοντέλο για αργίλους

Προκειμένου να προσομοιωθεί η ανακυκλική συμπεριφορά του αργιλικού εδάφους αναπτύσσεται μια απλοποιημένη εκδοχή του καταστατικού προσομοιώματος Ta-Ger εκφρασμένο σε όρους p-q, βάσει της παραδοχής μηδενικής επαυξητικής πλαστικής

διατμητικής παραμόρφωσης και συσχετίζοντας το M_s με την αστράγγιστη διατμητική αντοχή S_u της αργίλου. Ο εκθέτης *n* εκφράζεται συναρτήσει του δείκτη πλασιμότητας ως:

$$n = f\ \ln(PI) + h \qquad [7]$$

, όπου *f* και *h* έχουν σταθερές τιμές. Η μορφή της παραμέτρου απολεσθείσας υστερητικής ενέργειας η διατηρείται όπως στην Εξίσωση [6], με το s_1 να είναι σταθερό και το s_2 να αποτελεί συνάρτηση του δείκτη πλασιμότητας. Για το ελαστικό μέτρο διάτμησης G_{max} υιοθετείται η παρακάτω έκφραση, βάσει δεδομένων από πειραματικές δοκιμές (Kramer, 1996):

$$G_{max} = 625\ F(e)\ OCR^k (p_a\ \sigma'_m)^{0.5} \qquad [8]$$

, όπου *OCR* είναι ο δείκτης υπερστερεοποίησης και σ'_m η μέση κύρια ενεργός τάση:

$$\sigma'_m = \frac{\sigma'_1+\sigma'_2+\sigma'_3}{3} \qquad [9]$$

, p_a η ατμοσφαιρική πίεση στις ίδιες μονάδες με τα σ'_m και G_{max} και το *F(e)* αποτελεί συνάρτηση του δείκτη πόρων της αργίλου *e* (Hardin, 1978):

$$F(e) = \frac{1}{0.3+0.7\ e^2} \qquad [10]$$

Οι τιμές του εκθέτη του δείκτη υπερστερεοποίησης *k,* προτάθηκαν από τους Hardin και Drnevich (1972) για διακριτές τιμές του δείκτη πλασιμότητας (*PI* = 0, 20, 40, 60, 80 και ≥100). Με δεδομένο το G_{max} (Εξίσωση [8]), η αστράγγιστη διατμητική αντοχή S_u εκτιμάται κατά τον Weiler (1988), ο οποίος μέτρησε το S_u σε ανακυκλικές, αστράγγιστες, τριαξονικές δοκιμές συμπίεσης και συσχέτισε το λόγο G_{max} / S_u με το δείκτη πλασιμότητας *PI* και τον δείκτη υπερστερεοποίησης *OCR* (Kramer, 1996).

Βαθμονόμηση καταστατικού προσομοιώματος

Άμμος - στραγγιζόμενες συνθήκες φόρτισης

Η βαθμονόμηση του καταστατικού προσομοιώματος για στραγγιζόμενες συνθήκες φόρτισης βασίζεται στην αναπαραγωγή πειραματικών καμπυλών μείωσης του μέτρου διάτμησης και αύξησης της απόσβεσης, που καταδεικνύονται από τη διεθνή βιβλιογραφία. Το μοντέλο βαθμονομήθηκε για τρεις οικογένειες δημοσιευμένων καμπυλών *G:γ* , *ξ:γ* : (i) από τους

Ishibashi και Zhang (1993), (ii) από τους Vucetic και Dobry (1991) και (iii) από τους Darendeli et al. (2001). Τα αποτελέσματα παρουσιάζονται στο Σχήμα 1, μόνο για τις καμπύλες κατά Ishibashi and Zhang (1993) όπου έχει υποτεθεί δείκτης πλασιμότητας *PI* = 0, για 7 στάθμες μέσης ενεργού τάσης *p'(=20, 50, 100, 200, 300, 400, 500 kPa)*. Η σύγκλιση με όλες τις οικογένειες πειραματικών καμπυλών κρίνεται ικανοποιητική. Ωστόσο, η προσέγγιση των καμπυλών μείωσης του μέτρου διάτμησης γίνεται λιγότερο ακριβής καθώς αυξάνεται η τάση συμπίεσης, αντίθετα από την καμπύλη της απόσβεσης όπου οι αποκλίσεις αυξάνονται με τη μείωση της τάσης.

Άργιλος – αστράγγιστες συνθήκες φόρτισης

Εκτελώντας αριθμητικές δοκιμές απευθείας απλής διάτμησης, η απλοποιημένη εκδοχή του μοντέλου για αργίλους βαθμονομήθηκε ώστε να προσομοιάζει την πειραματική συμπεριφορά σε όρους καμπυλών μέτρου διάτμησης και απόσβεσης, συναρτήσει της τάσης και του δείκτη πλασιμότητας *PI*. Χρησιμοποιήθηκαν 2 οικογένειες πειραματικών καμπυλών *G:γ* , *ξ:γ* : (i) οι καμπύλες κατά Ishibashi and Zhang (1993), (ii) και Vucetic and Dobry (1991). Η σύγκλιση για την περίπτωση (i) παρουσιάζεται στο Σχήμα 1, για δείκτες πλασιμότητας: $0 < PI \leq 15,\ 15 < PI \leq 70$ και $70 \leq PI$.

Άμμος - αστράγγιστες συνθήκες φόρτισης

Η καμπύλη ανακυκλικής αντοχής σε ρευστοποίηση της καθαρής άμμου που προτάθηκε από τους Idriss and Boulanger, (2004, 2008):

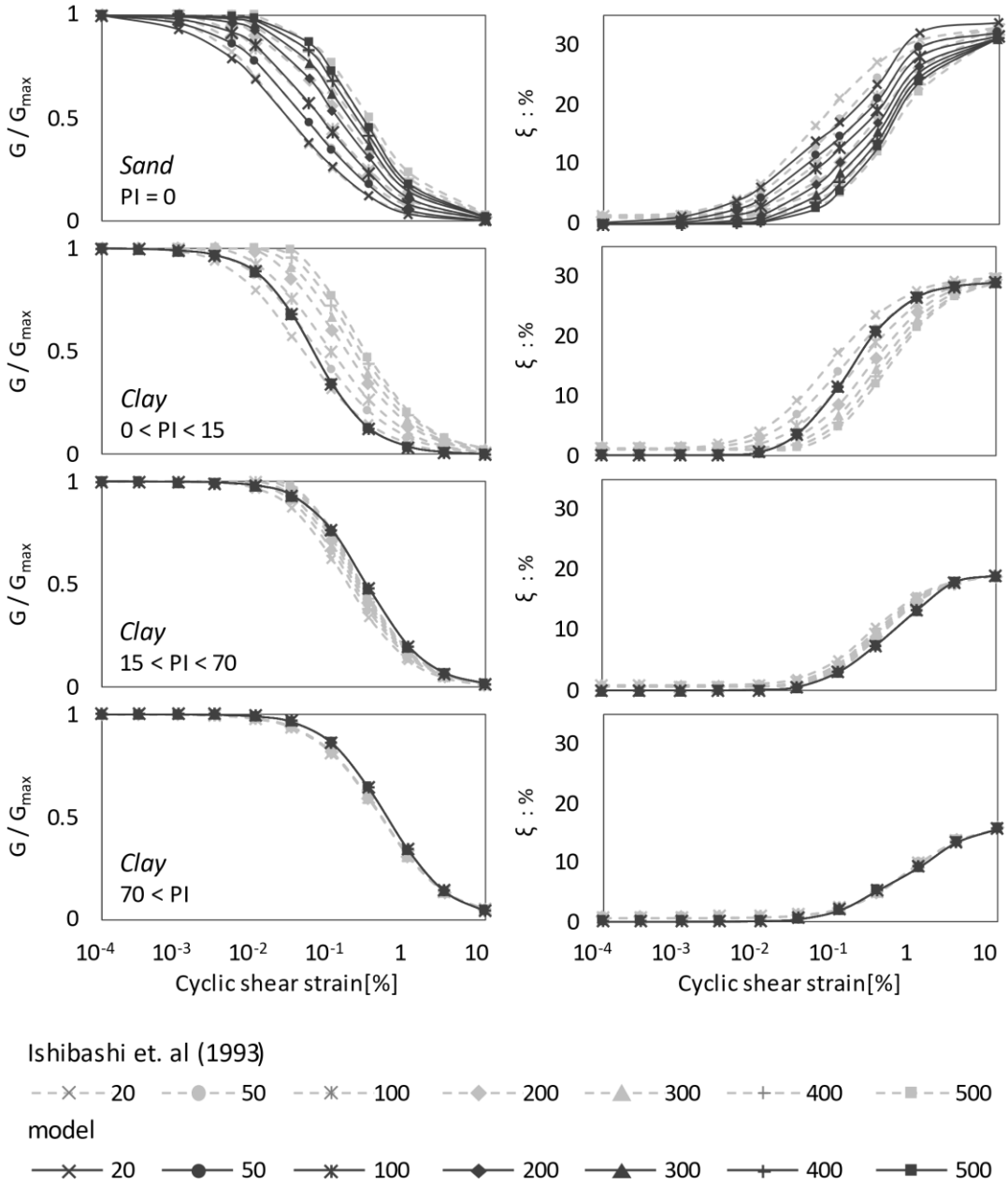

Σχήμα 1. Προσέγγιση από το βαθμονομημένο μοντέλο των καμπυλών μέτρου διάτμησης και απόσβεσης κατά Ishibashi & Zhang (1993) για άμμο (*PI=0*) και άργιλο (*0<PI<15, 15<PI<7 0 & 70<PI*) υπό κατακόρυφες τάσεις 20, 50, 100, 200, 300, 400 και 500 kPa.

$$CRR_{M_w=7.5,\sigma'_v=1atm} = exp\left\{\frac{(N_1)_{60cs}}{14.1} + \left[\frac{(N_1)_{60cs}}{126}\right]^2 - \left[\frac{(N_1)_{60cs}}{23.6}\right]^3 + \left[\frac{(N_1)_{60cs}}{25.4}\right]^4 - 2.8\right\} \qquad [11]$$

παρέχει το λόγο ανακυκλικής αντοχής αναφοράς, υπό κατακόρυφη ενεργό τάση ίση με 1 atm και μέγεθος σεισμού 7.5, συναρτήσει του διορθωμένου αριθμού *SPT*, $(N_1)_{60cs}$. Η αντοχή για σεισμικά μεγέθη διαφορετικά του 7.5, υπολογίζεται βάσει των συντελεστών διόρθωσης λόγω

σεισμικού μεγέθους “magnitude scaling factors” (*MSFs*). Κατά αυτόν τον τρόπο, ο συντελεστής ασφαλείας έναντι ρευστοποίησης ορίζεται ως:

$$FS = \left(\frac{CRR_{7.5}}{CSR}\right) MSF \quad [12]$$

, όπου *CSR* είναι η λόγος ανακυκλικής τάσης που προκαλείται από τη σεισμική διέγερση και $CRR_{7.5}$ είναι ο λόγος ανακυκλικής αντοχής για σεισμούς μεγέθους 7.5. Για τους σκοπούς της παρούσας διαδικασίας βαθμονόμησης, επιλέγονται οι καμπύλες *MSF* που προτάθηκαν από τους: (i) Idriss (1995) και (ii) Andrus και Stokoe (1997), οι οποίες θεωρούνται ως το κάτω και το πάνω όριο αντίστοιχα, του αποδεκτού εύρους των εκτιμήσεων της αντοχής σε ρευστοποίηση, σύμφωνα με τις επιταγές του 1998 NCEER/NSF workshop (Youd, 2001). Υιοθετώντας την Εξίσωση [11] και εκφράζοντας το $(N_1)_{60cs}$. ως προς τη σχετική πυκνότητα της άμμου (Idriss and Boulanger, 2010):

$$(N_1)_{60cs} = 46{D_r}^2 \quad [13]$$

η καμπύλη αντίστασης σε ρευστοποίηση για M_w=7.5, διατυπώνεται συναρτήσει του D_r. Έπειτα συσχετίζοντας το μέγεθος σεισμού M_w με τον ισοδύναμο αριθμό ομοιόμορφων κύκλων της σεισμικής διέγερσης (εμπειρική φόρμουλα κατά τους Seed and Idriss, 1982):

$$N_{cycle} = 0.0034{M_w}^{4.18} \quad [14]$$

και πολλαπλασιάζοντας τον λόγο αντίστασης αναφοράς ($CRR_{M=7.5,\ \sigma'v=1atm}$) με τον συντελεστή *MSF*, *η* αντίσταση στη ρευστοποίηση μπορεί να υπολογιστεί απευθείας ως συνάρτηση της σχετικής πυκνότητας και του αριθμού των ομοιόμορφων κύκλων φόρτισης. Θεωρείται πως, η αντίσταση αναφοράς καθώς βασίζεται σε παρατηρήσεις, αναφέρεται σε ανισοτροπικές συνθήκες στερεοποίησης με K_0 = 0.5. Απαιτείται επομένως η μετατροπή της καμπύλης *CRR* ώστε να αναφέρεται σε ισοτροπικές συνθήκες, με βάση τη συσχέτιση:

$$CRR_{K_0 \neq 1} = \left(\frac{1+2K_0}{3}\right) CRR_{K_0=1} \quad [15]$$

, η οποία έχει συχνές εφαρμογές στη βιβλιογραφία (π.χ. Idriss και Boulanger, 2010). Η επιλογή ισοτροπικών συνθηκών στερεοποίησης είναι σκόπιμη, καθώς η ανισοτροπική στερεοποίηση δεν είναι συμβατή με την καταστατική προσομοίωση σε όρους *p-q*. Είναι σαφές, ότι η επίδραση του συντελεστή ουδετέρων ωθήσεων K_0 αποδίδεται μόνο εμμέσως από το μοντέλο Ta-Ger, εκφρασμένο σε όρους *p-q*.

Η μη γραμμική σχέση μεταξύ του *CRR* και της ενεργού τάσης των υπερκείμενων γαιών αποκαθίσταται μέσω του συντελεστή διόρθωσης λόγω τάσης υπερκείμενων K_σ, για πιέσεις μεγαλύτερες από 1 atm, ως ακολούθως (NCEER 1996, 1998 workshops, Youd 2001):

$$CRR_{\sigma'_{vo}\neq 100} = K_\sigma CRR_{\sigma'_{vo}=100} \quad [16]$$

Η καμπύλη αντίστασης αναφοράς για ισοτροπικές συνθήκες στερεοποίησης (M_w=*7.5,* σ'_{v0}=*1atm και* K_0=*1*) που αποδίδεται από το βαθμονομημένο μοντέλο, συναρτήσει του διορθωμένου αριθμού κρούσεων *SPT*, παρουσιάζεται στο Σχήμα 2, σε σύγκριση με την καμπύλη σχεδιασμού κατά Idriss and Boulanger (2004, 2008) τροποποιημένη σύμφωνα με την Εξίσωση [15]. Για σχετικές πυκνότητες μεγαλύτερες από 60% η σύγκλιση είναι λιγότερο ικανοποιητική καθώς το μοντέλο φαίνεται να υπερεκτιμά την πιθανότητα ρευστοποίησης.

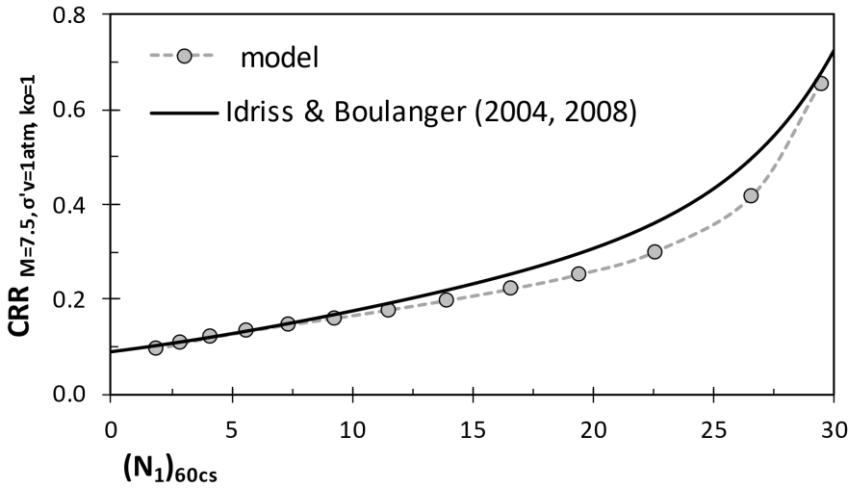

Σχήμα 2. Πρόβλεψη του προτεινόμενου μοντέλου σε σύγκριση με τις τιμές κατά Idriss and Boulanger (2004, 2008) για το λόγο ανακυκλικής αντίστασης σε ρευστοποίηση (M_w=7.5, σ'_v=1atm), τροποποιημένο σύμφωνα με την Εξίσωση [15] ώστε να αναφέρεται σε ισοτροπικές συνθήκες στερεοποίησης, ως προς το διορθωμένο *SPT*.

Η σύγκριση μεταξύ των προτεινόμενων τιμών και των προβλέψεων του βαθμονομημένου μοντέλου για το λόγο ανακυκλικής αντίστασης σε σχέση με τον αριθμό των ισοδύναμων κύκλων ώστε να προκληθεί αρχική ρευστοποίηση, παρουσιάζεται στο Σχήμα 3, για 5 τιμές της σχετικής πυκνότητας. Η σύγκριση παρουσιάζεται επίσης και σε όρους *MSF* ως προς M_w. Η επίδραση της τάσης των υπερκείμενων γαιών στην πρόβλεψη της αντοχής από το βαθμονομημένο μοντέλο απεικονίζεται στο Σχήμα 4. Σημειώνεται, πως τα αποτελέσματα που παρουσιάζονται στα Σχήματα 2, 3 και 4 έχουν παραχθεί θεωρώντας τις τιμές για τις

παραμέτρους του μοντέλου που επιλέχθησαν για την βαθμονόμηση σύμφωνα με την καμπύλη *MSF* κατά Idriss (1995).

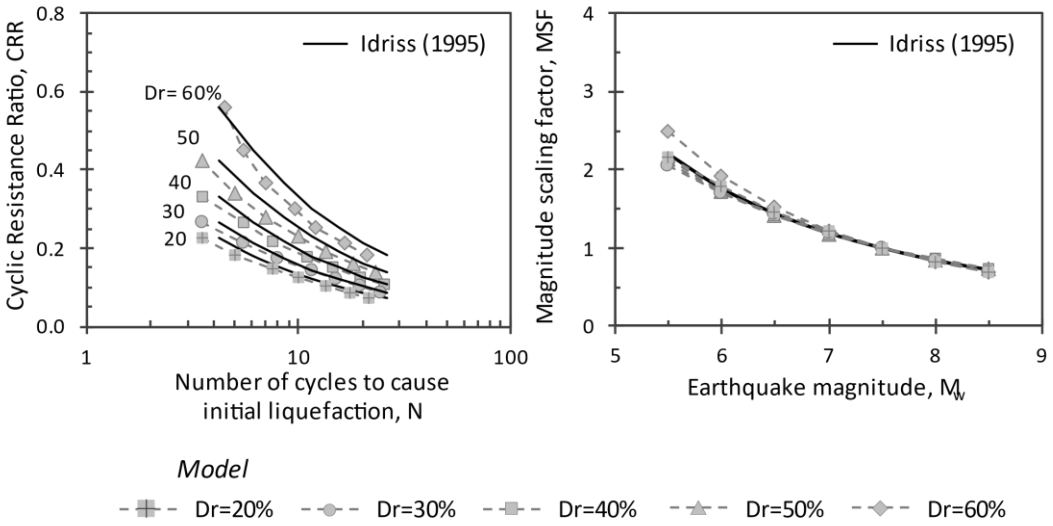

Σχήμα 3. [αριστερά] Λόγοι ανακυκλικής αντίστασης σε ρευστοποίηση συναρτήσει του ισοδύναμου αριθμού ομοιόμορφων κύκλων ώστε να προκληθεί αρχική ρευστοποίηση, για επιλεγμένες τιμές της σχετικής πυκνότητας (D_r = 20%, 30%, 40%, 50%, 60%). Σύγκριση μεταξύ των προβλέψεων του βαθμονομημένου μοντέλου και των καμπυλών που προκύπτουν από την καμπύλη MSF κατά Idriss (1995) σε συνδυασμό με το $CRR_{Mw=7.5,\sigma'v0=1atm}$ κατά Idriss & Boulanger (2004, 2008) και την Εξίσωση [15]. [δεξιά] Συντελεστής διόρθωσης για το σεισμικό μέγεθος *MSF* κατά Idriss (1995) συναρτήσει του σεισμικού μεγέθους που απαιτείται ώστε να προκληθεί αρχική ρευστοποίηση.

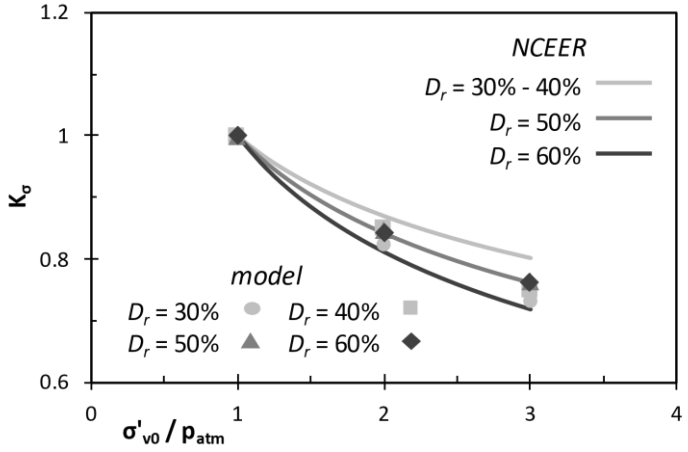

Σχήμα 4. Σύγκριση του παράγοντα K_σ που προβλέπεται από το βαθμονομημένο μοντέλο για επιλεγμένες τιμές της σχετικής πυκνότητας (D_r = 30%, 40%, 50%, 60%) για αρχική ρευστοποίηση σε 15 ομοιόμορφους κύκλους φόρτισης, σε σύγκριση με τις προτεινόμενες σχέσεις κατά το 1996 NCEER/1998 NCEER/NSF workshop (Youd, 2001).

Ανάπτυξη αριθμητικού αλγορίθμου για τη μονοδιάστατη, μη γραμμική, σεισμική απόκριση του εδάφους

Η απόκριση ενός πολύστρωτου εδαφικού σχηματισμού υποβαλλόμενου σε σεισμική διέγερση στη βάση του, διέπεται από την ακόλουθη διαφορική εξίσωση που εκφράζει τη μονοδιάστατη κατακόρυφη διάδοση του διατμητικού κύματος:

$$\rho \frac{\vartheta^2 u(t,z)}{\vartheta t^2} = \frac{\vartheta \tau(t,z)}{\vartheta z} + c \frac{\vartheta^3 u(t,z)}{\vartheta z^2 \vartheta t} \quad [17]$$

, όπου *z* είναι το βάθος από την επιφάνεια, *t* είναι ο χρόνος, *u* είναι η οριζόντια εδαφική μετακίνηση, *τ* είναι η διατμητική τάση του εδάφους, *ρ* η πυκνότητα του και το *c* αποτελεί ιξωδοελαστική σταθερά. Οι συνοριακές συνθήκες στη βάση *z*=H (βραχώδες υπόβαθρο) και στην ελεύθερη επιφάνεια του εδαφικού προφίλ *z=0,* είναι αντίστοιχα:

$$\tau(t,H) + c \frac{\vartheta^2 u(t,H)}{\vartheta z \vartheta t} = \rho_r V_r \left[\frac{du(t,H)}{dt} - \frac{du_g(t)}{dt}\right] \quad [18]$$

και

$$\frac{du(t,0)}{dz} = 0 \quad [19]$$

, όπου ρ_r και V_r είναι η πυκνότητα και η ταχύτητα διατμητικού κύματος αντίστοιχα του βράχου, *H* είναι το βάθος του εδαφικού προφίλ και u_g=$u_g(t)$ η χρονοϊστορία των μετακινήσεων της εισαχθείσας κίνησης του βραχώδους υποβάθρου (rock outcrop motion). Η επίλυση της διαφορικής Εξίσωσης [17] που βρίσκεται σε σύζευξη με την καταστατική Εξίσωση [1] και τις συνοριακές συνθήκες [18] και [19] βασίζεται στην κεντρική άμεση μέθοδο των πεπερασμένων διαφορών και εκτελείται εντός αριθμητικού αλγορίθμου, στη γλώσσα προγραμματισμού MATLAB.

Κατόπιν, ο αναπτυχθείς αλγόριθμος κυματικής απόκρισης του εδάφους επεκτείνεται ώστε να λαμβάνεται υπόψιν η ταυτόχρονη αποτόνωση των υπερπιέσεων των πόρων που αναπτύσσονται κατά την σεισμική διέγερση κορεσμένου μη συνεκτικού εδάφους, μέσω της κατακόρυφης στερεοποίησης του. Η αστράγγιστη φόρτιση μη συνεκτικού κορεσμένου εδάφους οδηγεί στην ανάπτυξη υπερπιέσεων του νερού των πόρων, που προκαλεί τη ροή του νερού διαμέσου των πόρων του εδάφους. Η κίνηση του νερού επιφέρει την αλλαγή του όγκου των εδαφικών πόρων, δηλ. προκαλεί ογκομετρικές παραμορφώσεις που οδηγούν κατ'

επέκταση σε μεταβολή των ενεργών τάσεων. Το φαινόμενο αυτό ονομάζεται εδαφική στερεοποίηση.

Λαμβάνοντας υπόψιν την αρχή διατήρησης της μάζας του νερού στους πόρους του εδάφους, το νόμο ροής του Darcy και υποθέτοντας ότι η ροή του νερού λαμβάνει χώρα μόνο κατά τον κατακόρυφο άξονα, προκύπτει η εξίσωση της μονοδιάστατης (κατακόρυφης) εδαφικής στερεοποίησης:

$$\frac{k}{\gamma_w}\frac{\vartheta^2 u_p(t,z)}{\vartheta z^2} = -\frac{\vartheta \varepsilon_{vol(t,z)}}{\vartheta t} \quad [20]$$

, που συσχετίζει την υπερπίεση του νερού των πόρων u_p με την εδαφική ογκομετρική παραμόρφωση ε_{vol}, όπου k η διαπερατότητα του εδάφους και γ_w το ειδικό βάρος του νερού. Η επίλυση της διαφορικής εξίσωσης της κατακόρυφης στερεοποίησης εδαφικού σχηματισμού λόγω επιβολής εξωτερικού επιφανειακού φορτίου q, με τη μέθοδο των πεπερασμένων διαφορών, επαληθεύτηκε μέσω σύγκρισης με την αναλυτική λύση κατά Terzaghi.

Επαλήθευση με αναλυτικές λύσεις

Η επίλυση της διαφορικής εξίσωσης της μονοδιάστατης κατακόρυφης διάδοσης σεισμικού κύματος με τη μέθοδο των πεπερασμένων διαφορών επαληθεύτηκε μέσω σύγκρισης με την αναλυτική λύση (Gazetas, 1982), για διάφορες γραμμικές κατανομές της διατμητικής ταχύτητας V_s με το βάθος:

$$V_s = V_{s0}(1 + bz) \quad [21]$$

, όπου V_{s0} είναι η ταχύτητα στην επιφάνεια, z είναι το βάθος από την επιφάνεια και b είναι ο βαθμός ανομοιογένειας. Εισάγεται ο αδιάστατος βαθμός ανομοιογένειας $\hat{b}$ (Gazetas, 1982) ως εξής:

$$\hat{b} = bH \quad [22]$$

Η σύγκριση μεταξύ των προβλέψεων του μοντέλου και των αναλυτικών λύσεων απεικονίζεται στο Σχήμα 5 για λόγους υστερητικής απόσβεσης 5% και 10%, για 4 περιπτώσεις γραμμικών κατανομών V_s με το βάθος, για εδαφικό προφίλ ύψους H=20m και πυκνότητας

ρ=2t/m^3. Δίδεται επίσης, ο συντελεστής εδαφικής ενίσχυσης του ομοιογενούς προφίλ, συναρτήσει του συντελεστή:

$$\alpha_0 = \omega H / V_{s0} \quad [23]$$

Παρατηρείται ότι η απόκλιση μεταξύ αναλυτικών και αριθμητικών αποτελεσμάτων αυξάνεται, αυξανομένου του βαθμού ανομοιογένειας $\hat{b}$ και γίνεται σημαντική για τιμές του $\hat{b}$ μεγαλύτερες του 6, κάτι που μπορεί να μετριαστεί με μείωση του χρονικού και του χωρικού βήματος εις βάρος του υπολογιστικού κόστους.

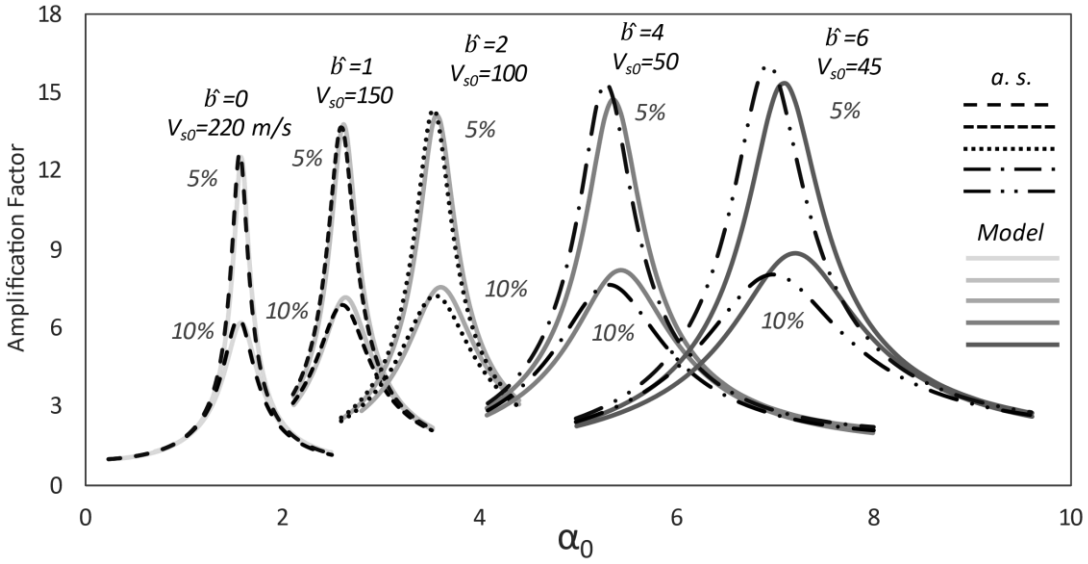

Σχήμα 5. Συντελεστές εδαφικής ενίσχυσης 4 εδαφικών προφίλ με γραμμικώς αυξανόμενη ταχύτητα διατμητικού κύματος V_s με το βάθος και του ομοιογενούς προφίλ, για υστερητική απόσβεση 5% και 10%, σε σύγκριση με τις αναλυτικές λύσεις κατά Gazetas (1982).

Επικύρωση του αριθμητικού αλγορίθμου

Επικύρωση βάσει πειραμάτων φυγοκεντριστή

Η απόδοση του προτεινόμενου μοντέλου επικυρώνεται βάσει δύο πειραμάτων σε φυγοκεντριστή, που εκτελέστηκαν στο Πανεπιστήμιο του Colorado Boulder από τους Hashash et al. (2015) και αναφέρονται στη διερεύνηση της μη γραμμικής απόκρισης εδαφικού προφίλ, υποβαλλόμενου σε σειρά σεισμικών διεγέρσεων στη βάση του. Πρόκειται για μία στρώση 26m (σε πρωτότυπη κλίμακα) ξηρής άμμου Nevada #120, για την οποία μετρήθηκαν τα εξής χαρακτηριστικά: D_r=60%, e_{min}=0.586, e_{max}=0.852, $\gamma_{d,min}$=14kN/m^3 και $\gamma_{d,max}$

=16.39kN/m^3. Προκειμένου να υπάρξει ένα μέτρο σύγκρισης ώστε να εκτιμηθεί το μέγεθος των αποκλίσεων μεταξύ των προβλέψεων του μοντέλου Ta-Ger και των πειραματικών αποτελεσμάτων, παρουσιάζονται ακόμα τα αποτελέσματα της προσομοίωσης του πειράματος με χρήση του αλγορίθμου για την πρόβλεψη της σεισμικής απόκρισης εδάφους DEEPSOIL v5.0 που εκτελέστηκε από τους Hashash et al. (2015).

Η διαδικασία βαθμονόμησης του μοντέλου Ta-Ger εφαρμόζεται όπως παρουσιάστηκε στη σχετική παράγραφο. Για τον υπολογισμό του ελαστικού μέτρου διάτμησης εφαρμόστηκε η Εξίσωση [2], ενώ η βαθμονόμηση των υπόλοιπων παραμέτρων βασίστηκε στις καμπύλες *G:γ*, *ξ:γ* κατά Vucetic et. al (1991).

Εξετάστηκαν δυο περιπτώσεις σεισμικών διεγέρσεων βάσης: (i) η καταγραφή Loma Prieta 1989 (station name: Santa Cruz Lick Observation) και (ii) η καταγραφή Kobe 1995 (station name: Takatori). Για την ανάλυση με το μοντέλο Ta-Ger ως διεγέρσεις βάσης χρησιμοποιήθηκαν οι καταγραφές που είναι διαθέσιμες στο Strong motion virtual data center VDC, ενώ στην ανάλυση με το DEEPSOIL (Hashash et.al, 2015) χρησιμοποιηθήκαν εκείνες που καταγράφηκαν στη βάση του φυγοκεντριστή, στη διάρκεια του πειράματος.

Στα Σχήματα 6 και 7 παρουσιάζεται η σύγκριση των πειραματικών αποτελεσμάτων με τις προβλέψεις των μοντέλων σε όρους: (i) προφίλ μέγιστων μετακινήσεων, διατμητικών παραμορφώσεων και επιταχύνσεων και (ii) φασμάτων απόκρισης επιταχύνσεων και χρονοϊστοριών του μεγέθους Arias Intensity στην επιφάνεια. Η σύγκλιση των κατανομών καθ' ύψος για την ασθενή διέγερση (Σχήμα 6) κρίνεται και για τα δύο μοντέλα ικανοποιητική. Το μοντέλο Ta-Ger προβλέπει με μεγαλύτερη ακρίβεια τις μέγιστες μετακινήσεις και διατμητικές παραμορφώσεις σε μικρότερα βάθη ενώ το DEEPSOIL παρουσιάζει καλύτερη απόδοση στις μέγιστες επιταχύνσεις σε μικρά βάθη και στις μέγιστες διατμητικές παραμορφώσεις στα μεσαία βάθη. Αναφορικά με τις φασματικές επιταχύνσεις επιφανείας και τα δυο μοντέλα αποδίδουν επαρκώς, ενώ παρατηρείται υποεκτίμηση της απόκρισης στις υψηλές συχνότητες και υπερεκτίμηση στις χαμηλές συχνότητες, και από τα δύο μοντέλα Παρατηρείται επίσης, σημαντική υπερεκτίμηση των φασματικών επιταχύνσεων και στα δύο μοντέλα, για τις περιόδους από 0.3s έως 0.6s περίπου, που είναι περισσότερο έντονη (σχεδόν διπλάσια) στην ανάλυση με το μοντέλο Ta-Ger. Τέλος, το μετρηθέν μέγεθος Arias Intensity αναπαράγεται με εξαιρετική ακρίβεια και από τα δύο μοντέλα.

Η ακρίβεια των προβλέψεων των μοντέλων στην ισχυρή διέγερση (Σχήμα 7) βρίσκεται μέσα στα αποδεκτά όρια, με το μοντέλο DEEPSOIL να σημειώνει καλύτερη απόδοση σχεδόν σε όλες τις περιπτώσεις, εκτός από την κατανομή των μέγιστων διατμητικών παραμορφώσεων, όπου η υπεροχή του μοντέλου Ta-Ger είναι εμφανής. Η καταγεγραμμένη μέγιστη φασματική επιτάχυνση επιφανείας σημειώνεται για T= 1.2s και ισούται με 2.3g, έναντι 3.2g που προβλέπονται από το μοντέλο Ta-Ger και 2.5g από το DEEPSOIL. Το διάγραμμα των φασματικών επιταχύνσεων του μοντέλου Ta-Ger εμφανίζει περίπου την ίδια μορφή με το καταγεγραμμένο, ωστόσο αποδίδει συστηματικά μεγαλύτερες επιταχύνσεις για ένα μεγάλο εύρος περιόδων. Αντίστοιχα συμπεράσματα προκύπτουν και από τις τιμές του Arias Intensity, που ξεπερνούν τις καταγεγραμμένες κατά 35% στην περίπτωση του μοντέλου Ta-Ger και κατά 29% στου DEEPSOIL.

Σε γενικές γραμμές, το μοντέλο Ta-Ger επιδεικνύει πιο δύσκαμπτη συμπεριφορά σε σχέση με το DEEPSOIL, κάτι που αποτυπώνεται στις υψηλότερες φασματικές επιταχύνσεις στην επιφάνεια, και στα υψηλότερα PGA και τις περιορισμένες διατμητικές παραμορφώσεις σε μικρά βάθη. Αντίθετα, το μοντέλο DEEPSOIL υπερεκτιμά την απόκριση σε όρους διατμητικών παραμορφώσεων κοντά στην επιφάνεια, ενώ προβλέπει με ακρίβεια τις φασματικές επιταχύνσεις στην επιφάνεια και τις τιμές του PGA. Οι αποκλίσεις αυτές μεταξύ των δύο μοντέλων θα μπορούσαν να αποδοθούν, πέρα από τη διαφορετική μαθηματική διατύπωση τους, στο γεγονός ότι ενώ και οι δύο προσεγγίσεις συμμορφώνονται με τα εδαφικά χαρακτηριστικά που μετρήθηκαν στο εργαστήριο (D_r, e_{min}, e_{max}, $\gamma_{d,min}$, $\gamma_{d,max}$), στη συνέχεια έχουν εφαρμοστεί διαφορετικές διαδικασίες βαθμονόμησης και υιοθετούνται διαφορετικές συσχετίσεις για την κατανομή του V_s και των καμπυλών μέτρου διάτμησης και απόσβεσης. Επιπλέον, υπενθυμίζεται ότι η ακρίβεια των προβλέψεων του μοντέλου Ta-Ger μετριάζεται από το γεγονός ότι η διέγερση βάσης που χρησιμοποιήθηκε ήταν ελαφρώς διαφορετική, δεδομένου ότι η πραγματική κίνηση που επιβλήθηκε ως διέγερση στη βάση του φυγοκεντριστή και χρησιμοποιήθηκε για την ανάλυση με το DEEPSOIL δεν ήταν διαθέσιμη. Ωστόσο, στην παρούσα εργασία δεν επιδιώκεται η σύγκριση μεταξύ των 2 μοντέλων, αλλά η παροχή ενός μέτρου σύγκρισης για την εκτίμηση των αποκλίσεων μεταξύ των πειραματικών αποτελεσμάτων και των προβλέψεων του μοντέλου Ta-Ger.

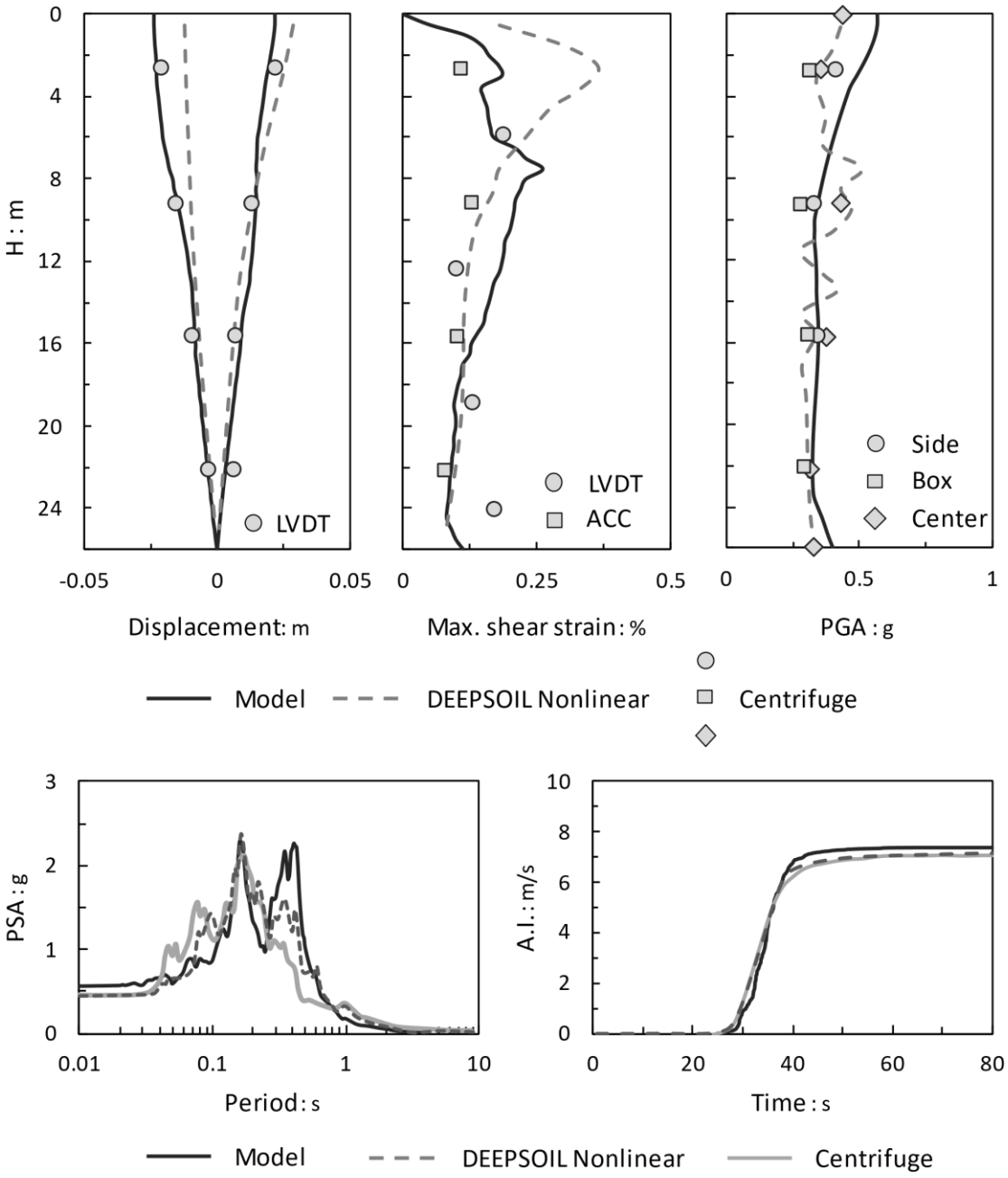

Σχήμα 6. Μετρήσεις φυγοκεντριστή σε σύγκριση με τις προβλέψεις των μοντέλων Ta-Ger και DEEPSOIL (διέγερση βάσης: Loma Prieta).

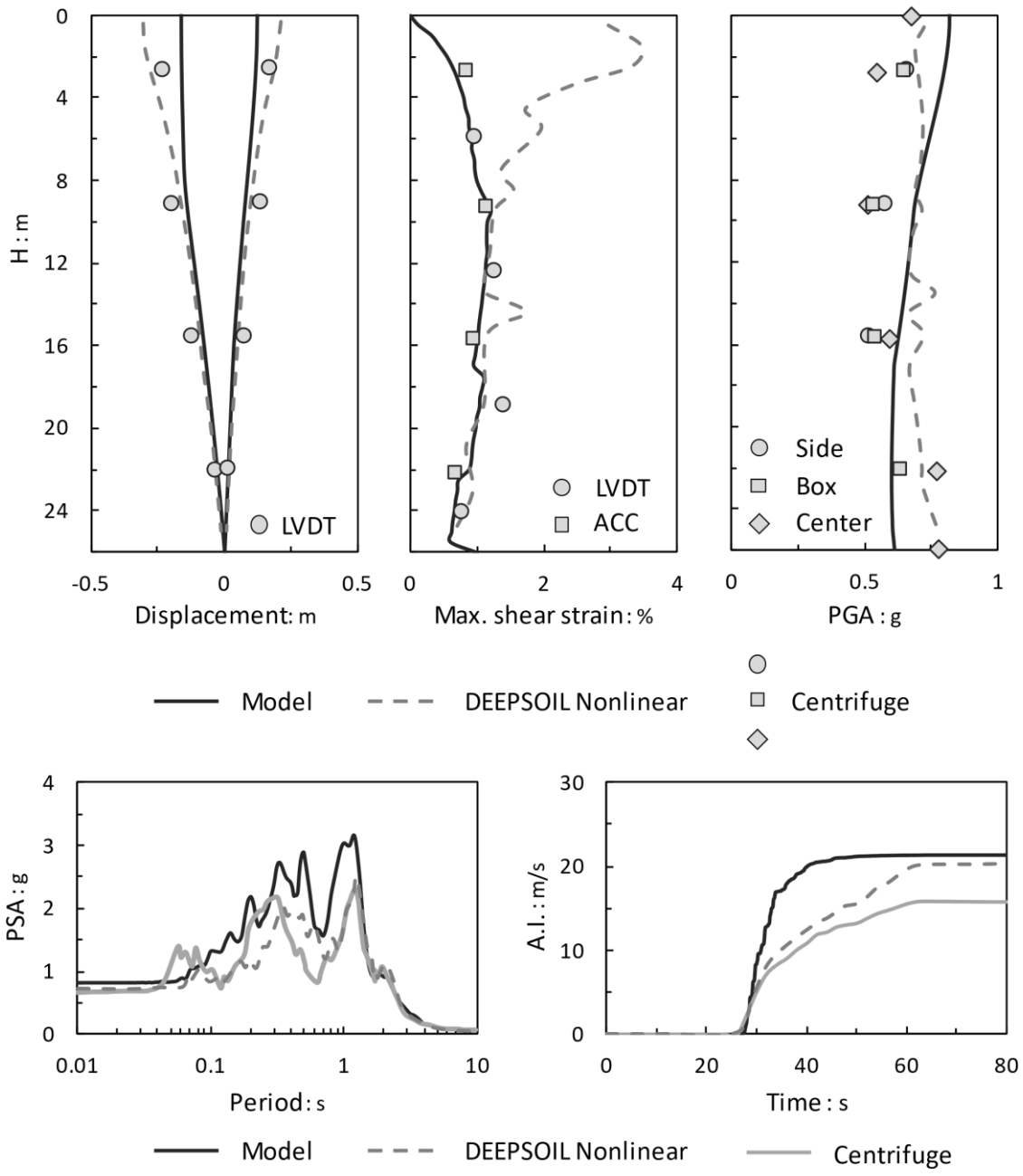

Σχήμα 7. Μετρήσεις φυγοκεντριστή σε σύγκριση με τις προβλέψεις των μοντέλων Ta-Ger και DEEPSOIL (διέγερση βάσης: Kobe Takatori).

Επικύρωση με βάση το ιστορικό περιστατικό του σεισμού του 1995 στο Kobe της Ιαπωνίας

Ο αλγόριθμος κυματικής απόκρισης επιστρατεύεται περαιτέρω για την πρόβλεψη της σεισμικής απόκρισης του πεδίου στη νότια περιοχή του Port Island, στο Kobe της Ιαπωνίας, στο σεισμό του 1995 (Iwasaki, 1996). Η κατακόρυφη σειρά από σεισμογράφους που κατέγραψαν την εδαφική κίνηση στα 0m, -16m, -32m και -83m στη διάρκεια του σεισμού Hyogo-ken Nanbu, σε συνδυασμό με την ενδελεχή γεωτεχνική έρευνα που διεξήχθη πριν και μετά από το συμβάν, χρησιμοποιούνται ως σημείο αναφοράς για τον έλεγχο της εγκυρότητας του προτεινόμενου μοντέλου.

Η διακριτοποίηση του εδαφικού προφίλ σε στρώσεις και τα χαρακτηριστικά της κάθε μίας, που θεωρήθηκαν για την αριθμητική ανάλυση συνοψίζονται στον Πίνακα 1. Η στρωματογραφία του πεδίου στη θέση που ήταν εγκατεστημένοι οι σεισμογράφοι, οι ταχύτητες των κυμάτων V_s και V_p (από *PS* logging που διεξήχθη στο πεδίο) και ο αριθμός των κρούσεων *SPT* αντλήθηκαν από τη βιβλιογραφία (Iwasaki 1995, 1996). Ο υδροφόρος ορίζοντας βρέθηκε σε βάθος 3m. Η σχετική πυκνότητα D_r υπολογίστηκε από την Εξίσωση [13] για τις αμμώδεις στρώσεις και η κατανομή του ελαστικού μέτρου διάτμησης G_{max} υπολογίστηκε σύμφωνα με τη σχέση:

$$G_{max} = \rho \, V_S{}^2 \qquad [24]$$

, όπου ρ είναι η πυκνότητα του εδάφους σύμφωνα με το κορεσμένο ειδικό βάρος του Πίνακα 1. Η αστράγγιστη διατμητική αντοχή των αργιλικών στρωμάτων #4 και #8 εκτιμήθηκε βάσει του G_{max} (Weiler, 1988), υποθέτοντας δείκτη υπερστερεοποίησης *OCR* ίσο με 1 και δείκτη πλασιμότητας *PI* ίσο με 25. Η βαθμονόμηση των υπόλοιπων παραμέτρων του μοντέλου βασίστηκε στις καμπύλες $G{:}\gamma$, $\xi{:}\gamma$ κατά Ishibashi and Zhang (1993) και στην καμπύλη *MSF* κατά Idriss (1995). Η κυματική ανάλυση εκτελέστηκε: (i) θεωρώντας πλήρως αστράγγιστες συνθήκες φόρτισης για τα στρώματα #3 έως #9 και πλήρως στραγγιζόμενες συνθήκες για τα επιφανειακά στρώματα #1 και #2 και (ii) λαμβάνοντας υπόψη την ταυτόχρονη κατακόρυφη στερεοποίηση των σχηματισμών σύμφωνα με τις διαπερατότητες *k* του Πίνακα 1.

Η σύγκριση των καταγεγραμμένων κινήσεων με τις προβλέψεις του μοντέλου παρουσιάζεται στο Σχήμα 8 για την επιφάνεια, τα -16m, -32m και -83 m. Εκτός από την περίπτωση των -16m

όπου ο αλγόριθμος υποτιμά σημαντικά την συμπεριφορά, η σύγκλιση είναι αρκετά ικανοποιητική. Ακόμη, διαπιστώνεται ότι οι αποκλίσεις μεταξύ των δύο αριθμητικών προσεγγίσεων που εκτελέστηκαν είναι αμελητέες. Η έντονη εξασθένιση των επιταχύνσεων στην επιφάνεια που καταδεικνύουν οι καταγραφές, και αναπαράγεται με αξιοσημείωτη ακρίβεια από το μοντέλο, θεωρείται ότι οφείλεται στη ρευστοποίηση που υπέστη το υλικό εξυγίανσης σε βάθος -19m (πρόκειται για τη βάση της αμμώδους στρώσης #3), σύμφωνα με τον Iwasaki (1995). Το γεγονός της ρευστοποίησης τεκμηριώνεται επίσης και από επιτόπου μετρήσεις των πιέσεων

Πίνακας 1. Διακριτοποίηση εδαφικών στρώσεων: ταχύτητα *P* και *S* κυμάτων από PS-logging και αριθμός κρούσεων $(N_1)_{60}$ κατά Iwasaki (1995). Δίδονται επίσης οι υπολογισθείσες/ εκτιμώμενες τιμές της σχετικής πυκνότητας D_r, του ελαστικού μέτρου διάτμησης G_{max}, της αστράγγιστης διατμητικής αντοχής S_u, του κορεσμένου ειδικού βάρους γ_{sat} και της διαπερατότητας *k* που θεωρήθηκαν για την ανάλυση με το προτεινόμενο μοντέλο. (*reclamation soil: χαλικοαμμώδης στρώση υψηλής διαπερατότητας και πολύ χαμηλής εκτιμώμενης αντοχής).

Layer #	Depth (m)	Soil Type	V_p (m/s)	V_s (m/s)	$(N_1)_{60}$	D_r	G_{max} (kPa)	S_u (kPa)	γ_{sat} (kN/m^3)	k (m/s)
1	0-5	Gravel*	305	170	4	0.29	57.8	-	20	10^{-4}
2	5-13	Gravel*	780	210	4	0.29	88.2	-	20	10^{-4}
3	13-19	Gravelly sand	1480	210	6	0.36	88.2	-	20	10^{-4}
4	19-27	Alluvial clay	1180	180	-	-	58.32	82	18	10^{-9}
5	27-33	Sand	1350	245	25	0.74	120.1	-	20	10^{-6}
6	33-50	Sand / Gravelly Sand	1530	305	40	0.93	186.1	-	20	10^{-6}
7	50-61	Sand	1610	350	45	0.99	245.0	-	20	10^{-6}
8	61-79	Stiff alluvial clay	1610	303	-	-	165.3	233	18	10^{-9}
9	79-83	Gravelly sand	2000	320	60	1.00	204.8	-	20	10^{-6}

πόρων σε ένα πεδίο νοτιότερα από το σημείο όπου ήταν τοποθετημένοι οι σεισμογράφοι, αλλά με παρόμοιες γεωλογικές συνθήκες. Στην περιοχή εκείνη, οι μετρήσεις των πιέσεων πόρων στο στρώμα αλουβιακής άμμου (που θεωρείται παρόμοιο με το στρώμα #5 του προφίλ της παρούσας ανάλυσης) υποδείκνυαν πως το στρώμα αυτό ,πιθανώς, ρευστοποιήθηκε επίσης. Επιπλέον, σύμφωνα με σεισμικές αναλύσεις που εκτελέστηκαν από τους Yamazaki et al. (1995), η ρευστοποίηση πρέπει να έλαβε χώρα σε βάθος -27 έως -33m και στην χαλαρή άμμο που υπέρκειται της αλουβιακής αργίλου σε βάθος -10 έως -16m. Η σύγκριση των φασμάτων απόκρισης των επιταχύνσεων επιφανείας που καταγράφηκαν και

εκείνων που προέκυψαν από τις αναλύσεις για τις δύο προαναφερθείσες μεθόδους ανάλυσης, απεικονίζεται στο Σχήμα 9. Και στις τρεις περιπτώσεις, παρατηρείται ενίσχυση των συνιστωσών χαμηλής συχνότητας ενώ η μέγιστη φασματική επιτάχυνση ισούται με περίπου 1g, για περιόδους μεταξύ 1s και 1.5s.

Τα αποτελέσματα σε όρους κατανομών με το βάθος των μέγιστων τιμών της επιτάχυνσης , της μετακίνησης, της διατμητικής τάσης, της διατμητικής παραμόρφωσης και του λόγου υπερπίεσης πόρων παρουσιάζονται στο Σχήμα 10. Στα στρώματα που θεωρείται ότι ρευστοποιήθηκαν σύμφωνα με όσα συζητήθηκαν παραπάνω, παρατηρούνται τιμές $r_{u,max}$ κοντά στη μονάδα, σε συνδυασμό με μεγάλες διατμητικές παραμορφώσεις (της τάξεως του 4% με 5%). Παρ' ότι η συμπεριφορά των δυο μεθόδων ανάλυσης παρουσιάζει σε γενικές γραμμές πολλές ομοιότητες, η προσομοίωση της *(πιθανής)* διαπερατότητας κάθε υλικού, και συγκεκριμένα των επιφανειακών χαλικοαμμωδών στρωμάτων χαμηλής αντοχής, επιτρέπει την ροή των υπερπιέσεων του νερού που δημιουργούνται σε βαθύτερα αμμώδη στρώματα προς την επιφάνεια, σε αντίθεση με την περίπτωση κατά την οποία θεωρούνται πλήρως στραγγιζόμενες συνθήκες για τα επιφανειακά στρώματα. Αυτό αποτυπώνεται στην κατανομή του μέγιστου r_u κοντά στην επιφάνεια, όπου πολύ υψηλές τιμές υπερπίεσης έχουν σημειωθεί, με συνεπαγόμενη αύξηση των παραμορφώσεων και των μετακινήσεων στα ίδια βάθη. Τέλος, η κατανομή των σχετικών ως προς τη βάση μετακινήσεων φανερώνει ότι ο μεγάλος όγκος των μετακινήσεων έλαβε χώρα σε μικρά βάθη, ενώ οι μετακινήσεις παρέμειναν σε χαμηλά επίπεδα για βάθη μεγαλύτερα των -30 m περίπου. Παρόμοια συμπεριφορά παρατηρήθηκε και στις σεισμικές αναλύσεις που εκτελέστηκαν από τους Elgamal et al. (1995), που κατέληξαν ότι το έδαφος συμπεριφέρθηκε γραμμικά σε βάθη μεγαλύτερα των -32m, όπου η μείωση της δυσκαμψίας ήταν περιορισμένη.

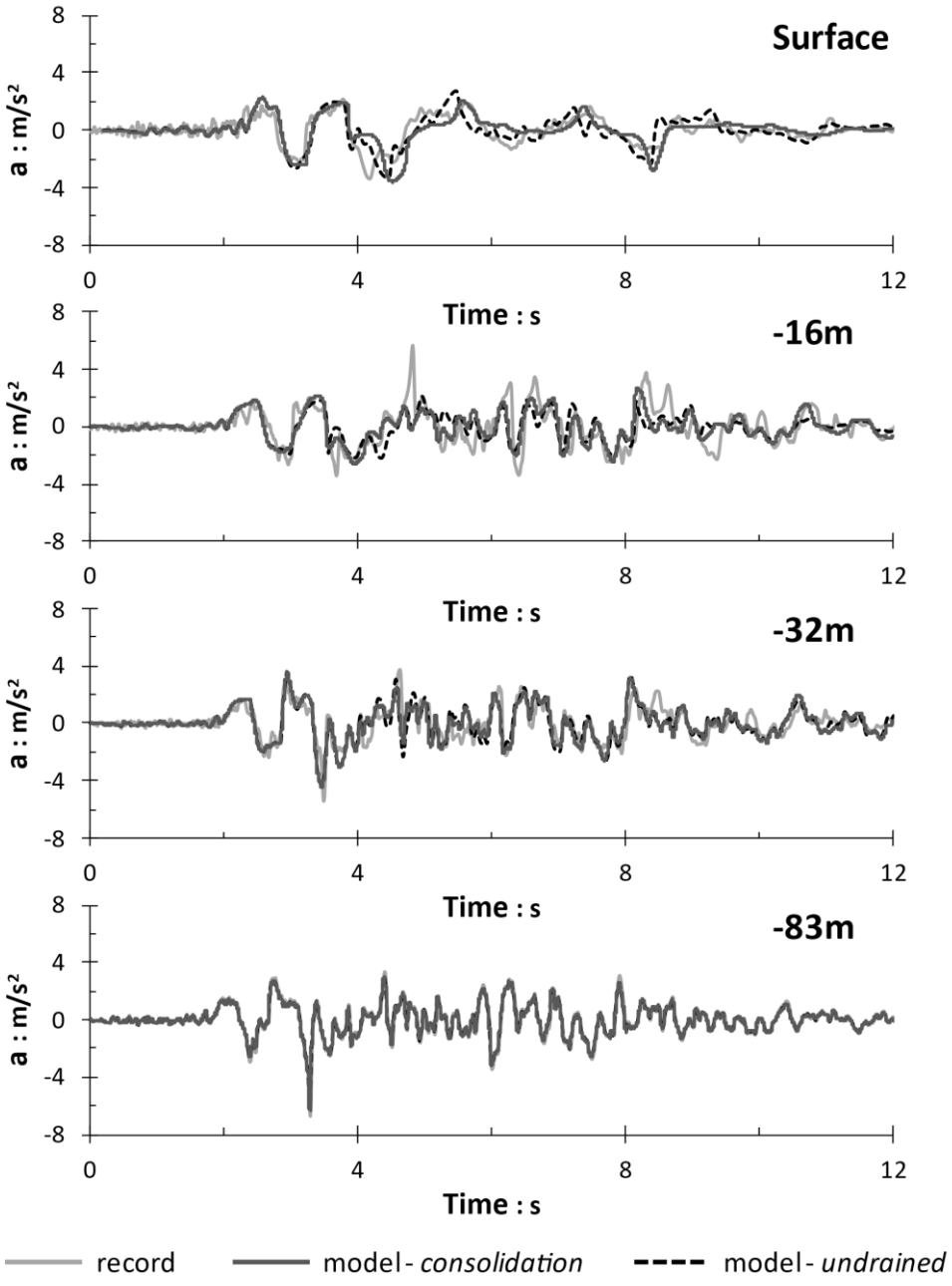

Σχήμα 8. Καταγραφές επιταχύνσεων της NS συνιστώσας στο Kobe Port Island (1995), σε σύγκριση με τις προβλέψεις του προτεινόμενου μοντέλου θεωρώντας αστράγγιστες συνθήκες φόρτισης (διακεκομμένες γραμμές) και λαμβάνοντας υπόψιν την κατακόρυφη στερεοποίηση του εδάφους κατά τη διάρκεια της διέγερσης (συνεχείς γραμμές) στην επιφάνεια και σε βάθη -16m, -32m και -83m.

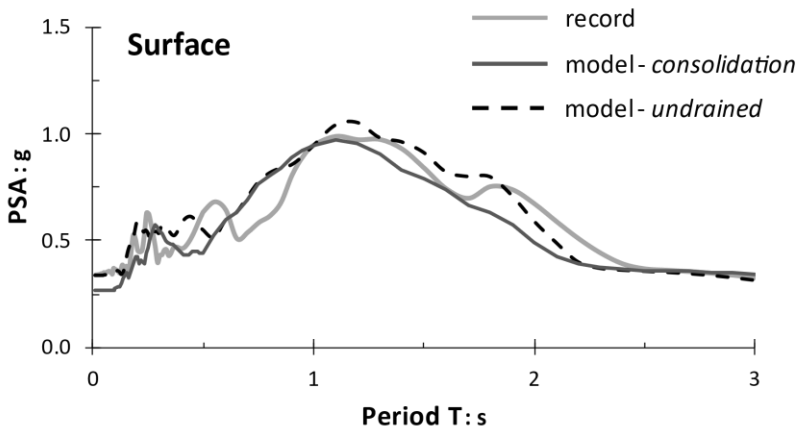

Σχήμα 9. Ελαστικό φάσμα απόκρισης επιφανείας της καταγραφής της NS συνιστώσας στο Kobe Port Island (1995), σε σύγκρισή με τις προβλέψεις του προτεινόμενου μοντέλου θεωρώντας αστράγγιστες συνθήκες φόρτισης (διακεκομμένη γραμμή) και λαμβάνοντας υπόψιν την κατακόρυφη στερεοποίηση του εδάφους κατά τη διάρκεια της διέγερσης (συνεχής γραμμή).

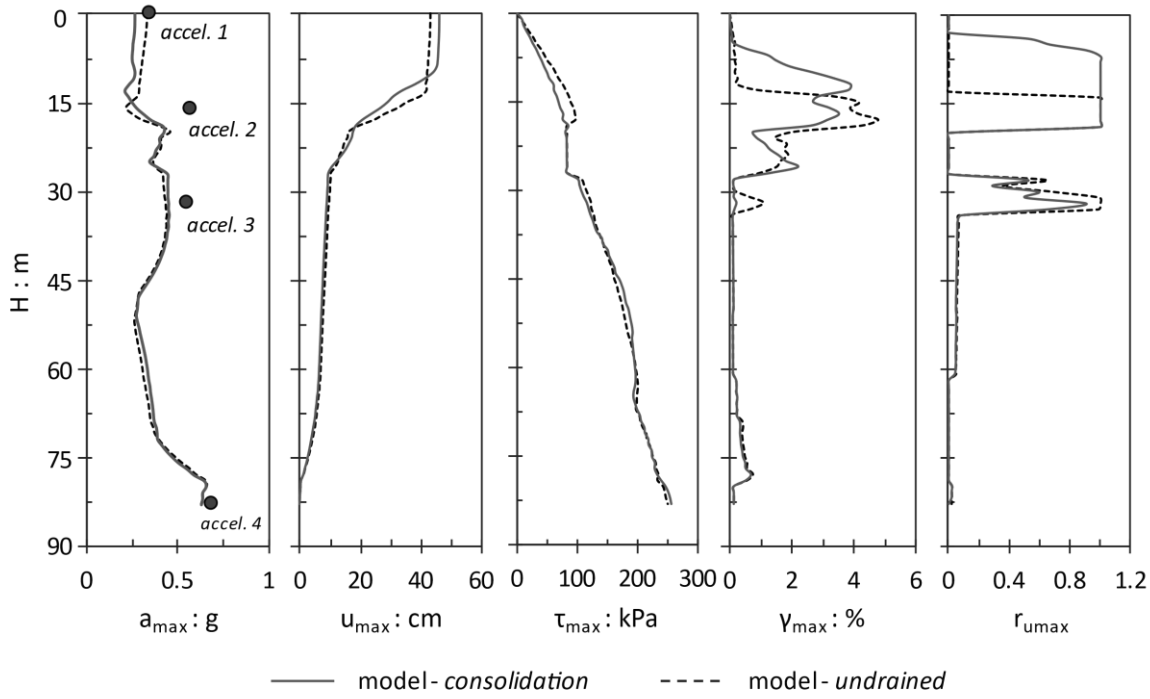

Σχήμα 10. Κατανομές καθ' ύψος των μέγιστων τιμών των παραμέτρων: (i) επιτάχυνση, (ii) σχετική μετακίνηση ως προς τη βάση, (iii) διατμητική τάση, (iv) διατμητική παραμόρφωση και (v) υπερπίεση πόρων για το εδαφικό προφίλ του Πίνακα 1, θεωρώντας αστράγγιστες συνθήκες φόρτισης (διακεκομμένες γραμμές) και λαμβάνοντας υπόψιν την κατακόρυφη στερεοποίηση του εδάφους κατά τη διάρκεια της διέγερσης (συνεχείς γραμμές) (διέγερση βάσης: NS συνιστώσα της καταγραφής στο Kobe Port Island, 1995).

Εφαρμογή του αλγορίθμου για την πρόβλεψη φασμάτων απόκρισης σε εδάφη με ρευστοποιήσιμες στρώσεις

Περιγραφή μεθοδολογίας

Η ενότητα αυτή αφορά την προκαταρκτική εφαρμογή του προτεινόμενου αλγορίθμου σεισμικής εδαφικής απόκρισης, με σκοπό τη σύνθεση ελαστικών φασμάτων απόκρισης για ρευστοποιήσιμα εδαφικά προφίλ, στα πλαίσια της ανάλυσης και του σχεδιασμού αντισεισμικών κατασκευών. Το κρίσιμο θέμα του αντισεισμικού σχεδιασμού σε δυνητικώς ρευστοποιήσιμα εδάφη δεν καλύπτεται ενδελεχώς από διεθνείς και εγχώριους κανονισμούς, ενώ ο EC8 υποδεικνύει ότι σε αυτές τις εδαφικές συνθήκες ειδικές μελέτες πρέπει να διεξαχθούν για τον προσδιορισμό της σεισμικής δράσης. Στη διεθνή βιβλιογραφία έχουν προταθεί διαφορετικές μεθοδολογίες για την εκτίμηση του φάσματος απόκρισης σε ρευστοποιήσιμα εδάφη· ανάμεσα τους οι Tsiapas and Bouckovalas (2019) πρότειναν τον υπολογισμό, με ισοδύναμη ελαστική μέθοδο, του φάσματος απόκρισης με τα αρχικά χαρακτηριστικά του εδάφους και εν συνεχεία με τα χαρακτηριστικά του ρευστοποιημένου εδάφους και κατόπιν την εφαρμογή κατάλληλης μεθόδου παρεμβολής μεταξύ αυτών. Η παρούσα εργασία επιχειρεί να προσεγγίσει το θέμα αυτό, εκτελώντας ένα μεγάλο αριθμό σεισμικών αναλύσεων σε διάφορα προφίλ δυνητικά ρευστοποιήσιμων εδαφών, υποβαλλόμενων σε πραγματικές σεισμικές καταγραφές στη βάση τους, με στόχο την παραγωγή του ελαστικού φάσματος απόκρισης επιταχύνσεων στην επιφάνεια.

Για το σκοπό αυτό συντέθηκαν 10 εδαφικά προφίλ, τα οποία περιλαμβάνουν μια δυνητικά ρευστοποιήσιμη στρώση, δηλ. μια στρώση κορεσμένης χαλαρής άμμου με D_r =35%. Οι βασικές παράμετροι βάσει των οποίων επιλέχθησαν τα διαφορετικά προφίλ είναι: (i) το ολικό ύψος H, (ii) ο τύπος (άμμος ή άργιλος) και τα χαρακτηριστικά (D_r, S_u, k) του περιβάλλοντος εδάφους, δηλ. του εδάφους που περικλείει τη ρευστοποιήσιμη στρώση, (iii) το πάχος της ρευστοποιήσιμης στρώσης h_L και (iv) το βάθος της ρευστοποιήσιμης στρώσης από την επιφάνεια h_f.

Οι σεισμικές καταγραφές που χρησιμοποιήθηκαν ως διεγέρσεις βάσης αντλήθηκαν από την βιβλιοθήκη του PEER Ground Motion Database (Pacific Earthquake Engineering Research Center Ground Motion Database, Ancheta et al. 2013). Δίνοντας τιμές σε συγκεκριμένες σεισμολογικές παραμέτρους, υπολογίζεται το “φάσμα στόχος” βάσει των σχέσεων εξασθένισης NGA – West2 GMMs (Next Generation Attenuation Relationships for Western US

Ground Motion Models). Στη συνέχεια, ο χρήστης λαμβάνει σεισμικές καταγραφές που ταιριάζουν με τα σεισμολογικά δεδομένα που έχει επιλέξει και αποδίδουν φάσμα συμβατό με το φάσμα στόχο. Για τους σκοπούς της μελέτης αυτής, επιλέχθησαν 9 σεισμικές κατηγορίες με βάση το μέγεθος του σεισμού και την απόσταση από το ρήγμα, που προκύπτουν από όλους τους πιθανούς συνδυασμούς μεταξύ των τιμών: M_w=7.5, 7 και 6.5 και R_{JB}=5km, 10km και 15km. Για την κάθε κατηγορία, επιλέχθησαν 7 σεισμικές καταγραφές με φάσμα συμβατό, κατά το δυνατόν, με εκείνο που προκύπτει από τις σχέσεις εξασθένισης NGA – West2 για τα σεισμικά χαρακτηριστικά της κατηγορίας αυτής, και μέγεθος και απόσταση από το ρήγμα ίσα ή περίπου ίσα με τα αντίστοιχα του φάσματος της κατηγορίας. Επιπλέον, οι σεισμικές κινήσεις απαιτήθηκε να έχουν καταγραφεί σε βραχώδη σχηματισμό με μέση διατμητική ταχύτητα $V_{s,30}$> 800m/s (έδαφος κατηγορίας *A* κατά τον EC8).

Προκειμένου να επιτευχθεί η σύγκλιση, με λογική ακρίβεια, των φασμάτων των επιλεγμένων καταγραφών με το φάσμα στόχο της κάθε κατηγορίας, ακολουθήθηκαν δυο διαφορετικές προσεγγίσεις. Αρχικά, τα επιταχυνσιογραφήματα υποβλήθηκαν σε προσαρμογή κλίμακας (η διαδικασία παρέχεται από το PEER), διατηρώντας συντελεστές κλίμακας εντός επιλεγμένου, μικρού εύρους γύρω από τη μονάδα ώστε να διατηρηθεί η *"φυσική ρεαλιστικότητα"* των καταγραφών. Κατά τη δεύτερη προσέγγιση, οι καταγραφές τροποποιήθηκαν πλήρως (κλίμακα και συχνοτικό περιεχόμενο) μέσω μαθηματικής διαδικασίας ώστε να προκύψει ακριβέστερη σύγκλιση. Κάθε ανάλυση διεξήχθη: (i) υπό στραγγιζόμενες συνθήκες φόρτισης (ii) υπό αστράγγιστες συνθήκες φόρτισης και (iii) λαμβάνοντας υπόψη την κατακόρυφη στερεοποίηση των σχηματισμών κατά τη διάρκεια της διέγερσης. Συνεπώς, για κάθε μία από τις προαναφερθείσες προσεγγίσεις (επιταχυνσιογραφήματα με προσαρμογή κλίμακας και πλήρως τροποποιημένα) εκτελέστηκαν 70 αναλύσεις για κάθε σεισμική κατηγορία [M_w, R_{JB}] (10 προφίλ × 7 διεγέρσεις βάσης), υπό 3 συνθήκες στράγγισης· συνολικά 3.780 δυναμικές αναλύσεις.

Αποτελέσματα

Τα Σχήματα 11 και 12 αποδίδουν τα αποτελέσματα των σεισμικών αναλύσεων, σε όρους ελαστικών φασμάτων απόκρισης επιφανείας για τις τρεις συνθήκες στράγγισης που μελετήθηκαν. Κάθε φάσμα αποτελεί το μέσο όρο 70 φασμάτων (10 προφίλ × 7 διεγέρσεις βάσης). Περιλαμβάνονται επίσης τα φάσματα των διεγέρσεων βάσης (μέσες τιμές). Το Σχήμα 11 αναφέρεται στη θεώρηση κατά την οποία τα φάσματα βάσης υποβλήθηκαν μόνο σε προσαρμογή κλίμακας ενώ το Σχήμα 12 σε φάσματα βάσης πλήρως τροποποιημένα.

Προκειμένου να αναδειχθεί η επιρροή της μεθόδου ανάλυσης (στραγγιζόμενες, αστράγγιστες ή συνθήκες στερεοποίησης) στο συχνοτικό περιεχόμενο των φασμάτων απόκρισης, οι επιταχύνσεις έχουν κανονικοποιηθεί ως προς τη μέγιστη εδαφική επιτάχυνση (*PSA* για *T*=0). Συνοπτικά, διεξάγονται τα κάτωθι συμπεράσματα: (i) οι αποκλίσεις στα φάσματα που υπολογίστηκαν με τη θεώρηση αστράγγιστων συνθηκών και υπό συνθήκες στερεοποίησης είναι αμελητέες· διαφορές υπάρχουν κυρίως

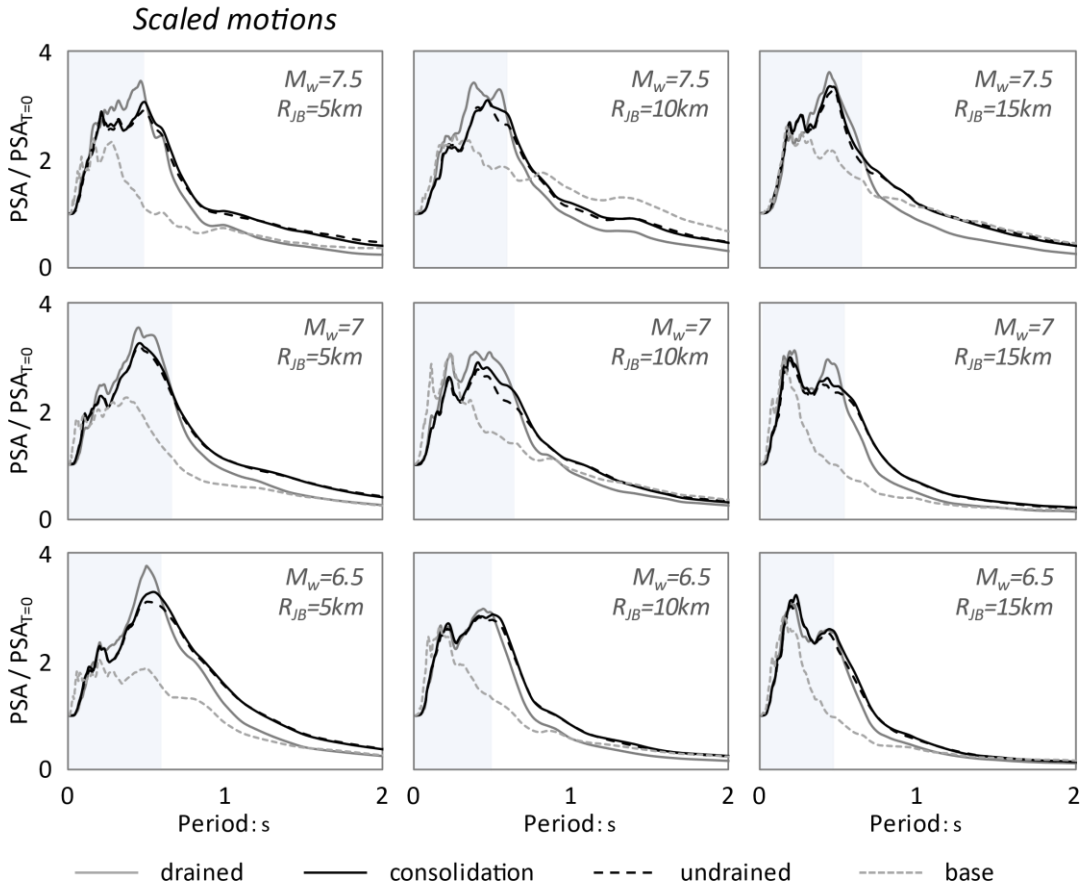

Σχήμα 11. Ελαστικά φάσματα επιτάχυνσης επιφανείας (μέσες τιμές) για 9 συνδυασμούς (M_w, R_{JB}) θεωρώντας (i) συνθήκες πλήρους στράγγισης, (ii) αστράγγιστες συνθήκες και (iii) κατακόρυφη εδαφική στερεοποίηση κατά τη διάρκεια της διέγερσης. Επίσης, παρουσιάζονται τα μέσα φάσματα βάσης των σεισμικών καταγραφών που έχουν υποστεί προσαρμογή κλίμακας ώστε να αποδίδουν ελαστικό φάσμα όμοιο με το φάσμα που προκύπτει από τις σχέσεις αλληλεπίδρασης.

μεταξύ αυτών και της στραγγιζόμενης συμπεριφοράς. Στις περισσότερες περιπτώσεις η απόκριση υπό συνθήκες στερεοποίησης οριοθετείται από την αστράγγιστη και τη στραγγιζόμενη συμπεριφορά. (ii) Όπως ήταν αναμενόμενο, η στραγγιζόμενη συμπεριφορά εμφανίζει μεγαλύτερες μέγιστες κανονικοποιημένες φασματικές επιταχύνσεις, καθώς η

ανάπτυξη υπερπιέσεων αποδυναμώνει τις επιταχύνσεις που σχετίζονται με υψηλές συχνότητες. (iii) Στην περιοχή υψηλών συχνοτήτων του φάσματος (σκιασμένη περιοχή των διαγραμμάτων) οι στραγγιζόμενες επιταχύνσεις είναι μεγαλύτερες σε σύγκριση με τις αστράγγιστες και τις υπό συνθήκες στερεοποίησης. Ωστόσο, υπάρχει μία κρίσιμη τιμή της περιόδου *T*, που παρατηρείται μετά την εμφάνιση της μέγιστης επιτάχυνσης, στην οποία η στραγγιζόμενη συμπεριφορά φθίνει γρηγορότερα από τις υπόλοιπες. Έτσι, παρόλο που η κανονικοποιημένη αστράγγιστη συμπεριφορά είναι πιο περιορισμένη σε όρους μεγίστων τιμών, υπερισχύει της στραγγιζόμενης για περιόδους μεγαλύτερες από το T_{cr}. Η μέση τιμή του T_{cr} είναι 0.57s για την περίπτωση του Σχήματος 11 και 0.51s για τα φάσματα του Σχήματος 12.

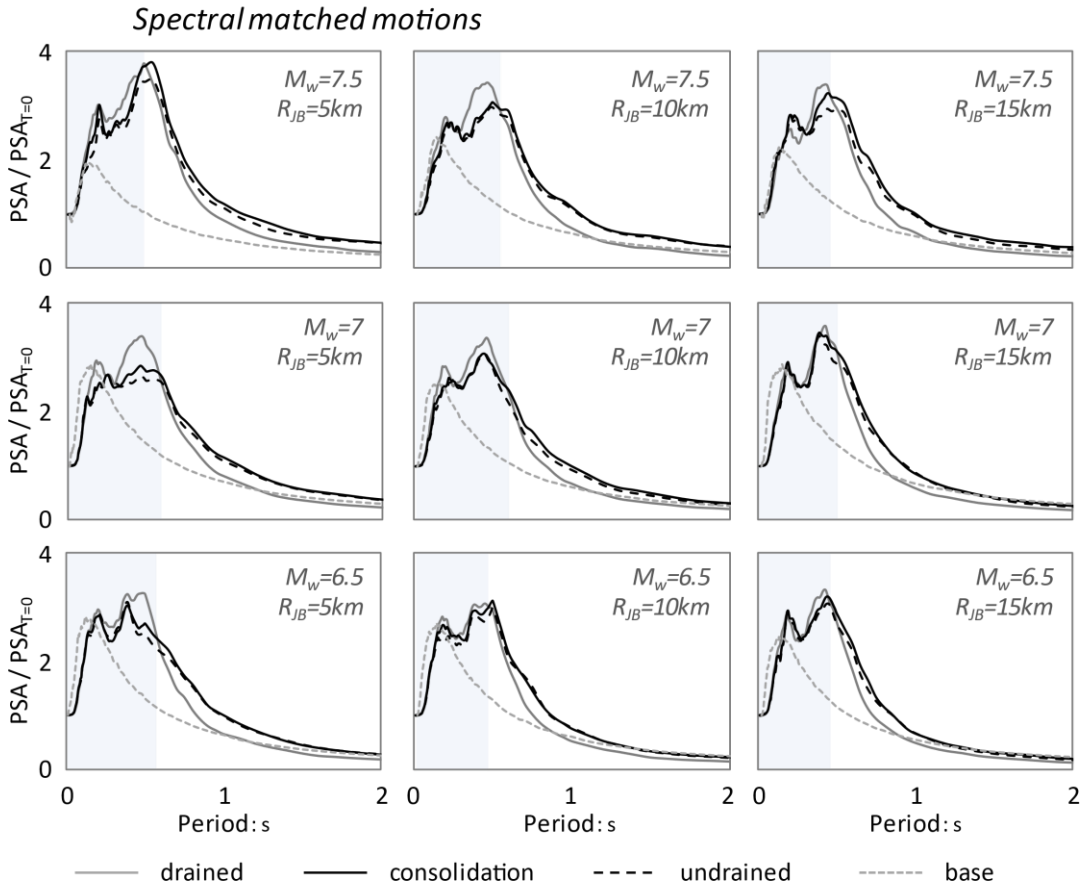

Σχήμα 12. Ελαστικά φάσματα επιτάχυνσης επιφανείας (μέσες τιμές) για 9 συνδυασμούς (M_w, R_{JB}) θεωρώντας (i) συνθήκες πλήρους στράγγισης, (ii) αστράγγιστες συνθήκες και (iii) κατακόρυφη εδαφική στερεοποίηση κατά τη διάρκεια της διέγερσης. Επίσης, παρουσιάζονται τα μέσα φάσματα βάσης των σεισμικών καταγραφών που τροποποιήθηκαν πλήρως ώστε να αποδίδουν ελαστικό φάσμα όμοιο με το φάσμα που προκύπτει από τις σχέσεις αλληλεπίδρασης.

Με βάση τη συμπεριφορά υπό συνθήκες στερεοποίησης, αφού θεωρείται η πιο αντιπροσωπευτική των πραγματικών συνθηκών του πεδίου, τα μέσα κανονικοποιημένα φάσματα όλων των σεισμικών κατηγοριών παρουσιάζονται στο Σχήμα 13. Τα φάσματα απόκρισης σε όρους S_e/a_g απεικονίζονται με γκρι διακεκομμένες γραμμές και με μαύρη συνεχή γραμμή ο μέσος όρος αυτών, όπου a_g είναι η κορυφαία εδαφική επιτάχυνση σχεδιασμού σε έδαφος κατηγορίας *A* (S_e για T=0 του μέσου φάσματος της βάσης). Είναι ενδιαφέρον το γεγονός ότι, ανάμεσα στις δυο διαφορετικές προσεγγίσεις που εφαρμόστηκαν τα τελικά φάσματα εμφανίζουν ελάχιστες αποκλίσεις.

Κατά τον EC8, η εδαφική κίνηση σε ένα δεδομένο σημείο της επιφάνειας αναπαρίσταται από ένα ελαστικό φάσμα επιταχύνσεων, αποτελούμενο από 4 κλάδους, η μορφή του οποίου καθορίζεται από τις τιμές των παραμέτρων: εδαφική επιτάχυνση σχεδιασμού για έδαφος τύπου *A*, a_g, περίοδοι T_B, T_C, T_D, εδαφικός παράγοντας S και παράγοντας διόρθωσης απόσβεσης η (η =1 για 5% απόσβεση), με τα T_B, T_C, T_D και S να

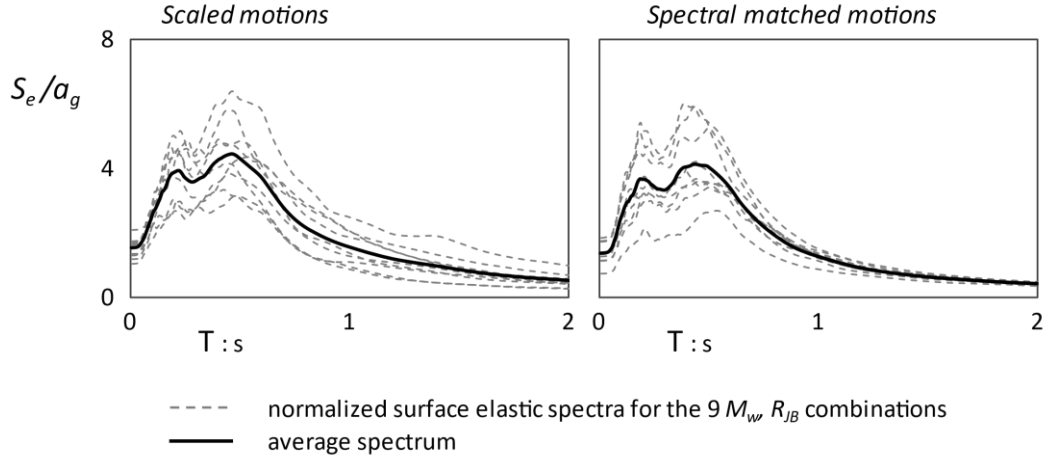

Σχήμα 13. Ελαστικά φάσματα απόκρισης επιφανείας, λαμβάνοντας υπόψιν την κατακόρυφη στερεοποίηση του εδάφους, κανονικοποιημένα ως προς την κορυφαία εδαφική επιτάχυνση a_g και μέσο φάσμα αυτών.

εξαρτώνται από τον τύπο του εδάφους. Για τους εδαφικούς τύπους *A, B, C, D* και *E* καθορίζονται συγκεκριμένες τιμές για τις παραμέτρους αυτές, ενώ για τύπο εδάφους S_2 απαιτείται ειδική μελέτη για τον καθορισμό της σεισμικής δράσης.

Στο πλαίσιο αυτό, τα μέσα φάσματα απόκρισης του Σχήματος 13 όπως και τα αντίστοιχα μέσα φάσματα στη βάση περιγράφονται σύμφωνα με το ελαστικό φάσμα 4 κλάδων του EC8 και

παρουσιάζονται στο Σχήμα 14. Στο σχήμα αυτό, η γκρι συνεχής γραμμή αντιπροσωπεύει το ελαστικό φάσμα για έδαφος κατηγορίας *A*, η μαύρη συνεχής γραμμή είναι το φάσμα απόκρισης για έδαφος με ρευστοποιήσιμη στρώση κατηγορίας S_2, ενώ οι διακεκομμένες γραμμές αποτελούν τη γραμμικοποίηση τους κατά το φάσμα σχεδιασμού του EC8. Οι παράμετροι που καθορίζουν το σχήμα των γραμμικοποιημένων φασμάτων *A* και S_2 έχουν υπολογιστεί στο Σχήμα 15.

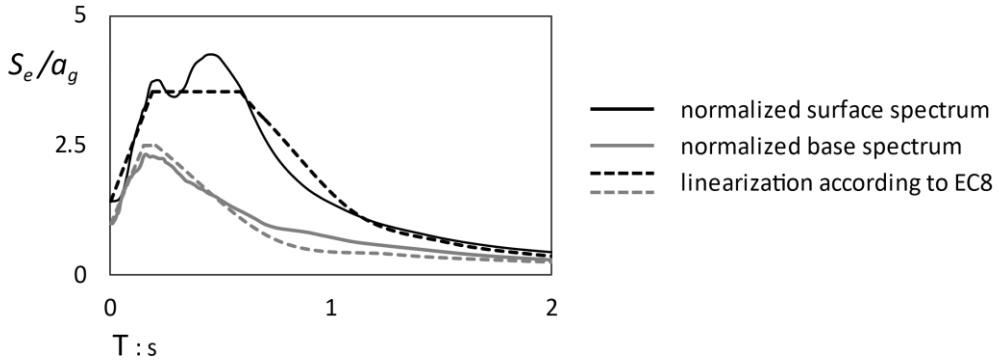

Σχήμα 14. Μέσο ελαστικό κανονικοποιημένο φάσμα επιφανείας (μέση τιμή των δύο προσεγγίσεων που ακολουθήθηκαν – μαύρες γραμμές του Σχήματος 13) και βάσης (έδαφος κατηγορίας *A*) και γραμμικοποίηση τους κατά το ελαστικό φάσμα απόκρισης 4 κλάδων που προτείνεται στον EC8.

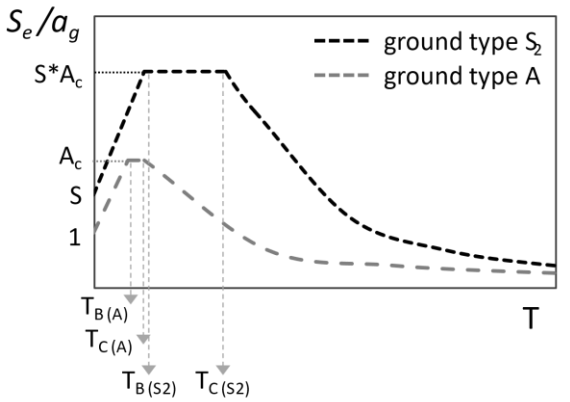

	A_C	S	T_B [s]	T_C [s]
Soil *A*	2.5	1	0.15	0.21
Soil S_2		1.42	0.19	0.59

Σχήμα 15. Τιμές των παραμέτρων A_c, S, T_B, και T_C (σύμφωνα με το ελαστικό φάσμα 4 κλάδων του EC8) των φασμάτων απόκρισης εδάφους κατηγορίας S_2 και *A* που προκύπτουν από την προτεινόμενη μεθοδολογία.

Θα πρέπει να τονιστεί, ότι η προτεινόμενη μεθοδολογία δεν στοχεύει στην τροπολογία ή τη συμπλήρωση του κανονισμού, ούτε αποβλέπει στην αντικατάσταση των ειδικών εδαφοδυναμικών αναλύσεων που απαιτούνται από τον κανονισμό, αλλά αποτελεί ένα βήμα

προς τη στοιχειοθέτηση κατευθυντήριων οδηγιών στο επίπεδο του προκαταρκτικού σχεδιασμού. Επιπλέον, δεν εξετάστηκαν όλες οι υποπεριπτώσεις δυνητικά ρευστοποιήσιμων προφίλ αλλά μελετήθηκαν κατά κύριο λόγο προφίλ με ρευστοποιήσιμη στρώση περιορισμένου πάχους, καθώς θεωρήθηκαν πιο αντιπροσωπευτικά από εκείνα που αποτελούνται εξ ολοκλήρου από ρευστοποιήσιμο εδαφικό υλικό. Ωστόσο, το ελαστικό φάσμα τέτοιων προφίλ με σχετικά λεπτή ρευστοποιήσιμη στρώση είναι εν γένει πιο συντηρητικό, σε συμφωνία με το πνεύμα του κανονισμού.

Επέκταση του αριθμητικού αλγορίθμου για την προσομοίωση εδαφικών στραγγιστηρίων

Περιγραφή της μεθοδολογίας

Ο αναπτυχθείς αριθμητικός αλγόριθμος αξιοποιείται για την προσομοίωση της σεισμικής απόκρισης εδαφικού σχηματισμού, που έχει ενισχυθεί μέσω τοποθέτησης στραγγιστηρίων με σκοπό την αποτόνωση των υπερπιέσεων των πόρων του εδάφους. Η τοποθέτηση στραγγιστηρίων σε συνδυασμό με την δονητική συμπύκνωση της περιβάλλουσας χαλαρής άμμου έχουν χρησιμοποιηθεί ευρέως για τον περιορισμό των επιπτώσεων της ρευστοποίησης, που λαμβάνει χώρα κατά τη διάρκεια ενός σεισμού. Ένα στραγγιστήριο - χαλικοπάσσαλος μετριάζει την ανάπτυξη των υπερπιέσεων μέσω πολλαπλών μηχανισμών· ενεργοποιεί την ακτινική στράγγιση του εδάφους, αυξάνει την συνολική αντοχή του σύμμικτου σχηματισμού έδαφος- χαλικοπάσσαλος, ενώ συνήθως η τοποθέτηση του συνοδεύεται από συμπύκνωση του περιβάλλοντος εδάφους. Ωστόσο, είναι σημαντική η εκτίμηση της βελτίωσης που προσφέρεται αποκλειστικά από την ακτινική στράγγιση, στην περίπτωση προκατασκευασμένων στραγγιστηρίων *PVDs*, που αντλούν τα οφέλη τους κυρίως από την ακτινική στράγγιση. Ο σχεδιασμός ενός συστήματος στράγγισης έγκειται κυρίως στην επιλογή της διαμέτρου των στραγγιστηρίων και της απόστασης μεταξύ τους, ώστε να διατηρηθεί η μέγιστη τιμή της υπερπίεσης κάτω από ένα προκαθορισμένο όριο, για το σεισμό σχεδιασμού. Στην κατεύθυνση αυτή, υπάρχουν διαθέσιμες στη διεθνή βιβλιογραφία διάφορες προτάσεις, όπως διαγράμματα σχεδιασμού (Seed and Booker (1977), Onoue (1988)) αλλά και αριθμητικές 2D και 3D προσεγγίσεις (Pestana et al. (1997), Bouckovalas et al. (2009, 2011b, 2012), Seid- Karbasi and Byrne (2007), Vytiniotis and Whittle (2013)).

Στη παρούσα εργασία, η διαφορική εξίσωση της εδαφικής στερεοποίησης επαναδιατυπώνεται ώστε να ληφθεί υπόψη και η οριζόντια αξονοσυμμετρική υδατική ροή. Έτσι, η υπερπίεση του νερού των πόρων $u_p = u_p(t, z, r)$ υπολογίζεται ως ακολούθως:

$$\frac{k_r}{\gamma_w}\left(\frac{\partial^2 u_p}{\partial r^2} + \frac{1}{r}\frac{\partial u_p}{\partial r}\right) + \frac{k_z}{\gamma_w}\frac{\partial^2 u_p}{\partial z^2} = -\frac{\partial \varepsilon_{vol}}{\partial t} \quad [25]$$

, όπου *r* είναι η ακτίνα και k_r, k_z οι διαπερατότητες κατά την ακτινική και την κατακόρυφη διεύθυνση αντίστοιχα, με τον 1ο όρο της εξίσωσης να αναφέρεται στην οριζόντια, ακτινική ροή και το 2ο στην κατακόρυφη ροή. Η επίλυση της διαφορικής εξίσωσης [25], σε σύζευξη με την καταστατική εξίσωση [1], εκτελείται με την έμμεση μέθοδο των πεπερασμένων διαφορών. Μία σχηματική απεικόνιση της μεθόδου διακριτοποίησης του κανάβου στην οριζόντια διεύθυνση, παρουσιάζεται στο Σχήμα 16 για στραγγιστήριο ακτίνας R_d και ακτίνα κύκλου του επηρεαζόμενου εδάφους R_e. Από τις εξισώσεις [25] και [1] υπολογίζεται η τιμή του u_p σε κάθε σημείο του κανάβου καθ΄ύψος και κατά μήκος μίας ακτίνας, στο τέλος κάθε χρονικού βήματος *dt*. Ωστόσο, καθώς η διάδοση του διατμητικού κύματος εκτελείται μονοδιάστατα κατά την κατακόρυφη διεύθυνση, οι παράμετροι που συμμετέχουν στην εξίσωση της διάδοσης του κύματος υπολογίζονται βάσει μιας χαρακτηριστικής τιμής της πίεσης πόρων ${u_p}^* = {u_p}^*(t, z)$, που αντιστοιχεί στον γεωμετρικό μέσο όρο της πίεσης πόρων κατά μήκος μίας ακτίνας:

$${u^*}_{p\,i,j} = \left.\sum_{=1}^{M+1}\left(\frac{r_k}{R_e}\right)^2 u_{i,j,k}\right/ \sum_{=1}^{M+1}\left(\frac{r_k}{R_e}\right)^2 \quad [26]$$

, εκτελείται δηλαδή συμπύκνωση του ακτινικού βαθμού ελευθερίας. Οι συνοριακές συνθήκες κατά την οριζόντια διεύθυνση (Σχήμα 16) είναι η αδιαπέρατη περιφέρεια του εδάφους για $r = R_e$ και η διαπερατή περιφέρεια του στραγγιστηρίου για $r = R_d$.(ισοδυναμεί με στραγγιστήριο άπειρης διαπερατότητας) Εναλλακτικά, προσομοιώνεται η πραγματική, πεπερασμένη διαπερατότητα του στραγγιστηρίου, επεκτείνοντας τον κάναβο μέχρι το κέντρο του στραγγιστηρίου και τότε η αντίστοιχη συνοριακή συνθήκη αντικαθίσταται από το αδιαπέρατο (για λόγους συμμετρίας) κέντρο του στραγγιστηρίου. Η μηχανική αλληλεπίδραση μεταξύ εδάφους και στραγγιστηρίου / χαλικοπασσάλου λαμβάνεται υπόψιν στο ισοδύναμο μέτρο διάτμησης του συστήματος έδαφος - χαλικοπάσσαλος, το οποίο σύμφωνα με την υπόθεση της ενιαίας διατμητικής

παραμόρφωσης μεταξύ χαλικοπασσάλου και περιβάλλοντος εδάφους (Baez and Martin, 1993) εκφράζεται ως ακολούθως:

$$G_{system} = (1 - a_s)G_{soil} + a_s G_{drain} \quad [27]$$

, όπου $a_s = \left(\frac{R_d}{R_e}\right)^2$ ο συντελεστής αντικατάστασης εδάφους.

Εναλλακτικά, η ισοδύναμη μηχανική συμπεριφορά του συστήματος έδαφος-χαλικοπάσσαλος μπορεί να ληφθεί υπόψιν σύμφωνα με την υπόθεση της ενιαίας διατμητικής τάσης στον χαλικοπάσσαλο και το περιβάλλον έδαφος (Bouckovalas et al., 2006), ως εξής:

$${G_{system}}^{-1} = (1 - a_s){G_{soil}}^{-1} + a_s {G_{drain}}^{-1} \quad [28]$$

Επικύρωση του αλγορίθμου

Ο αλγόριθμος επαληθεύεται μέσω σύγκρισης με μη γραμμικές, δυναμικές, τρισδιάστατες αριθμητικές αναλύσεις που εκτελέστηκαν στο πρόγραμμα π.δ. FLAC3D (Itasca, 2006) από τους Tsiapas and Tsioulou (2009) και Bouckovalas et al. (2011a) και αφορούν λεπτή στρώση άμμου D_r=60%, περιβαλλόμενη από αργιλικές στρώσεις ώστε να αποτρέπεται η κατακόρυφη στράγγιση, ενισχυμένη με κατακόρυφο

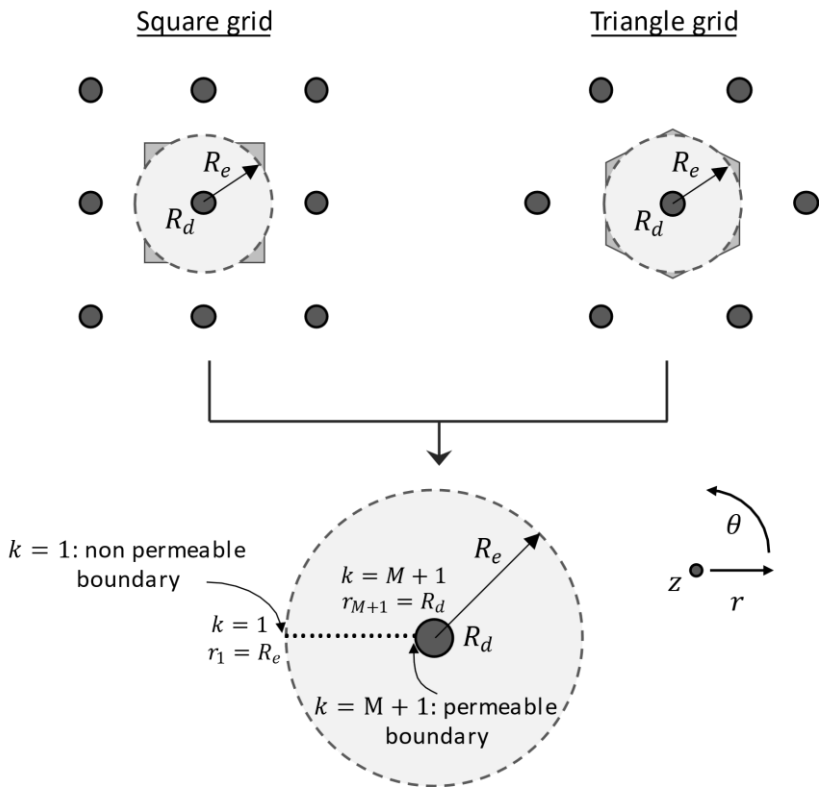

Σχήμα 16. Τετραγωνική και τριγωνική διάταξη στραγγιστηρίων ακτίνας R_d με ακτίνα επιρροής εδάφους R_e και σχηματική απεικόνιση της διακριτοποίησης και των συνοριακών συνθηκών κατά μήκος μιας ακτίνας που θεωρούνται από τον προτεινόμενο αλγόριθμο.

χαλικοπάσσαλο ακτίνας R_d=0.5m σε ακτίνα επιρροής εδάφους R_e=1.4m. Η βάση του μοντέλου υπεβλήθη σε ημιτονοειδή χρονοϊστορία επιταχύνσεων 12 κύκλων, πλάτους a_{max}=0.08 g και περιόδου T=0.2s και κατεγράφη η εξέλιξη του r_u με το χρόνο στο μέσο της αμμώδους στρώσης, για 5 τιμές διαπερατότητας k της άμμου. Το καταστατικό προσομοίωμα που χρησιμοποιήθηκε ήταν το ελαστοπλαστικό μοντέλο με οριακή επιφάνεια αστοχίας *NTUA-SAND* από τους Andrianopoulos et al. (2010).

Η βαθμονόμηση του μοντέλου Ta-Ger έγινε με σκοπό η απόκριση του να προσεγγίζει εκείνη της αριθμητικής ανάλυσης με το FLAC3D, για αστράγγιστες συνθήκες φόρτισης, για τη δεδομένη άμμο με D_r=60% υπό αρχική μέση ενεργό τάση p_0'=66.6 kPa. Το Σχήμα 17 απεικονίζει τη συμπεριφορά του αμμώδους εδαφικού στοιχείου υπό τις συνθήκες αυτές, σε *DSS* δοκιμή που εκτελέστηκε με το βαθμονομημένο Ta-Ger υπό επιβαλλόμενη διατμητική τάση σταθερού πλάτους τ_{max}=8kPa. Σε συμφωνία με τις εργαστηριακές παρατηρήσεις αστράγγιστων, ανακυκλικών *DSS* δοκιμών επιβαλλόμενης τάσης, οι αρχικοί κύκλοι φόρτισης χαρακτηρίζονται από ραγδαία μείωση της μέσης ενεργού τάσης, ενώ στη συνέχεια ο ρυθμός

μείωσης της τάσης μειώνεται μέχρι ένα κρίσιμο σημείο όπου η μείωση επιταχύνεται ξανά και οδηγεί τελικά στη ρευστοποίηση. Οι μεταβολές στο ρυθμό μείωσης του p' περιγράφονται από την παράμετρο n_u (Εξίσωση [5]), μέσω της μετάβασης της από μια αρχική τιμή n_0, στην ασυμπτωτικά μέγιστη τιμή της n_{peak}, ενώ στη συνέχεια μειώνεται ξανά μέχρι την τελική τιμή n_f.

Η σύγκλιση των προβλέψεων του μοντέλου με τις τρισδιάστατες αναλύσεις απεικονίζεται στο Σχήμα 18, για τις εξεταζόμενες διαπερατότητες k= 5 10^{-6}, 10^{-5}, 2 10^{-5}, 5 10^{-5} και 10^{-4} m/s. Περιλαμβάνεται ακόμα, η συμπεριφορά υπό αστράγγιστες συνθήκες φόρτισης (k=0). Η σύγκλιση ως προς τη μέγιστη τιμή της υπερπίεσης είναι ικανοποιητική, ενώ ταυτόχρονα αποτυπώνεται η χαρακτηριστική μορφή των καμπυλών εξέλιξης του r_u παρουσία ακτινικής στράγγισης, κατά την οποία η μέγιστη τιμή επιτυγχάνεται σε ένα αρχικό στάδιο της φόρτισης και στη συνέχεια βαίνει μειούμενη παρά τη συνεχιζόμενη επιβαλλόμενη διέγερση. Ο μηχανισμός της συμπεριφοράς αυτής παρουσιάζεται αναλυτικά στο Bouckovalas et al. (2011a).

Τέλος, η κατανομή των μέγιστων υπερπιέσεων κατά μήκος μίας ακτίνας από την περιφέρεια του εδάφους έως την περιφέρεια του στραγγιστηρίου, για τις διαπερατότητες που μελετήθηκαν, έχει αποτυπωθεί στο Σχήμα 19. Στο ίδιο σχήμα σημειώνεται επίσης, ο γεωμετρικός μέσος όρος των υπερπιέσεων κατά μήκος της ακτίνας, που χρησιμοποιείται ως χαρακτηριστική τιμή για τη κατακόρυφη διάδοση του διατμητικού κύματος.

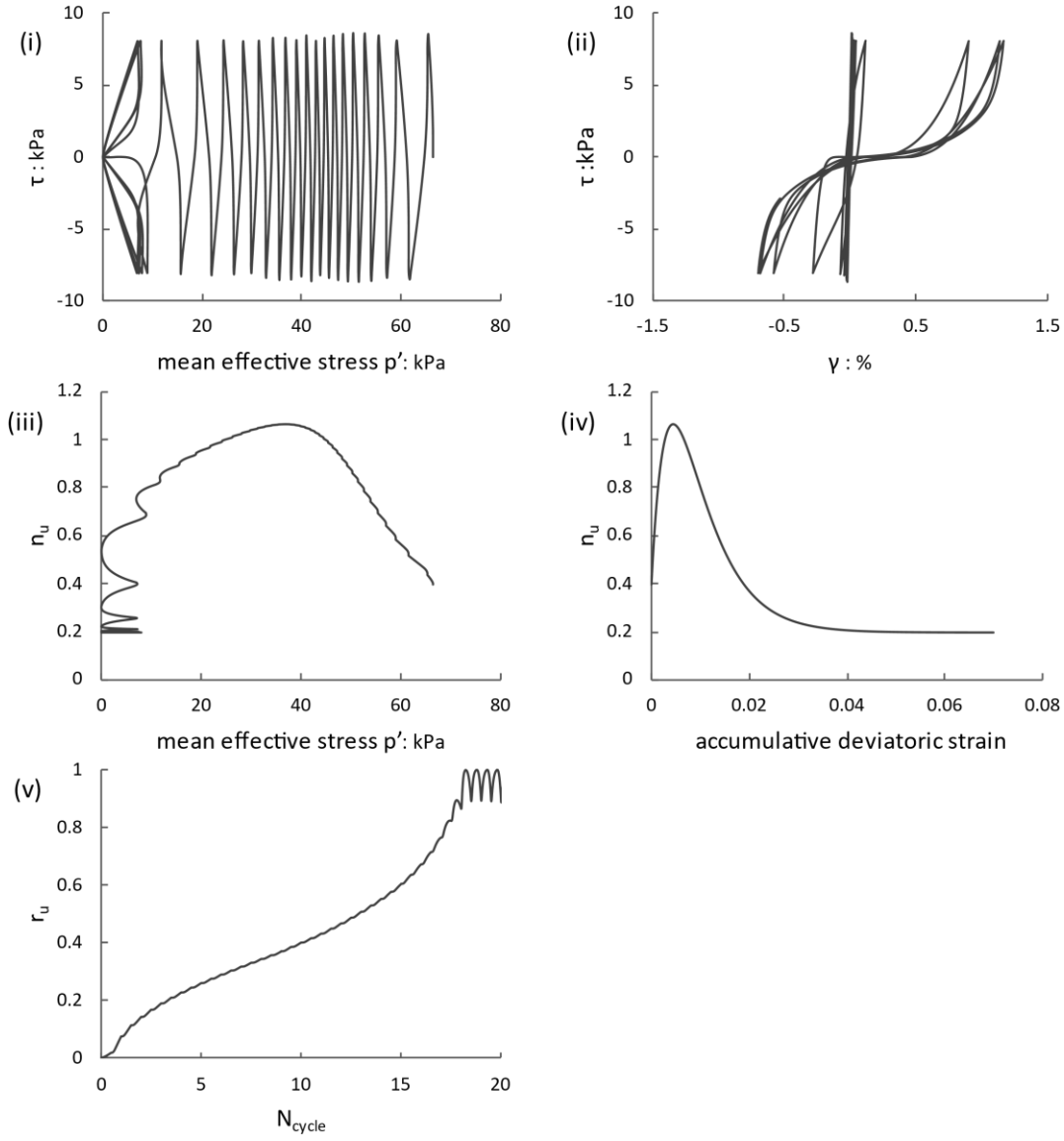

Σχήμα 17. Συμπεριφορά εδαφικού στοιχείου με D_r=60% σε DSS δοκιμή επιβαλλόμενης διατμητικής τάσης σταθερού πλάτους τ_{max}=8kPa, σύμφωνα με τη βαθμονόμηση του καταστατικού που επιλέχθηκε με σκοπό την επικύρωση του αναπτυχθέντος αλγορίθμου με βάση τρισδιάστατες αναλύσεις (Bouckovalas et al. 2011a) στο πρόγραμμα π.δ. FLAC 3D Itasca σε όρους: (i) μέσης ενεργού τάσης – διατμητικής τάσης, (ii) διατμητικής παραμόρφωσης – διατμητικής τάσης, (iii) μέσης ενεργού τάσης – εκθέτη *n*, (iv) αθροιστικής αποκλίνουσας τάσης – εκθέτη *n*, (v) ημιτονοειδών κύκλων φόρτισης – πίεσης πόρων.

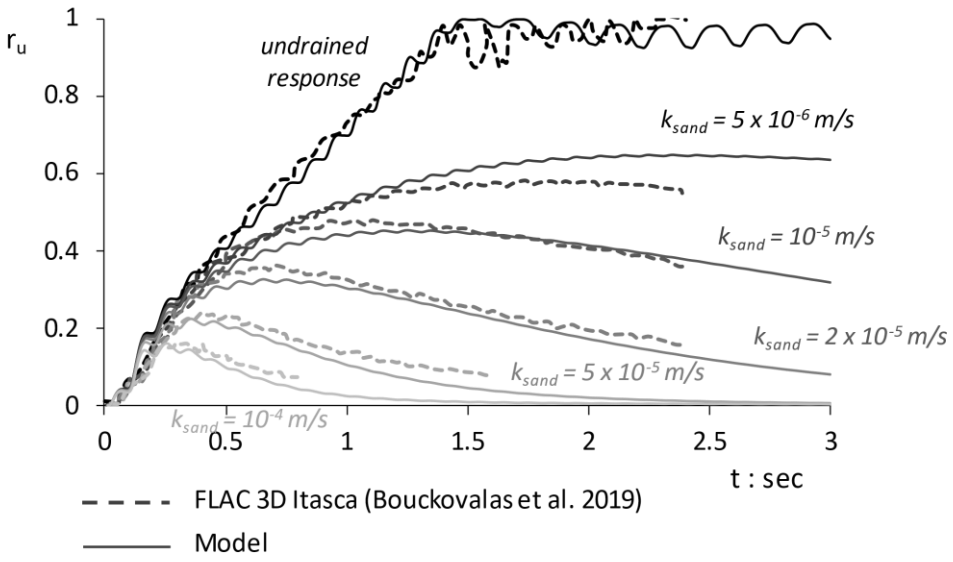

Σχήμα 18. Επικύρωση του αναπτυχθέντος αλγορίθμου με βάση τρισδιάστατες αναλύσεις (Bouckovalas et al., 2011a) στο πρόγραμμα π.δ. FLAC 3D Itasca, σε όρους χρονοϊστορίας υπερπίεσης πόρων του κέντρου λεπτής στρώσης άμμου ανάμεσα σε αργιλικά στρώματα, με κατακόρυφα στραγγιστήρια με R_d=0.5m και R_e=1.4m για τις εξής διαπερατότητες άμμου k: (i) 5 10^{-6} m/s, (ii) 10^{-5} m/s, (iii) 2 10^{-5} m/s, (iv) 5 10^{-5} m/s και (v) 10^{-4} m/s.

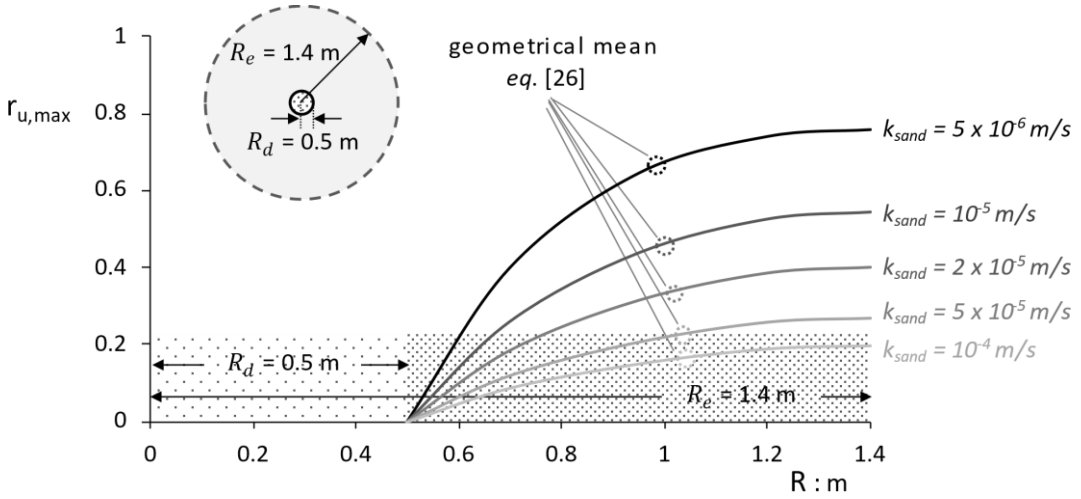

Σχήμα 19. Κατανομή των μεγίστων τιμών της υπερπίεσης πόρων κατά μήκος μιας ακτίνας εδάφους με κέντρο το κέντρο του στραγγιστηρίου με R_d=0.5m και R_e=1.4m για τις εξής διαπερατότητες άμμου k: (i) 5 10^{-6} m/s, (ii) 10^{-5} m/s, (iii) 2 10^{-5} m/s, (iv) 5 10^{-5} m/s και (v) 10^{-4} m/s. Παρουσιάζεται επίσης, ο γεωμετρικός μέσος όρος των τιμών κατά μήκος μιας ακτίνας, ως αντιπροσωπευτική τιμή της υπερπίεσης για τη μονοδιάστατη κατακόρυφη διάδοση του διατμητικού κύματος.

Εφαρμογές

Ομοιόμορφο αμμώδες προφίλ υπό ημιτονοειδή διέγερση

Εκτελείται μία απλή εφαρμογή του αλγορίθμου για την πρόβλεψη της μείωσης, χρήσει στραγγιστηρίων, των μέγιστων υπερπιέσεων $r_{u,\,max}$ καθ' ύψος απόθεσης H=15m ομοιόμορφης άμμου D_r=50%, υποβαλλόμενης σε ημιτονοειδή σεισμική διέγερση 15 κύκλων στη βάση της. Οι περιπτώσεις που εξετάζονται είναι οι εξής: (i) αστράγγιστες συνθήκες φόρτισης, (ii) κατακόρυφη στερεοποίηση του σχηματισμού εδραζόμενου σε διαπερατό βράχο και (iii) ταυτόχρονη κατακόρυφη και ακτινική στερεοποίηση με χαλικοπάσσαλο ακτίνας R_d τοποθετημένο μέχρι τη βάση του βράχου σε έδαφος ακτίνας R_e=1m, για λόγους R_d / R_e= 0.1, 0.2, 0.3 και 0.4. Εξετάζονται διαπερατότητες άμμου από k=2 10^{-5}m/s έως k=2 10^{-6}m/s. Η επίδραση της κατακόρυφης στράγγισης είναι αμελητέα (οι διαπερατότητες της άμμου που εξετάστηκαν είναι σχετικά μικρές) και είναι ορατή στη βάση του σχηματισμού (διαπερατό σύνορο) σε σχέση με τις πλήρως αστράγγιστες συνθήκες. Το μέγεθος της θετικής επίδρασης από την τοποθέτηση των στραγγιστηρίων κυμαίνεται ανάλογα με τη διάμετρο του στραγγιστηρίου και τη διαπερατότητα της άμμου. Για τη μεγαλύτερη από τις διαπερατότητες k=2 10^{-5}m/s οι τιμές κάλυψης που εξετάστηκαν επαρκούν για τη διατήρηση της μέγιστης υπερπίεσης σε πολύ χαμηλά επίπεδα, ενώ σταδιακά με την μείωση της διαπερατότητας της άμμου τα μέγιστα r_u αυξάνονται, μέχρι που η απόκριση οριακά συμπίπτει με την αστράγγιστη συμπεριφορά για k=2 10^{-6}m/s.

Το προφίλ του Port Island στο σεισμό του Kobe, 1995 ενισχυμένο με χαλικοπασσάλους

Τέλος, μελετάται η θεωρητική περίπτωση κατά την οποία το εδαφικό προφίλ του Port Island (Πίνακας 1) στο σεισμό του Kobe (1995) ενισχύεται με χαλικοπάσσαλο μήκους 16 m, με σκοπό το μετριασμό των επιπτώσεων της ρευστοποίησης. Τα αποτελέσματα της ανάλυσης δίδονται στο Σχήμα 21 σε όρους κατανομών μεγίστων με το βάθος. Ο μετριασμός της μέγιστης υπερπίεσης από την επιφάνεια έως και τα -16m συνεπάγεται τη μείωση των διατμητικών παραμορφώσεων και των οριζόντιων μετακινήσεων στα ίδια βάθη. Προκύπτει ότι η ελάχιστη κάλυψη ώστε να επιτευχθεί $r_{u\,max} < 0.5$ καθ' όλο το ύψος των 16m, είναι R_d/R_e=0.67. Η τιμή αυτή είναι φαινομενικά πολύ μεγάλη, υπενθυμίζεται όμως ότι πρόκειται για μία πολύ χαλαρή άμμο με D_r=30% περίπου, υποβαλλόμενη σε μία σφοδρότατη διέγερση. Υπό αυτές τις συνθήκες, θα ήταν σκόπιμη η δονητική συμπύκνωση του εδάφους σε συνδυασμό με τοποθέτηση στραγγιστηρίων,

προκειμένου να μειωθεί η απαιτούμενη κάλυψη. Σημειώνεται ότι για τις αναλύσεις αυτές, δεν έχει ληφθεί υπόψιν η μηχανική αλληλεπίδραση μεταξύ του χαλαρού εδάφους και του μεγαλύτερης αντοχής υλικού του στραγγιστηρίου σύμφωνα με την Εξίσωση [27-28], προκειμένου να δοθεί έμφαση στην μείωση του $r_{u,max}$ λόγω της επιρροής της στράγγισης και μόνο. Θα πρέπει να τονιστεί, ότι για τις αναλύσεις αυτές (όπως και στην περίπτωση προηγούμενης παραγράφου όπου το προφίλ του Kobe Port Island μελετάται χωρίς την ύπαρξη στραγγιστηρίων), η βαθμονόμηση έχει διατηρηθεί όπως παρουσιάστηκε αρχικά (μεθοδολογία και τιμές παραμέτρων), αντλώντας δεδομένα από τη βιβλιογραφία το χαρακτηρισμό της στρωματογραφίας και τις κατανομές των V_p, V_s και *SPT* του εξεταζόμενου προφίλ.

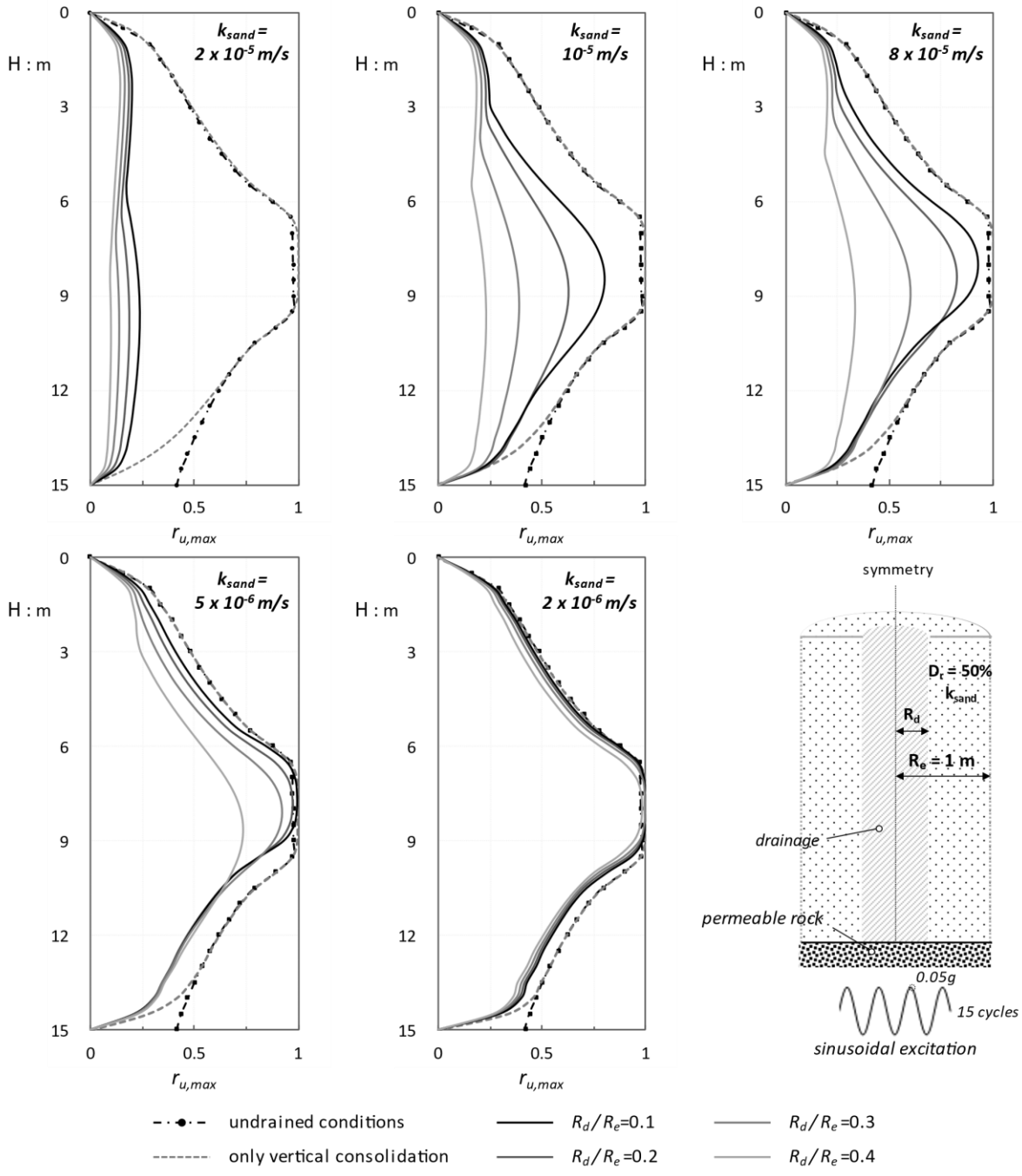

Σχήμα 20. Κατανομές καθ' ύψος της μέγιστης τιμής της υπερπίεσης πόρων $r_{u,max}$ θεωρώντας: (i) αστράγγιστες συνθήκες, (ii) κατακόρυφη στερεοποίηση, (iii) κατακόρυφη και οριζόντια στερεοποίηση με δείκτη R_d/R_e=0.1, (iv) R_d/R_e=0.2, (v) R_d/R_e=0.3 και (vi) R_d/R_e=0.4, όπου R_d η ακτίνα του στραγγιστηρίου και R_e η εδαφική ακτίνα επιρροής.

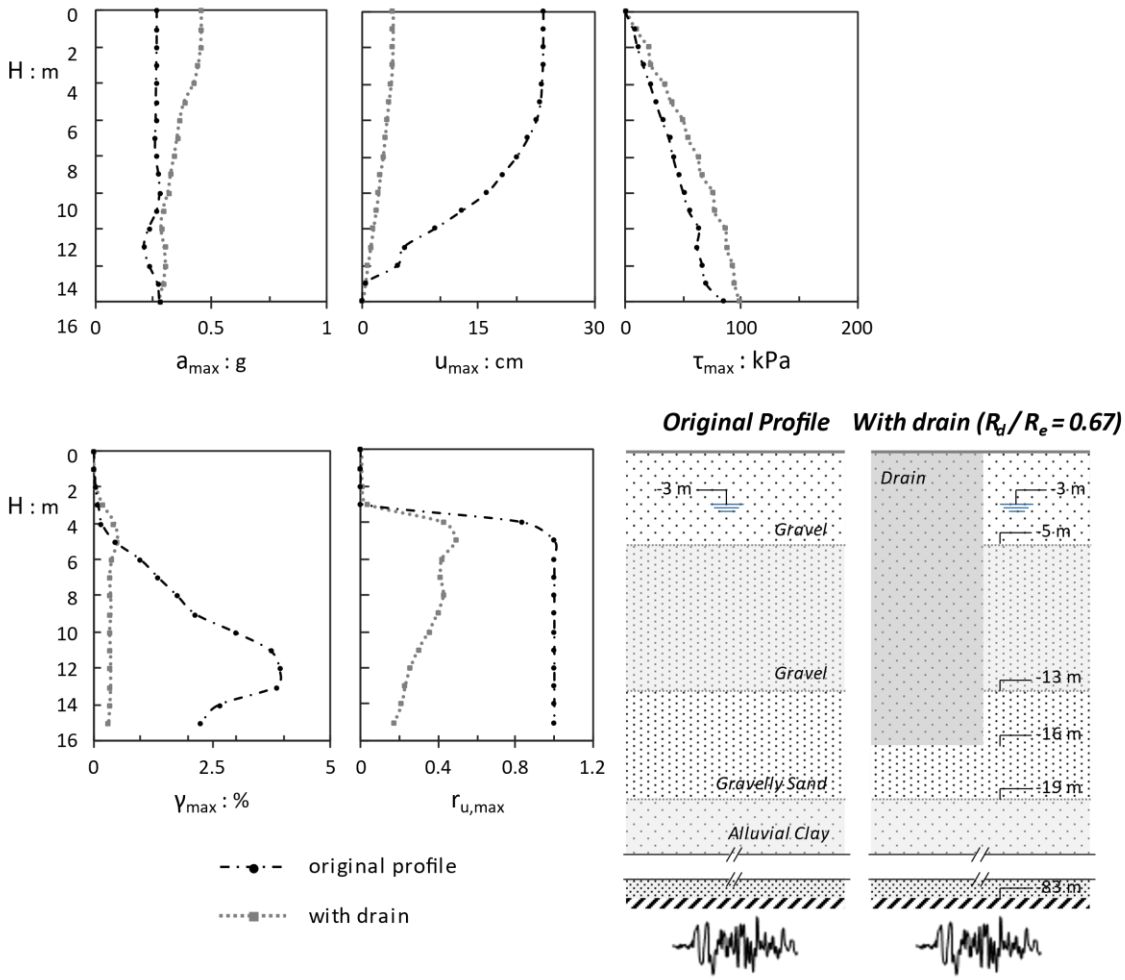

Σχήμα 21. Κατανομές καθ' ύψος των μέγιστων τιμών των παραμέτρων: (i) επιτάχυνση, (ii) σχετική μετακίνηση ως προς τη μετακίνηση σε βάθος 16m, (iii) διατμητική τάση, (iv) διατμητική παραμόρφωση και (v) υπερπίεση πόρων για το εδαφικό προφίλ του Πίνακα 1 (έως βάθος 16m) και για το ίδιο προφίλ θεωρώντας κατακόρυφο στραγγιστήριο ύψους 16m, με R_d=1m και R_e=1.5m (διέγερση βάσης: NS συνιστώσα της καταγραφής στο Kobe Port Island, 1995).

Η χρονοϊστορία των επιταχύνσεων στην επιφάνεια, με και χωρίς τη θεώρηση στραγγιστηρίων, παρουσιάζεται στο σχήμα 22. Το πρώτο τμήμα της απόκρισης (σκιασμένη περιοχή σχήματος) είναι σχεδόν όμοιο και στις δύο περιπτώσεις και αντιπροσωπεύει την απόκριση πριν την ρευστοποίηση. Κατά τη διάρκεια αυτού του τμήματος της κίνησης φαινόμενα εδαφικής ενίσχυσης ενδέχεται να εμφανιστούν, όπως τεκμηριώνεται και από τη διεθνή βιβλιογραφία (Tsiapas and Bouckovalas, 2019). Το εναπομείναν τμήμα της απόκρισης είναι στην περίπτωση με το στραγγιστήριο πολύ περισσότερο έντονο σε σχέση με την εξασθενημένη συμπεριφορά που σηματοδοτεί την εκδήλωση φαινομένων ρευστοποίησης. Παρόμοιες επισημάνσεις προκύπτουν και από τα αντίστοιχα ελαστικά φάσματα του

Σχήματος 23, όπου στην περίπτωση που λαμβάνεται υπόψη το στραγγιστήριο παρατηρείται ενίσχυση των υψηλών και αποδυνάμωση των χαμηλών συχνοτήτων, ενώ αντίθετη συμπεριφορά παρουσιάζει το αρχικό προφίλ.

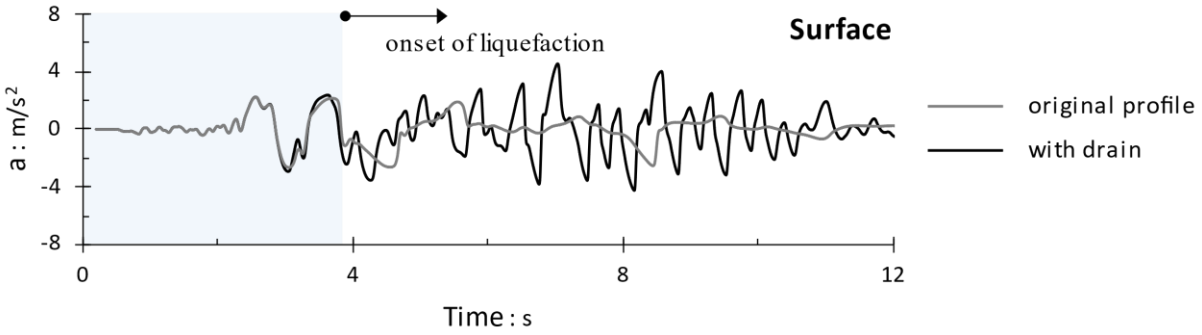

Σχήμα 22. Χρονοϊστορία επιταχύνσεων στην επιφάνεια για το εδαφικό προφίλ του Πίνακα 1 και για το ίδιο προφίλ θεωρώντας κατακόρυφο στραγγιστήριο ύψους 16m, με R_d=1m και R_e=1.5m (διέγερση βάσης: NS συνιστώσα της καταγραφής στο Kobe Port Island, 1995).

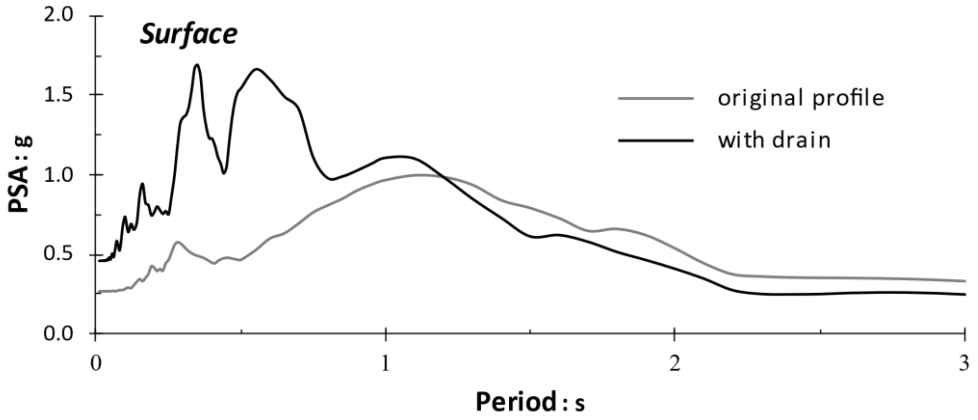

Σχήμα 23. Ελαστικό φάσμα επιτάχυνσης στην επιφάνεια για το εδαφικό προφίλ του Πίνακα 1 και για το ίδιο προφίλ θεωρώντας κατακόρυφο στραγγιστήριο ύψους 16m, με R_d=1m και R_e=1.5m (διέγερση βάσης: NS συνιστώσα της καταγραφής στο Kobe Port Island, 1995).

References

Ancheta T D, Darragh R B, Stewart J P, Seyhan E, Silva W J, Chiou B SJ, Wooddell K E, Graves R W, Kottke A R, Boore D M, Kishida T and Donahue J L (2013). PEER NGA-West2 Database, PEER Report 2013/03, Pacific Earthquake Engineering Research Center, Headquarters at the University of California, Berkeley, May 2013.

Andrianopoulos K I, Papadimitriou A G, Bouckovalas G D (2010). Bounding surface plasticity model for the seismic liquefaction analysis of geostructures. Soil Dynamics and Earthquake Engineering 2010; 30 (10): 895–911.

Andrus RD, Stokoe KH (1997). Liquefaction resistance based on shear wave velocity. In: Proceedings of the NCEER workshop on evaluation of liquefaction resistance of soils, national center for earthquake engineering research, state university of New York at buffalo; 1997. p. 89–128.

Baez J, Martin G. (1993, May). Advances in the design of vibro systems for the improvement of liquefaction resistance. In *Symposium Ground Improvement* (pp. 1-16).

Bouckovalas G, Dimitriadi V, Tsiapas Y, Tsioulou A. (2011a). Numerical simulation of drain performance in liquefiable soils. In: Proceedings of the 5th International Conference on Earthquake Geotechnical Engineering, Santiago, Chile; 10–13 January 2011.

Bouckovalas G, Papadimitriou A, Dimitriadi V (2012). Gravel drain performance in liquefiable soils: Numerical simulation and applicability. Proc., 2nd Int. Conf. on Performance-Based Design in Earthquake Geotechnical Engineering, International Society for Soil Mechanics and Geotechnical Engineering, London.

Bouckovalas G, Papadimitriou A, Kondis A, Bakas G (2006, September). Equivalent-uniform soil model for the seismic response analysis of sites improved with inclusions. In *Proc., 6th European Conf. on Numerical Methods in Geotechnical Engineering* (pp. 801-807).

Bouckovalas G, Papadimitriou A, Niarchos D (2009). Gravel drains for the remediation of liquefiable sites: The Seed & Booker (1977) approach revisited. Proc., Int. Conf. on Performance-Based Design (IS-Tokyo), International Society for Soil Mechanics and Geotechnical Engineering, London, 61–75.

Bouckovalas G, Papadimitriou A, Niarchos D, Tsiapas Y (2011b). Sand fabric evolution effects on drain design for liquefaction mitigation. *Soil Dynamics and Earthquake Engineering*, *31*(10), 1426-1439.

Darendeli MB, Stokoe KH, Rathje EM, Roblee CJ (2001). Importance of confining pressure on nonlinear soil behavior and its impact on earthquake response predictions of deep sites. In: Proceedings of the 15th international conference on soil mechanics and geotechnical engineering, August. Turkey: Istanbul; 2001. p. 27–31.

Drosos V, Gerolymos N, Gazetas G (2012). Constitutive model for soil amplification of ground shaking: parameter calibration, comparisons, validation. Soil Dynam Earthq Eng 2012; 42:255–74.

Elgamal AW, Zeghal M, Parra E (1995). Identification and modeling of earthquake ground response. Proc. 1st Int. Conf Earthquake Geotech. Engrg., Tokyo 1995;3. 1369- 1406.

Gazetas G (1982). Vibrational characteristics of soil deposits with variable wave velocity. Int J Numer Anal Methods GeoMech 1982; 6:1–20.

Gerolymos N, Gazetas G (2005). Constitutive model for 1-D cyclic soil behavior applied to seismic analysis of layered deposits. Soils Found 2005;45(3):147–59.

Gerolymos N, Gazetas G, Vardoulakis I A (2007). Thermo-poro-visco-plastic shear band model for seismic triggering and evolution of catastrophic landslides. Soils Found 2007;47(1):11–25.

Hardin BO (1978). The nature of stress-strain behavior of soils. Proceedings, Earthquake engineering and soil dynamics, 1. California: ASCE Pasadena; 1978. p. 3–89.

Hardin BO, Drnevich VP (1972). Shear modulus and damping in soils: design equations and curves. Journal of the Soil Mechanics and foundation division, ASCE 1972;98 (SM7):667–92.

Hashash Y, Dashti S, Romero MI, Ghayoomi M, Musgrove M (2015). Evaluation of 1-D seismic response modeling of sand using centrifuge experiments. Soil Dynam Earthq Eng 2015; 78:19–31.

Idriss IM (1995). Seed memorial lecture. University of California at Berkeley (I.M. Idriss, personal communication to T.L. Youd, 1997); 1995.

Idriss IM, Boulanger RW (2004). Semi-empirical procedures for evaluating liquefaction potential during earthquakes. In: Doolin D, et al., editors. Proceedings, 11th international conference on soil dynamics and earthquake engineering, and 3rd international conference on earthquake geotechnical engineering, 1. Stallion Press; 2004. p. 32–56.

Idriss IM, Boulanger RW (2008). Soil liquefaction during earthquakes. Monograph MNO- 12. Earthquake Engineering Research Institute, Oakland, CA, 2008:261.

Idriss IM, Boulanger RW (2010). SPT-based liquefaction triggering procedures. Report UCD/CGM-10/02. Davis, CA: Department of civil and environmental engineering, University of California; 2010. p. 259. 2010.

Ishibashi I, Zhang X (1993). Unified dynamic shear moduli and damping ratios of sand and clay. Soils Found 1993;33(1):182–91.

Iwasaki Y (1995). Geological and geotechnical characteristics of Kobe area and strong ground motion records by 1995 Kobe earthquake, soils and foundations, special issue on geotechnical aspects of the january 17, 1995. Hyogoken-Nambu Earthquake 1995;43(6):15–20.

Iwasaki Y, Masaru T (1996). Strong motion records at Kobe Port Island. Special issue of soils and foundations. Japanese Geotechnical Society Jan 1996;29–40.

Kramer SL (1996). Geotechnical earthquake engineering. Prentice Hall; 1996.

Onoue A (1988). Diagrams considering well resistance for designing spacing ratio of gravel drains. Soils Found., 28(3), 160–168.

Pestana J M, Hunt C E, Goughnour R R (1997). FEQDrain: A finite element computer program for the analysis of the earthquake generation and dissipation of pore water pressure in layered sand deposits with vertical drains. Rep. No. EERC 97-15, Earthquake Engineering Research Center, Univ. of California, Berkeley, CA.

Seed H B, Booker J R (1977). Stabilization of potentially liquefiable sand deposits. J. Geotech. Engrg. Div., 103(7), 757–768.

Seed HB, Idriss IM (1982). Ground motions and soil liquefaction during earthquakes. Oakland, California: Earthquake Engineering Research Institute Monograph; 1982.

Seid-Karbasi M, Byrne P M (2007). Seismic liquefaction, lateral spreading and flow slides: A numerical investigation into void redistribution. Can. Geotech. J., 44(7), 873–890.

Tasiopoulou P, Gerolymos N (2016) (a). Constitutive modeling of sand: formulation of a new plasticity approach. Soil Dynam Earthq Eng 2016; 82:205–21.

Tasiopoulou P, Gerolymos N (2016) (b). Constitutive modelling of sand: a progressive calibration procedure accounting for intrinsic and stress-induced anisotropy. Geotechnique 2016;66(9):1–17.

Tsiapas Y Z, Bouckovalas G D (2019). Equivalent linear computation of response spectra for liquefiable sites: The spectral interpolation method, Soil Dynamics and Earthquake Engineering 116 (2019) 541–551.

Tsiapas I, Tsioulou A (2009). Revised design of drains for seismic liquefaction mitigation. Diploma Thesis, School of Civil Engineering, National Technical University of Athens; 2009 [in Greek].

Vucetic M, Dobry R (1991). Effect of soil plasticity on cyclic response. Journal of Geotechnical Engineering 1991;117(1):89–107.

Vytiniotis A, Whittle A J (2013). Effectiveness of PV drains for mitigating earthquake-induced deformations in sandy slopes. Proc., Geo-Congress 2013: Stability and Performance of Slopes and Embankments III, C. Meehan, D. Pradel, M. A. Pando, and J. F. Labuz, eds., ASCE, Reston, VA, 908–917.

Weiler WA (1988). Small strain shear modulus of clay. In: Proceedings, ASCE conference on earthquake engineering and soil dynamics II: recent advances in ground motion evaluation. New York: Geotechnical special publication 20, ASCE; 1988. p. 331–5.

Yamazaki F, Ansary MA, Towhata I (1995). Application of a dynamic effective stress model at a reclaimed site during the Great Hanshin earthquake, 1995. Proc. 1st Int. Conf. Earthquake Geotech. Engrg., Tokyo 1995;1:591–7.

Youd TL, Idriss IM, Andrus RD, Arango I, Castro G, Christian JT, et al. (2001). Liquefaction resistance of soils: summary report from the 1996 NCEER and NCEER/NSF workshops on evaluation of liquefaction resistance of soils. Journal of Geotechnical and Geoenvironmental Engineering, ASCE 2001 2001;127:817–33. October 2001.

Table of Contents

Chapter 1

Introduction

Evaluating soil response to strong earthquake motions, has always been a major issue in earthquake engineering, since it provides essential information in case of constructing an earthquake resistance structure in seismically active areas. Modelling the seismic wave propagation, usually precedes the calculation of the structure response during an earthquake event, since the latter is directly affected by the propagation of seismic waves through the soil deposit. Furthermore, the performance-based design method has increasingly drawn the attention of academic community and thus, a substantial effort has been devoted in the last decades in developing analytical techniques and numerical methods for evaluating the response of soil deposits to strong earthquake motions.

Several constitutive models and numerical codes have been proposed for 1D seismic response analysis of horizontally layered soils subjected to vertically-polarized S waves. In general, they can be categorized into three major groups: (a) The equivalent linear viscoelastic models (e.g. Schnabel 1972, Rathje et al. 2006, Bardet et al. 2000, Asimaki and Kausel 2002), (b) the nonlinear hysteretic (or phenomenological) models (e.g. Lee 1978, Ishihara and Towhata 1980, Hashash and Park 2001, Gerolymos and Gazetas 2005, Bonilla et al 2005, Lo Presti et al. 2006, Drosos et al. 2012, Tropeano et al. 2016, Shi and Asimaki 2017), and (c) the plasticity-based models (e.g. Prevost 1989, Yang et al. 2004, Iai et al. 1990, Elgamal et al. 1998, Borja et al. 2002, Modaressi and Foerster 2000, Pisano and Jeremic 2014).

Equivalent linear models are the most popular owing to their computational convenience and simplicity. Their main limitations include their inability to efficiently predict the behavior of a

nonlinear system under strong ground motions where large cyclic shear strains dominate the response and the violation of the principle of physical causality (Ching and Glaser, 2001). Well identified features of cyclic soil behavior, such as: densification, cyclic mobility, stiffness decay and loss of strength due to pore pressure generation and asymmetric response with loading direction are inherently impossible to be reproduced.

Hysteretic models are plausible alternatives to plasticity-based models, but, while capable of overcoming most of the aforementioned limitations, the calibration process is often an arduous task in which the physical meaning of the model parameters is often jeopardized in favour of case-specific accuracy. The absence of a physical law for relating volumetric with shear strains is the main source of this drawback.

In this paper a downscale version of the Ta-Ger model by Tasiopoulou and Gerolymos (2016a, b) is developed and is implemented into a finite difference code for performing dynamic nonlinear analysis of horizontally layered soil deposits subjected to vertically propagated S waves. Ta-Ger model for sand is based on a new theoretical framework that combines features of perfect elasto-plasticity and smooth hysteresis. It provides remarkable versatility in capturing complex patterns of sand behavior such as cyclic mobility, static liquefaction and densification (Tasiopoulou and Gerolymos, 2016a). The one-dimensional version of the Ta-Ger model is reformulated (a) to provide a unified calibration procedure for both drained and undrained response analysis of sand emphasizing on liquefaction and cyclic mobility, and (b) to describe the hysteretic behavior of clay by assuming fully undrained loading conditions. The calibration of the model parameters for sand is based on a procedure that targets to the optimum performance in both drained and undrained load conditions by simultaneously matching the response in terms of: (a) the cyclic resistance ratio curves as per the NCEER/NSF methodology, and (b) widely-used experimental shear modulus and damping ratio curves available in the literature. For the clay-like soil the calibration involves only the second step under the assumption of fully undrained conditions

Consequently, a finite differences algorithm for conducting nonlinear seismic ground response analyses of horizontally layered sites, including liquefaction effects, is developed. Seismic base excitation is assumed to be the result of exclusively vertically polarized S waves, and hence the analysis is reduced to 1-D wave propagation. The developed numerical algorithm involves the 1D consolidation equation to simultaneously account for the generation of excess pore water pressures within sandy layers due to cyclic loading, their

distribution and dissipation during and after earthquake shaking and their impact on the transmitted waves. The developed wave-propagation algorithm is verified against analytical solutions for soil amplification of homogeneous and linearly increasing shear wave velocity profiles (Gazetas, 1982). The versatility of the model to calculate the seismic soil response is tested against two centrifuge tests in dry Nevada sand specimens (Hashash et al., 2015). It is then applied to reproduce the case history of Port Island array in 1995 Kobe earthquake (Iwasaki, 1995, 1996).

The model is then applied to estimate the elastic response spectra at the surface of soil profiles with liquefiable layers (ground type S_2) as per EC8:2004. The prediction of the response spectra of liquefiable soil deposits is not rigorously investigated in the literature (Gingery et al. 2015) and not adequately covered by the national and global codes, since constructing in such conditions should be generally avoided according to the code guidelines, unless special measures are taken, such as soil reclamation, piles, etc. However, a number of studies evince that such precautions may not be inflicted, on condition that a surface non liquefiable soil layer will be used to mitigate structure settlements (Ishihara et al. 1993, Acacio et al 2001, Cascone and Bouckovalas 1998, Naesgaard et al. 1998, Dashti et al. 2010, Karamitros et al. 2013, Dimitriadi et al. 2017) Thus, estimating the seismic response in prone to liquefaction sites has recently arouse academic interest, since the evaluation of ground response is usually the first step in the calculation of structural response in soil-structure interaction problems. To this direction, as a preliminary application, the proposed model is employed to investigate the calculation of the ground surface elastic response spectra for type S_2 soil profiles (with liquefiable layers), by analyzing the seismic response of an ensemble of idealized, susceptible to liquefaction configurations, submitted to a considerable number of actual seismic records with varying characteristics covering a variety of seismological conditions. Similar to previous studies for non-liquifiable soils (e.g. Rey et al. 2002, Pitilakis et al. 2013, Anastasiadis and Riga 2014), processing of the results leads to the recommendation of an idealized ground surface response spectrum in terms of the design spectrum parameters S, T_B and T_C, as per the EC8.

The developed numerical algorithm is finally employed for the simulation of the seismic response of liquefiable sandy sites improved with vertical drains. The differential equation of soil consolidation is reformulated to account not only for the vertical water flow up to the ground surface, but also for the axisymmetric flow of water, through the ground towards the

drain. The placement of gravel columns and the vibration compaction of the surrounding soil have traditionally been used to mitigate liquefaction hazardous effects. More recently, an alternative preventive measure has been applied; the use of prefabricated vertical drains (*PVDs*), an environment friendly solution that causes less site disruption than other soil improvement methods (Rollins et al. 2004, Harada et al. 2006, Marinucci et al. 2008). Among their other benefits, *PVDs* are better protected against clogging inflicted by thin, silty soil, that can diminish their permeability. The simulation of drain improved sites and the prediction of drains mitigation effects have long been studied in the literature; Seed & Booker (1977) were the first to propose design charts that predict $r_{u,max}$ within the unit cell around a single drain, for a specified geometry, soil characteristics and a given earthquake shaking. These design charts were repeatedly modified and improved by several investigators, such as Onoue (1988), Matsubara et al. (1988), Iai and Koizumi (1986) and Bouckovals et al. (2009, 2011b). Numerical modelling has also been employed to model liquefiable sites improved with drains, e.g. Pestana et al. (1997), Bouckovalas et al (2011a), Papadimitriou et al. (2007), Seid Karbasi & Byrne (2007) and Vytiniotis and Whittle (2013) along with experimental approaches, e.g. Howell et al. (2012), Marinucci et al. (2008), Indraratna et al. (2009) and Parsa-Pajouh et al. (2016).

References

Acacio, A. A., Kobayashi, Y., Towhata, I., Bautista, R. T., & Ishihara, K. (2001). Subsidence of building foundation resting upon liquefied subsoil: case studies and assessment. *Soils and Foundations*, *41*(6), 111-128.

Anastasiadis, A., & Riga, E. (2014). Site classification and spectral amplification for seismic code provisions. In *Earthquake Geotechnical Engineering Design* (pp. 23-72). Springer, Cham.

Assimaki, D., & Kausel, E. (2002). An equivalent linear algorithm with frequency-and pressure-dependent moduli and damping for the seismic analysis of deep sites. *Soil Dynamics and Earthquake Engineering*, *22*(9-12), 959-965.

Bardet, J. P., Ichii, K., & Lin, C. H. (2000). *EERA: a computer program for equivalent-linear earthquake site response analyses of layered soil deposits*. University of Southern California, Department of Civil Engineering.

Bonilla, L. F., Archuleta, R. J., & Lavallée, D. (2005). Hysteretic and dilatant behavior of cohesionless soils and their effects on nonlinear site response: Field data observations and modeling. *Bulletin of the Seismological Society of America*, *95*(6), 2373-2395.

Borja, R. I., Duvernay, B. G., & Lin, C. H. (2002). Ground response in Lotung: total stress analyses and parametric studies. *Journal of Geotechnical and Geoenvironmental Engineering*, *128*(1), 54-63.

Bouckovalas, G., Dimitriadi, V., Tsiapas, Y., & Tsioulou, A. (2011a, January). Numerical simulation of drain performance in liquefiable soils. In *Proceedings of the 5th International Conference on Earthquake Geotechnical Engineering, Santiago, Chile* (pp. 10-13).

Bouckovalas, G. D., Papadimitriou, A. G., & Niarchos, D. (2009). Gravel drains for the remediation of liquefiable sites: the Seed & Booker (1977) approach revisited. In *Proceedings of International Conference on Performance-Based Design in Earthquake, IS-Tokyo*.

Bouckovalas, G. D., Papadimitriou, A. G., Niarchos, D. G., & Tsiapas, Y. Z. (2011b). Sand fabric evolution effects on drain design for liquefaction mitigation. *Soil Dynamics and Earthquake Engineering*, *31*(10), 1426-1439.

Cascone, E., & Bouckovalas, G. (1998, September). Seismic bearing capacity of footings on saturated sand with a clay cap. In *Proc., 11th European Conf. on Earthquake Engineering*.

Ching, J. Y., & Glaser, S. D. (2001). 1D time-domain solution for seismic ground motion prediction. *Journal of geotechnical and geoenvironmental engineering*, *127*(1), 36-47.

Dashti, S., Bray, J. D., Pestana, J. M., Riemer, M., & Wilson, D. (2010). Mechanisms of seismically induced settlement of buildings with shallow foundations on liquefiable soil. *Journal of geotechnical and geoenvironmental engineering*, *136*(1), 151-164.

Dimitriadi, V. E., Bouckovalas, G. D., & Papadimitriou, A. G. (2017). Seismic performance of strip foundations on liquefiable soils with a permeable crust. *Soil Dynamics and Earthquake Engineering*, *100*, 396-409.

Drosos, V. A., Gerolymos, N., & Gazetas, G. (2012). Constitutive model for soil amplification of ground shaking: Parameter calibration, comparisons, validation. *Soil Dynamics and Earthquake Engineering*, *42*, 255-274.

Elgamal, A. W., Yang, Z., Parra, E., & Ragheb, A. (1998). CYCLIC 1D: An Internet-based finite element computer program for one-dimensional site amplification analysis using an incremental plasticity coupled solid-fluid (u-p) formulation. *Univ. of California at San Diego,(http://casagrande. ucsd. edu/cyclic1d/cyclic1d. html*.

Gerolymos, N., & Gazetas, G. (2005). Constitutive model for 1-D cyclic soil behaviour applied to seismic analysis of layered deposits. *Soils and Foundations*, *45*(3), 147-159.

Gingery, J. R., Elgamal, A., & Bray, J. D. (2015). Response spectra at liquefaction sites during shallow crustal earthquakes. *Earthquake Spectra*, *31*(4), 2325-2349.

Harada, N., Towhata, I., Takatsu, T., Tsunoda, S., & Sesov, V. (2006). Development of new drain method for protection of existing pile foundations from liquefaction effects. *Soil Dynamics and Earthquake Engineering*, *26*(2-4), 297-312.

Hashash, Y. M., Dashti, S., Romero, M. I., Ghayoomi, M., & Musgrove, M. (2015). Evaluation of 1-D seismic site response modeling of sand using centrifuge experiments. *Soil Dynamics and Earthquake Engineering*, *78*, 19-31.

Hashash, Y. M., & Park, D. (2001). Non-linear one-dimensional seismic ground motion propagation in the Mississippi embayment. *Engineering Geology*, *62*(1-3), 185-206.

Howell, R., Rathje, E. M., Kamai, R., & Boulanger, R. (2012). Centrifuge modeling of prefabricated vertical drains for liquefaction remediation. *Journal of geotechnical and geoenvironmental engineering*, *138*(3), 262-271.

Iai S, Koizumi K. Estimation of earthquake induced excess pore pressure for gravel drains. In: Proceedings of the 7th Japan Earthquake Symposium; 1986, p. 679–84.

Iai, S., Matsunaga, Y., & Kameoka, T. (1990). Strain space plasticity model for cyclic mobility. *Report of the Port and harbour Research Institute*, *29*(4).

Indraratna, B., Attya, A., & Rujikiatkamjorn, C. (2009). Experimental investigation on effectiveness of a vertical drain under cyclic loads. *Journal of geotechnical and geoenvironmental engineering*, *135*(6), 835-839.

Ishihara, K., Acacio, A. A., & Towhata, I. (1993). Liquefaction-induced ground damage in Dagupan in the July 16, 1990 Luzon earthquake. *Soils and Foundations*, *33*(1), 133-154.

Ishihara K, Towhata I (1980). One-dimensional soil response analysis during earthquakes based on effective stress model. J Facul Eng Univ Tokyo; 35 (4).

Iwasaki, Y. (1995). Geological and geotechnical characteristics of Kobe area and strong ground motion records by 1995 Kobe earthquake. *Tsuchi to kiso*, *43*(6), 15-20.

Iwasaki, Y. (1996). Strong motion records at Kobe Port Island. Special Issue on Geotechnical Aspects of the January 17 1995 Hyogoken-Nambu Earthquake. *Soil and Fundations*, 19-40.

Karamitros, D. K., Bouckovalas, G. D., & Chaloulos, Y. K. (2013). Insight into the seismic liquefaction performance of shallow foundations. *Journal of Geotechnical and Geoenvironmental Engineering*, *139*(4), 599-607.

Lee, M. K. D. (1978). DESRA-2: Dynamic effective stress response analysis of soil deposits with energy transmitting boundary including assessment of liquefaction potential. *Research Report, University of British Columbia*.

Lo Presti, D. C., Lai, C. G., & Puci, I. (2006). ONDA: Computer code for nonlinear seismic response analyses of soil deposits. *Journal of Geotechnical and Geoenvironmental Engineering*, *132*(2), 223-236.

Marinucci, A., Rathje, E., Kano, S., Kamai, R., Conlee, C., Howell, R., ... & Gallagher, P. (2008). Centrifuge testing of prefabricated vertical drains for liquefaction remediation. In *Geotechnical earthquake engineering and soil dynamics IV* (pp. 1-10).

Matsubara, K., Mihara, M., & Tsujita, M. (1988). Analysis of gravel drain against liquefaction and its application to design. In *Proceedings, 9th World Conference on Earthquake Engineering* (Vol. 3, pp. 249-254).

Modaressi, H., & Foerster, E. (2000). CyberQuake. *User's manual, BRGM, France*.

Naesgaard, E., Byrne, P. M., & Huizen, G. V. (1998). Behaviour of Light Structures Founded on Soil "Crust" over Liquefied Ground. In *Geotechnical Earthquake Engineering and Soil Dynamics III* (pp. 422-433). ASCE.

Onoue, A. (1988). Diagrams considering well resistance for designing spacing ratio of gravel drains. Soils Found., 28(3), 160–168.

Papadimitrou, A., Moutsopoulou, M. E., Bouckovalas, G., & Brennan, A. (2007, June). Numerical investigation of liquefaction mitigation using gravel drains. In *4th International Conference on Geotechnical Earthquake Engineering*.

Parsa-Pajouh, A., Fatahi, B., & Khabbaz, H. (2016). Experimental and numerical investigations to evaluate two-dimensional modeling of vertical drain–assisted preloading. *International Journal of Geomechanics*, *16*(1), B4015003.

Pestana, J. M., Hunt, C. E., & Goughnour, R. R. (1997). *FEQDrain: A finite element computer program for the analysis of the earthquake generation and dissipation of pore water pressure in layered sand deposits with vertical drains*. Earthquake Engineering Research Center, University of California.

Pisanò, F., & Jeremić, B. (2014). Simulating stiffness degradation and damping in soils via a simple visco-elastic–plastic model. *Soil Dynamics and Earthquake Engineering*, *63*, 98-109.

Pitilakis, K., Riga, E., & Anastasiadis, A. (2013). New code site classification, amplification factors and normalized response spectra based on a worldwide ground-motion database. *Bulletin of Earthquake Engineering*, *11*(4), 925-966.

Prevost, J. H. (1989). *DYNA1D: a computer program for nonlinear seismic site response analysis technical documentation*. Buffalo, N. Y: National Center for Earthquake Engineering Research.

Rathje, E. M., Ozbey, M. C., & Kottke, A. (2006). Site Amplification Predictions using Random Vibration Theory. In *Proceedings, First European Conference on Earthquake Engineering and Seismology, Paper* (No. 337).

Rey, J., Faccioli, E., & Bommer, J. J. (2002). Derivation of design soil coefficients (S) and response spectral shapes for Eurocode 8 using the European Strong-Motion Database. *Journal of seismology*, *6*(4), 547-555.

Rollins, K., Anderson, J. K., Goughnour, R. R., & McCain, A. K. (2004, August). Liquefaction hazard mitigation using vertical composite drains. In *The 13th World Conference on Earthquake Engineering. Vancouver BC, Canada*.

Schnabel, P. B. (1972). SHAKE: A computer program for earthquake response analysis of horizontally layered sites. *EERC Report 72-12, University of California, Berkeley.*

Seed, H. B., and Booker, J. R. (1977). Stabilization of potentially liquefiable sand deposits. J. Geotech. Engrg. Div., 103(7), 757–768.

Seid-Karbasi, M., & Byrne, P. M. (2007). Seismic liquefaction, lateral spreading, and flow slides: a numerical investigation into void redistribution. *Canadian Geotechnical Journal*, *44*(7), 873-890.

Shi, J., & Asimaki, D. (2017). From stiffness to strength: Formulation and validation of a hybrid hyperbolic nonlinear soil model for site-response analyses. *Bulletin of the Seismological Society of America*, *107*(3), 1336-1355.

Tasiopoulou, P., & Gerolymos, N. (2016a). Constitutive modeling of sand: Formulation of a new plasticity approach. *Soil Dynamics and Earthquake Engineering*, *82*, 205-221.

Tasiopoulou, P., & Gerolymos, N. (2016b). Constitutive modelling of sand: a progressive calibration procedure accounting for intrinsic and stress-induced anisotropy. *Géotechnique*, *66*(9), 754-770.

Tropeano, G., Chiaradonna, A., d'Onofrio, A., & Silvestri, F. (2016). An innovative computer code for 1D seismic response analysis including shear strength of soils. *Géotechnique*, *66*(2), 95-105.

Vytiniotis, A., & Whittle, A. J. (2013). Effectiveness of PV drains for mitigating earthquake-induced deformations in sandy slopes. In *Geo-Congress 2013: Stability and Performance of Slopes and Embankments III* (pp. 908-917).

Yang, Z., Lu, J., & Elgamal, A. (2004). A web-based platform for computer simulation of seismic ground response. *Advances in Engineering Software*, *35*(5), 249-259.

Chapter 2

The p-q version of the plasticity - based constitutive model Ta-Ger

2.1. Model description

2.1.1. Cyclic response of sand

Ta-Ger model for sand behavior (Tasiopoulou and Gerolymos, 2016 a & b) is fundamentally formulated in the 6-dimenional stress space. The *p-q* version of this model can be written in the following incremental stress-strain form (Gerolymos et al. 2018, Anthi and Gerolymos, 2019):

$$\begin{bmatrix} dp \\ dq \end{bmatrix} = \eta \begin{bmatrix} K - \frac{-K^2 M_s d}{-KM_s d+3G}\zeta_a{}^n & \frac{3KGd}{-KM_s d+3G}\zeta_a{}^n \\ \frac{-3KGM_s}{-KM_s d+3G}\zeta_a{}^n & 3G - \frac{9G^2}{-KM_s d+3G}\zeta_a{}^n \end{bmatrix} \begin{bmatrix} d\varepsilon_p \\ d\varepsilon_q \end{bmatrix} \tag{2.1}$$

in which K and G are the elastic (small strain) bulk and shear modulus respectively, d is the ratio of the plastic volumetric strain increment $d\varepsilon_p{}^p$ over the plastic deviatoric strain increment $d\varepsilon_q{}^p$ and is based on Rowe's dilatancy theory as it depends on the distance of the

current stress ratio q/p from the phase transformation line. M_{pt} and M_s are the phase transformation and failure stress ratio representing the ultimate strength. Parameter ζ_α (Tasiopoulou and Gerolymos, 2016a) is a hysteretic dimensionless quantity that provides the loading and unloading rule and is a function of the Bouc–Wen parameter ζ (Gerolymos and Gazetas 2005, Gerolymos et al. 2007), while the exponent n controls the rate of transition from the elastic state to the perfectly plastic one. Finally, η is inserted as a multiplier of the hardening elastoplastic matrix expressing the dissipated hysteretic energy. The following formulation for the elastic shear modulus G is adopted:

$$G = 1592.6\, p_a\, {D_r}^{0.6464} \left(\frac{p\prime}{p_a}\right)^m \tag{2.2}$$

where p_a is the atmospheric pressure, D_r is the sand relative density and p' is the mean effective confinement pressure. The expression is based on the empirical relationship for the maximum shear modulus of sand:

$$G_{max} = 1000\, k_{2max}\, p'^{0.5} \tag{2.3}$$

where the parameter $K_{2,max}$ is directly determined from relative density D_r or void ratio e and p' is in lb/ft^2. (Seed and Idriss, 1970). Following a curve fitting procedure, equation (2.2) for G_{max} arises (Souliotis, 2015). The bulk modulus is given by:

$$K = \frac{2(1+\nu)}{3(1-2\nu)} G \tag{2.4}$$

in which v stands for the Poisson's ratio. In equation (2.2) exponent m is expressed as a function of the excess pore water pressure ratio r_u according to:

$$m = m_{peak} + \left(m_0 - m_{peak}\right) e^{-r_u} \tag{2.5}$$

The initial value of m, m_0, is 0.5 for zero r_u (drained conditions), and it tends asymptotically to m_{peak} equal to 1, when r_u approaches unity. Exponent n can be expressed as the sum of an undrained n_u and a drained loading component n_d as:

$$n = n_u e^{-A\frac{D_r - D_{r0}}{1-D_{r0}}} + n_d \left(1 - e^{-A\frac{D_r - D_{r0}}{1-D_{r0}}}\right) \tag{2.6}$$

in which D_{r0} is the initial value of the relative density, and A a large number (e.g. $A \approx 100$). n_u is a function of the cumulative deviatoric strain increment according to the following relationship:

$$n_u = n_f + \left[n_{peak} + \left(n_0 - n_{peak}\right)e^{-b\sum de_q} - n_f\right]e^{-g\sum de_q} \tag{2.7}$$

where n_o is the initial value of n, n_{peak} is a potentially reached peak value, n_f is the final value of n and $\Sigma d\varepsilon_q$ stands for the cumulative deviatoric strain increment. n_d is a constant and is practically activated when the relative density evolves (drained conditions). b is a constant and g is expressed as a function of the relative density D_r and the initial mean effective stress p'_0, according to:

$$g = g_1 + g_2 D_r + g_3 \ln(p'_0) \tag{2.8}$$

where g_1, g_2 and g_3 are constants. The bounding stress ratio has been slightly revised from its original version (Tasiopoulou and Gerolymos, 2016a) according to:

$$M_s = M_{cs} + \left[M_{s_p} + \left(M_{s_0} - M_{s_p}\right)e^{-2c\sum de_q} - M_{cs}\right]e^{-2c\sum de_q} \tag{2.9}$$

where M_{s0} is an initial value, M_{cs} is the critical state value and M_{sp} is a maximum value that can be potentially reached depending on the model parameter c. The latter is given by:

$$c = 6 + 4Ir_0 \tag{2.10}$$

in which Ir_0 represents the initial Bolton's relative dilatancy index:

$$Ir_0 = D_{r0}(Q - \ln(p_0)) - \mathrm{R} \tag{2.11}$$

where Q=9.15 and R=0.77. In the same context, the phase transformation stress ratio is revised as follows:

$$M_{pt} = M_{cs} + \left(M_{pt_0} - M_{cs}\right)e^{-6c\sum de_q} \tag{2.12}$$

with its initial value M_{pt0} according to the following relationship:

$$M_{pt_0} = \left(M_{s_{peak}} - \frac{0.9I_r}{3+0.3I_r}\right)\zeta_a \tag{2.13}$$

Parameter R_d was extended to account not only for drained but also for undrained loading as a function of ΔD_r and r_u:

$$R_d = e^{-a_1 r_u} e^{-a_2 (D_r - D_{r0})} \tag{2.14}$$

in which α_1 and α_2 are constant values.

Finally, the dissipated hysteretic energy parameter η, which is activated only under drained conditions of loading, initially proposed by Gerolymos and Gazetas (2005) and Drosos et al. (2012):

$$\eta = \frac{s_1}{s_1 + \mu s_2} \tag{2.15}$$

where μ is a reference ductility defined in terms of the shear strain and s_1, s_2 are functions of the effective confinement pressure p':

$$s_1 = B p'^{\,k} \tag{2.16}$$

$$s_2 = C p'^{\,m} \tag{2.17}$$

2.1.2. Simplified version for clayey soils

A simplified version of the developed *p-q* version of Ta-Ger model is used to represent the behavior of clay in cyclic loading, based on the assumption of zero incremental volumetric strains and relating M_s with the undrained strength S_u. Numerical simulations of direct simple shear tests were conducted in order to match the model response with the experimentally measured pressure and plasticity dependent shear modulus reduction and damping curves. Exponent *n* is expressed as a function of the plasticity index according to:

$$n = f\ ln(PI) + h \tag{2.18}$$

The dissipated hysteretic energy parameter η, is preserved as it was presented in equation (2.15), with s_1 taking constant values and s_2 being function of the plasticity index:

$$s_2 = q\ ln(PI) + l \tag{2.19}$$

For the elastic shear modulus G_{max} the following expression derived from laboratory test data, is adopted (Kramer, 1996):

$$G_{max} = 625\ F(e)\ OCR^{k}(p_a\ \sigma'_m)^{0.5} \quad (2.20)$$

where *OCR* is the overconsolidation ratio, σ'_m is the mean principal effective stress:

$$\sigma'_m = \frac{\sigma'_1+\sigma'_2+\sigma'_3}{3} \quad (2.21)$$

, p_a is the atmospheric pressure at the same units as σ'_m and G_{max} and *F(e)* is related with clay void ratio *e* (Hardin, 1978):

$$F(e) = \frac{1}{0.3+0.7\ e^2} \quad (2.22)$$

The proposed by Hardin and Drnevich, (1972) values of the overconsolidation ratio exponent *k* for discrete values of the plasticity index (*PI* = 0, 20, 40, 60, 80 and ≥100) are employed herein. Given the G_{max} (equation 2.20), the undrained strength S_u can be estimated after Weiler (1988), who measured the S_u in CU triaxial compression tests and related the G_{max}/S_u ratio to the plasticity index *PI* and overconsolidation stress ratio *OCR* (Kramer, 1996).

2.2. Calibration methodology

2.2.1. Drained conditions of sand

The calibration of the model for drained loading was based on matching some established experimental shear modulus and damping ratio curves from the literature. Three published families of *G:γ* , *ξ:γ* curves have been utilized: (a) the Ishibashi and Zhang (1993), (b) the pressure (*p'*)-independent curves of Vucetic and Dobry (1991) and (c) the Darendeli et al. (2001) curves. Starting from the Ishibashi and Zhang (1993) curves and assuming a plasticity index *PI* = 0 for sand, comparison with the predictions of the model for four levels of the mean effective stress *p'(=50, 100, 200, 500 kPa)* is presented in figure 2.1. Similarly, figure 2.1 shows comparison between the computed *G:γ* , *ξ:γ* curves and those suggested by Vucetic and Dobry (1991) for a unique *p'=80 kPa* and Darendeli et al. (2001) curves for *p' =25, 100, 400, 1600 kPa*. The agreement between computed and experimental results is quite satisfactory. However, the approximation of the shear modulus curves becomes generally less accurate as the confining pressure increases. The inverse picture is observed for the damping curves, where the deviation is increases with increasing σ'_v.

The hardening exponent n has been expressed as a function of n_d and n_u (equation 2.6) to model soil response for intermediate drainage conditions, i.e. when water dissipation is taken into consideration. For the two extreme conditions of drainage, n is trivialized to n_d or n_u, for drained and undrained condition respectively. Calibration under drained conditions is mainly based on the calibration of the exponent n_d and the hysteretic parameter η (equation 2.15). The smaller the n_d the milder the transition from the elastic branch to the perfectly plastic one. In terms of the shear modulus curve, n_d shifts the G/G_{max} curve upwards or downwards in the y axis, with a more intense impact for small values of the cyclic shear strain. Very large values of n_d will result in a $G/G_{max} = 1$ for a wide range of cyclic shear strains. n_d has also an impact on the damping curve, which is however less prominent, making ξ values to decrease for small shear strains and increase for large shear strains, as n_d increases. The hysteretic parameter η, and essentially the parameters s_1 and s_2, controls the volume of the hysteretic loop and has a strong effect on the damping curve, mainly for large strains. To better reproduce the impact of the confining pressure on curves, s_1 and s_2 are expressed as functions of p'_0. Then, following a curve fitting procedure, the parameters B, k (equation 2.16), C and m (equation 2.17) are estimated. The exponent α_2 that contributes to the formulation of R_d (equation 2.14) controls the densification that builds up after each load cycle in drained conditions and has a negligible effect on the shape of the shear modulus and damping curves. Setting α_2 equal to 10, proved to achieve reasonable results regarding the accumulated volumetric strain, in accordance with experimental observations. The calibration procedure is briefly presented in Figure 2.2 along with the qualitative influence of n_d and η on the cyclic response in terms of the stress-strain curve.

2.2.2. Undrained conditions of sand

The clean – sand based liquefaction resistance *CRR* curve that was composed by Idriss and Boulanger, (2004, 2008):

$$CRR_{M_w=7.5,\sigma'_v=1atm} = exp\left\{\frac{(N_1)_{60cs}}{14.1} + \left[\frac{(N_1)_{60cs}}{126}\right]^2 - \left[\frac{(N_1)_{60cs}}{23.6}\right]^3 + \left[\frac{(N_1)_{60cs}}{25.4}\right]^4 - 2.8\right\} \quad (2.23)$$

provides the reference cyclic resistance ratio, under vertical effective stress equal to $1atm$ and magnitude 7.5 earthquakes, with the corrected SPT number $(N_1)_{60cs}$. To adjust the aforementioned reference curves to magnitudes smaller or larger than 7.5, Seed and Idriss

(1982) and several investigators afterwards introduced correction factors termed “magnitude scaling factors” (*MSFs*), (Youd et al., 2001). These factors are used to scale up or down the reference curves on CRR versus $(N_1)_{60cs}$, q_{c1N} or V_{s1} plots. The factor of safety against liquefaction is then defined according to:

$$FS = \left(\frac{CRR_{7.5}}{CSR}\right) MSF \tag{2.24}$$

where *CSR* is the calculated cyclic stress ratio generated by the earthquake shaking and $CRR_{7.5}$ is the cyclic resistance ratio for magnitude 7.5 earthquakes. Magnitude scaling factors proposed by Idriss (1995) and Andrus and Stokoe (1997) are considered as a lower-bound and upper-bound estimation of the liquefaction resistance, respectively, according to the recommendations by the 1998 NCEER/NSF workshop participants. They are thus formed the basis of the developed calibration procedure. The values of *MSF* for magnitudes from 5.5 to 8.5 are provided in table 2.1.

Adopting equation (2.23) and assuming that $(N_1)_{60cs}$ is related to the sand relative density according to (Idriss and Boulanger, 2010):

$$(N_1)_{60cs} = 46{D_r}^2 \tag{2.25}$$

the liquefaction resistance curve can be obtained as a function of the relative density. Then, by using the following curve fitting function (Seed and Idriss, 1982):

$$N = 0.0034{M_w}^{4.18} \tag{2.26}$$

, that associates the earthquake magnitude M_w with the equivalent number of uniform cycles of the seismic motion and multiplying the reference cyclic resistance ratio ($CRR_{M=7.5,\,\sigma'v=1atm}$) by the magnitude scaling factor, the liquefaction resistance curve can be explicitly determined as a function of both the relative density and the number of uniform cycles.

Since it is arbitrarily assumed that the “observed” $CRR_{Mw=7.5,\sigma'v0=1atm}$ refers to anisotropic consolidation conditions with K_0 = 0.5, it is necessary to convert the anisotropic *CRR* values to equivalent isotropic (K_0 = 1) ones. The adopted transformation expression:

$$CRR_{K_0 \neq 1} = \left(\frac{1+2K_0}{3}\right) CRR_{K_0=1} \tag{2.27}$$

has been frequently applied in the literature (e.g. Idriss and Boulanger, 2010) and is also used for the purposes of this calibration study. Isotropic consolidation condition was arbitrarily chosen as anisotropic consolidation is not compatible with *p-q* constitutive modeling. Evidently, the *p-q* version of Ta-Ger model can only indirectly capture K_0 effects.

To account for the nonlinearity between *CRR* and effective overburden pressure, the correction factor K_σ is introduced for overburden pressures over 1 *atm*, as follows:

$$CRR_{\sigma'_{v0}\neq 100} = K_\sigma CRR_{\sigma'_{v0}=100} \tag{2.28}$$

The expression for K_σ factor by the NCEER (1996, 1998) workshops is:

$$K_\sigma = \left(\frac{\sigma'_{v0}}{p_a}\right)^{(f-1)} \tag{2.29}$$

in which σ'_{v0} is the effective overburden pressure, p_a is the atmospheric pressure and f is an exponent that is a function of the relative density D_r of sand:

$$f = 1 - \frac{D_r}{2} \leq 0.8 \tag{2.30}$$

The comparison between computed and suggested values for the cyclic resistance ratio is given in figure 2.3 against the number of uniform cycles to cause liquefaction, for five values of relative density. The results refer to undrained cyclic direct simple shear tests with uniform stress-controlled loading, under an initial mean effective stress of p'_0=100 kPa. The onset of liquefaction for the computed *CRR* curves is deliberately assumed when the excess pore water pressure ratio r_u exceeds 0.98. Comparison in terms of *MSF vs* M_w is also depicted in figure 2.3. According to the literature, the magnitude scaling factors are supposed to be D_r independent. However, the *MSF* vs M_w curves predicted by the calibrated model (Figure 2.3b.) exhibit a mild D_r dependence. The steepest curve (Andrus and Stokoe, 1997) is better reproduced by the calibrated model for high values of the relative density, contrary to the less steep curve (Idriss, 1995) which is matched for lower values of the relative density. In any case, however, the predictions of the model regarding *MSF* are bounded by the lower and highest values suggested by NCEER.

The effect of the overburden stress on the predictions of the calibrated models is illustrated in figure 2.4. It is noted that the *CRR* value is determined as the cyclic stress ratio required to cause liquefaction in 15 uniform loading cycles.

The performance of the model in terms of the reference cyclic resistance ratio (M_w=7.5, σ'_{v0}=1atm and K_0=1) as a function of the corrected SPT value is depicted in figure 2.5 in comparison with the design curve by Idriss and Boulanger (2004, 2008) transformed according to equation (2.28). For D_r values greater than 0.6, the approximation of the suggested curve becomes less reliable and the model tends to overpredict the liquefaction potential.

Calibration for undrained conditions, is mainly based on the estimation of model parameters n_u and its auxiliary parameters n_0, n_{peak}, n_f, b and g. In an undrained cyclic direst shear test under a constant amplitude of imposed shear stress, the first loading cycles are characterized by a rapid decrease of mean effective stress followed by a gradual decrease at a decreasing rate, until a critical cycle threshold marked by an abrupt decrease, eventually leading to liquefaction. The transitions in the rate of the p' reduction are described with the evolution of n_u from an initial value n_0, to a potentially reached maximum value n_{peak} down to a final low value n_f when the effective stress gets close to zero (figure 2.2). The evolution of n_u is a function of the cumulative deviatoric strain increment $\Sigma d\varepsilon_q$ and is controlled by the two exponents b and g. A genetic algorithm-based optimization procedure, implemented in MATLAB, was applied for the best estimate of the aforementioned model parameters. The performed optimization targeted to the best fit on the *CRR* curve for a wide range of number of uniform cycles required to cause liquefaction (i.e. to achieve $r_u > 0.98$) and for various initial conditions in terms of the relative density and mean effective stress, by minimizing the mean squared error (the objective function) of the model predictions with respect to the literature suggestions.

In summary, the constitutive model parameters are grouped into two weakly-coupled sets; those activated for drained load conditions and those when the response is undrained. The results of the calibration regarding the two aforementioned extreme load conditions are summarized in table 2.2.

2.2.3. Calibration of model version for clayey soils

The calibration procedure was based on matching two families of *G:γ and ξ:γ* curves; the Ishibashi and Zhang (1993) and the Vucetic and Dobry (1991). They are presented in figures 2.6 and 2.7 respectively, in comparison with the prediction of the model. The values of the calibrated parameters are shown in table 2.2. Similarly to what has been discussed for the calibration of the drained response of sand, the most suitable values of n, s_1 and s_2 are

determined to better approximate the literature $G:\gamma$, $\xi:\gamma$ curves for clay, for a reference plasticity index. Finally, n and s_2 are expressed as functions of PI to better reproduce its influence on the curves and f, h (equation 2.18), q and l (equation 2.19) are estimated.

2.3. Microscale response

The capability of the model to reproduce the phenomenological response of the soil in terms of the shear modulus—damping ratio curves does not guarantee a realistic prediction at the stress-strain level. On the contrary, the successful performance at both response levels is often a very difficult task. To demonstrate that the calibrated model yields physically meaningful results at the stress-strain level, consistent with the observed behavior of sand, indicative model predictions are shown in figure 2.8a regarding the numerical simulation of a drained strain-controlled (γ_{max} = 1%) cyclic direct simple shear test of a sand with relative density of D_r =50 % and p_0' =100 kPa. The results correspond to the calibrated parameters for the Ishibashi and Zhang (1993) shear modulus-damping ratio curves.

Similarly, to check the validity of the calibrated model in terms of the stress-strain response, the same sand specimen is tested against stress-controlled undrained cyclic direct simple shear loading of constant amplitude τ_{max} = 18 kPa (figure 2.8b). The results correspond to the calibration process according to the Idriss (1995) magnification scaling factor. The model reproduces salient details of the effective stress evolution. Indeed, a rapid increase of the excess pore water pressure is observed in the first two cycles followed by a gradual increase at a decreasing rate for the next few cycles. The pore water pressure builds up continuously at an increasing rate up to a cycle threshold marked by an abrupt increase, eventually leading to liquefaction.

References

Andrus, R. D., & Stokoe, K. H. (1997). Liquefaction resistance based on shear wave velocity: Report to the NCEER Workshop on Evaluation of Liquefaction Resistance (9/18/97 version).

Anthi, M., & Gerolymos, N. (2019, June). A Calibration procedure for sand plasticity modeling in earthquake engineering: Application to TA-GER, UBCSAND and PM4SAND. In *Proceedings of the 7th International Conference on Earthquake Geotechnical Engineering, Rome, Italy* (pp. 17-20).

Darendeli, M. B., Stokoe, K. H., & II, R. EM and Roblee, CJ (2001b),"Importance of Confining Pressure on Nonlinear Soil Behavior and its Impact on Earthquake Response Predictions of Deep Sites,". In *Proc. 15th International Conference on Soil Mechanics and Geotechnical Engineering, Istanbul, Turkey*.

Drosos, V. A., Gerolymos, N., & Gazetas, G. (2012). Constitutive model for soil amplification of ground shaking: Parameter calibration, comparisons, validation. *Soil Dynamics and Earthquake Engineering*, *42*, 255-274.

Gerolymos, N., Anthi, M., & Tasiopoulou, P. (2018) A plasticity model for 1D site response analysis accounting for liquefaction induced ground movements, *Proceedings on 16th* European conference on earthquake engineering, Thessaloniki, 2018

Gerolymos, N., & Gazetas, G. (2005). Constitutive model for 1-D cyclic soil behaviour applied to seismic analysis of layered deposits. *Soils and Foundations*, *45*(3), 147-159.

Gerolymos, N., Vardoulakis, I., & Gazetas, G. (2007). A thermo-poro-visco-plastic shear band model for seismic triggering and evolution of catastrophic landslides. *Soils and Foundations*, *47*(1), 11-25.

Hardin, B. O. (1978, June). The nature of stress-strain behavior for soils. In *From Volume I of Earthquake Engineering and Soil Dynamics--Proceedings of the ASCE Geotechnical Engineering Division Specialty Conference, June 19-21, 1978, Pasadena, California. Sponsored by Geotechnical Engineering Division of ASCE in cooperation with:* (No. Proceeding).

Hardin, B. O., & Drnevich, V. P. (1972). Shear modulus and damping in soils: design equations and curves. *Journal of the Soil mechanics and Foundations Division*, *98*(7), 667-692.

Idriss, I. M. (1995). Seed memorial lecture. *University of California at Berkeley (IM Idriss, personal communication to TL Youd, 1997)*.

Idriss IM, Boulanger RW (2004). Semi-empirical procedures for evaluating liquefaction potential during earthquakes. In: Doolin D, et al., editors. Proceedings, 11th international conference on soil dynamics and earthquake engineering, and 3rd international conference on earthquake geotechnical engineering, 1. Stallion Press; 2004. p. 32–56

Idriss, I. M., & Boulanger, R. W. (2008). Monograph MNO-12. *Earthquake Engineering Research Institute*.

Idriss, I. M., & Boulanger, R. W. (2010). SPT-based liquefaction triggering procedures. *Rep. UCD/CGM-10*, *2*, 4-13.

Ishibashi, I., & Zhang, X. (1993). Unified dynamic shear moduli and damping ratios of sand and clay. *Soils and foundations*, *33*(1), 182-191.

Kramer, S. L. (1996). *Geotechnical earthquake engineering*. Pearson Education India.

Seed HB, Idriss IM. (1970) Soil moduli and damping factors for dynamic response analyses, Report EERC 70-10, Earthquake engineering research center. Berkeley: University of California.

Seed HB, Idriss IM (1982). Ground motions and soil liquefaction during earthquakes. Earthquake Engineering Research Institute Monograph, Oakland, California.

Souliotis C. (2015) A calibration procedure for the UBC3D – PLM constitutive model: application to the seismic response of gravity quay walls. M.Sc. Thesis, NTUA, Athens, 2015

Tasiopoulou, P., & Gerolymos, N. (2016a). Constitutive modeling of sand: Formulation of a new plasticity approach. *Soil Dynamics and Earthquake Engineering*, *82*, 205-221.

Tasiopoulou, P., & Gerolymos, N. (2016b). Constitutive modelling of sand: a progressive calibration procedure accounting for intrinsic and stress-induced anisotropy. *Géotechnique 66*(9), 754-770.

Vucetic, M., & Dobry, R. (1991). Effect of soil plasticity on cyclic response. *Journal of geotechnical engineering*, *117*(1), 89-107.

Weiler Jr, W. A. (1998). Small strain shear modulus of clay. *Earthquake Engineering and Soil Dynamics, Recent Advances in Ground-Motion Evaluation*, 331-345.

Youd TL, Idriss IM, Andrus RD, Arango I, Castro G, Christian JT, et al (2001). Liquefaction resistance of soils: Summary report from the 1996 NCEER and NCEER/NSF workshops on evaluation of liquefaction resistance of soils. Journal of Geotechnical and Geoenvironmental Engineering, ASCE 2001.127:817-833, October 2001.

.

Figures

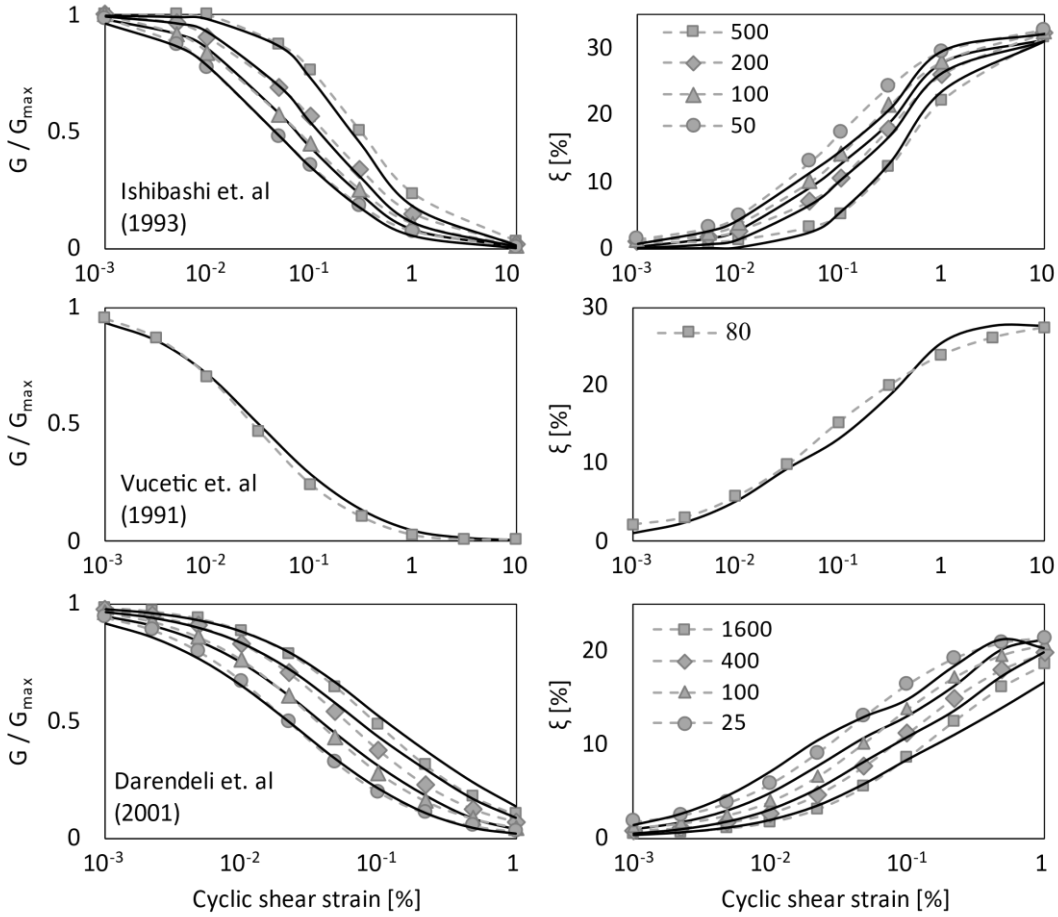

Figure 2.1. Approximation of the shear modulus and damping curves for sand published by Ishibashi & Zhang (1993), Vucetic & Dobry (1991) and Darendeli et. al (2001) for various levels of confinement pressure.

Table 2.1. Magnitude scaling factor values recommended by Idriss (1995) and Andrus and Stokoe (1997). (Source: Youd and Noble 1997a, Summary report from the 1996 NCEER and1998 NCEER/NSF workshops on evaluation of liquefaction resistance of soils, Journal of Geotechnical and Geoenviromental Engineering, October 2001.127:817-833).

Magnitude Scaling Factor							
Magnitude M_w	5.5	6	6.5	7	7.5	8	8.5
Idriss (1995)	2.2	1.76	1.44	1.19	1	0.84	0.72
Andrus and Stokoe (1997)	2.8	2.1	1.6	1.25	1	0.8	0.65

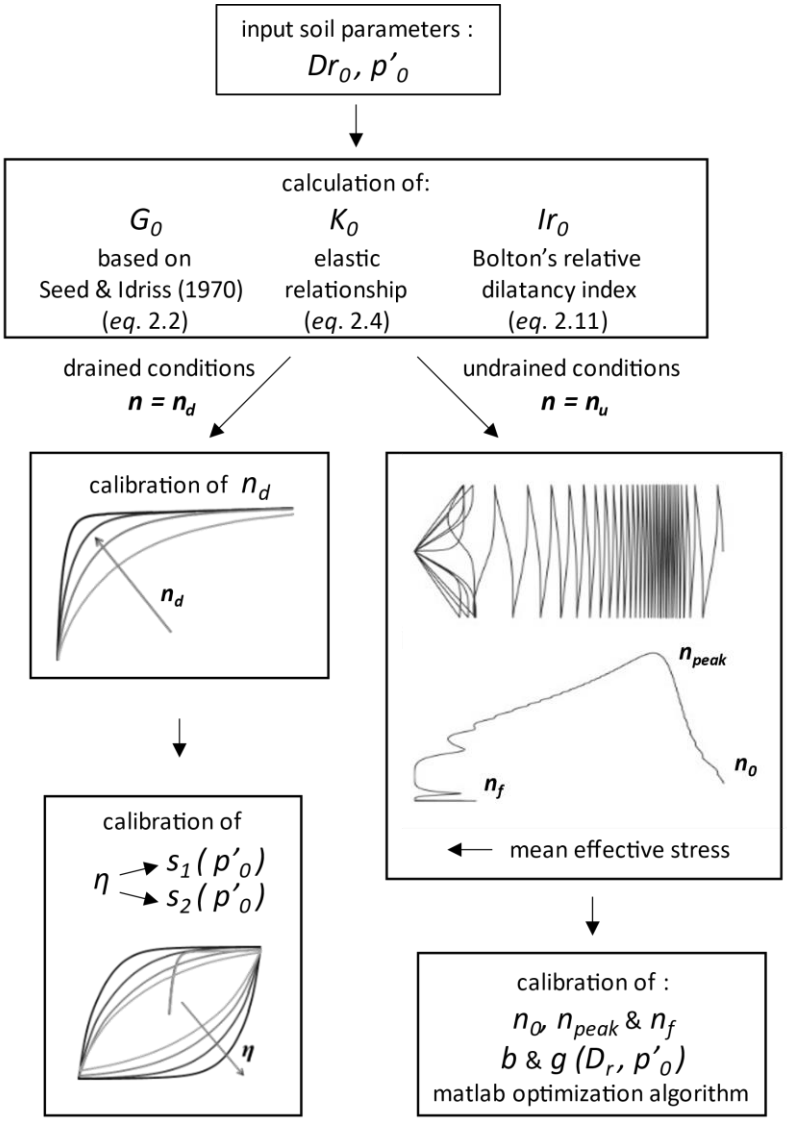

Figure 2.2. Schematic depiction summarizing the model calibration procedure and the basic parameters effects on soil response, for drained and undrained conditions.

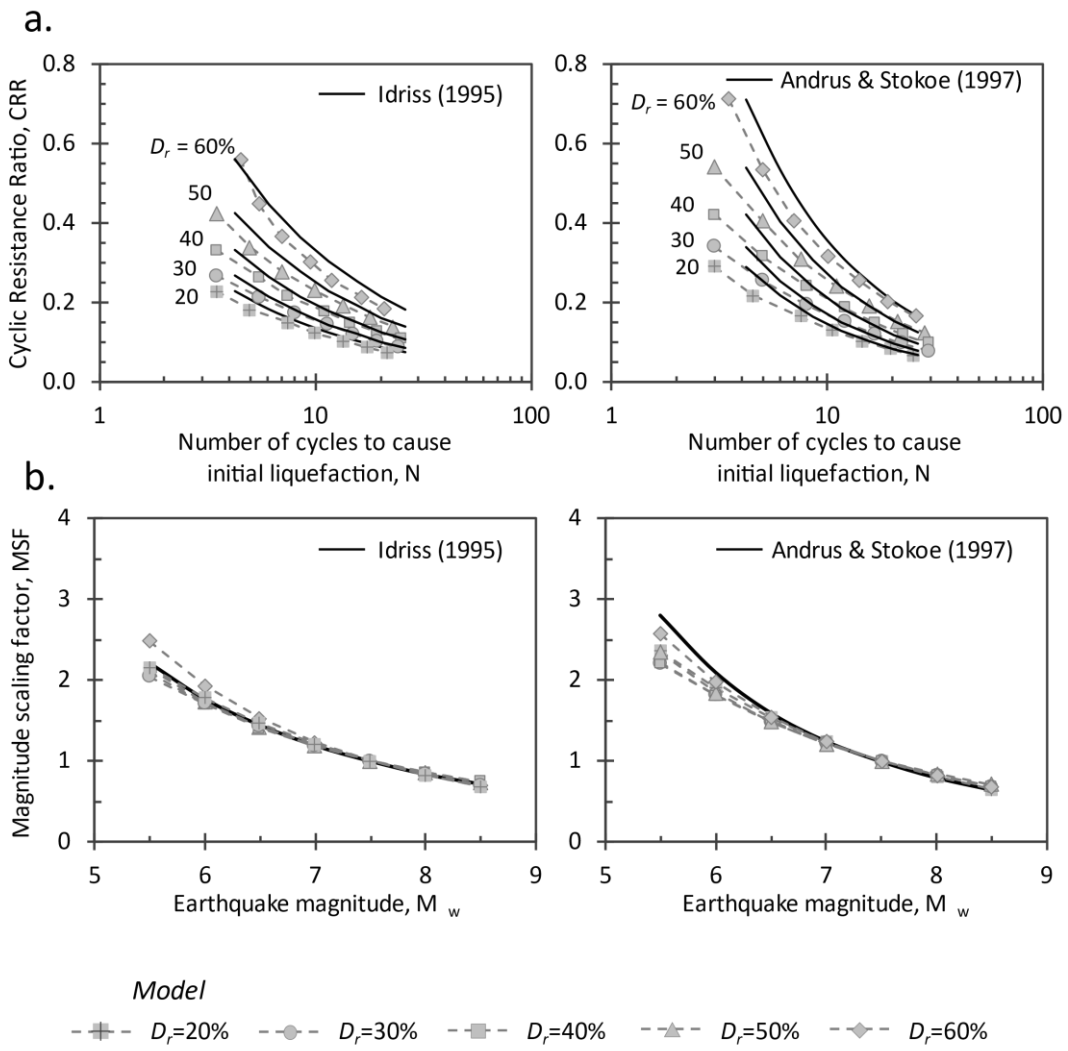

Figure 2.3. [a.] Cyclic resistance ratios as functions of the equivalent number of uniform cycles in order to trigger liquefaction for selected values of the relative density. Comparison is given between the predictions of the calibrated model and the corresponding curves derived by the Idriss (1995) [left] and Andrus & Stokoe (1997) [right] magnitude scaling factors curves, the Idriss & Boulanger (2004, 2008) reference $CRR_{Mw=7.5,\sigma'v0=1atm}$ and equation (2.27) to correct the reference *CRR* for isotropic consolidation conditions. [b.] Corresponding magnitude scaling factors as functions of the earthquake magnitude in order to trigger liquefaction.

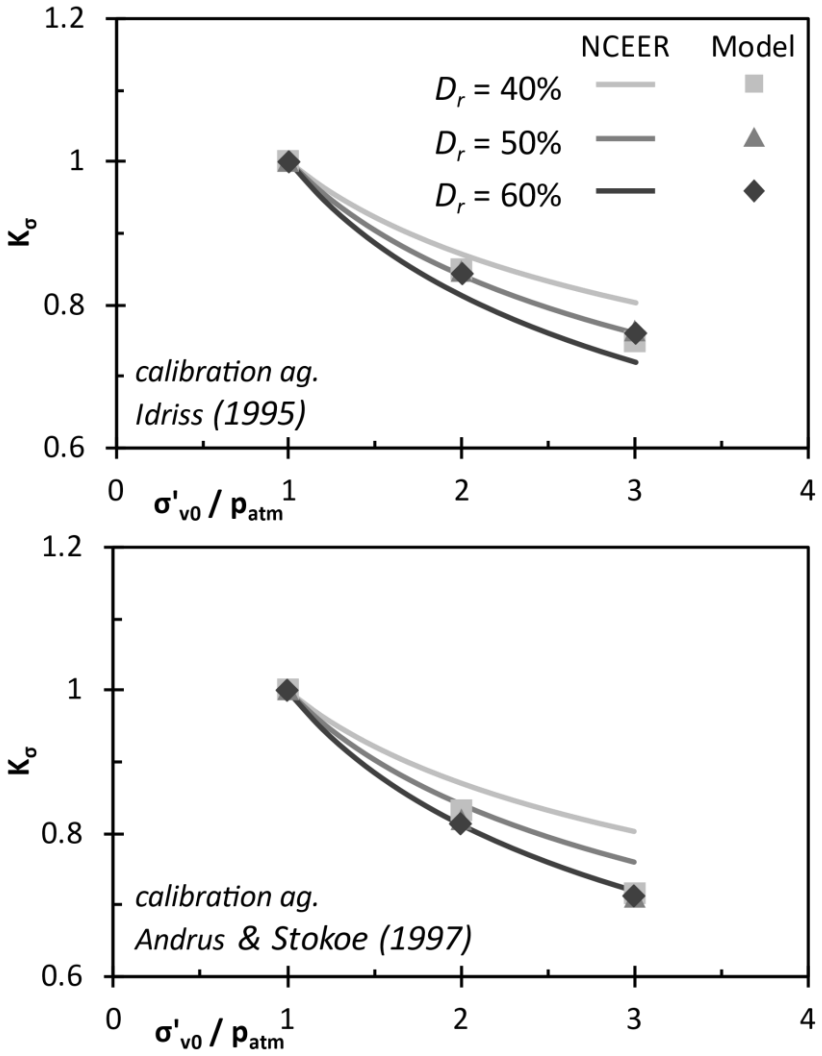

Figure 2.4. Comparison of K_σ factors derived from the calibrated model (calibration against Idriss (1995) [up] and Andrus and Stokoe (1997) [down] *MSF* curves, for selected values of the relative density (D_r = 40%, 50%, 60%) for liquefaction triggering in 15 uniform loading cycles. Comparison is given with the expressions recommended by the 1996 NCEER/1998 NCEER/NSF workshops.

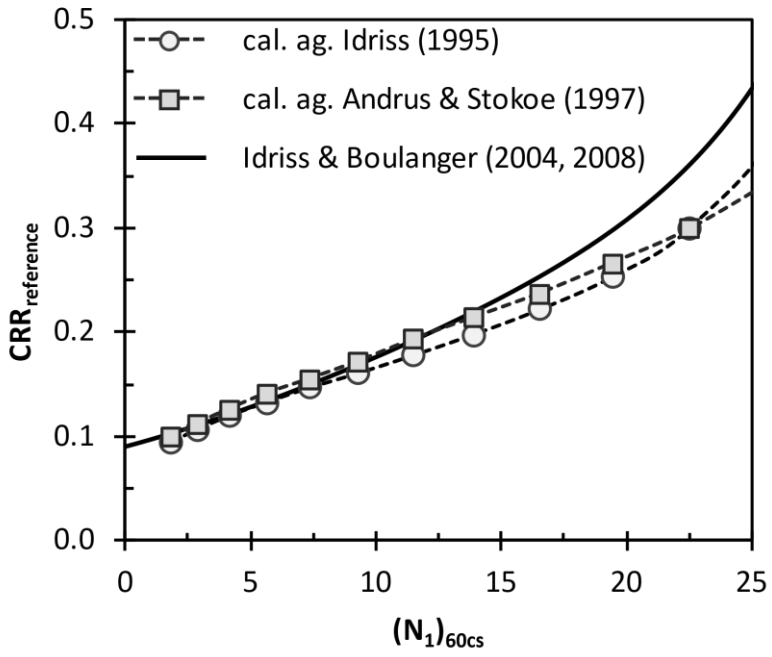

Figure 2.5. Computed versus suggested by Idriss and Boulanger (2004, 2008) reference cyclic resistance ratio, transformed according to equation 2.27, against the corrected SPT number.

Table 2.2. Values of the calibrated model parameters.

		Calibrated Model Parameters							
		B	***k***	***C***	***m***	n_d	a_2		
sand - dr. cond.	*Vucetic et.al (1991)*	5.3	0	1.06	0	*	10		
	Darendeli et al. (2001)	36.13	-0.3	1.68	-0.06	0.7	10		
	Ishibashi et. al (1993)	19.16	-0.2	1.14	0	0.74	10		
		n_0	n_{peak}	n_f	***b***	g_1	g_2	g_3	a_1
sand - undr. cond.	*Idriss (1995)*	0.4	25	0.2	30	288	424	27	0.6
	Andrus et. al (1997)	0.4	42	0.2	30	372	433	27	0.7
		s_1	***f***	***h***	***q***	***l***			
clay - undr. cond.	*Ishibashi et. al (1993)*	2.2	-0.63	4.28	0.03	0.94			
	Vucetic et.al (1991)	2	0	1	0	0.8			

*0.0022 p + 0.7, *p=effective pressure*

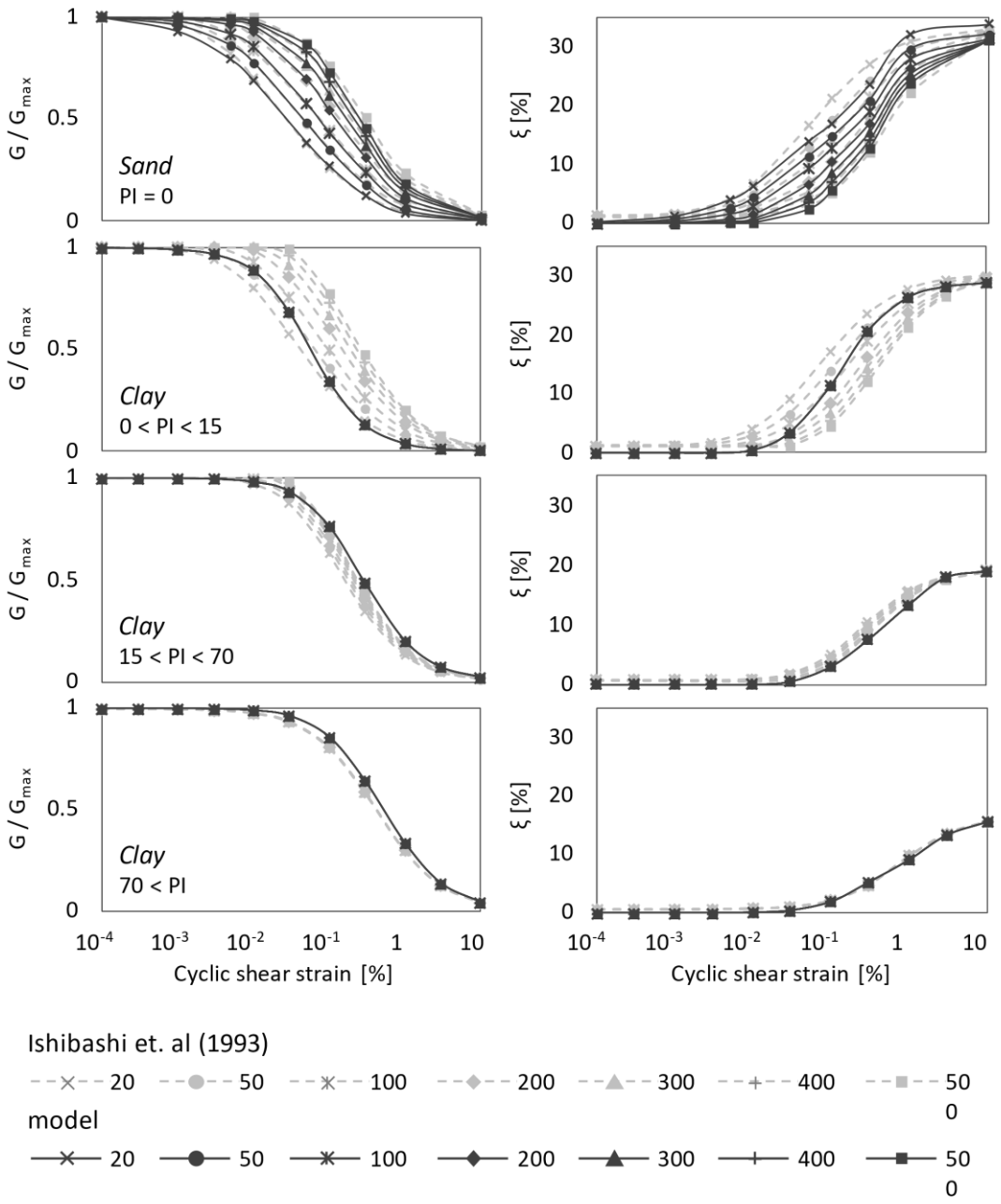

Figure 2.6. Approximation of the Ishibashi & Zhang (1993) shear modulus and damping curves for sand (*PI=0*) and clay (*0<PI<15, 15<PI<7 0 & 70<PI*) for confinement pressures 20, 50, 100, 200, 300, 400 and 500 kPa.

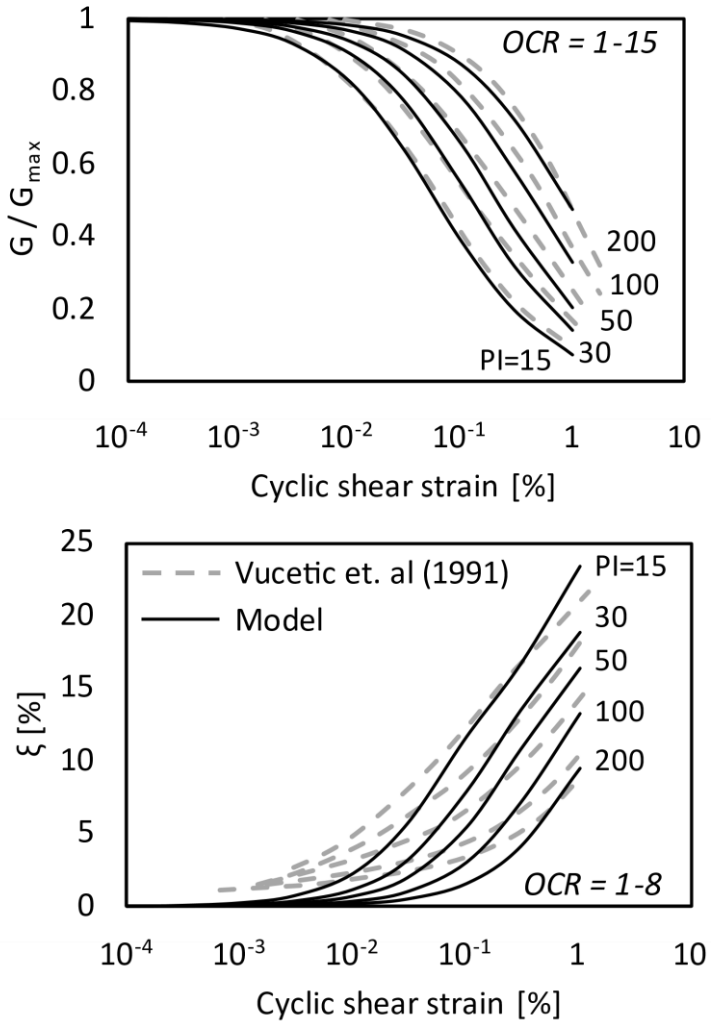

Figure 2.7. Approximation of the Vucetic & Dobry (1991) shear modulus and damping curves for clay, for *PI*: 15, 30, 50, 100 and 200. The presented model curves were calculated under σ'_v=100kPa.

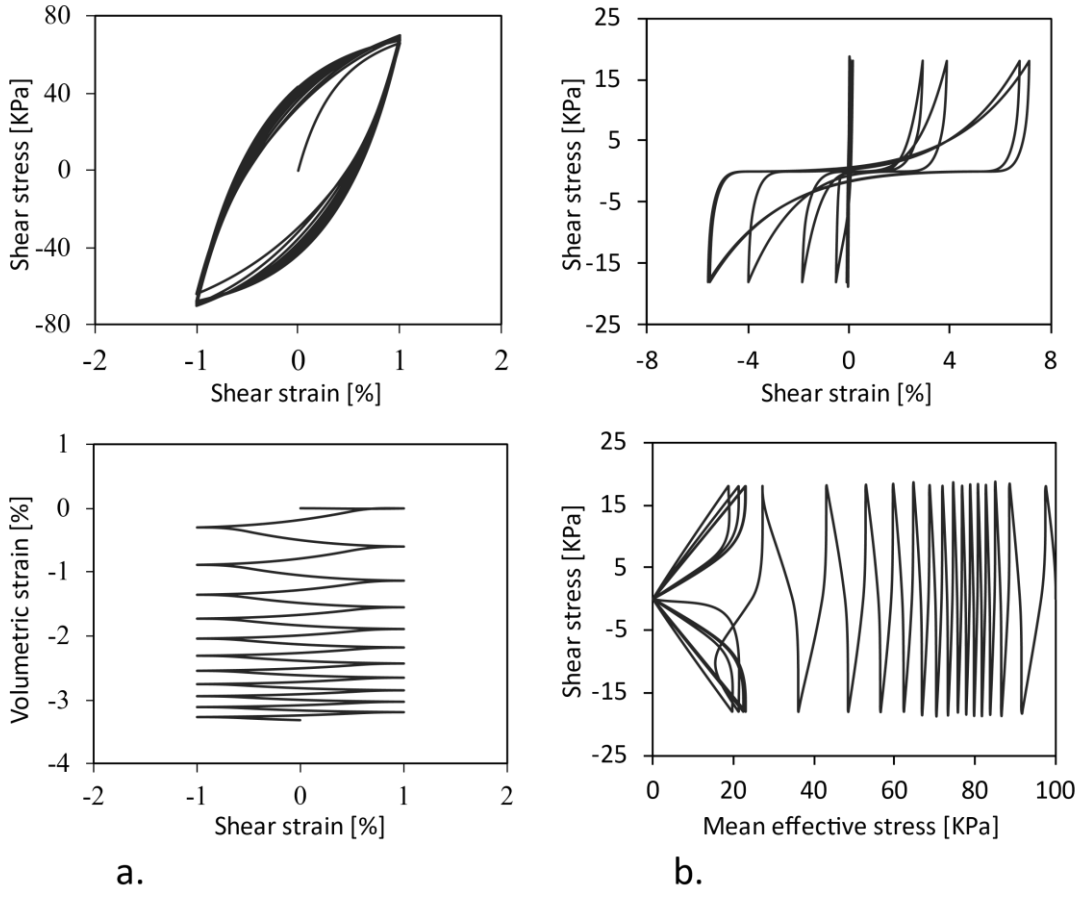

Figure 2.8. Numerical simulation of a cyclic direct simple shear test of a sand with D_r =50 % and $p_{initial}$ =100 kPa with the developed constitutive model. [a] Drained shear strain-controlled test, under γ_{max} = 1%. The response is plotted in the form of stress-strain hysteretic loops and volumetric strain evolution with shear strain. The calibration of the model has been based on the Ishibashi & Zhang (1993) shear modulus and damping ratio curves. [b] Undrained shear stress-controlled, under τ_{max} = 18kPa. The response is illustrated in the form of shear stress-strain loops and evolution of the response in terms of the shear stress versus mean effective stress. The calibration of the model has been based on the Idriss (1995) magnification scaling factor.

Chapter 3

Numerical algorithm for one dimensional ground response analysis

3.1. One dimensional shear wave propagation through a continuous medium

3.1.1. Elastic soil

In a continuous medium two types of waves can be primarily developed:

- Transversal or Shear waves: ***S***
- Longwise or Dilative waves: ***P***

The remaining types of waves (e. g. the surface waves) are generated through the combination of *P* and *S* waves, when the existing boundaries impose kinematic or dynamic restrictions incompatible with the primary types of waves.

The problem studied in the present section is that of a layered soil profile subjected to a seismic excitation at its base (Anthi et al. 2017, Anthi and Gerolymos, 2021). If seismic base

excitation is assumed to be the result of exclusively vertically polarized *S* waves, and hence the analysis is reduced to 1-D wave propagation, as is described in Figure 3.1 the dynamic equilibrium is (Kramer, 1996):

$$\frac{\partial \tau_{zx}}{\partial z} = \rho \ddot{u}_x \tag{3.1}$$

, where *z* is the vertical height from column base, *u* is the soil displacement, *τ* is soil shear stress and *ρ* is soil density. Assuming linear elastic soil response:

$$\tau_{zx} = G\,\gamma_{zx} = G\,\frac{\partial u_x}{\partial z} \Rightarrow \frac{\partial \tau_{zx}}{\partial z} = G\,\frac{\partial^2 u_x}{\partial z^2} \tag{3.2}$$

, where *G* is the soil shear modulus and *γ* the soil shear strain, by substituting into equation (3.1) we obtain:

$$\frac{\partial^2 u_x}{\partial z^2} = \frac{\rho}{G}\frac{\partial^2 u_x}{\partial t^2} \tag{3.3}$$

, which is the differential equation that describes the vertical propagation of shear waves on linear elastic soil.

According to the finite differences method for solving differential equations, derivatives are approximated by finite differences, as follows:

<u>1st order derivative</u>

$\left(\frac{\partial u}{\partial x}\right)_i = \frac{u_{i+1}-u_i}{\Delta x} + O(\Delta x)$ *forward difference*

$\left(\frac{\partial u}{\partial x}\right)_i = \frac{u_i-u_{i-1}}{\Delta x} + O(\Delta x)$ *backward difference*

$\left(\frac{\partial u}{\partial x}\right)_i = \frac{u_{i+1}-u_{i-1}}{2\Delta x} + O[(\Delta x)]^2$ *central difference*

<u>2nd order derivative</u>

$\left(\frac{\partial^2 u}{\partial x^2}\right)_i = \frac{u_i-2u_{i+1}+u_{i+2}}{(\Delta x)^2} + O[(\Delta x)]^2$ *forward difference*

$\left(\frac{\partial^2 u}{\partial x^2}\right)_i = \frac{u_{i-2}-2u_{i-1}+u_i}{(\Delta x)^2} + O[(\Delta x)]^2$ *backward difference*

$$\left(\frac{\partial^2 u}{\partial x^2}\right)_i = \frac{u_{i-1} - 2u_i + u_{i+1}}{(\Delta x)^2} + O[(\Delta x)]^2 \qquad \textit{central difference}$$

A discretization error arises, since the terms of *(n+1)* order or bigger have been excluded from the Taylor's series.

Time t is discretized in N steps, of $\Delta t = k$ size, so that $t_{total} = N * k$:

$$t_i = (i-1)k \qquad for\ i = 1{:}\,N+1$$

Soli deposit is vertically discretized in Z steps, of $\Delta z = h$ size, so that $H = Z * h$:

$$z_j = (j-1)h \qquad for\ j = 1{:}\,Z+1$$

Considering that horizontal displacement of the soil is a function of time *t* and height *z*: $u_{t,z} = u_{i,j}$,and according to the central difference of 2nd order derivative, we obtain:

$$\left(\frac{\partial^2 u}{\partial z^2}\right)_{i,j} = \frac{u_{i,j+1} - 2u_{i,j} + u_{i,j-1}}{h^2} \qquad (3.4)$$

and:

$$\left(\frac{\partial^2 u}{\partial t^2}\right)_{i,j} = \frac{u_{i+1,j} - 2u_{i,j} + u_{i-1,j}}{k^2} \qquad (3.5)$$

By substituting equations (3.4) and (3.5) into equation (3.3), we obtain:

$$\frac{u_{i,j+1} - 2u_{i,j} + u_{i,j-1}}{h^2} = \frac{\rho}{G}\frac{u_{i+1,j} - 2u_{i,j} + u_{i-1,j}}{k^2} \Rightarrow$$

$$u_{i+1,j} = \frac{k^2 G}{h^2 \rho}\left(u_{i,j+1} - 2u_{i,j} + u_{i,j-1}\right) + 2u_{i,j} - u_{i-1,j} \quad for\ j = 2{:}\,Z\ and\ i = 2{:}\,N \qquad (3.6)$$

Thus, horizontal displacements along the soil profile $u_{i+1,j}$ at time $t = t_{i+1}$ are calculated based on their values at time $t = t_i$ and $t = t_{i-1}$. This approximation of solving the dif. eq. (3.3) represents the explicit finite differences technique.

The initial conditions of the problem are:

- Zero initial displacement:

$$u_{1,j} = 0 \qquad for\ j = 1{:}\,Z+1 \qquad (3.7a)$$

- Zero initial velocity:

$$\left(\frac{\partial u}{\partial t}\right)_{1,j} = 0 \qquad for\ j = 1{:}\ Z+1$$

which according to the 1st order forward difference becomes:

$$\frac{u_{2,j}-u_{1,j}}{k} = 0 \Rightarrow u_{2,j} = u_{1,j} = 0 \qquad for\ j = 1{:}\ Z+1 \tag{3.7b}$$

The boundary conditions of the problem are:

- Zero shear stress at the soil surface:

$$\tau_{i,Z+1} = 0 \qquad for\ i = 1{:}\ N+1$$

and assuming a non-zero shear modulus at the soil surface:

$$\gamma_{i,Z+1} = 0 \Rightarrow \left(\frac{\partial u}{\partial z}\right)_{i,Z+1} = 0$$

Employing the 1st order backward difference:

$$\frac{u_{i,Z+1}-u_{i,Z}}{h} = 0 \Rightarrow u_{i,Z+1} = u_{i,Z} \qquad for\ i = 1{:}\ N+1 \tag{3.8a}$$

- Displacement history of the input "rock outcrop" motion u_g=$u_g(t)$, assuming an incompliant base rock:

$$u_{i,1} = u_{g_i} \qquad for\ i = 1{:}\ N+1 \tag{3.8b}$$

3.1.2. Soil with viscous damping *c*

In the previous section no dissipation of energy, or damping was assumed in the soil. Since damping is present in all materials, the dynamic equilibrium described in Figure 3.1 that was expressed according to equation (3.3), is reformulated accordingly:

$$\frac{\partial \tau_{zx}}{\partial z} = \rho \ddot{u}_x - c\frac{\partial^3 u_x}{\partial z^2 \partial t} \tag{3.9}$$

and assuming linear, elastic soil:

$$G\frac{\partial^2 u_x}{\partial z^2} = \rho \ddot{u}_x - c\frac{\partial^3 u_x}{\partial z^2 \partial t} \Rightarrow \frac{\partial^2 u_x}{\partial z^2} = \frac{\rho}{G}\frac{\partial^2 u_x}{\partial t^2} - \frac{c}{G}\frac{\partial^3 u_x}{\partial z^2 \partial t} \tag{3.10}$$

, which is the differential equation of the vertical shear wave propagation in an elastic soil, with viscous damping *c*.

Employing the backward difference for the 1st order time derivative and the central difference for the 2nd order derivatives:

- $\left(\frac{\partial^3 u_x}{\partial z^2 \partial t}\right)_{i,j} = \frac{u_{i,j+1}-2u_{i,j}+u_{i,j-1}-u_{i-1,j+1}+2u_{i-1,j}-u_{i-1,j-1}}{h^2 k}$ *1st order backward & 2nd order central difference*
- $\left(\frac{\partial^2 u_x}{\partial z^2}\right)_{i,j} = \frac{u_{i,j+1}-2u_{i,j}+u_{i,j-1}}{h^2}$ *central difference*
- $\left(\frac{\partial^2 u_x}{\partial t^2}\right)_{i,j} = \frac{u_{i,j+1}-2u_{i,j}+u_{i,j-1}}{k^2}$ *central difference*

and by substituting into equation (3.10), we obtain:

$$\frac{u_{i,j+1}-2u_{i,j}+u_{i,j-1}}{h^2} = \frac{\rho}{G}\frac{u_{i+1,j}-2u_{i,j}+u_{i-1,j}}{k^2} - \frac{c}{Gh^2 k}\left(u_{i,j+1} - 2u_{i,j} + u_{i,j-1} - u_{i-1,j+1} + 2u_{i-1,j} - u_{i-1,j-1}\right) \Rightarrow$$

$$u_{i+1,j} = \frac{k^2 G + kc}{\rho h^2}\left(u_{i,j+1} - 2u_{i,j} + u_{i,j-1}\right) - \frac{kc}{\rho h^2}\left(u_{i-1,j+1} - 2u_{i-1,j} + u_{i-1,j-1}\right) + 2u_{i,j} - u_{i-1,j} \quad (3.11)$$

The same initial and boundary conditions are valid, as were presented for the case of the elastic soil, in equations (3.7) and (3.8) respectively.

3.1.3. Hysteretic damping soil

In the present section, the one-dimensional, vertical, shear wave propagation described by the differential equation (3.9), is solved according to the finite differences technique, employing the explicit and the implicit method, for the case of a hysteretic damping soil.

Explicit method

Employing the backward difference for the 1st order time derivative and the central difference for the remaining derivatives of equation (3.9):

- $\left(\frac{\partial^3 u_x}{\partial z^2 \partial t}\right)_{i,j} = \frac{u_{i,j+1}-2u_{i,j}+u_{i,j-1}-u_{i-1,j+1}-2u_{i-1,j}-u_{i-1,j-1}}{h^2 k}$ *1st order backward & 2nd order central differences*
- $\left(\frac{\partial \tau}{\partial z}\right)_{i,j} = \frac{\tau_{i,j+1}-\tau_{i,j-1}}{2h}$ *central difference*
- $\left(\frac{\partial^2 u_x}{\partial t^2}\right)_{i,j} = \frac{u_{i+1,j}-2u_{i,j}+u_{i-1,j}}{k^2}$ *central difference*

and by substituting into equation (3.9), we obtain:

$$u_{i+1,j} = \frac{k^2}{2\rho h}\left(\tau_{i,j+1} - \tau_{i,j-1}\right) + \frac{ck}{h^2\rho}\left(u_{i,j+1} - 2u_{i,j} + u_{i,j-1} - u_{i-1,j+1} + 2u_{i-1,j} - u_{i-1,j-1}\right) + 2u_{i,j} - u_{i-1,j} \qquad for\ i = 2{:}N\ and\ j = 2{:}Z \tag{3.12}$$

The initial and boundary conditions of equations (3.7) and (3.8) respectively, are valid. Thus, horizontal displacements along the soil profile $u_{i+1,j}$ at time $t = t_{i+1}$ are calculated based on their values at time $t = t_i$ and $t = t_{i-1}$, as well as the soil shear stresses $\tau_{i,j}$ which are calculated trough the constitutive relation (2.1).

Implicit method

If the central difference for the 1st order time derivative of equation (3.9) is employed:

- $\left(\frac{\partial^3 u_x}{\partial z^2 \partial t}\right)_{i,j} = \frac{u_{i+1,j+1} - 2u_{i+1,j} + u_{i+1,j-1} - u_{i-1,j+1} - 2u_{i-1,j} - u_{i-1,j-1}}{2h^2 k}$ *1st and 2nd order central differences*

and the remaining derivatives of equation (3.9) are calculated as was presented in the previous paragraph, by substituting into equation (3.9), we obtain:

$$\left(\tau_{i,j+1} - \tau_{i,j-1}\right)\frac{k^2}{2h\rho} = \left(u_{i+1,j} - 2u_{i,j} + u_{i-1,j}\right) - \frac{ck}{2\rho h^2}\left(u_{i+1,j+1} - 2u_{i+1,j} + u_{i+1,j-1} - u_{i-1,j+1} + 2u_{i-1,j} - u_{i-1,j-1}\right) \tag{3.13}$$

Assuming that:

$$T = \frac{ck}{2\rho h^2} \qquad \text{and} \qquad K_{i+1,j} = -\frac{hk}{c}\left(\tau_{i,j+1} - \tau_{i,j-1}\right) - \frac{2}{T}u_{i,j} + \frac{1}{T}u_{i-1,j} + \left(u_{i-1,j+1} - 2u_{i-1,j} + u_{i-1,j-1}\right)$$

, we finally obtain:

$$u_{i+1,j+1} + \left(-2 - \frac{1}{T}\right)u_{i+1,j} + u_{i+1,j-1} = K_{i+1,j} \qquad ,for\ i = 2{:}N\ and\ j = 2{:}Z \tag{3.14}$$

The initial and boundary conditions of equations (3.7) and (3.8) respectively, are written in matrix form:

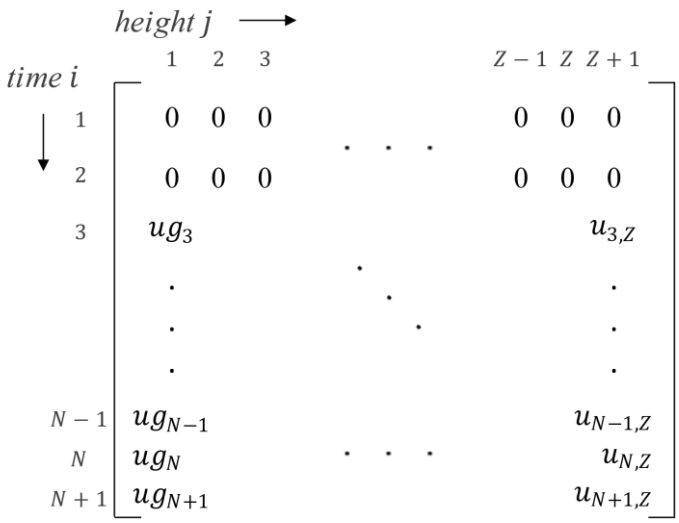

Matrix 3.1

Thus, at time $t = t_i$, $for\ i > 2$, a system of $(Z + 1)$ linear equations has to be solved, with unknown variables the soil horizontal displacements $u_{i,j}$, $for\ j = 1{:}Z + 1$. The system is written in matrix form as follows:

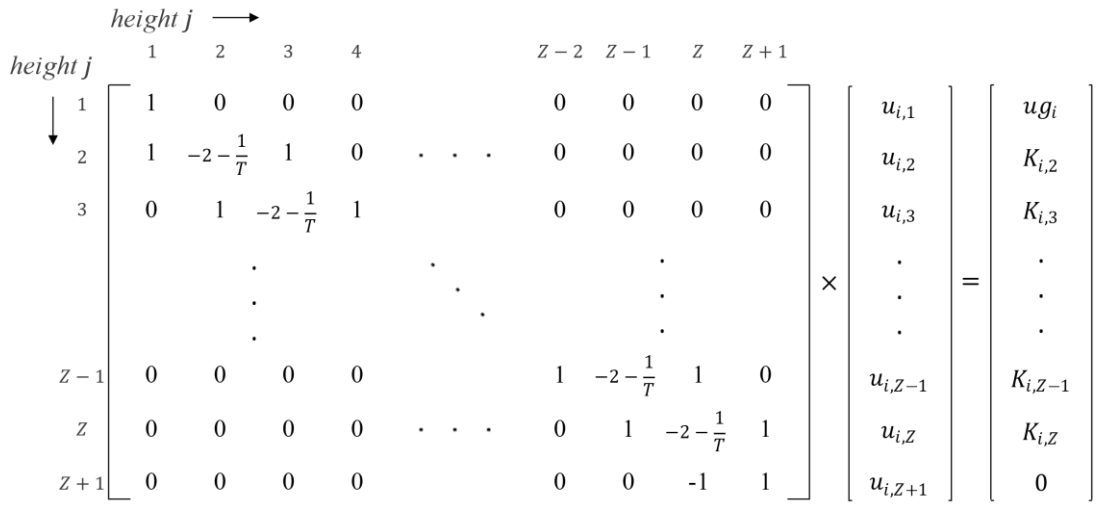

Matrix 3.2

According to what has been discussed in this chapter, a rigid rock was assumed at the base of the soil column. If soil lays on a compliant rock of density ρ_r and shear wave velocity $V_{r,}$ then the boundary condition at the base of the soil column is reformulated accordingly (Gerolymos & Gazetas, 2005 and Joyner and Chen, 1975):

$$\tau_{i,1} + c\left(\frac{\partial^2 u}{\partial z \partial t}\right)_{i,1} = \rho_r V_r \left(\frac{du_{i,1}}{dt} - \frac{du_{g_i}}{dt}\right) \tag{3.15}$$

, which is approximated according to:

- $\left(\frac{\partial^2 u}{\partial z \partial t}\right)_{i,1} = \frac{u_{i,2} - u_{i,1} - u_{i-1,2} + u_{i-1,1}}{hk}$ *backward diff. for time derivative & forward diff. for spatial derivative*
- $\left(\frac{\partial u}{\partial t}\right)_{i,1} = \frac{u_{i+1,1} - u_{i,1}}{k}$ *forward difference*
- $\left(\frac{\partial u_g}{\partial t}\right)_{i} = \frac{u_{g_i} - u_{g_{i-1}}}{k}$ *backward difference*

By substituting into equation (3.15), we obtain:

$$\tau_{i,1} + \frac{c}{hk}\left(u_{i,2} - u_{i,1} - u_{i-1,2} + u_{i-1,1}\right) = \frac{\rho_r V_r}{k}\left(u_{i+1,1} - u_{i-1} - u_{g_i} + u_{g_{i-1}}\right) \Rightarrow$$

$$u_{i+1,1} = \frac{k}{\rho_r V_r}\tau_{i,1} + \frac{c}{h\rho_r V_r}\left(u_{i,2} - u_{i,1} - u_{i-1,2} + u_{i-1,1}\right) + u_{i,1} + u_{g_i} - u_{g_{i-1}} \tag{3.16}$$

Thus, for a compliant base rock, the system of linear equations is written in matrix form as follows:

$$\begin{array}{c} \textit{height } j \longrightarrow \\ \textit{height } j \downarrow \end{array}$$

	1	2	3	4			$Z-2$	$Z-1$	Z	$Z+1$			
1	1	0	0	0			0	0	0	0		$u_{i,1}$	$\boldsymbol{B_{i,1}}$
2	1	$-2-\frac{1}{T}$	1	0	.	. .	0	0	0	0		$u_{i,2}$	$K_{i,2}$
3	0	1	$-2-\frac{1}{T}$	1			0	0	0	0		$u_{i,3}$	$K_{i,3}$
			.		.			.				.	.
			.		.			.			$\times$	.	.
			.		.			.				.	.
$Z-1$	0	0	0	0			1	$-2-\frac{1}{T}$	1	0		$u_{i,Z-1}$	$K_{i,Z-1}$
Z	0	0	0	0	.	. .	0	1	$-2-\frac{1}{T}$	1		$u_{i,Z}$	$K_{i,Z}$
$Z+1$	0	0	0	0			0	0	-1	1		$u_{i,Z+1}$	0

Matrix 3.3

, where $B_{i,1} = \frac{k}{\rho_r V_r}\tau_{i-1,1} + \frac{c}{h\rho_r V_r}\left(u_{i-1,2} - u_{i-1,1} - u_{i-2,2} + u_{i-2,1}\right) + u_{i-1,1} + u_{g_{i-1}} - u_{g_{i-2}}$.

3.2. Verification against analytical solutions

3.2.1. Homogenous soil profile

The developed algorithm is verified against analytical solutions for soil amplification due to a vertically propagating shear wave. For a homogeneous soil deposit (constant velocity or shear modulus), the amplification function and mode shapes are given respectively by:

$$A(\omega) = \frac{1}{\cos\left(\frac{\omega H}{V_S(1+i\xi)}\right)} \tag{3.17}$$

$$U_n(z) = cos\frac{(2n-1)\pi z}{2\mathrm{H}} \tag{3.18}$$

, which is in accordance with model predictions, for ξ=5%, 10%, 15% and 20% and n=1,2,3 and 4 (first four eigenmodes) as shown in figures 3.2 and 3.3.

3.2.2. Inhomogenous soil profile

For the case of an inhomogeneous soil profile, deposits with linearly increasing shear wave velocity were examined, with V_s varying with depth according to:

$$V_s = V_{s0}(1 + bz) \tag{3.19}$$

where V_{s0} is the velocity at the surface, z is soil depth from surface and b is the rate of heterogeneity. The dimensionless rate of heterogeneity $\hat{b}$ (Gazetas, 1982) is being introduced according to:

$$\hat{b} = bH \tag{3.20}$$

The soil amplification function is given by (Gazetas, 1982):

$$A(a_0) = \frac{2q}{(-0.5+q)(1+\hat{b})^{-0.5-q}+(-0.5+q)(1+\hat{b})^{-0.5+q}} \tag{3.21}$$

$$q = \left(\frac{1}{4} - \frac{\omega^2}{{V_{s0}}^2 b^2(1+2i\xi)}\right)^{1/2} \tag{3.22}$$

$$\alpha_0 = \omega H/V_{s0} \tag{3.23}$$

For a 20 m thick soil deposit with density ρ=2t/m^3, four cases of linear V_s distribution with depth are examined. The corresponding shear modulus profiles are depicted in figure 3.4 in comparison with that of a homogeneous profile with V_s=220 m/s. To serve as a benchmark, the G_{max} distribution (according to eq. 2.2), of a sand deposit with D_r =0.5 γ =20kN/m^3 and K_0=0.5 is also portrayed in this figure. The amplification factors at the surface are calculated for each case for two values of the hysteretic damping ratio: 5% and 10%. The comparison between the model prediction and the analytical solution is presented in figure 3.5. It is observed that the deviation between numerical and analytical solution increases with increasing rate of heterogeneity $\hat{b}$, becoming notable for values of $\hat{b}$ greater than 6. A discussion on this divergence has been provided by Towhata (1996). Reducing the time and spatial steps in the dynamic analysis of such highly inhomogeneous profiles attenuates the discrepancy at the cost of extra computational time.

3.3. One dimensional vertical soil consolidation

3.3.1. Uniform surface load *q*

3.3.1.1 Linear elastic soil

The undrained loading of cohesionless saturated soils generates excess pore water pressure, that forces the water to flow through the pores of soil. The water movement changes the volume of the pores, i.e. causes volumetric strains that consequentially lead to effective stresses change. The phenomenon is called soil consolidation and is discussed in the present section.

The principle of water mass conservation inside the pores of soil is expressed as follows:

$$div(\vec{v}) = \frac{\vartheta \varepsilon_{vol}}{\vartheta t} \tag{3.24}$$

where $\vec{v}$ is water velocity, ε_{vol} stands for the volumetric strain and t for time. By deploying Darcy's law:

$$\vec{v} = -k\,\vec{\nabla}\,h \tag{3.25}$$

in which k is the soil permeability and h is the hydraulic gradient:

$$h \equiv z + \frac{u_p}{\gamma_w} \tag{3.26}$$

with z being the soil depth and γ_w the water special weight, and assuming that water flow takes place only across the vertical axis, one can obtain the following equation that relates the pore water pressure u_p with the soil volumetric strain ε_{vol}:

$$\frac{k}{\gamma_w}\frac{\vartheta^2 u_{p\,(t,z)}}{\vartheta z^2} = -\frac{\vartheta \varepsilon_{vol(t,z)}}{\vartheta t} \tag{3.27}$$

which expresses the one dimensional (vertical) soil consolidation.

By replacing the pore water pressure u_p, with respect to the cumulative mean effective stress increment Σdp, we obtain:

$$\frac{k}{\gamma_w}\frac{\partial^2 -\Sigma dp_{(t,z)}}{\partial z^2} = -\frac{\partial \varepsilon_{vol_{(t,z)}}}{\vartheta t} \tag{3.28}$$

In one dimensional compression of an isotropic, linear elastic soil:

$$\frac{\partial \varepsilon_{vol_{(t,z)}}}{\vartheta t} = \frac{1}{K}\frac{\partial p_{(t,z)}}{\vartheta t} \tag{3.29}$$

, where K is the soil bulk modulus. Thus, by substituting into equation (3.28):

$$\frac{\partial^2 -\Sigma dp_{(t,z)}}{\partial z^2} = -\frac{1}{K}\frac{\partial p_{(t,z)}}{\vartheta t} \tag{3.30}$$

The implicit technique for solving equation (3.30) is presented in the following section. Employing the central difference for the 2nd order spatial derivative and the backward difference for the 1st order time derivative of equation (3.30):

- $\left(\frac{\partial^2(-\Sigma dp)}{\vartheta z^2}\right)_{i,j} = -\frac{\left(\Sigma dp_{i,j+1} - 2\Sigma dp_{i,j} + \Sigma dp_{i,j-1}\right)}{h^2}$ *central difference*
- $\left(\frac{\partial p}{\vartheta t}\right)_{i,j} = \frac{p_{i,j} - p_{i-1,j}}{\Delta t}$ *backward difference*

and by substituting into equation (3.30), we obtain:

$$\frac{k}{\gamma_w}\frac{\left(\Sigma dp_{i,j+1} - 2\Sigma dp_{i,j} + \Sigma dp_{i,j-1}\right)}{h^2} = \frac{1}{K}\frac{p_{i,j} - p_{i-1,j}}{\Delta t} \Rightarrow$$

$$\frac{K\,\Delta t\,k}{\gamma_w h^2}\left(p_{i,j+1} - p_{0,j+1} - 2p_{i,j} + 2p_{0,j} + p_{i,j-1} - p_{0,j-1}\right) = p_{i,j} - p_{i-1,j} \tag{3.31}$$

Assuming that:

$$\frac{K\,\Delta t\,k}{\gamma_w h^2} = E \tag{3.32}$$

, we finally have:

$$E\left(-p_{i,j+1} + 2p_{i,j} - p_{i,j-1}\right) + p_{i,j} = p_{i-1,j} + E\left(-p_{0,j+1} + 2p_{0,j} - p_{0,j-1}\right) \Rightarrow$$
$$-p_{i,j-1} + \left(2 + \frac{1}{E}\right)p_{i,j} - p_{i,j+1} = \frac{p_{i-1,j}}{E} + -p_{0,j+1} + 2p_{0,j} - p_{0,j-1} \;\; for\; j = 2{:}\,Z \tag{3.33}$$

The initial conditions of the problem are the geostatic stresses at the field:

- $p_{1,j} = p_{0,j} \;\; for\; j = 1{:}\,Z+1$ (3.34)

The boundary condition at the soil column surface, which is loaded with a uniform load q of infinite length, is:

- $p_{i,Z+1} = p_{0,Z+1} + q \;\; for\; i = 1{:}\,N+1$ (3.35)

and at the soil column base is:

- $p_{i,1} = p_{0,1} + q \qquad for\; i = 1{:}\,N+1$ (3.36a)

, in case of a permeable base rock or:

- $\frac{\vartheta \varepsilon_{vol_{i,1}}}{\vartheta t} = 0 \qquad for\; i = 1{:}\,N+1$ (3.36b)

for a non permeable base rock.

Thus, at time $t = t_i$, a system of $(Z+1)$ linear equations has to be solved, with unknown variables the mean effective stresses along the soil profile: $p_{i,j} \;\; for\; j = 1{:}\,Z$+1. The system is written in the following matrix form (under the assumption of a permeable base rock):

$$
\begin{array}{c}
\text{height } j \longrightarrow \\
\text{height } j \downarrow
\end{array}
\begin{array}{c}
\begin{array}{cccccccccc}
1 & 2 & 3 & 4 & & & Z-2 & Z-1 & Z & Z+1
\end{array} \\
\begin{bmatrix}
1 & 0 & 0 & 0 & & & 0 & 0 & 0 & 0 \\
-1 & D & -1 & 0 & \cdots & & 0 & 0 & 0 & 0 \\
0 & -1 & D & -1 & & & 0 & 0 & 0 & 0 \\
 & & \ddots & & \ddots & & & \ddots & & \\
0 & 0 & 0 & 0 & & & -1 & D & -1 & 0 \\
0 & 0 & 0 & 0 & \cdots & & 0 & -1 & D & -1 \\
0 & 0 & 0 & 0 & & & 0 & 0 & 0 & 1
\end{bmatrix}
\end{array}
\begin{array}{c}
1 \\ 2 \\ 3 \\ \\ \\ \\ Z-1 \\ Z \\ Z+1
\end{array}
\times
\begin{bmatrix} p_{i,1} \\ p_{i,2} \\ p_{i,3} \\ \vdots \\ p_{i,Z-1} \\ p_{i,Z} \\ p_{i,Z+1} \end{bmatrix}
=
\begin{bmatrix} p_{0.1} + q \\ L_{i-1,2} \\ H_{i-1,3} \\ \vdots \\ L_{i-1,Z-1} \\ L_{i-1,Z} \\ p_{0,Z+1} + q \end{bmatrix}
$$

Matrix 3.4

, where: $D = \frac{1}{E} + 2$ and $L_{i-1,j} = \frac{p_{i-1,j}}{E} + -p_{0,j+1} + 2p_{0,j} - p_{0,j-1}$.

Assuming a uniform, isotropic, linear elastic soil, Terzaghi 's theory provides the analytical solution of the one dimensional consolidation equation for a saturated soil column of height 2*H*, permeable on its base with a uniform load *q* of infinite length on its surface. The isochronous curves of Figure 3.6a provide the consolidation ratio *U* with the depth, for values of the time factor T_v, from 0.1 to 1. It is noted that:

$$U = 1 - \frac{\Delta u_p}{q} \tag{3.37}$$

and

$$T_v = \frac{k\,D}{\gamma_w\,H^2}\,t \tag{3.38}$$

in which *k* is soil permeability, *D* is the soil uniaxial compression modulus, γ_w is the water special weight, *H* is the half height of the soil profile and *t* is time.

Markers of figure 3.6, stand for the solution of the set of equations (3.33) to (3.36) with the implicit finite differences technique, that was presented above. The convergence is also noted in figure 3.6b in terms of the evolution of the dimensionless rate of consolidation:

$$U(t) = \frac{\delta(t)}{\delta(t=\infty)} \tag{3.39}$$

against the time factor T_v. $U(t)$ expresses the evolution with time of the surface soil settlements $\delta(t)$ in respect of the full soil settlement when consolidation has ended $\delta(t=\infty)$:

$$\delta(t=\infty) = 2H\ q/D \tag{3.40}$$

It is noted, that the case that was examined with the f.d. algorithm is referred to a $2H$=10m deep soil profile, permeable on its base, with k=10^{-4}m/s, D=30MPa, soil effective special weight γ_{act}=10 kN/m^3, initial relative density D_{r0}=0.5, surface load q=200kPa and water special weight γ_w=10 kN/m^3. Time step Δt was set equal to $5\cdot10^2$s and spatial step h equal to 0.1m.

3.3.1.2 Hysteretic damping soil

The one dimensional, vertical, soil consolidation described by the differential equation (3.28), is solved with the finite differences technique, according to the implicit method, for the case of hysteretic damping soil. Employing the central difference for the 2nd order spatial derivative and the backward difference for the 1st order time derivative:

- $\left(\frac{\partial^2(-\Sigma dp)}{\vartheta z^2}\right)_{i,j} = -\frac{\left(\Sigma dp_{i,j+1} - 2\Sigma dp_{i,j} + \Sigma dp_{i,j-1}\right)}{h^2}$ *central difference*
- $\left(\frac{\partial \varepsilon_{vol}}{\vartheta t}\right)_{i,j} = \frac{\varepsilon_{vol_{i,j}} - \varepsilon_{vol_{i-1,j}}}{\Delta t}$ *backward difference*

and by substituting into equation (3.28), we obtain:

$$\frac{k}{\gamma_w}\frac{\left(\Sigma dp_{i,j+1} - 2\Sigma dp_{i,j} + \Sigma dp_{i,j-1}\right)}{h^2} = \frac{\varepsilon_{vol_{i,j}} - \varepsilon_{vol_{i-1,j}}}{\Delta t} \tag{3.41}$$

The constitutive relation (2.1), assuming zero deviatoric strain increment $d\varepsilon_q$, is used in order to calculate the volumetric strain increment:

$$d\varepsilon_{vol_{i,j}} = \varepsilon_{vol}{}_{i,j} - \varepsilon_{vol}{}_{i-1,j} = \frac{dp_{i,j}}{A_{i-1,j}} \Rightarrow \tag{3.42}$$

By substituting into equation (3.41), we obtain:

$$\frac{k}{\gamma_w}\frac{\left(\Sigma dp_{i,j+1} - 2\Sigma dp_{i,j} + \Sigma dp_{i,j-1}\right)}{h^2} = \frac{dp_{i,j}}{A_{i-1,j}\Delta t} \Rightarrow$$

$$\frac{A_{i-1,j}\,\Delta t\,k}{\gamma_w h^2}\left(p_{i,j+1} - p_{0,j+1} - 2p_{i,j} + 2p_{0,j} + p_{i,j-1} - p_{0,j-1}\right) = p_{i,j} - p_{i-1,j} \tag{3.43}$$

Assuming that:

$$\frac{A_{i-1,j}\,\Delta t\,k}{\gamma_w h^2} = V_{i-1,j} \tag{3.44}$$

, we finally have:

$$V_{i-1,j}\left(-p_{i,j+1} + 2p_{i,j} - p_{i,j-1}\right) + p_{i,j} = p_{i-1,j} + V_{i-1,j}\left(-p_{0,j+1} + 2p_{0,j} - p_{0,j-1}\right) \Rightarrow$$

$$-p_{i,j-1} + \left(2 + \frac{1}{V_{i-1,j}}\right)p_{i,j} - p_{i,j+1} = \frac{p_{i-1,j}}{V_{i-1,j}} + -p_{0,j+1} + 2p_{0,j} - p_{0,j-1} \quad for\ j = 2{:}\,Z \tag{3.45}$$

The initial and the boundary conditions are the same as were presented for the case of the elastic soil, namely equations (3.34), (3.35) and (3.36).

Thus, at time $t = t_i$, a system of $(Z + 1)$ linear equations has to be solved, with unknown variables the mean effective stresses along the soil profile: $p_{i,j}\ \ for\ j = 1{:}\,Z$+1. The system is written in the following matrix form (under the assumption of a permeable base rock):

$$\begin{array}{c} \textit{height } j \longrightarrow \\ \textit{height } j \downarrow \end{array}$$

	1	2	3	4			$Z-2$	$Z-1$	Z	$Z+1$			
1	1	0	0	0			0	0	0	0		$p_{i,1}$	$p_{0.1} + q$
2	-1	$G_{i-1,2}$	-1	0	·	· ·	0	0	0	0		$p_{i,2}$	$H_{i-1,2}$
3	0	-1	$G_{i-1,3}$	-1			0	0	0	0		$p_{i,3}$	$H_{i-1,3}$
			·		·			·				·	·
			·		·			·			×	·	·
			·		·			·				·	·
$Z-1$	0	0	0	0			-1	$G_{i-1,Z-1}$	-1	0		$p_{i,Z-1}$	$H_{i-1,Z-1}$
Z	0	0	0	0	·	· ·	0	-1	$G_{i-1,Z}$	-1		$p_{i,Z}$	$H_{i-1,Z}$
$Z+1$	0	0	0	0			0	0	0	1		$p_{i,Z+1}$	$p_{0,Z+1} + q$

Matrix 3.5

, where: $G_{i-1,j} = \frac{1}{V_{i-1,j}} + 2$ and $H_{i-1,j} = \frac{p_{i-1,j}}{V_{i-1,j}} + -p_{0,j+1} + 2p_{0,j} - p_{0,j-1}$.

3.3.2. Model response in one dimensional deformation soil element test

The one dimensional soil deformation is a condition very commonly encountered in geotechnical engineering, e. g. consolidation, sedimentation, road embankments, large layout structures resting on mat foundation etc. The extensive applications in addition to the simplicity of the laboratory implementation make the oedometer test one the most common

geotechnical investigations in soil mechanics. A typical laboratory layout provides conditions similar to those previously described. Figure 3.7 renders qualitatively the typical experimental response of saturated cohesionless soil in oedometer testing (Wils et al. 2015, Pestana and Whittle 1995, Amundsen et al. 2015) in comparison with model response under one dimensional compression loading. It is noted that in one dimensional deformation loading, soil element is imposed to normal deformation in the vertical axis, while preventing the normal horizontal and shear deformations, e. g.: $\varepsilon_{zz} \neq 0$, while $\varepsilon_{xx} = \varepsilon_{yy} = \gamma_{xy} = \gamma_{xz} = \gamma_{yz} = 0$. According to experimental observations, the vertical effective stress *vs* corresponding normal strain (or volumetric strain or void ratio) curve, is characterized by the following; as vertical stress increases the sand specimen is condensed, it gets denser and therefore less compressible. If a critical stress is exceeded, grain crush is observed, the soil "yields" and becomes less stiff, though with the continuously increasing vertical stress hardening soil response is reacquired. The "yield" region that is attributed to the grain crush is not captured by the model, however its contribution to the deformation is considered to be limited in practical consolidation problems, since the stresses between the grains remail small. Since the lateral expansion is restricted, as the vertical normal stress increases horizontal compressive stresses are developed. A number of laboratory tests evince that the horizontal over the vertical stress ratio K_0 remains constant, which is also reproduced by the model.

3.3.3. Implementation of the consolidation equation into the wave propagation algorithm

In the present section, the developed numerical algorithm for the one dimensional shear wave propagation is extended to simultaneously account for the dissipation of the excess pore water pressure, that is generated within sandy layers due to cyclic loading. The sets of equations that refer to the vertical soil consolidation and those that describe the one dimensional shear wave propagation, are treated with the finite difference method. The procedure followed by the algorithm is that one set of equations is solved first and the obtained results are used for the solution of the second set of equations (at a certain point in time $t = t_i$). These results in turn, are fed back into the first set of equations to calculate the response at the next point in time $t = t_{i+1}$. Figure 3.8 gives a schematic depiction of the algorithm procedure. Forward, backward or central finite differences technique is used contextually, resulting in an implicit or an explicit solution method. The alternative solution techniques drawn in Figure 3.8 that were examined (*f.d.*, *b.d.* or *c.d.* at certain positions)

display insignificant deviations, however attention must be given when deciding the size of time and spatial step of the analysis, e.g. if the explicit technique is applied, the discretization should be adequate enough when modelling high soil permeabilities (i.e. k > 1 m/s). In what follows, the implicit, the explicit and the Crank-Nicolson technique for solving the consolidation equation (3.28) are presented.

Implicit method

The central difference is employed for the 2nd order spatial derivative and the backward difference is employed for the 1st order time derivative of equation (3.28):

- $\left(\frac{\partial^2(-\Sigma dp)}{\partial z^2}\right)_{i,j} = -\frac{\Sigma dp_{i,j+1} - 2\Sigma dp_{i,j} + \Sigma dp_{i,j-1}}{h^2}$ *central difference*
- $\left(\frac{\partial \varepsilon_{vol}}{\partial t}\right)_{i,j} = \frac{\varepsilon_{vol\,i,j} - \varepsilon_{vol\,i-1,j}}{\Delta t}$ *backward difference*

By substituting into equation (3.28), we obtain:

$$\frac{k}{\gamma_w}\frac{\Sigma dp'_{i,j+1} - 2\Sigma dp'_{i,j} + \Sigma dp'_{i,j-1}}{h^2} = \frac{\varepsilon_{vol\,i,j} - \varepsilon_{vol\,i-1,j}}{\Delta t} = \frac{d\varepsilon_{vol\,i,j}}{\Delta t} \quad (3.46)$$

The constitutive relation (2.1) is used in order to calculate the volumetric strain increment:

$$\frac{d\varepsilon_{vol\,i,j}}{\Delta t} = \frac{dp_{i,j} - B_{i-1,j} de_{q\,i,j}}{A_{i-1,j}\Delta t} \quad (3.47)$$

, where the deviatoric strain increment $de_{q\,i,j}$, is calculated by the solution of the wave propagation diff. eq. (3.9). Thus:

$$\frac{A_{i-1.j}\,\Delta t\,k}{\gamma_w\,h^2}\left(\Sigma dp'_{i,j+1} - 2\Sigma dp'_{i,j} + \Sigma dp'_{i,j-1}\right) - p_{i,j} = -p_{i-1,j} - B_{i-1,j} de_{q\,i,j} \quad (3.48)$$

Assuming that:

$$\frac{A_{i-1.j}\,\Delta t\,k}{\gamma_w\,h^2} = F_{i-1,j} \quad \& \quad \frac{\gamma_w\,h^2}{A_{i-1.j}\,\Delta t\,k}\left(p_{i-1,j} + B_{i-1,j} d\varepsilon_{q\,i,j}\right) = G_{i-1,j}$$

, we obtain:

$$-\Sigma dp'_{i,j+1} + 2\Sigma dp'_{i,j} - \Sigma dp'_{i,j-1} + \frac{p'_{i,j}}{F_{i-1,j}} = G_{i-1,j} \quad (3.49)$$

, where

$$\Sigma dp'_{i,j} = p'_{i,j} - p'_{0,j} \tag{3.50}$$

Assuming that:

$$\frac{1}{F_{i-1,j}} + 2 = \Pi_{i-1,j} \quad \& \quad -p_{0,j+1} + 2p_{0,j} - p_{0,j-1} + G_{i-1,j} = S_{i-1,j}$$

, we finally have:

$$-p_{i,j-1} + \Pi_{i-1,j} p_{i,j} - p_{i,j+1} = S_{i-1,j} \qquad for\ j = 2{:}Z \tag{3.51}$$

The initial conditions of the problem are the geostatic filed stresses:

- $p_{1,j} = p_{0,j} \quad for\ j = 1{:}Z+1$ (3.52)

The boundary conditions of the problem are:

- The free surface permeable boundary:

$$p_{i,Z+1} = p_{0,Z+1} \quad for\ i = 1{:}N+1 \tag{3.53}$$

- if soil column base is assumed a permeable boundary:

$$p_{i,1} = p_{0,1} \quad for\ i = 1{:}N+1 \tag{3.54a}$$

If soil base is considered a non permeable boundary, zero volumetric strain increment is assumed at this point and employing the constitutive relationship (equation 2.1):

$$\frac{\vartheta \varepsilon_{vol_{i,1}}}{\vartheta t} = 0 \Rightarrow d\varepsilon_{vol\ i,1} = 0 \Rightarrow dp_{i,1} = B_{i-1,1} d\varepsilon_{q\ i,1} \Rightarrow p_{i,1} = p_{i-1,1} +$$

$$B_{i-1,1} d\varepsilon_{q\ i,1} \qquad for\ i = 2{:}N+1 \tag{3.54b}$$

Initial and boundary conditions (for the case of a permeable base rock) are written in the following matrix form:

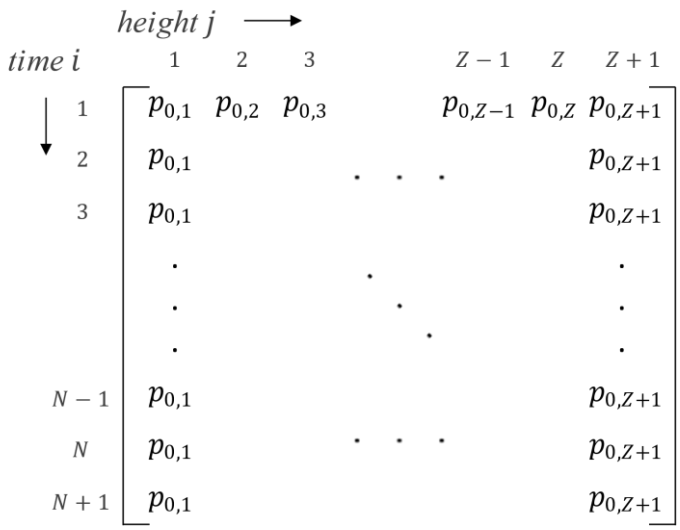

Matrix 3.6

Thus, at time $t = t_i$, a system of $(Z + 1)$ linear equations has to be solved, with unknown parameters the mean effective stresses along the soil profile: $p_{i,j}$ $for\ j = 1$: Z+1. The system is written in the following matrix form (under the assumption of a permeable base rock):

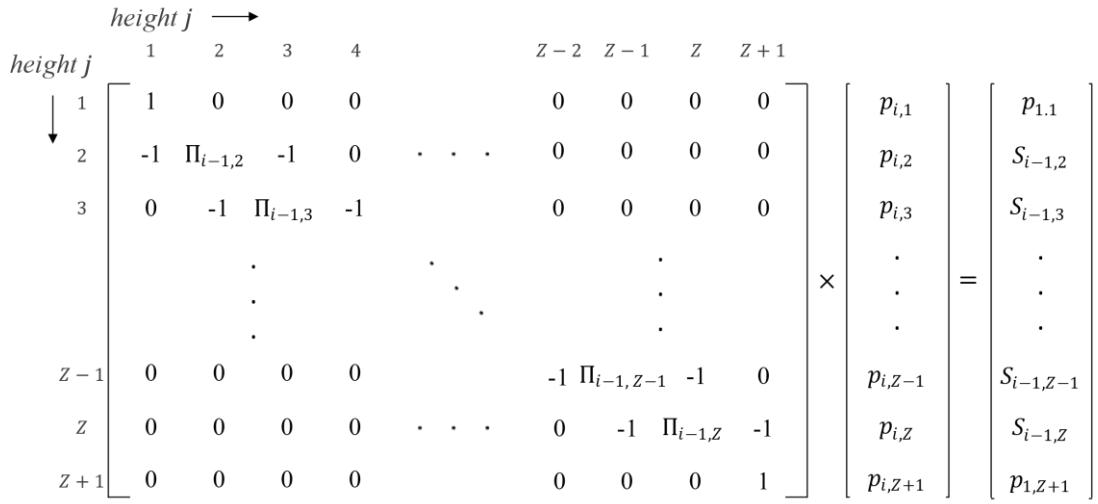

Matrix 3.7

and for the case of a non permeable base rock:

$$
\begin{array}{c}
\textit{height } j \longrightarrow \\
\textit{height } j \\
\downarrow
\end{array}
\begin{array}{c}
\begin{matrix} 1 & 2 & 3 & 4 & & & & Z-2 & Z-1 & Z & Z+1 \end{matrix} \\
\begin{bmatrix}
1 & 0 & 0 & 0 & & & & 0 & 0 & 0 & 0 \\
-1 & \Pi_{i-1,2} & -1 & 0 & \cdots & & & 0 & 0 & 0 & 0 \\
0 & -1 & \Pi_{i-1,3} & -1 & & & & 0 & 0 & 0 & 0 \\
 & & \cdot & & \cdot & & & & \cdot & & \\
 & & \cdot & & \cdot & & & & \cdot & & \\
 & & \cdot & & \cdot & & & & \cdot & & \\
0 & 0 & 0 & 0 & & & & -1 & \Pi_{i-1,Z-1} & -1 & 0 \\
0 & 0 & 0 & 0 & \cdots & & & 0 & -1 & \Pi_{i-1,Z} & -1 \\
0 & 0 & 0 & 0 & & & & 0 & 0 & 0 & 1
\end{bmatrix}
\end{array}
\times
\begin{bmatrix} p_{i,1} \\ p_{i,2} \\ p_{i,3} \\ \cdot \\ \cdot \\ \cdot \\ p_{i,Z-1} \\ p_{i,Z} \\ p_{i,Z+1} \end{bmatrix}
=
\begin{bmatrix} \Gamma_{i-1.1} \\ S_{i-1,2} \\ S_{i-1,3} \\ \cdot \\ \cdot \\ \cdot \\ S_{i-1,Z-1} \\ S_{i-1,Z} \\ p_{1,Z+1} \end{bmatrix}
$$

Matrix 3.8

, where $\Gamma_{i-1,1} = p_{i-1,1} + B_{i-1,1} d\varepsilon_{q\,i,1}$.

Schematically, the implicit method can be depicted as follows:

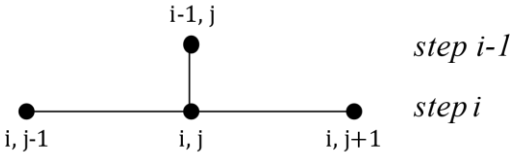

Explicit method error: $\Delta u = O(\Delta t) + O(h^2)$, is linear over time step and quadratic over spatial step. The implicit method is always numerically stable and convergent but more numerically intensive than the explicit method, as it requires solving a system of numerical equations on each time step.

Explicit method

The central difference is employed for the 2nd order spatial derivative and the forward difference is employed fir the 1st order time derivative of equation (3.28):

- $\left(\frac{\partial^2(-\Sigma dp)}{\partial z^2}\right)_{i-1,j} = -\frac{\Sigma dp_{i-1,j+1} - 2\Sigma dp_{i-1,j} + \Sigma dp_{i-1,j-1}}{h^2}$ *central difference*
- $\left(\frac{\partial \varepsilon_{vol}}{\partial t}\right)_{i-1,j} = \frac{\varepsilon_{vol\,i,j} + \varepsilon_{vol\,i-1,j}}{\Delta t}$ *forward difference*

By substituting into equation (3.28), we obtain:

$$\frac{k}{\gamma_w}\frac{\Sigma dp_{i-1,j+1}-2\Sigma dp_{i-1,j}+\Sigma dp_{i-1,j-1}}{h^2}=\frac{\varepsilon_{vol\,i,j}-\varepsilon_{vol\,i-1,j}}{\Delta t}=\frac{d\varepsilon_{vol\,i,j}}{\Delta t} \quad (3.55)$$

The volumetric strain increment is calculated according to Equation (3.47). Thus:

$$F_{i-1,j}\left(\Sigma dp_{i-1,j+1}-2\Sigma dp_{i-1,j}+\Sigma dp_{i-1,j-1}\right)=p_{i,j}-p_{i-1,j}-B_{i-1,j}de_{q\,i,j}\Rightarrow$$

$$p_{i,j}=F_{i-1,j}\,p_{i-1,j+1}+\left(1-2F_{i-1,j}\right)p_{i-1,j}+F_{i-1,j}\,p_{i-1,j-1}+B_{i-1,j}\,d\varepsilon_{q\,i,j}-p_{0,j+1}+2p_{0,j}-p_{0,j-1} \quad (3.56)$$

Equation (3.56) is solved in conjunction with the initial condition (3.52) and the boundary conditions (3.53) and (3.54). Schematically, the implicit method can be illustrated as follows:

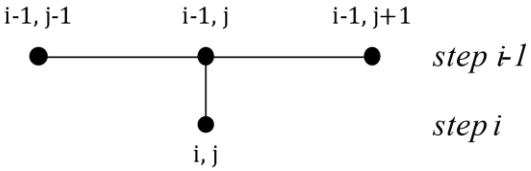

Explicit method error: $\Delta u = O(\Delta t) + O(h^2)$, is linear over time step and quadratic over spatial step. The explicit method is least accurate and can be unstable, but is easy to implement and least numerically intensive. The explicit method is generally numerically stable and convergence if:

$$\Delta t \leq \frac{h^2}{2} \quad (3.57)$$

Crank – Nicolson method

Equation (3.28) is expressed at time $t = t_{i-\frac{1}{2}}$ as follows:

$$\frac{k}{2\,\gamma_w}\left[\left(\frac{\partial^2(-\Sigma dp)}{\partial z^2}\right)_{i-1,j}+\left(\frac{\partial^2(-\Sigma dp)}{\partial z^2}\right)_{i,j}\right]=-\left(\frac{\partial \varepsilon_{vol}}{\vartheta t}\right)_{i-\frac{1}{2},j} \quad (3.58)$$

By calculating the central differences:

- $\left(\frac{\partial^2(-\Sigma dp)}{\partial z^2}\right)_{i-1,j}=-\frac{\Sigma dp_{i-1,j+1}-2\Sigma dp_{i-1,j}+\Sigma dp_{i-1,j-1}}{h^2}$ *central difference*
- $\left(\frac{\partial^2(-\Sigma dp)}{\partial z^2}\right)_{i,j}=-\frac{\Sigma dp_{i,j+1}-2\Sigma dp_{i,j}+\Sigma dp_{i,j-1}}{h^2}$ *central difference*
- $\left(\frac{\partial \varepsilon_{vol}}{\partial t}\right)_{i-\frac{1}{2},j}=\frac{\varepsilon_{vol\,i,j}+\varepsilon_{vol\,i-1,j}}{\Delta t}$ *central difference*

and substituting into equation (3.58), we obtain:

$$\frac{F_{i-1,j}}{2}\left(\Sigma dp_{i-1,j-1} - 2\Sigma dp_{i-1,j} + \Sigma dp_{i-1,j+1} + \Sigma dp_{i,j-1} - 2\Sigma dp_{i,j} + p_{i,j+1}\right) = p_{i,j} - p_{i-1,j} - B_{i-1,j} d\varepsilon_{q\,i,j} \Rightarrow$$

$$\frac{F_{i-1,j}}{2} p_{i,j-1} + \left(-1 - F_{i-1,j}\right) p_{i,j} + \frac{F_{i-1,j}}{2} p_{i,j+1} = -\frac{F_{i-1,j}}{2} p_{i-1,j-1} + \left(-1 + F_{i-1,j}\right) p_{i-1,j} - \frac{F_{i-1,j}}{2} p_{i-1,j+1} - B_{i-1,j} d\varepsilon_{q\,i,j} + 2p_{0,j-1} - 4p_{0,j} + 2p_{0,j+1} \Rightarrow \quad (3.59)$$

Assuming that:

$$\frac{2}{F_{i-1,j}} + 2 = N_{i-1,j} \qquad \text{and}$$

$$p_{i-1,j-1} + \left(\frac{2}{F_{i-1,j}} - 2\right) p_{i-1,j} + p_{i-1,j+1} + \frac{2}{F_{i-1,j}} B_{i-1,j} d\varepsilon_{q\,i,j} - \frac{4}{F_{i-1,j}} p_{0,j-1} + \frac{8}{F_{i-1,j}} p_{0,j} - \frac{4}{F_{i-1,j}} p_{0,j+1} = W_{i-1,j}$$

, we finally have:

$$-p_{i,j-1} + N_{i-1,j} p_{i,j} - p_{i,j+1} = W_{i-1,j} \qquad for\ j = 2{:}\ Z \quad (3.60)$$

, in conjunction with the initial condition (3.52) and the boundary conditions (3.53) and (3.54). The solution of a system of $(Z+1)$ linear equations is required at each time step $t = t_i$. For the case of a permeable base rock, the system is written in matrix form as follows:

$$\begin{array}{c} \textit{height } j \longrightarrow \\ \textit{height } j \end{array}$$

	1	2	3	4			$Z-2$	$Z-1$	Z	$Z+1$			
1	1	0	0	0			0	0	0	0		$p_{i,1}$	$p_{1.1}$
2	-1	$N_{i-1,2}$	-1	0	·	· ·	0	0	0	0		$p_{i,2}$	$W_{i-1,2}$
3	0	-1	$N_{i-1,3}$	-1			0	0	0	0		$p_{i,3}$	$W_{i-1,3}$
			·		·			·				·	·
			·			·		·			×	·	= ·
			·			·		·				·	·
$Z-1$	0	0	0	0			-1	$N_{i-1,Z-1}$	-1	0		$p_{i,Z-1}$	$W_{i-1,Z-1}$
Z	0	0	0	0	·	· ·	0	-1	$N_{i-1,Z}$	-1		$p_{i,Z}$	$W_{i-1,Z}$
$Z+1$	0	0	0	0			0	0	0	1		$p_{i,Z+1}$	$p_{1,Z+1}$

Matrix 3.9

, while for the case of a non permeable base rock:

$$
\begin{array}{c}
\text{height } j \longrightarrow \\
\text{height } j \downarrow
\end{array}
\begin{array}{c}
\begin{array}{cccccccccc}
1 & 2 & 3 & 4 & & & Z-2 & Z-1 & Z & Z+1
\end{array} \\
\begin{bmatrix}
1 & 0 & 0 & 0 & & & 0 & 0 & 0 & 0 \\
-1 & N_{i-1,2} & -1 & 0 & & & 0 & 0 & 0 & 0 \\
0 & -1 & N_{i-1,3} & -1 & & & 0 & 0 & 0 & 0 \\
 & & \cdot & & \cdot & & & \cdot & & \\
 & & \cdot & & \cdot & & & \cdot & & \\
 & & \cdot & & \cdot & & & \cdot & & \\
0 & 0 & 0 & 0 & & & -1 & N_{i-1,Z-1} & -1 & 0 \\
0 & 0 & 0 & 0 & & & 0 & -1 & N_{i-1,Z} & -1 \\
0 & 0 & 0 & 0 & & & 0 & 0 & 0 & 1
\end{bmatrix}
\end{array}
\times
\begin{bmatrix}
p_{i,1} \\ p_{i,2} \\ p_{i,3} \\ \cdot \\ \cdot \\ \cdot \\ p_{i,Z-1} \\ p_{i,Z} \\ p_{i,Z+1}
\end{bmatrix}
=
\begin{bmatrix}
\Gamma_{i-1.1} \\ W_{i-1,2} \\ W_{i-1,3} \\ \cdot \\ \cdot \\ \cdot \\ W_{i-1,Z-1} \\ W_{i-1,Z} \\ p_{1,Z+1}
\end{bmatrix}
$$

Matrix 3.10

The Crank – Nicolson method is schematically depicted as:

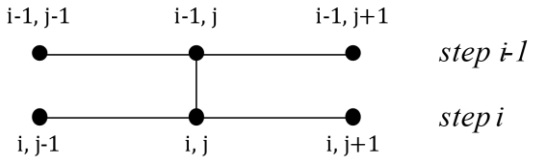

Crank – Nicolson method error: $\Delta u = O(\Delta t^2) + O(h^2)$, is quadratic over time and spatial step. Crank – Nicolson method is numerically stable and convergent but usually more numerically intensive as it requires solving a system of numerical equations at each time step.

3.3.4. Considering the coupling term on the consolidation differential equation

According to equation (3.27) that describes the one dimensional vertical soil consolidation, a constant coefficient of permeability k_z was assumed along the soil profile. In case that a non uniform stratigraphy, consisted of consecutive soil layers of different permeability is examined, the equation of vertical consolidation is reformulated as follows:

$$\frac{k_z}{\gamma_w}\frac{\vartheta^2 u_{p\,(t,z)}}{\vartheta z^2} + \frac{1}{\gamma_w}\frac{\partial k_z}{\vartheta z}\frac{\partial u_{p\,(t,z)}}{\vartheta z} = -\frac{\vartheta \varepsilon_{vol(t,z)}}{\vartheta t} \qquad (3.61)$$

, where k_z is the variant coefficient of soil permeability in the vertical axis. By substituting with respect to the mean effective stress, we obtain:

$$\frac{k_z}{\gamma_w}\frac{\vartheta^2 - \Sigma dp_{(t,z)}}{\vartheta z^2} + \frac{1}{\gamma_w}\frac{\partial k_z}{\vartheta z}\frac{\partial - \Sigma dp_{(t,z)}}{\vartheta z} = -\frac{\vartheta \varepsilon_{vol(t,z)}}{\vartheta t} \quad (3.62)$$

Following the implicit finite differences technique to solve eq. (3.62):

- $\left(\frac{\partial^2(-\Sigma dp)}{\partial z^2}\right)_{i,j} = -\frac{\Sigma dp_{i,j+1} - 2\Sigma dp_{i,j} + \Sigma dp_{i,j-1}}{h^2}$ *central difference*
- $\left(\frac{\partial \varepsilon_{vol}}{\partial t}\right)_{i,j} = \frac{\varepsilon_{vol\, i,j} - \varepsilon_{vol\, i-1,j}}{\Delta t}$ *backward difference*
- $\left(\frac{\partial k}{\partial z}\right)_{i,j} = \frac{k_{i,j+1} - k_{i,j-1}}{2h}$ *central difference*
- $\left(\frac{\partial \Sigma dp}{\partial z}\right)_{i,j} = \frac{\Sigma dp_{i,j+1} - \Sigma dp_{i,j-1}}{2h}$ *central difference*

and by substituting to eq. (3.62),we have:

$$\left(F_{i-1,j} - F'_{i-1,j}\right)p_{i,j-1} + \left(-2F_{i-1,j} - 1\right)p_{i,j} + \left(F_{i-1,j} + F'_{i-1,j}\right)p_{i,j+1} = R_{i-1,j} \quad for\ j = 2{:}\ Z \quad (3.63)$$

, where:

$F_{i-1,j} = \frac{A_{i-1.j}\,\Delta t\, k_j}{\gamma_w\, h^2}$, $F'_{i-1,j} = \frac{A_{i-1.j}\,\Delta t\,(k_{j+1} - k_{j-1})}{4\,\gamma_w\, h^2}$ and

$$R_{i-1,j} = -p_{i-1,j} - B_{i-1,j}de_{q_{i,j}} + F_{i-1,j}\left(p_{0,j+1} - 2p_{0,j} + p_{0,j-1}\right) + F'_{i-1,j}\left(p_{0,j+1} - p_{0,j-1}\right)$$

The initial are boundary conditions are described in eq. (3.52) and (3.53) – (3.54) respectively. The system is written in matrix form (for the case of a permeable bae rock) as follows:

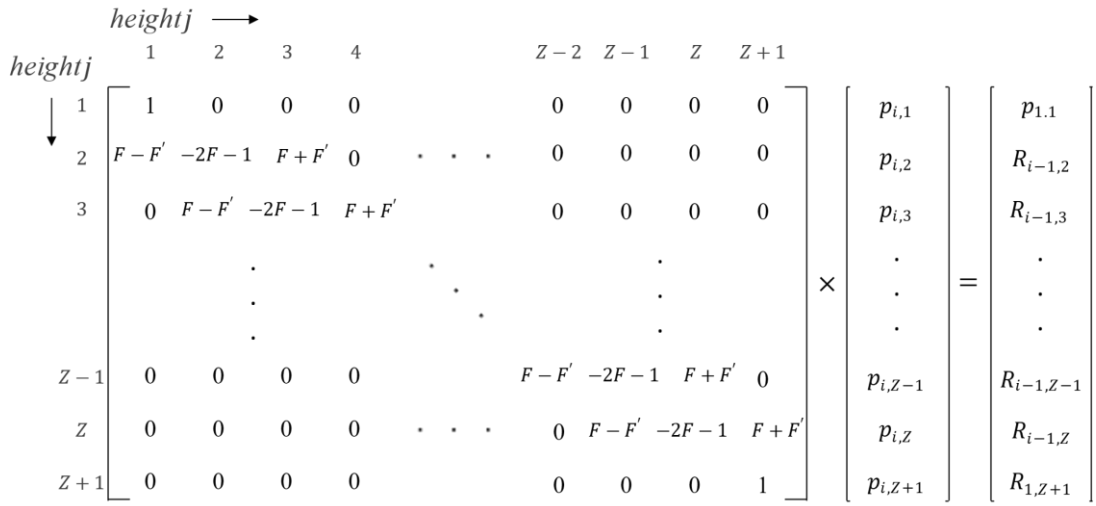

Matrix 3.11

, which for $F' = 0$ equals to Matrix 3.7 that stands for the case of constant k_z along the soil profile. The non-diagonal term F' considerably adds to the computational cost, especially when modelling profiles with substantially varying permeabilities.

The 10m deep soil profile of Figure 3.9, consisting of a 5m sandy layer encased between 2.5m clayey layers of permeability k_{clay} =10^{-8} m/s, will be examined in order to provide an example of the effect on model predictions of equation (3.61), compared to the originally presented consolidation equation (3.27), according to which zero coupling term is assumed. However, the analysis according to eq. (3.27) was executed assuming a varying $k_z = k_j \; for \; j = 1: Z + 1$ along the soil profile. A sinusoidal excitation of total duration equal to 3s is applied on the base of the soil column. The sand permeability is parametrically examined starting from k_{sand} =10^{-8} m/s (homogenous profile) to k_{sand} =10^{-4} m/s and the results in terms of maximum excess pore pressure $r_{u,max}$ with depth are provided in Figure 3.10, for the two aforementioned approaches. The deviations between the two approaches are negligible for k_{sand} =10^{-8} m/s to 10^{-5} m/s, while for k_{sand} =10^{-4} m/s variation in the predictions is observed. The excess pore pressure at the interfaces between sandy and clayey layers attains a peak value of r_u=1, while the distributions within the sandy layer follow broadly the same pattern, i.e. greater r_u values at the middle of the layer that decrease towards the boundaries. This type of response, namely a high r_u value that is locally detected at the interface between a non permeable layer and a layer of high permeability has been observed in the literature (Kokusho 2000, El Shamy & Sizkow 2021). designated as “thin water film”.

The mean effective stress time histories of each sub-layer during the ground shaking of Figure 3.11 illustrate more descriptively the response of the sublayers at the interfaces, which has been modelled according to the constitutive relation and the soil characteristics of the clay. The r_u snapshots of the same figure at t =1s ,2s and 3s of ground shaking, indicate that at t =2s approximately an increase in the r_u values at the interfaces has been developed that rapidly escalates up to 3s. Finally, model predictions for the response at the middle of the sand layer for 17s after the end of shaking is depicted in Figure 3.12, for the two above discussed approaches. In case that the coupling term is omitted, a quick dissipation of the excess pore pressures is noted, while r_u remains undiminished after the end of shaking in case that the coupling terms is included in the diff. equation. Therefore, it can be deduced that the subtraction of the coupling term plays a significant role in case that a layer of high permeability is encased between two practically impermeable layers, since only when this term is taken into consideration the response resembles the expected one, i.e. no dissipation of pore pressure generated in the liquefied sand, through the impermeable top and bottom layers.

However, due to the massive time and computational cost that is required in order to include the coupling term in the analysis (compared to the analysis with zero coupling term with varying $k_z = k_j \; for \; j = 1{:}Z + 1$ along the soil profile) the simplification of using eq. (3.27) instead of eq. (3.61), frequently encountered in the literature (Hashash et al. 2016, Wang et al. 2005), could be adopted, at the expense of accuracy. However, significant inaccuracy could arise when modelling soil profiles of high heterogeneity (with regard to the permeability) and relatively high permeabilities are involved.

References

Amundsen, H. A., Thakur, V., & Emdal, A. (2015). Comparison of two sample quality assessment methods applied to oedometer test results. In *Deformation Characteristics of Geomaterials* (pp. 923-930). IOS Press.

Anthi, M., & Gerolymos, N. (2021). A wave propagation algorithm for nonlinear site response analysis of layered soil accounting for liquefaction. *Soil Dynamics and Earthquake Engineering*, *149*, 106860.

Anthi, M., Tasiopoulou, P., & Gerolymos, N. (2017). A plasticity model for 1D soil response analysis. In *6th International Conference on Computational Methods in Structural Dynamics and Earthquake Engineering*.

El Shamy, U., & Sizkow, S. F. (2021). Coupled SPH-DEM simulations of liquefaction-induced flow failure. *Soil Dynamics and Earthquake Engineering*, *144*, 106683.

Gazetas, G. (1982). Vibrational characteristics of soil deposits with variable wave velocity. *International journal for numerical and analytical methods in Geomechanics*, *6*(1), 1-20.

Gerolymos, N., & Gazetas, G. (2005). Constitutive model for 1-D cyclic soil behaviour applied to seismic analysis of layered deposits. *Soils and Foundations*, *45*(3), 147-159.

Hashash, Y.M.A., Musgrove, M.I., Harmon, J.A., Groholski, D.R., Phillips, C.A., and Park, D. (2016) "DEEPSOIL 6.1, User Manual".

Joyner, W. B., & Chen, A. T. (1975). Calculation of nonlinear ground response in earthquakes. *Bulletin of the Seismological Society of America*, *65*(5), 1315-1336.

Kokusho, T. (2000). Mechanism for water film generation and lateral flow in liquefied sand layer. *Soils and Foundations*, *40*(5), 99-111.

Kramer, S. L. (1996). *Geotechnical earthquake engineering*. Pearson Education India.

Pestana, J. M., & Whittle, A. J. (1995). Compression model for cohesionless soils. *Géotechnique*, *45*(4), 611-631.

Towhata, I. (1996). Seismic wave propagation in elastic soil with continuous variation of shear modulus in the vertical direction. *Soils and Foundations*, *36*(1), 61-72.

Wang, J. G., Yan, L., & Liu, G. R. (2005). A local radial point interpolation method for dissipation process of excess pore water pressure. *International Journal of Numerical Methods for Heat & Fluid Flow*.

Wils, L., Van Impe, P., & Haegeman, W. (2015). One-dimensional compression of a crushable sand in dry and wet conditions. In *3rd International Symposium on Geomechanics from Micro to Macro* (Vol. 2, pp. 1403-1408). Taylor and Francis Group-London.

Figures

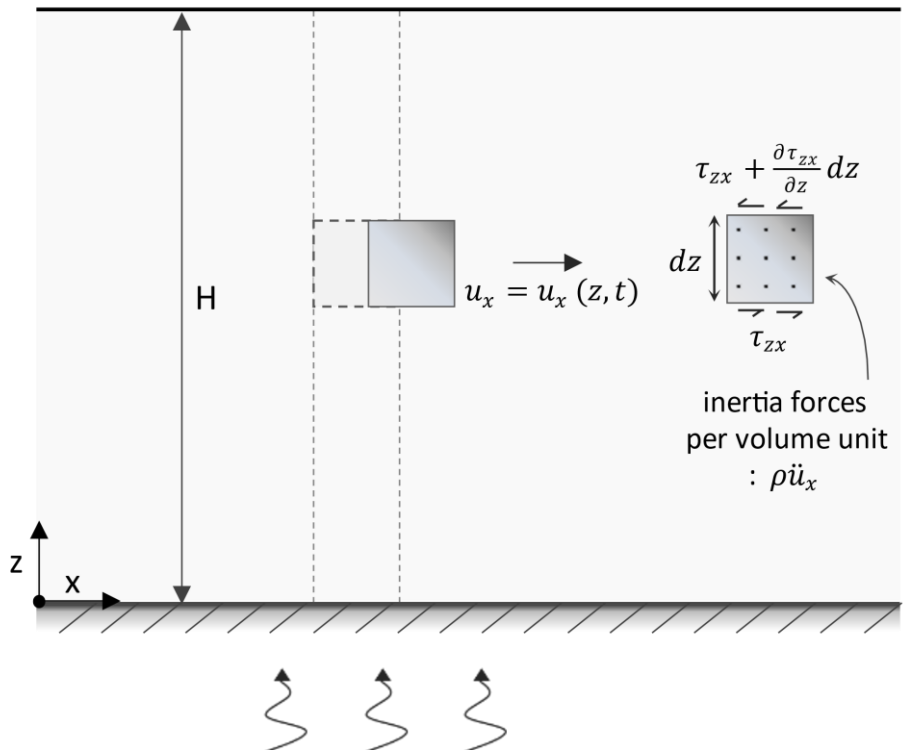

Figure 3.1. Shear wave propagation on a continuous medium.

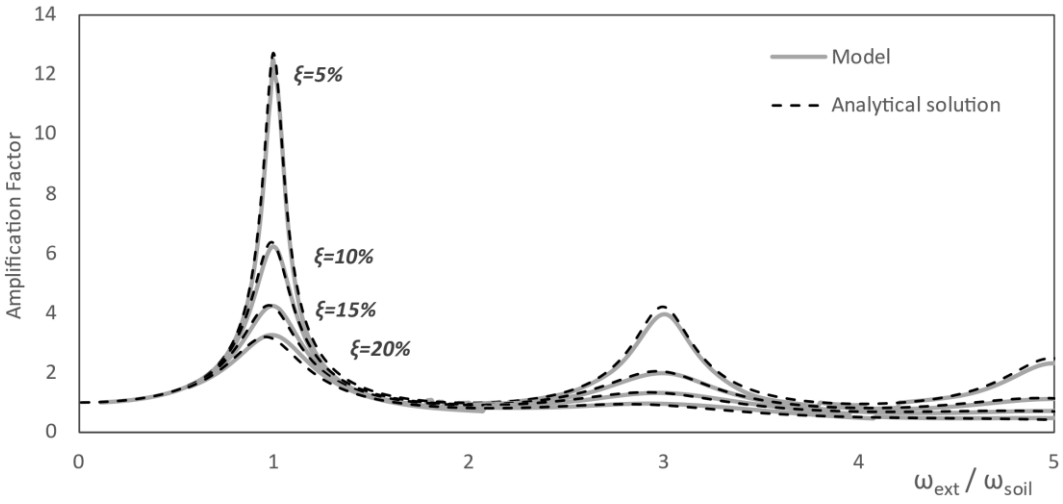

Figure 3.2. Homogeneous soil profile amplification function for 5%, 10%, 15%, and 20% hysteretic damping, against analytical solution.

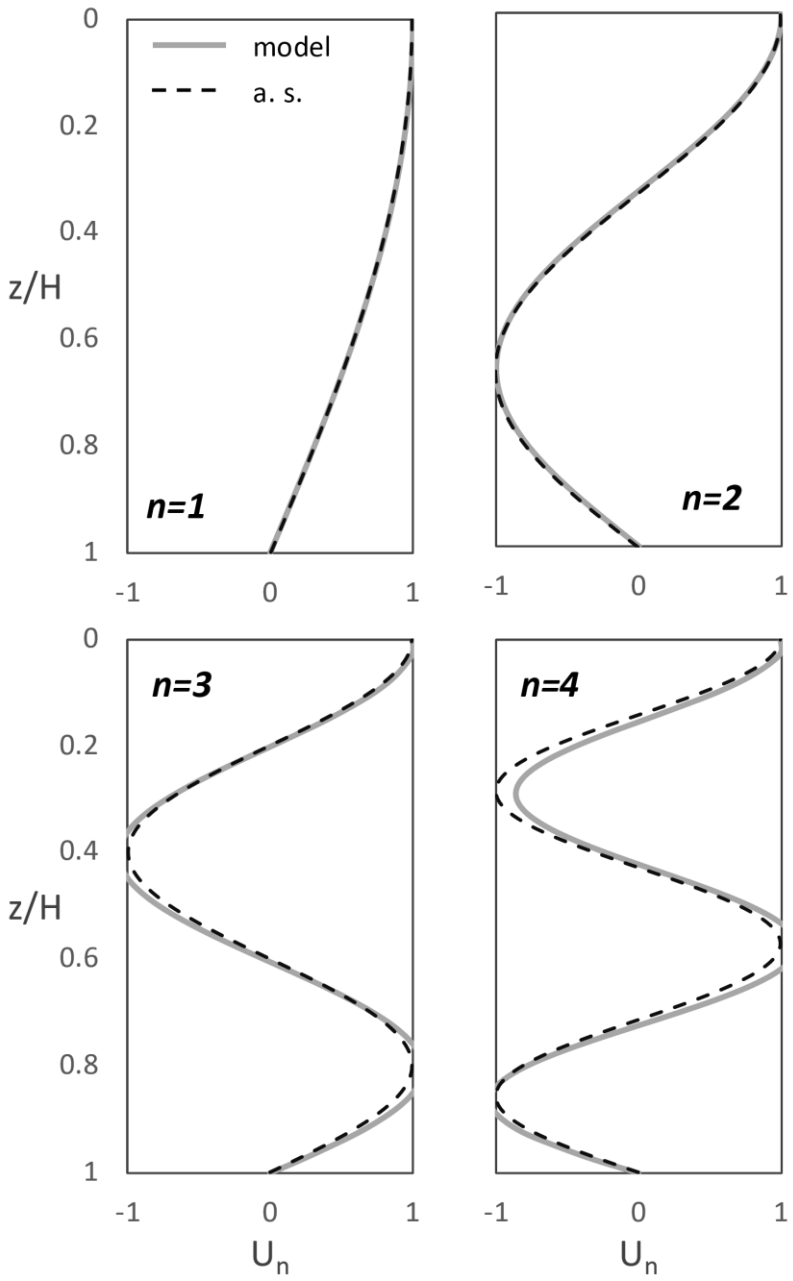

Figure 3.3. First four fundamental mode shapes (*n*=1,2,3,4) of homogeneous soil profile, against analytical solution.

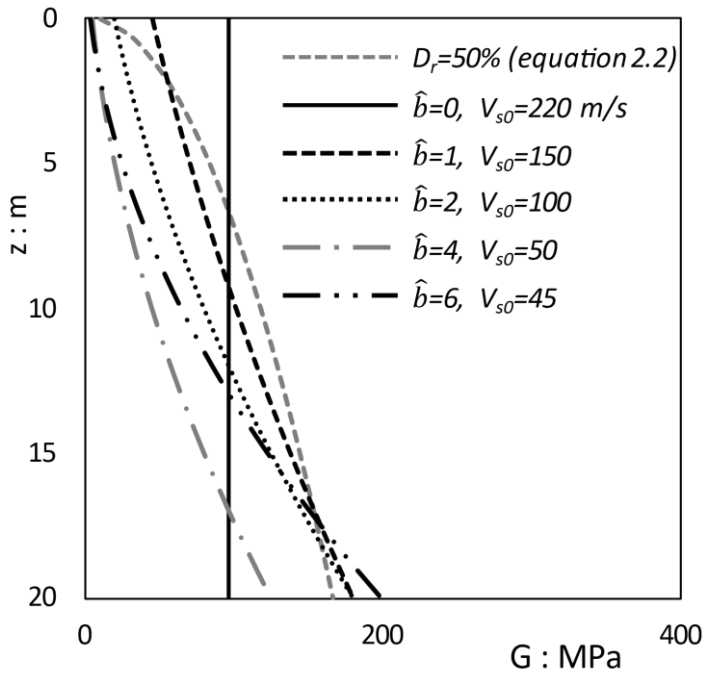

Figure 3.4. Shear modulus distribution for five soil profiles with V_s increasing with depth according to: (i) V_s=220 m/s, (ii) V_s=150(1+0.05z), (iii) V_s=100(1+0.1z), (iv) V_s=50(1+0.2z) and (v) V_s=45(1+0.3z) .G_{max} distribution according to equation (2.2) for D_r=0.5, γ_{act}=20 kN / m^3 and K_o= 0.5 also provided.

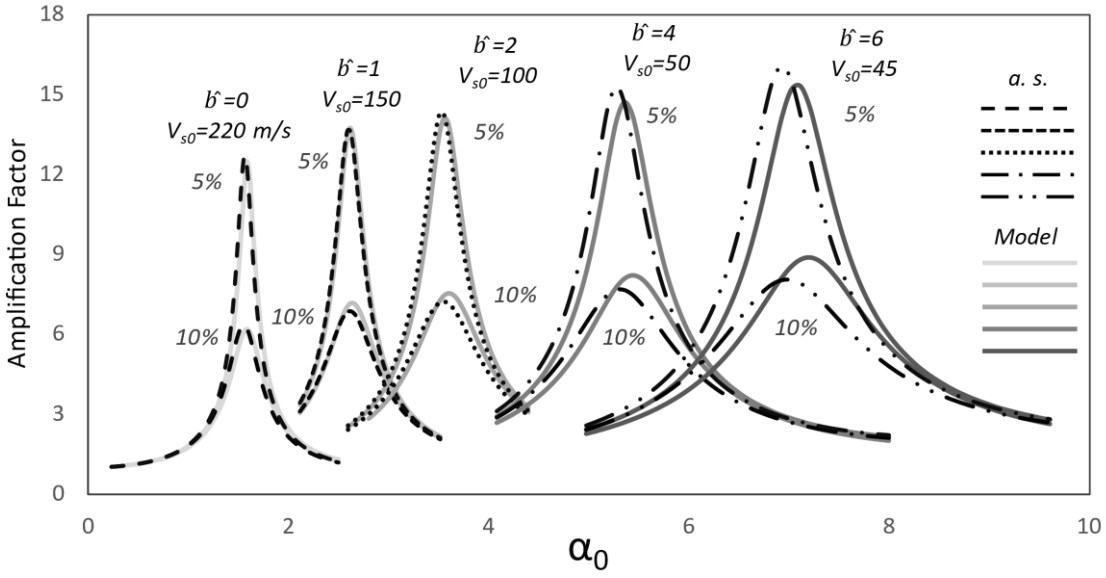

Figure 3.5. Amplification function of five soil profiles with linearly increasing shear wave velocity (G_{max} distribution with depth provided in Fig. 3.4) for 5% and 10% hysteretic damping against analytical solution (Gazetas, 1982).

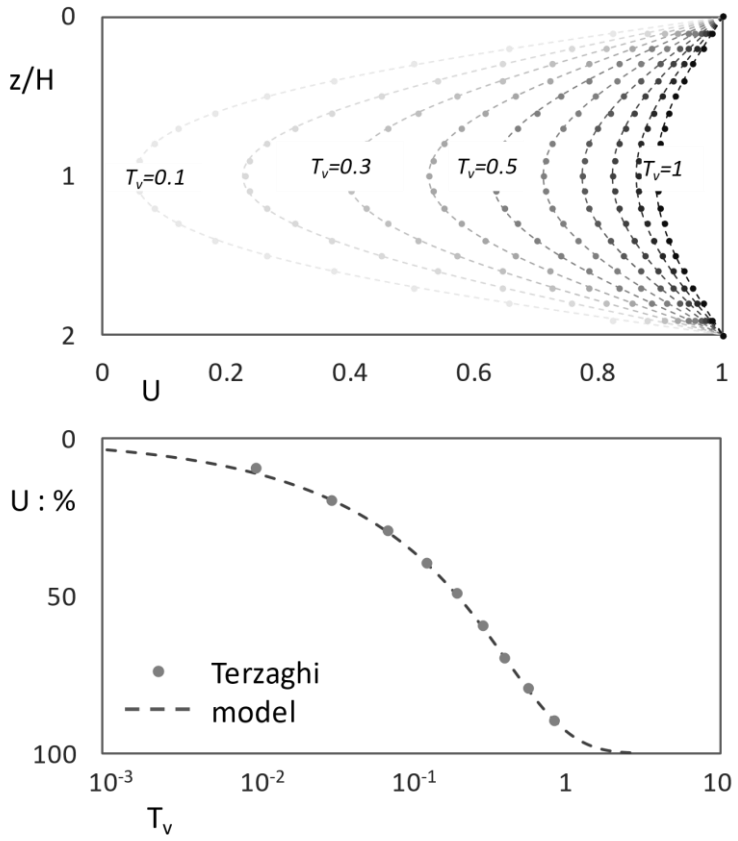

Figure 3.6. Solution of the 1-dimensional vertical consolidation equation of soil using the finite difference method, against Terzaghi's analytical solution; (a) [left] Isochronous curves of consolidation ratio *U* distribution with depth, (b) [right] Consolidation ratio *U* evolution with time.

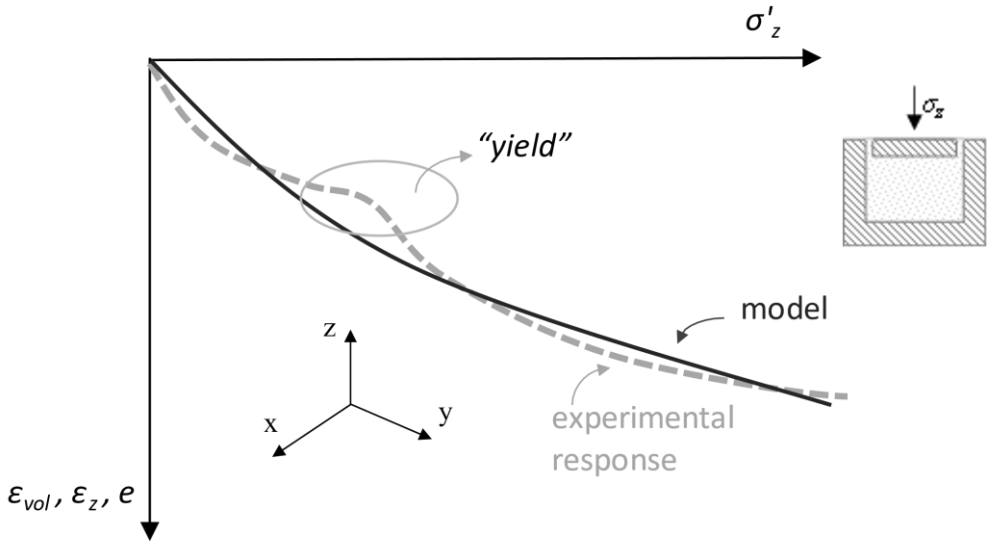

Figure 3.7. Typical qualitative experimental response of cohesionless soil in oedometer testing (dry specimen or drained conditions) in comparison with model response in one dimensional deformation loading.

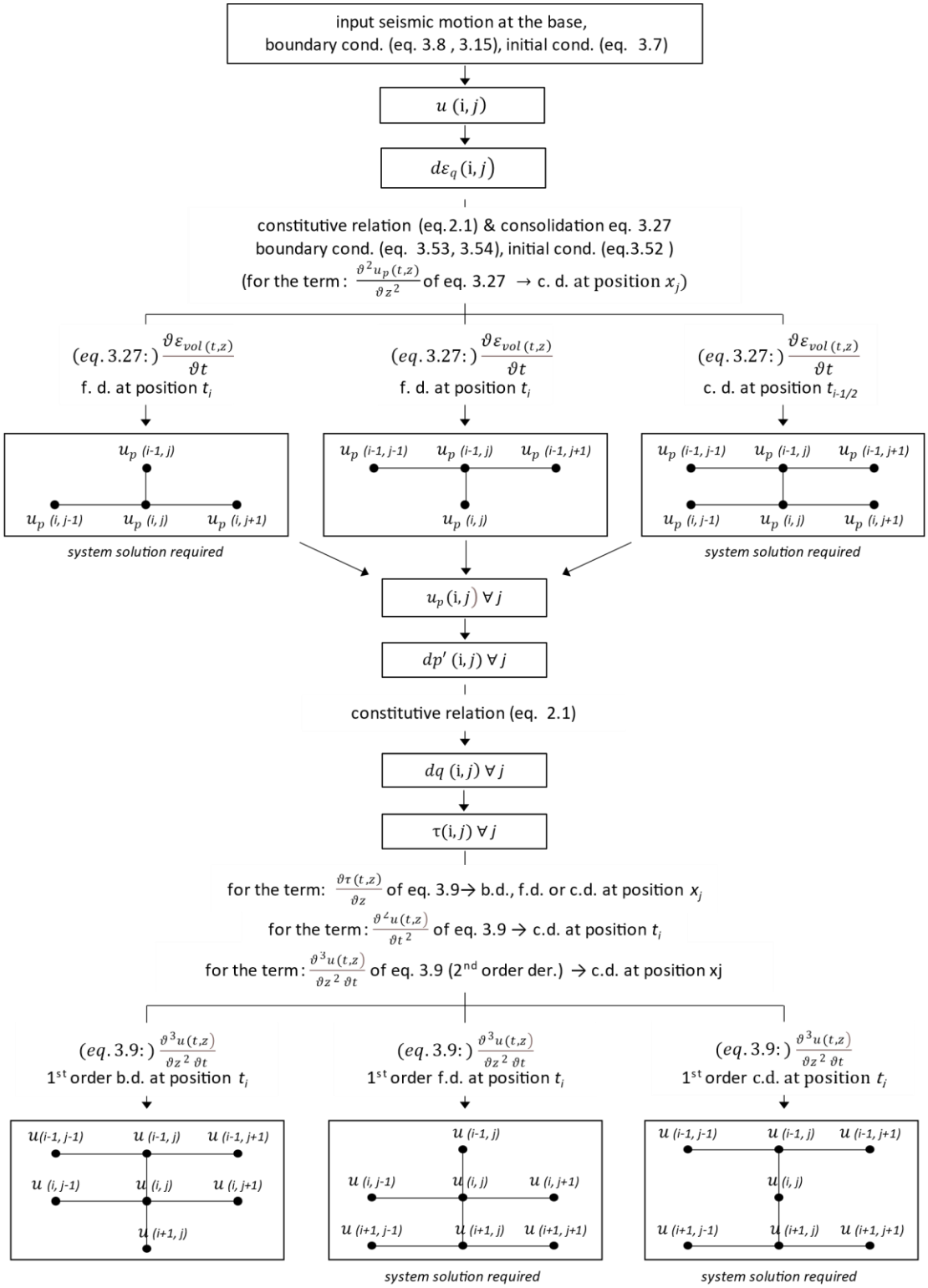

Figure 3.8. Wave propagation algorithm flowchart.

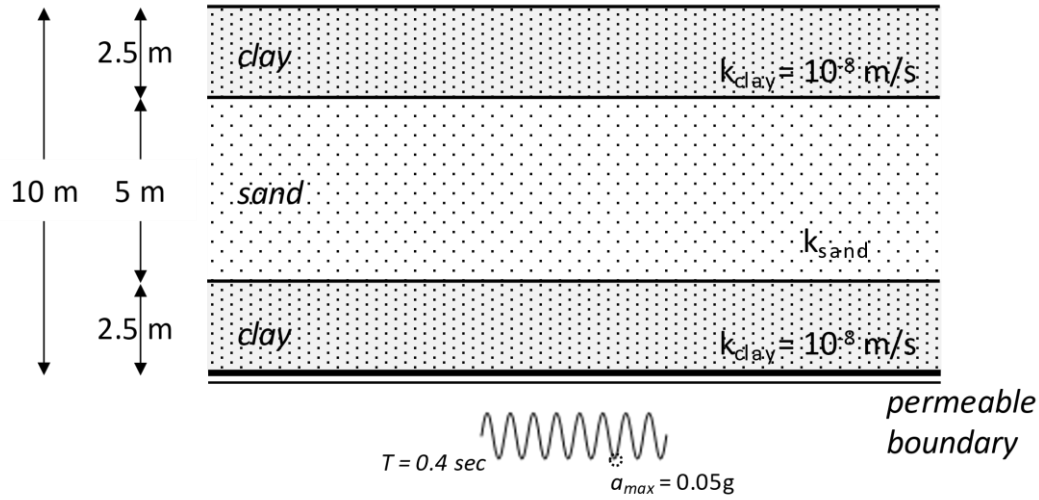

Figure 3.9. Schematic illustration of the stratigraphy under consideration.

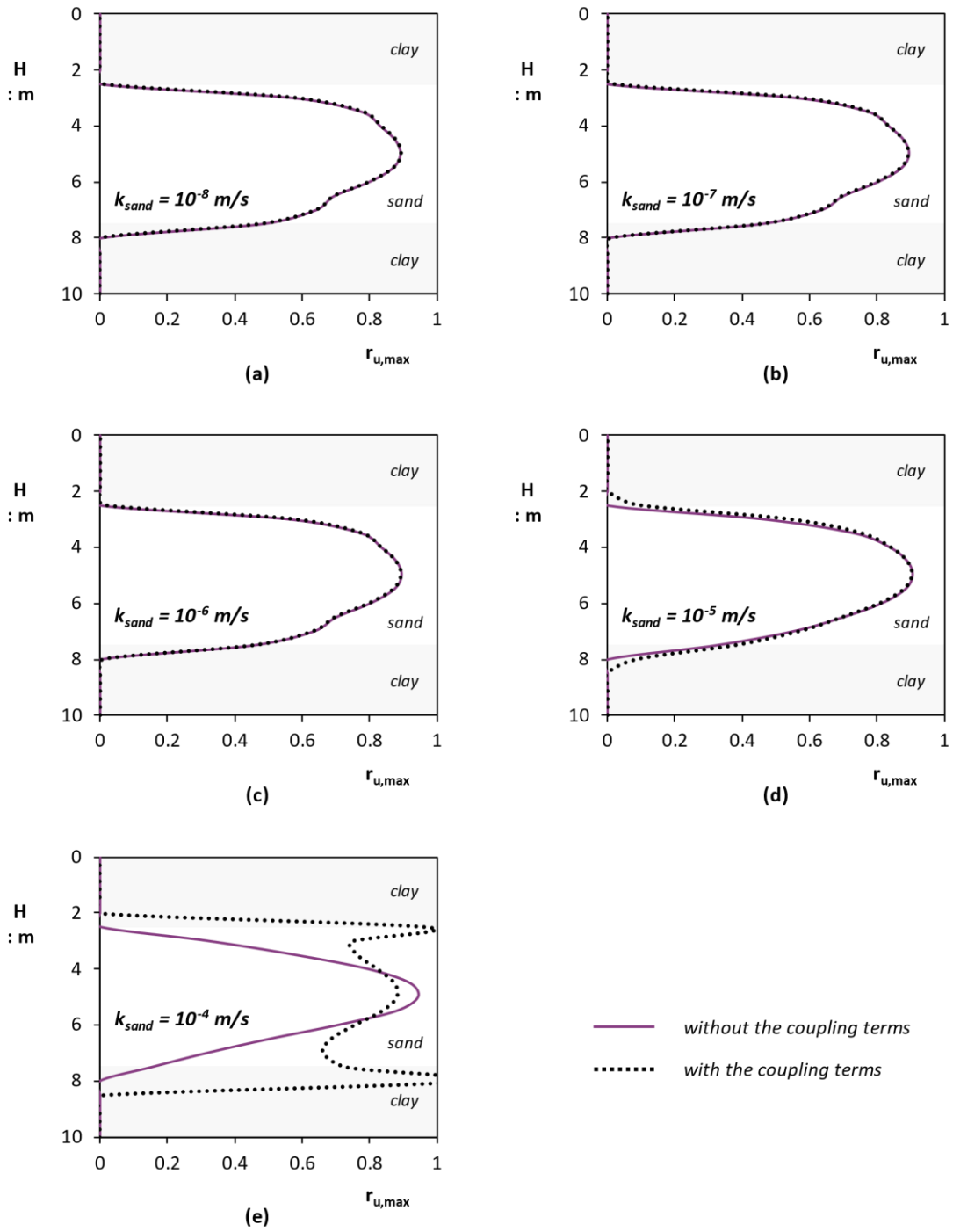

Figure 3.10. Distributions with depth of the maximum excess pore water pressure $r_{u,max}$ of the configuration of Figure 3.9, including and omitting the coupling term of consolidation equation (3.61), for sand permeability from k_{sand} =10^{-8} m/s to 10^{-4} m/s.

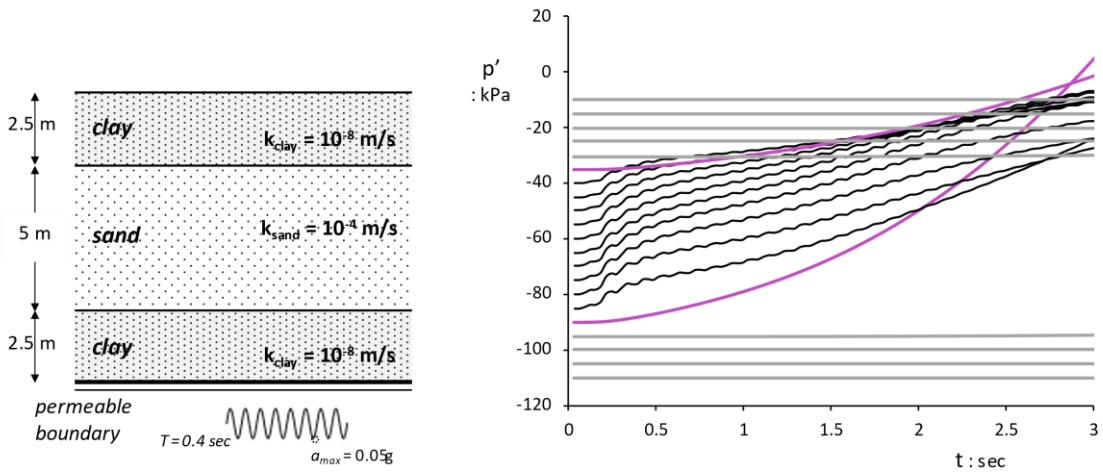

(a)

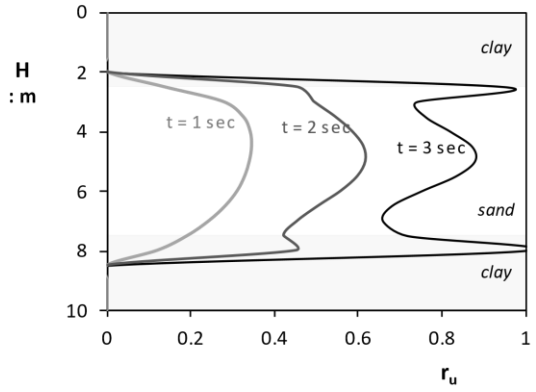

(b)

Figure 3.11. Mean effective stress *p*' time histories of the depicted profile sublayers, for a ground shaking of *t* =3s and r_u distribution with depth snapshots, at *t* =1s, 2s and 3s of shaking. Coupling term is taken into consideration according to consolidation eq. (3.61).

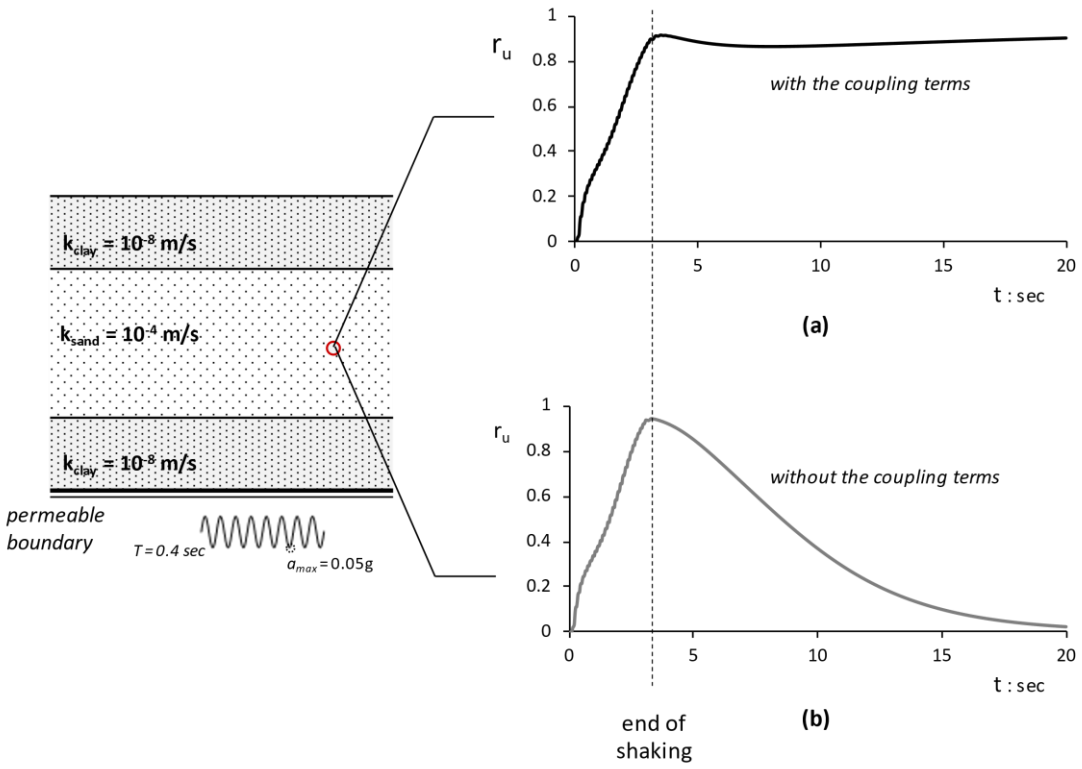

Figure 3.12. Excess pore water pressure time histories at the middle of the sand layer of the given configuration up to 20s, for 3s of ground shaking (a) including and (b) omitting the coupling term of consolidation equation (3.61).

Chapter 4

Numerical algorithm validation

4.1. Comparison with centrifuge experiments

The performance of the model is validated against experimental data from two centrifuge experiments. Hashash et al. (2015) reported on a series of tests in the centrifuge facility of the University of Colorado Boulder, investigating the nonlinear response of a soil deposit to ground shaking. A 26 m thick in prototype scale layer of #120 dry Nevada sand (388 mm thick in model scale) with an estimated relative density of approximately 60% and estimated unit weight of 15.34 kN/m^3 was installed in a flexible-shear-beam (FSB) container (Chayoomi et al., 2013) (container inner dimensions: 30.48cm × 69.85cm × 33.8cm; width × length × height, in model scale). The soil specimen was dry-pluviated into the container using a barrel hopper at a constant drop-height to achieve the aforementioned D_r and spun to a centrifugal acceleration of 77 g. Then, it was subjected to a series of one-dimensional earthquake input motions.

The instrumentation included a vertical array of horizontal linear variable displacement transducers (LVDTs), adjusted on the container frames in order to record their horizontal movement, that yielded the shear strain and the lateral displacement profiles. Additionally, three vertical arrays of accelerometers were used; the central array (6 accelerometers placed

inside the soil in the center of the container), the side array (4 accelerometers placed inside the soil close to the boundary of the container) and the box array (5 accelerometers placed externally on the container frames). Their recordings were used to estimate the PGA profile and the center array of accelerometers was also used to estimate the shear strain profile according to Zeghal et al (1995). Two LVDTs placed on the soil surface measured the surface settlement during the earthquake events. The resulting volumetric strain after the end of each excitation appeared to be relatively small. Thus, soil density is considered equal to D_r=60% in all numerical analyses included in this paper. More details regarding the experiment configuration and instrumentation and the recordings processing procedure can be found at the original publication by Hashash et al. (2015).

Table 4.1, summarizes the sand properties measured by the investigators (relative density, min and max void ratio, min and max dry unit weight) along with critical model parameters used in the analyses with Ta-Ger model. Its calibration procedure was the same as was presented in chapter 2. Equation (2.2) was applied to calculate the shear modulus at small deformations while the calibration of the rest of the model parameters was based on matching the Vucetic et. al (1991) *G:γ, ξ:γ* curves (figure 2.1 and table 2.2).

Two cases were examined, each corresponding to a different seismic excitation as input motion at the base of the container: (i) the Loma Prieta 1989 record (station name: Santa Cruz Lick Observation) and (ii) the Kobe 1995 record (station name: Takatori). The time histories of the actual records and those of the actually imposed motions at the base of the centrifuge container are contrasted in figure 4.1. The records, as derived from the Strong motion virtual data center VDC, were used as inputs for the site response analyses with the developed *p-q* version of the Ta-Ger model. Characteristic features of all acceleration time histories involved in the study are summarized in table 4.2.

The computed and measured seismic soil response by means of: (a) peak displacement, shear strain and ground acceleration profiles and (b) acceleration response spectra and corresponding Arias Intensity at ground surface are presented in figures 4.2 and 4.3, for the Loma Prieta and the Kobe Takatori input base motions respectively. Broadly, for the weakest excitation (figure 4.2), the *p-q* version of Ta-Ger reproduces the distributions satisfactorily. The model predicts more accurately the peak displacements, the maximum shear strains at shallow and large depths and the peak accelerations at mid and large depths, whereas performs less satisfactory in terms of maximum shear strain at mid-depths and peak

accelerations at shallow depths. Specifically, the top LVDT record (-2.7m) of the minimum displacement is by 10% overestimated, while a reverse picture is observed for the maximum displacement which is by 15% underpredicted. The maximum shear strain based on the ACC recording at -2.7 m (in prototype scale) is exceeded by 68% by the model. An overestimation of the peak surface acceleration by 30% is also noticed in the analysis with Ta-Ger model. Regarding the spectral accelerations at ground surface, model depresses the high-frequency components and over-predicts the long-period pulses. A considerable exaggeration in spectral accelerations is observed for periods from 0.3 s to 0.6 s approximately. The peak in spectral accelerations that appears at around 0.17s is only slightly overestimated by approximately 8%. Finally, the measured Arias intensity is reproduced with remarkable accuracy by the wave propagation algorithm.

The results for the strongest input motion are portrayed in figure 4.3. From an engineering point of view, the calculated response is within acceptable margins. It is reminded, however, that the predictability of Ta-Ger is compromised by the divergence between the used input motion and that actually imposed as base excitation in the centrifuge tests. Ta-Ger model has underpredicted the minimum and maximum displacements at -2.7m, by 28% and 37% respectively. Deviations are also observed in the PGA profile where Ta-Ger model predicts a maximum surface acceleration 22% larger than the experimental one. The maximum spectral acceleration at surface is observed in both cases at T= 1.2s and equals to 3.2g for the Ta-Ger model against 2.3g recorded at the centrifuge. Ta-Ger model systematically predicts greater spectral accelerations for a wide range of periods. Similar conclusions can be drawn from the calculated Arias intensity values which exceed the measured ones by 35%.

To better evaluate the deviations between Ta-Ger predictions and centrifuge measurements, the analyses results of several 1D site response analysis techniques, that were presented in Hashash et al. (2015) are included in this section. Specifically, the numerical tools that were used to simulate the experiments were (i) the DEEPSOIL Nonlinear, (ii) the DEEPSOIL Equivalent Linear (iii) the OpenSees Nonlinear (class C predictions) and (iv) the OpenSees Nonlinear (class C_1 predictions). A prediction is categorized as class C if it is made after the event but without knowing the results at the time the prediction is made, whereas a class C_1 prediction is made after the event and the results are known at the time of prediction (Lambe, 1973).

In Nonlinear site response analysis with DEEPSOIL, a hyperbolic constitutive model is used to describe the soil backbone response. The hysteretic behavior is modeled using the four extended unload – reload Masing rules with the modification proposed by Phillips and Hashash (2009). The soil profile was subdivided into 16, 1m-thick layers from the surface to 16m depth and five, 2m-thick layers from 16 m to 26 m depth. Taking into consideration the measured sand properties listed in table 4.1, the calibration methodology included the estimation of the shear wave velocity as the average distribution between Bardet et al. (1993) and Seed and Idriss (1970) proposed correlations. The Darendeli' s (2001) shear modulus reduction and damping curves were adopted, modified for the top layer following the procedure described by Hashash et al. (2010), to approximate the target shear strength of the soil at large strains.

The results of the nonlinear finite element site response analysis with OpenSees (Mazzoni et al., 2006) that incorporates a multiyield surface plasticity constitutive model (Elgamal et al. 2002, Parra 1996, Yang 2000), are also presented. A shear beam approach was used with 21 elements to define the 26 m soil column, following the same discretization as was decided for the analysis with DEEPSOIL Nonlinear. Several of the parameters required to execute the analysis were estimated and others were selected according to the recommendations of the OpenSees manual. The shear modulus curves were then automatically generated. The shear wave velocity profile was the same with the one that was considered in the analyses with DEEPSOIL. After comparing OpenSees prediction with the experiment measures the authors repeated the finite element analysis recalibrating certain parameters (class C_1 predictions). Whereas the soil V_s profile was maintained the same, the modulus reduction curves were updated to match the strength- corrected Darendeli' s curves used in the DEEPSOIL Nonlinear analysis, and were manually incorporated in OpenSees. The acceleration records measured at the base of the container during centrifuge testing served as input to the analyses with all the aforementioned techniques. For detailed information regarding all the site response analysis that serve as a yardstick herein and the calibration of the constitutive models employed, the reader is referred to the original publication (Hashash et. al, 2015).

Figures 4.4. and 4.5 present the comparison, in the same terms with figures 4.2 and 4.3, between the four types of analyses executed by Hashash et al (2015), the centrifuge experiment measures and the predictions of Ta-Ger model, for the Loma Prieta and the Kobe Takatori base motions, respectively. For the majority of the examined parameters, models

perform well during the Loma Prieta motion. Maximum displacements are in accordance with the centrifuge experiments as well as the minimum displacements predicted by Ta-Ger model, DEEPSOIL Equivalent Linear and OpenSees - class C. The maximum shear strain profiles predicted by all numerical models is in very good agreement with the LVDT and the ACC measures below 9m, except for the Ta-Ger model which overpredicts the response between 17m and 6m depth. However, above 9m DEEPSOIL Nonlinear and DEEPSOIL Equivalent linear considerably overpredict the response. The predictions of the PGA values of DEEPSOIL Non linear are very competent along the whole soil profile, while Ta-Ger model and DEEPSOIL Equivalent Linear perform very well from the column base up to 6m. The exaggeration of the surface spectral accelerations between 0.3s and 0.6s approximately that was observed in the analysis with Ta-Ger model is also reproduced by the DEEPSOIL Equivalent Linear and the OpenSees - class C, and less significantly by the DEEPSOIL Non Linear and the OpenSees – class C_1 models. Finally, the biggest deviations from the experimental Arias Intensity values are observed for the OpenSees – class C model, in contrast to the DEEPSOIL Non Linear and Ta-Ger remarkable performance.

For the strongest base excitation, comparisons depicted in Figure 4.5 evince that while DEEPSOIL Non Linear and Equivalent Linear perform better than the rest models in terms of maximum and minimum displacements, they greatly overpredict the near-to-surface maximum shear strains. The same trend was observed for the case of the weakest excitation. DEEPSOIL Non Linear and Ta-Ger model present the smallest deviations from the experimental values for the PGA profile, except for the PGAs at shallow depths that are slightly overpredicted by Ta-Ger. It is interesting, that all five models generally predicted greater Arias Intensity values and in the most cases greater surface spectral accelerations than the experimentally recorded, with DEEPSOIL Non Linear, OpenSees – class C_1 and Ta-Ger models having the most accurate predictions. The last-mentioned parameters obtained from the OpenSees Class C_1 analysis improved noticeably compared to the Class C predictions.

Accordingly to what has been presented in Hashash et al. 2015, numerical predictions against experimental measures are evaluated in terms of residual values, calculated for each parameter according to the following:

$$Residual\ X = \log\left(\frac{X_{measured}}{X_{predicted}}\right)$$

$Residual\ X < 0$: Underestimation

$Residual\ X > 0$: Overestimation

where X refers to a given response parameter of interest. Figures 4.6 and 4.7 depict the residuals of the maximum and minimum displacements, maximum shear strains, PGAs, surface spectra and Arias intensity values for the Loma Prieta and the Kobe Takatori base motions respectively, for the five presented ground response analysis techniques. In general, Ta-Ger model appears to be consistently in good agreement with the centrifuge measurements compared to the rest models employed, for all the examined parameters, except for the case of the maximum displacements at the strong earthquake motion (Figure 4.7), where Ta-Ger presents the maximum deviations between -6m and -13m approximately. Considerably competent performance is provided by the DEEPSOIL Non Linear model especially for the Arias Intensity values, while the DEEPSOIL Equivalent Linear shows relatively large deviations from the experimental measurements, especially for the strong earthquake motion, a performance within expectations. The overestimation of the surface spectral accelerations and Arias intensity values by OpenSees - Class C predictions that implied a stiffer soil response, was mildly attenuated by the modification of the modulus reduction curves, as is shown by the class C_1 analyses results. Deviations between Ta-Ger and the other models could be attributed to the fact that, besides their different mathematical formulation, the two approaches complied with the soil properties measured at the laboratory (D_r, e_{min}, e_{max}, $\gamma_{d\,min}$, $\gamma_{d\,max}$) but followed different calibration methodologies, adopting different V_s correlations and shear modulus reduction and damping curves available in the literature. Furthermore, as has already been mentioned, the numerical analyses with Ta-Ger were executed using two slightly different base excitations, since the actual centrifuge base records that were used in the numerical analysis executed by Hashash et al. (2015) were not available. It is pointed out, however, that the authors' scope is not to make a comparison between the models, but to provide the reader a yardstick to evaluate the magnitude of deviations between the Ta-Ger predictions and experimental results.

Finally, the stress-strain hysteretic loops computed with Ta-Ger model at two depths of 4m and 17m are portrayed in figure 4.8 for both base excitations. High non-linear response is observed in the case of the strong base motion of Kobe Takatori. In this case, the loops are much broader evincing the substantial amount of the dissipated energy associated with double-amplitude mobilized shear strength.

4.2. Validation against the case history of Port Island

4.2.1. Analysis of the case history

The developed model is further used to predict the seismic response of a site at the northern area of Kobe's Port island (Iwasaki, 1996), in the 1995 earthquake (figure 4.9). During the Hyogo-ken nanbu earthquake a vertical array of instruments recorded the shaking at 0m, -16m, -32m and -83m. The detailed geotechnical investigation carried out before and after the event along with the seismographic instrumentation that recorded the shaking provide a benchmark for testing the validity of the developed wave propagation algorithm.

The boring log for the borehole where the vertical array was installed is shown in figure 4.10 along with the standard penetration blow counts and the shear wave velocity distribution, after P-S logging that was carried out at the field. The water table was found at -3m. The shear modulus distribution considered in the analysis is also depicted in the same figure. Table 4.3 summarizes characteristic soil properties along with associated borehole depths at the location of the seismographic array. They were either estimated based on empirical correlations or drawn directly from the literature. The idealized soil profile was sectioned in 9 layers. Soil characterization, *P* and *S* wave velocity profiles are according to Iwasaki (1995) and the associated shear modulus distribution are according to:

$$G_{max} = \rho \, V_S{}^2 \tag{4.1}$$

in which the soil density ρ is calculated according to the saturated specific weight listed in the same table (20kN/m^3 for sandy soils and 18kN/m^3 for clays). The $(N_1)_{60}$ values of the standard penetration blow counts distribution of figure 4.10 are employed in equation 2.20 to calculate the relative density D_r for each sandy soil layer. The undrained shear strength of the clayey layers # *4* and *# 8* is estimated according to Weiler (1988), who provided the undrained strength measured in CU triaxial compression tests, depending on the plasticity index and the over-consolidation ratio. For the specific layers an *OCR* equal to 1 and a *PI* equal to 25 were assumed. Ground response analysis was executed assuming: (i) undrained loading conditions for all soil layers, apart from the gravelly layers *# 1* and # *2* at near surface level for which fully drained conditions were considered. Reclamation layers #1 and #2, according to the literature, consisted of sandy gravel soil of high permeability and very low estimated strength. (ii)

Consolidation conditions during shaking, according to what has been presented in chapter 3. Permeability *k* was estimated according to soil type and was assumed $k=10^{-4}$ m/s for the close to surface reclamation soil, $k=10^{-6}$ m/s for sand/ gravelly sand and $k=10^{-9}$ m/s for the alluvial clay (Table 4.3). Model base at -83m is considered a permeable boundary. The model parameters for all layers (clays and sands) were calibrated against the Ishibashi and Zhang (1993) shear modulus reduction and damping curves, while the undrained response of sand was based on the Idriss (1995) *MSF* curve (table 2.2).

Figures 4.11, 4.12 and 4.13 provide comparison between seismographic instrumentation records and model results for the two aforementioned approaches of drainage conditions. It can be concluded, that the convergence with the measured response is broadly sufficient for engineering accuracy, excluding certain cases, while divergence between numerical results considering consolidation or undrained conditions is generally negligible. Specifically, Figure 4.11 shows comparison between recorded motions at the ground surface, -16m, -32m and -83 m and calculated response Except for the case of -16m, where the model has significantly underestimated the response, the agreement is satisfactory. Specifically, PGAs equal to 3.34 m/s^2 and 2.63 m/s^2 were predicted at the surface for drainage conditions (i) and (ii) respectively, against the recorded 3.41 m/s^2, 2.20 m/s^2 and 2.75 m/s^2 were predicted against the recorded 5.65 m/s^2 at -16m and 4.34 m/s^2 and 4.47 m/s^2 against 5.44 m/s^2 at -32m. One can observe that according to the records, accelerations are strongly de-amplified at the ground surface level which is remarkably reproduced by the model. According to Iwasaki (1995), the reclaimed fill material in the Port island at the depth of -19m (the base of the sandy soil layer *#3* in the analysis) is believed to have liquefied and the liquefaction caused de-amplification of the higher frequency components. The fact that liquefaction must have occurred at the field was also supported by the measured pore water pressure profile at a site of similar geological conditions that is located south of the area of the seismographic array. In this area, the pore pressure measurements in the alluvial sand layer (which is considered to be similar to the one designated as layer *# 5* in the studied profile) indicated that liquefaction probably took place at this layer also. Furthermore, according to Yamazaki et al. (1995) who analyzed the seismic response of the site, liquefaction may have had occurred in both the layer at -27 to -33m depth and in the loose sandy layer above the alluvial clay at -10 to -16m.

The acceleration response spectra of Figure 4.12, present in all three cases an amplification of the low frequency components and a maximum spectral acceleration of about 1g, for periods

between 1 and 1.5 second. The “weak” response of the surface along with the amplification of the low frequency spectral accelerations, evince an intense non-linear response, conceivably accompanied by liquefaction phenomena.

Figure 4.13 portrays the numerical results for the two types of analysis, in terms of distributions with depth of the peak values of acceleration, horizontal displacement, shear stress, shear strain and pore water pressure ratio. Both analyses predict that liquefaction took place to the sandy layers #3 and #5, with values of $r_{u,max}$ close to unity, associated with large shear strains (of the order of 4 % to 5%). While the response predicted by the two different approaches is generally very similar, the simulation of the actual permeability of the surface gravelly layers, instead of considering drained conditions for the same layers that fundamentally prohibit the development of the r_u, allow the excess pore pressure generated to the lower sandy layers (with $r_{u,max}$ very close to unity) to dissipate up to the surface. This is illustrated in the near to surface maximum r_u distribution, where very high r_u values are observed, consequently leading to increased shear strains and displacements at the same depths. According to Elgamal et al. (1997), the soil behaved quasi linearly below -32m with limited reduction in stiffness, which is in agreement with the present analysis since displacements are accumulated in shallow depths, above -30m approximately.

Finally, Figure 4.14 shows comparison between the two types of analysis in terms of shear stress-strain loops at -10m and -16m. The left figures (undrained conditions except for layers #1 and #2 where drained conditions were considered) are indicative of liquefaction only for the case of gravelly sand (z=-16m) with the gravel (z=-10m) responding almost linearly, whereas the right figures, that correspond to consolidation conditions, denote that the surface layers were affected by the dissipated pore pressures.

4.2.2. Sensitivity analysis

To investigate in more detail how the diffusion of the excess pore water pressure is performed by the model, the seismic response of Port Island site in the 1995 Kobe earthquake is presented in terms of the evolution with time of the mean effective stress, developed in each soil sub-layer. Along with the original configuration as was considered in the previous paragraph (case #1), three alternative cases are examined (Table 4.4) for different permeability conditions. Each layer is designated with a different color, according to the first column of Table 4.4. Each soil profile is subdivided into 83, 1m-thick sub-layers.

In accordance with the $r_{u,max}$ distribution of Figure 4.13, the highest values of the excess pore pressure were accumulated in layers #3 and #5, as is denoted in Figure 4.15a by the corresponding curves of p' that tend to zero at approximately 5s and 10s of shaking, respectively. The effective stress of #2 layer is also decreased to zero, following almost the same pattern with its underlaying layer. The clayey layers #4 and #8 undergo practically zero decrease of the effective stress, since no pore pressure is assumed to be generated in the clayey layers and their very small permeability (k=10^{-9} m/s) prevents the drainage within them. A very modest decrease in p' is observer for the deeper sandy layers #6, #7 and #9 most likely due to their significantly high relative density (Table 4.3). Figure 4.16 provides the evolution of p' up to 30s. Since the earthquake motion lasts only 12s, after the end of shaking no more pore pressures are generated and the already developed pressures are diffused within the soil layers. According to figure 4.16a, the relatively small permeability of the surface layers #1 and #2 causes a slow increase of p' of the liquified soil up to 19m.

In case #2 of Table 4.4, a profile with permeability k=10^{-1} m/s for the first two surface layers is examined. Compared to case #1, it is observed that the response is quite similar up to 12s (Figure 4.15b), though it is observed that due to the greater permeability of the surface layers the post-earthquake rate of pore-pressure dissipation is more prominent in case #2. In case #3, the increased permeability of the deeper layers (#4 to bottom) allows for the pressures of the liquified sand #5 to dissipate rapidly within its underlying layers, which is designated by the disturbance of the effective stress propagated to the deeper layers (Figures 4.15c and 4.16c).

It would be interesting to identify, whether the decrease of the effective stress of layers #1 and #2 is caused by the pressures generated inside these layers (sandy soil of very low D_r) or they are affected by the dissipation up to the surface of the pressures generated in the underlain liquified layer #3. Thus, case #4 is examined, where the first two surface sandy layers are replaced with clayey soil, in which pore pressures are not generated due to cyclic loading. The permeabilities of the soil layers are the same as in case #1. Figures 4.15d and 4.16d suggest that these layers are affected by the dissipated pressures of the underlaying liquefied layer, but the decrease of p' is milder. Consequently, it can be deduced that both processes (dissipation and generation) of pore water pressure evolution contribute to the resultant response.

References

Bardet J.P., Huang Q., Chi S.W. (1993) Numerical prediction Model No1. Paper Presented at the Proceedings of the international conference on the verification of numerical procedures for the analysis of soil liquefaction problems. U.C. Davis, USA, 17–20 October; 1993.

Darendeli, M. B. (2001). *Development of a new family of normalized modulus reduction and material damping curves*. The university of Texas at Austin.

Elgamal, A., Yang, Z., & Parra, E. (2002). Computational modeling of cyclic mobility and post-liquefaction site response. *Soil Dynamics and Earthquake Engineering*, *22*(4), 259-271.

Elgamal, A. W., Zeghal, M., & Parra, E. (1997). Identification and modeling of earthquake ground response. In *Earthquake Geotechnical Engineering* (pp. 1369-1406).

Ghayoomi, M., Dashti, S., & McCartney, J. S. (2013). Performance of a transparent Flexible Shear Beam container for geotechnical centrifuge modeling of dynamic problems. *Soil Dynamics and Earthquake Engineerin 53*, 230-239.

Hashash, Y. M., Dashti, S., Romero, M. I., Ghayoomi, M., & Musgrove, M. (2015). Evaluation of 1-D seismic site response modeling of sand using centrifuge experiments. *Soil Dynamics and Earthquake Engineering*, *78*, 19-31.

Hashash, Y. M., Phillips, C., & Groholski, D. R. (2010, May). Recent advances in non-linear site response analysis. In *5th International Conference on Recent Advances in Geotechnical Earthquake Engineering and Soil Dynamics* (No. 4).

Idriss, I. M. (1995). Seed memorial lecture. *University of California at Berkeley (IM Idriss, personal communication to TL Youd, 1997)*.

Ishibashi, I., & Zhang, X. (1993). Unified dynamic shear moduli and damping ratios of sand and clay. *Soils and foundations*, *33*(1), 182-191.

Iwasaki, Y. (1995). Geological and geotechnical characteristics of Kobe area and strong ground motion records by 1995 Kobe earthquake. *Tsuchi to kiso*, *43*(6), 15-20.

Iwasaki, Y., & Tai, M. (1996). Strong motion records at Kobe port island. *Soils and foundations*, *36*(Special), 29-40.

Lambe, T. W. (1973). Predictions in soil engineering. *Géotechnique*, *23*(2), 151-202.

Mazzoni, S., McKenna, F., Scott, M. H., & Fenves, G. L. (2006). OpenSees command language manual. *Pacific Earthquake Engineering Research (PEER) Center*, *264*, 137-158.

Parra-Colmenares, E. J. (1996). *Numerical modeling of liquefaction and lateral ground deformation including cyclic mobility and dilation response in soil systems* (Doctoral dissertation, Rensselaer Polytechnic Institute).

Phillips, C., & Hashash, Y. M. (2009). Damping formulation for nonlinear 1D site response analyses. *Soil Dynamics and Earthquake Engineering*, *29*(7), 1143-1158.

Seed, H. B. (1970). Soil moduli and damping factors for dynamic response analysis. *EERC*.

Vucetic, M., & Dobry, R. (1991). Effect of soil plasticity on cyclic response. *Journal of geotechnical engineering*, *117*(1), 89-107.

Weiler Jr, W. A. (1998). Small strain shear modulus of clay. *Earthquake Engineering and Soil Dynamics, Recent Advances in Ground-Motion Evaluation*, 331-345.

Yamazaki, F., Ansary, M. A., & Towhata, I. (1995). Application of a dynamic effective stress model at a reclaimed site during the Great Hanshin earthquake, 1995. *Earthquake Geotechnical Engineering, IS TOKYO*, *95*, 591-597.

Yang, Z. (2000). *Numerical modeling of earthquake site response including dilation and liquefaction*. Columbia University.

Zeghal, M., Elgamal, A. W., Tang, H. T., & Stepp, J. C. (1995). Lotung downhole array. II: Evaluation of soil nonlinear properties. *Journal of geotechnical engineering*, *121*(4), 363-378.

Figures

Table 4.1. Measured properties of Nevada Sand used in the centrifuge experiment (Hashash et al., 2015) and estimated sand properties used in the analyses with Ta-Ger model.

Variable	**Value**	**Unit**
Measured sand properties		
Relative density, D_r	0.6	-
Minimum void ratio, e_{min}	0.586	-
Maximum void ratio, e_{max}	0.852	-
Minimum dry unit weight, $\gamma_{d,min}$	14	kN/m³
Maximum dry unit weight, $\gamma_{d,max}$	16.39	kN/m³
Estimated sand properties used in the analysis		
Low strain shear modulus, G_{max}	equation [2.2]	
Bulk modulus, K_{max}	elastic relashionship G_{max} - ν	
Poisson's ratio, ν	0.25	-
η	cal. ag. Vucetic et. al (1991)	
n	cal. ag. Vucetic et. al (1991)	
Dry unit weight, γ_d	16	KN/m³
Dry density, ρ_d	1.63	Mg/m³
Relative density, D_r	as measured	
Minimum void ratio, e_{min}	as measured	
Maximum void ratio, e_{max}	as measured	
Critical state friction angle, φ_{cs}	32	degrees
Dynamic analysis properties		
time step	10^{-3}	s
height step	0.5	m
viscoelastic constant c	200	t / (m·s)

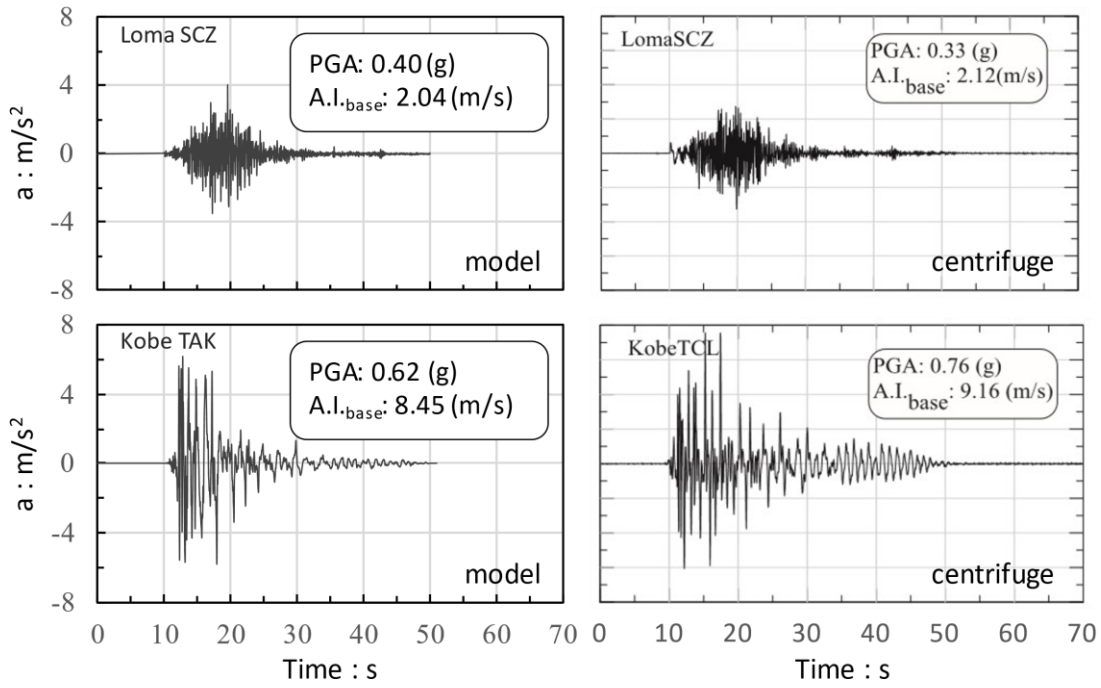

Figure 4.1. Acceleration records used in the analyses (data from Strong motion virtual data center *VDC*) [left] in comparison with recorded container base motions [right].

Table 4.2. Properties of the ground motions used as input into the analyses in comparison with corresponding variables of the recorded container base motions.

	Loma Prieta SCLO		***Kobe Takatori***	
	Centrifuge	*Analysis*	*Centrifuge*	*Analysis*
PGA (g)	0.33	0.40	0.76	0.62
T_p (s)	0.16	0.16	0.4	0.18
AI (m/s)	2.12	2.04	9.16	8.45
D_{5-95} (s)	11.34	9.7	25.78	9.93

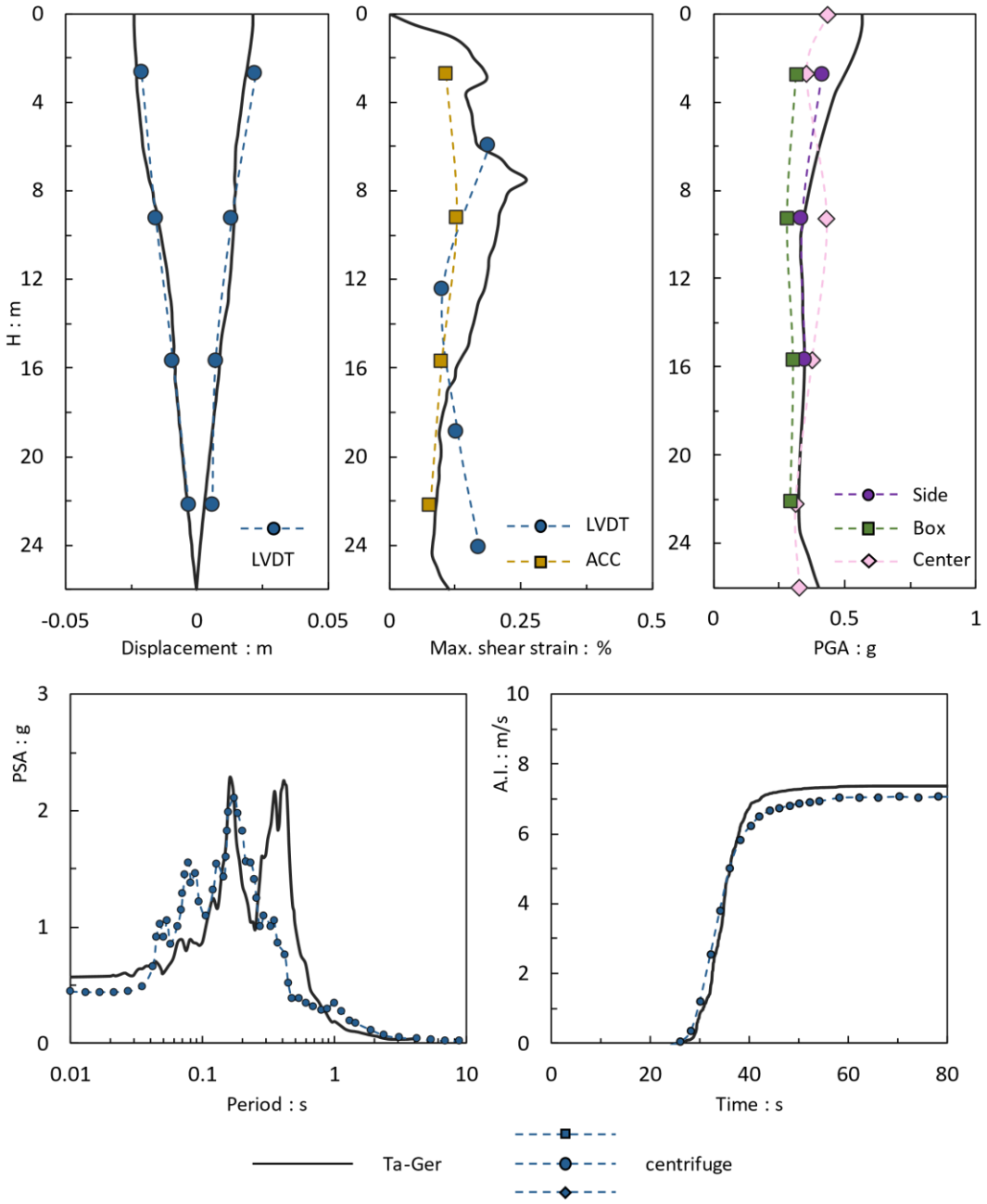

Figure 4.2. Centrifuge measurements against Ta-Ger model predictions (base excitation: Loma Prieta).

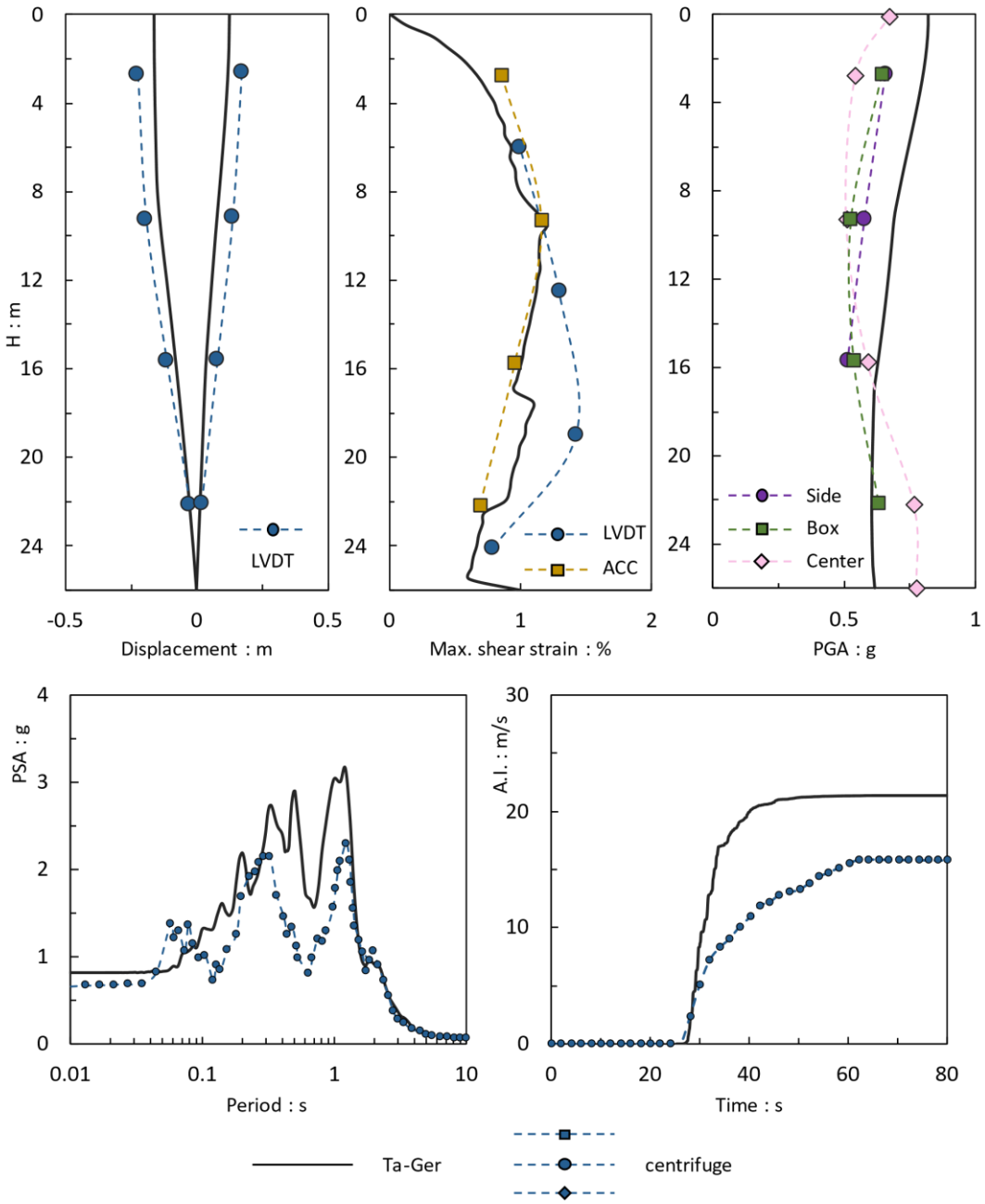

Figure 4.3. Centrifuge measurements against Ta-Ger model predictions (base excitation: Kobe Takatori).

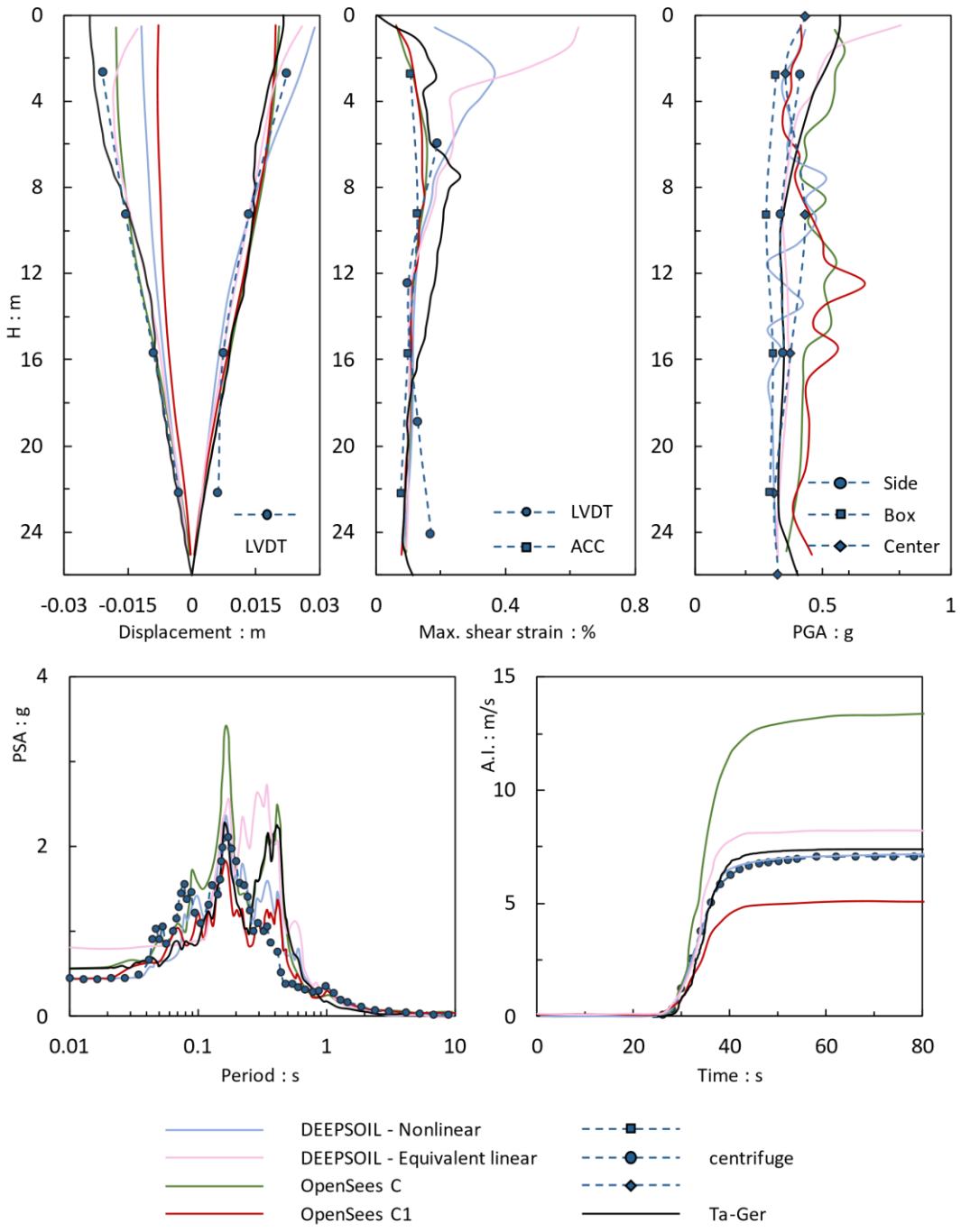

Figure 4.4. Centrifuge measurements against Ta-Ger model predictions (base excitation: Loma Prieta).

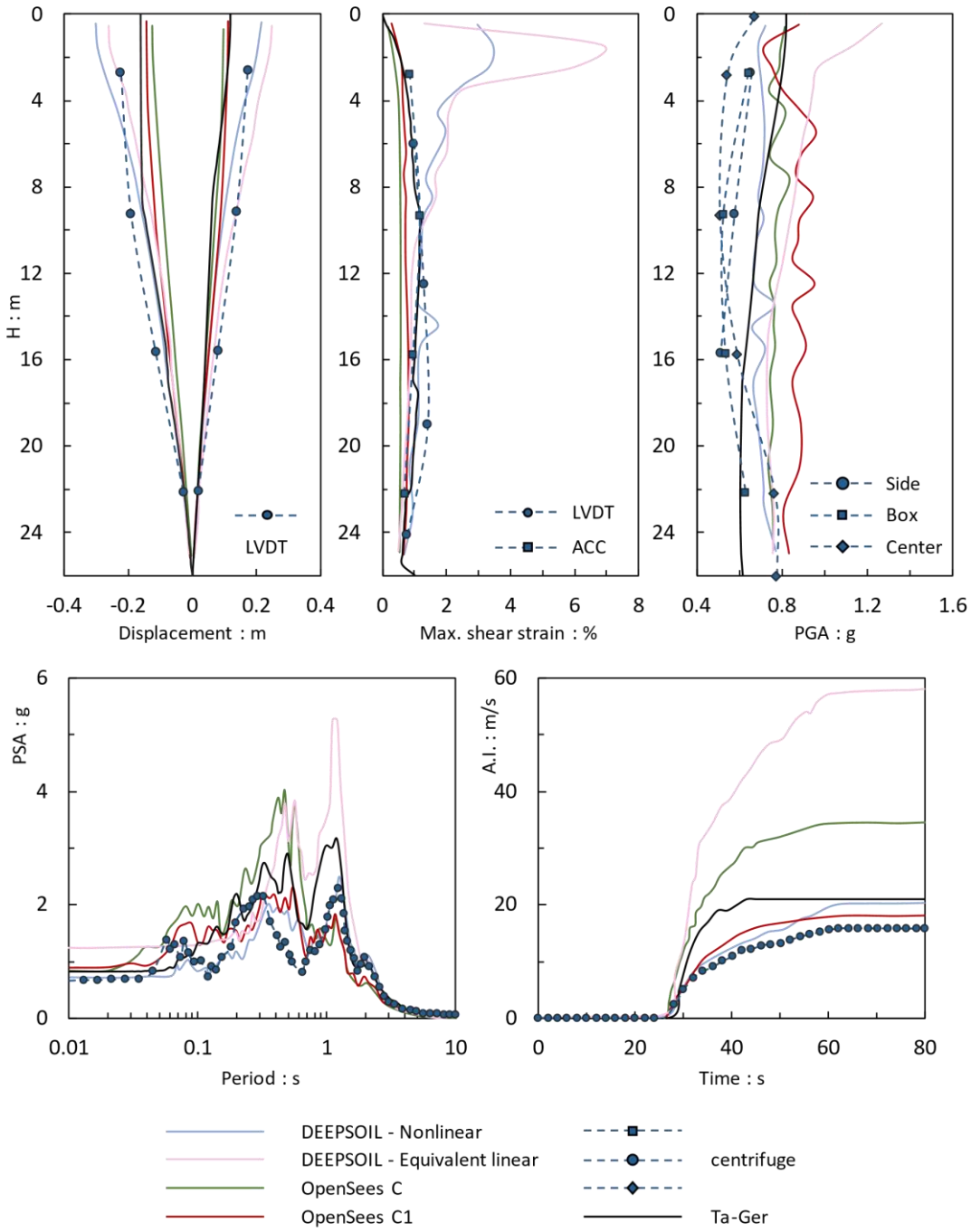

Figure 4.5. Centrifuge measurements against Ta-Ger model predictions (base excitation: Kobe Takatori).

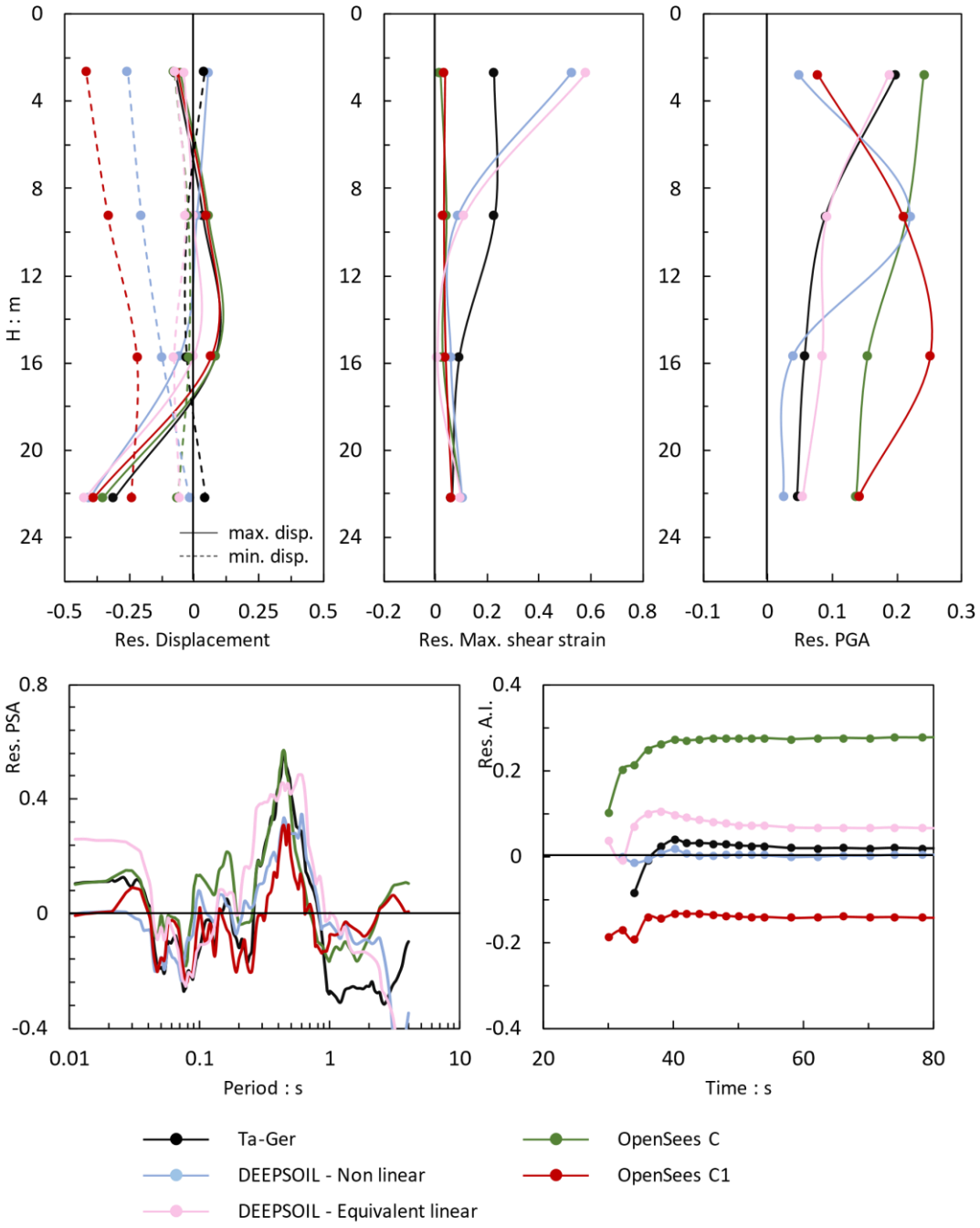

Figure 4.6. Centrifuge measurements against Ta-Ger model predictions (base excitation: Loma Prieta).

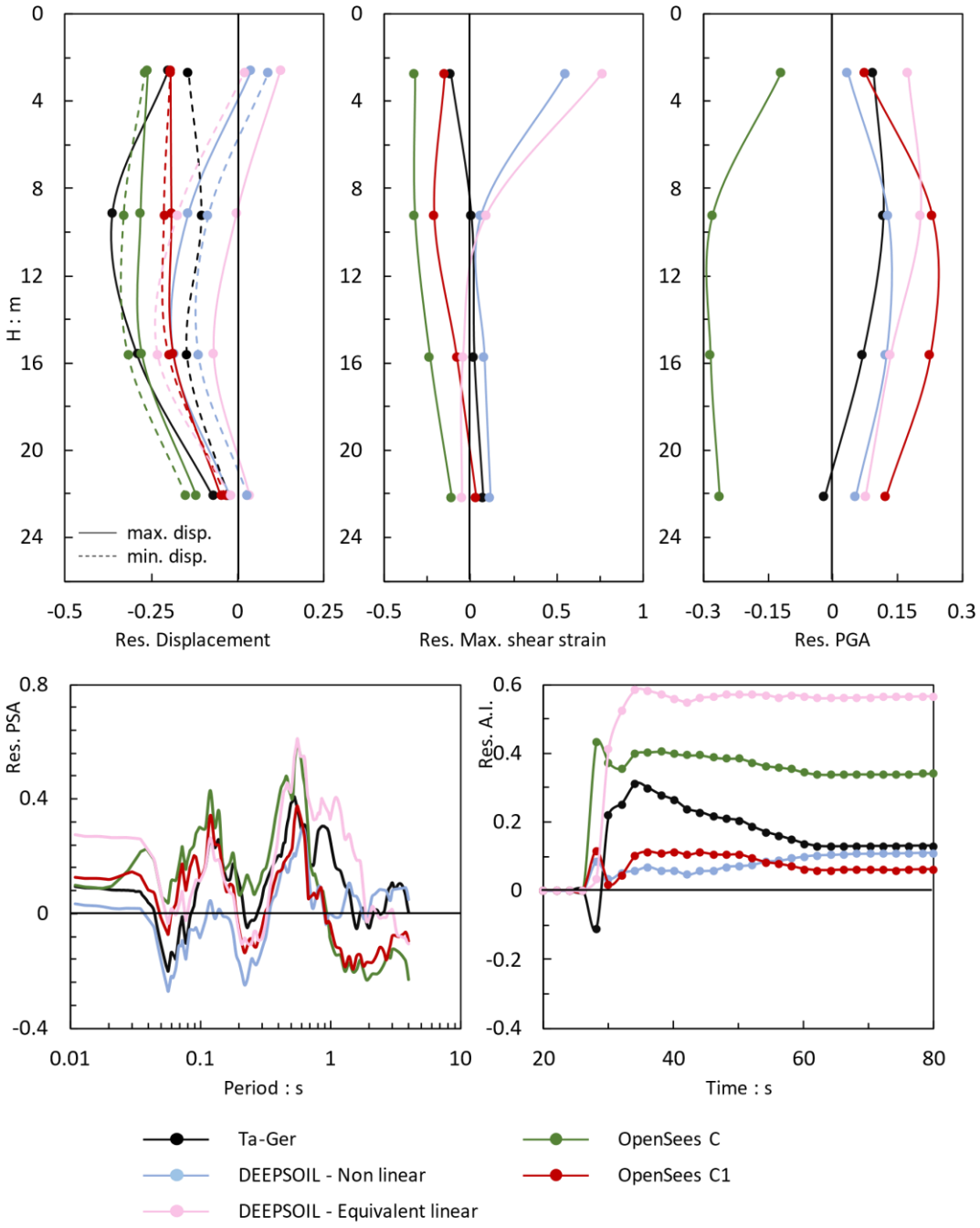

Figure 4.7. Centrifuge measurements against Ta-Ger model predictions (base excitation: Kobe Takatori).

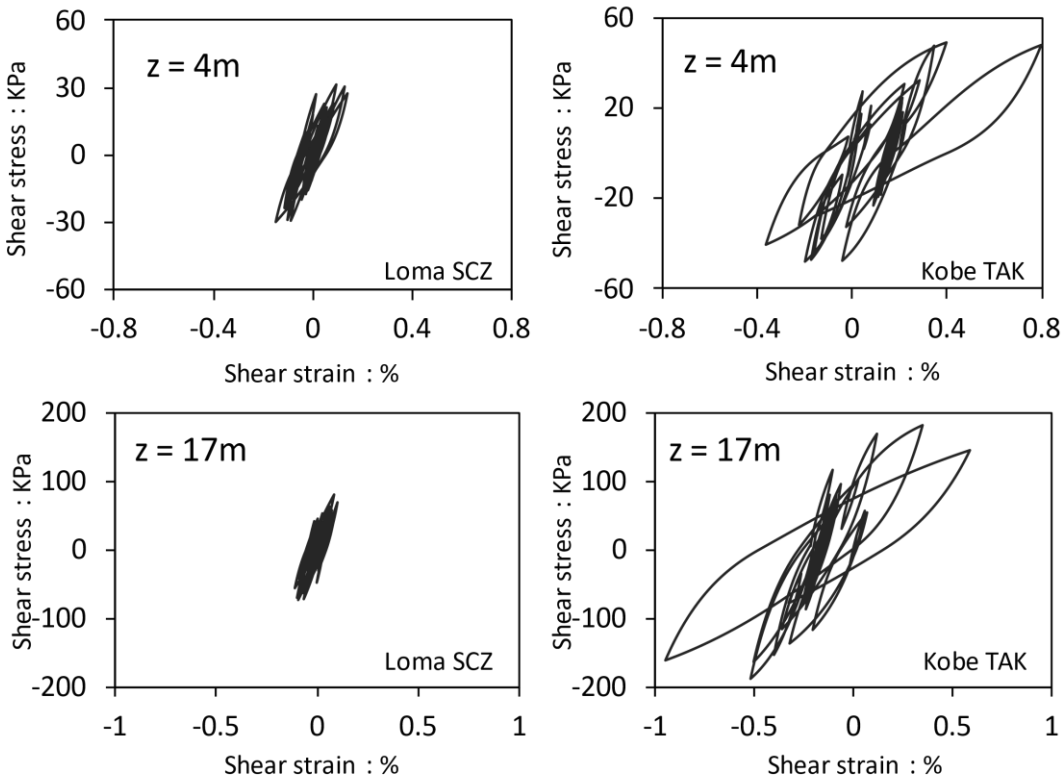

Figure 4.8. Shear stress – strain loops computed with Ta-Ger model at z=4m and z=17m (base excitation: Loma Prieta Santa Cruz [left] and Kobe Takatori [right]).

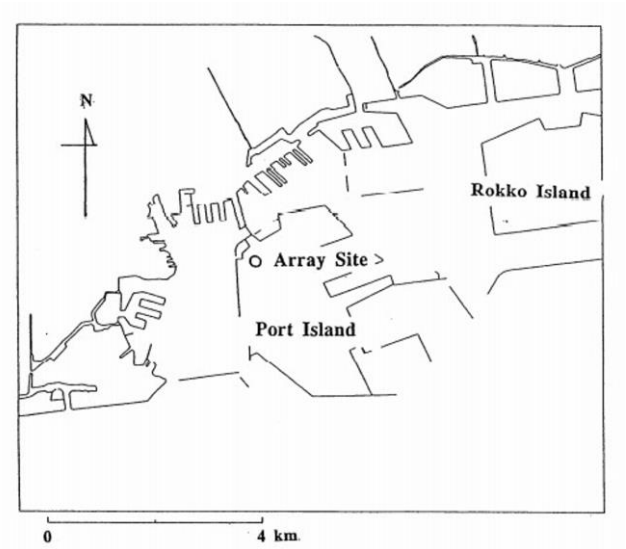

Figure 4.9. The location of record site at Kobe Port Island (after Iwasaki and Tai, 1996).

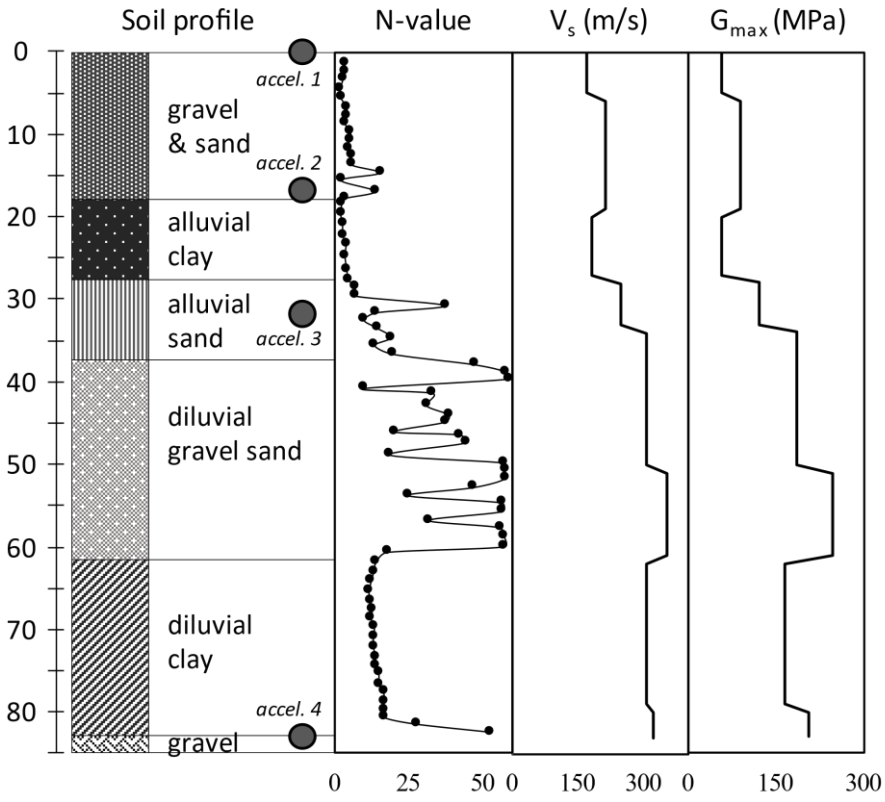

Figure 4.10. Soil profile, SPT values of the borehole and V_s distribution by PS logging (after Iwasaki, 1995) and estimated initial shear modulus distribution used in the analysis.

Layer #	Depth (m)	Soil Type	V_p (m/s)	V_s (m/s)	$(N_1)_{60}$	D_r	G_{max} (KPa)	S_u (KPa)	γ_{sat} (KN/m^3)	k (m/s)
1	0-5	Gravel*	305	170	4	0.29	57.8	-	20	10^{-4}
2	5-13	Gravel*	780	210	4	0.29	88.2	-	20	10^{-4}
3	13-19	Gravelly sand	1480	210	6	0.36	88.2	-	20	10^{-4}
4	19-27	Alluvial clay	1180	180	-	-	58.32	82	18	10^{-9}
5	27-33	Sand	1350	245	25	0.74	120.1	-	20	10^{-6}
6	33-50	Sand / Gravelly Sand	1530	305	40	0.93	186.1	-	20	10^{-6}
7	50-61	Sand	1610	350	45	0.99	245.0	-	20	10^{-6}
8	61-79	Stiff alluvial clay	1610	303	-	-	165.3	233	18	10^{-9}
9	79-83	Gravelly sand	2000	320	60	1.00	204.8	-	20	10^{-6}

Table 4.3. Discretization of soil layers: velocity of *P* and *S* waves by PS-logging [boring log at the site, K.P.: Kobe Peil (Reference level for marine work in Kobe)] and standard penetration blow counts (*N* values) (Iwasaki, 1995). Calculated / estimated values of relative density D_r, elastic shear modulus G_{max}, undrained shear strength S_u, saturated specific weight γ_{sat} and permeability k are also listed (*reclamation soil: sandy gravel soil of high permeability and very low estimated strength).

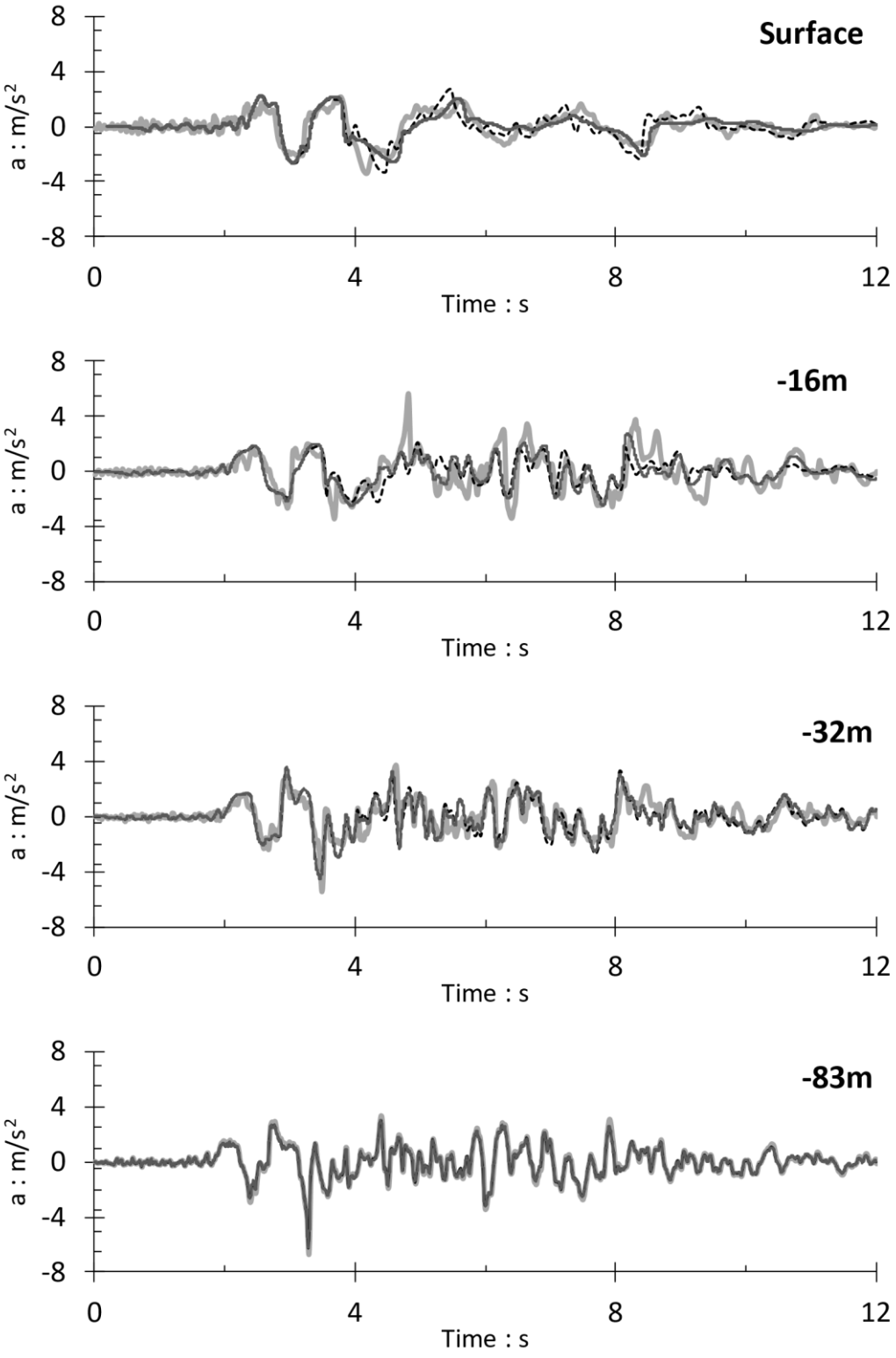

Figure 4.11. Recorded motions of NS component at Kobe Port Island against model predictions assuming consolidation conditions and undrained loading conditions during shaking, at the surface, -16m, -32m and -83m.

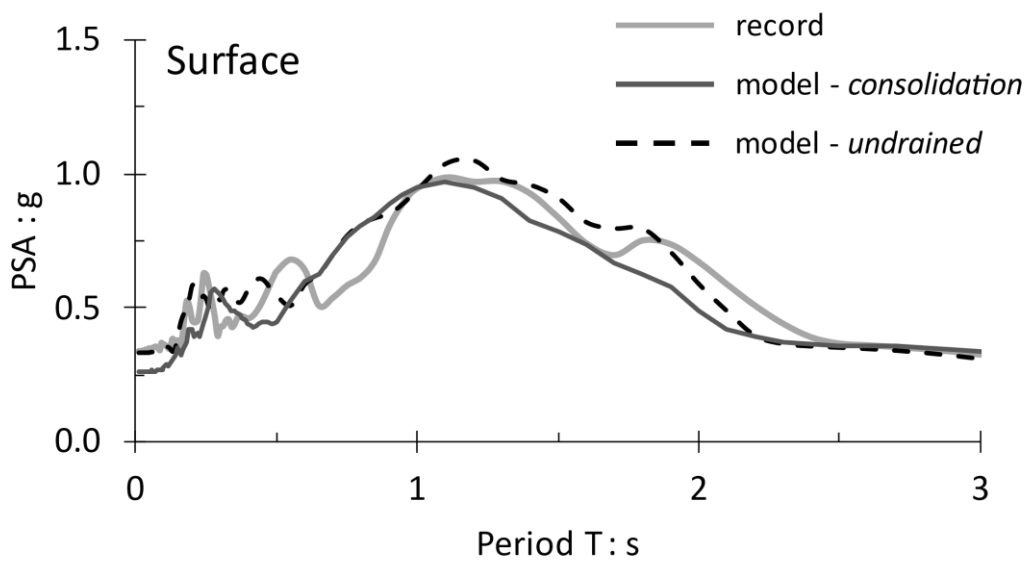

Figure 4.12. Recorded acceleration spectrum of NS component at Kobe Port Island at the surface, against model predictions assuming consolidation conditions and undrained loading conditions during shaking.

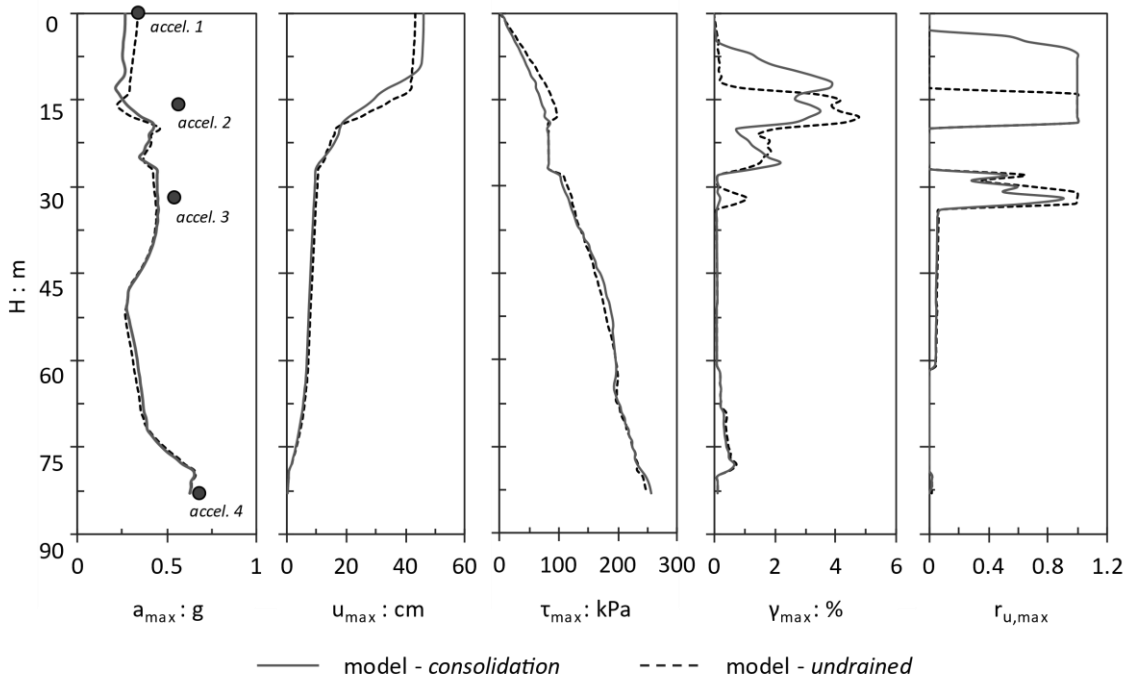

Figure 4.13. Distributions with depth of the peak values of acceleration, pore pressure ratio, shear strain, shear stress and displacement, predicted assuming consolidation conditions and undrained loading conditions during shaking (base excitation: NS component at Kobe Port Island).

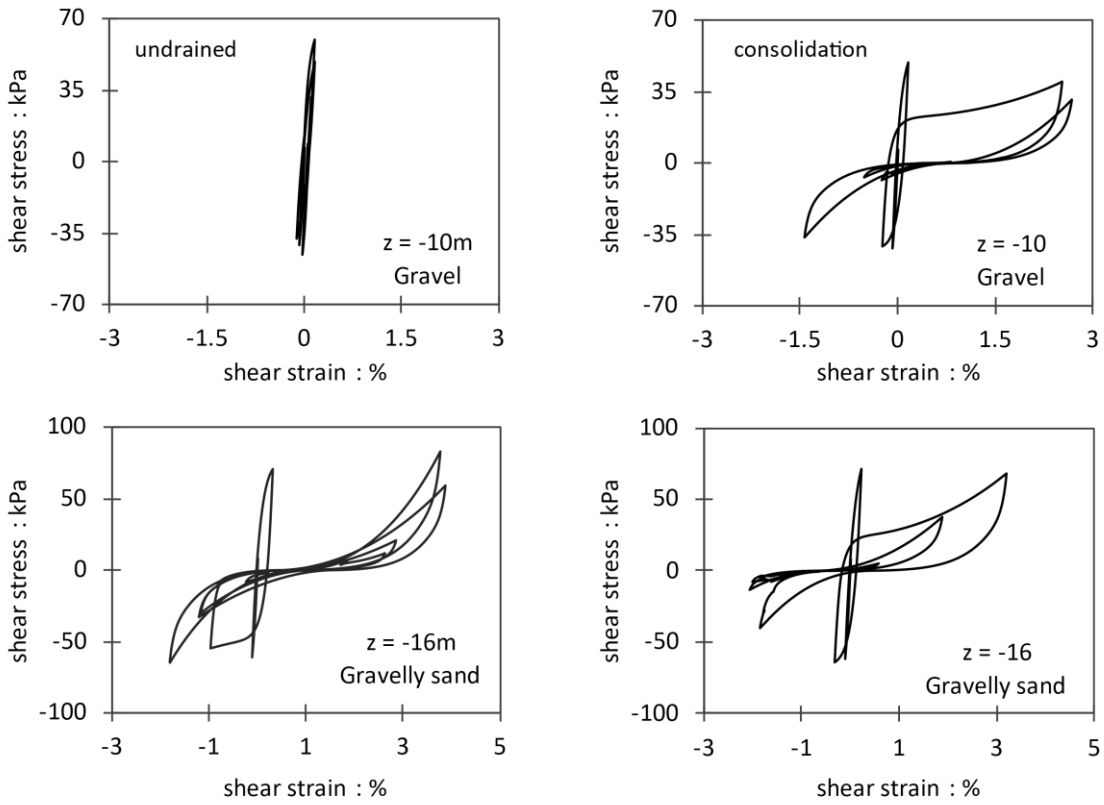

Figure 4.14. Shear stress – strain loops computed with Ta- Ger model at z = -10m and z = -16m assuming consolidation conditions [right] and undrained loading conditions during shaking [left] (base excitation: NS component at Kobe Port Island).

Table 4.4. Alternative examined profiles of the Port Island site in the 1995 Kobe earthquake.

Layer #	Depth from surface (m)	case #1		case #2		case #3		case #4	
		soil type	k (m/s)	soil type	k (m/s)	soil type	k (m/s)	soil type	k (m/s)
1	0-5	sand	10^{-4}	sand	10^{-1}	sand	10^{-1}	clay	10^{-4}
2	5-13	sand	10^{-4}	sand	10^{-1}	sand	10^{-1}	clay	10^{-4}
3	13-19	sand	10^{-4}	sand	10^{-4}	sand	10^{-4}	sand	10^{-4}
4	19-27	clay	10^{-9}	clay	10^{-9}	clay	10^{-6}	clay	10^{-9}
5	27-33	sand	10^{-6}	sand	10^{-6}	sand	10^{-4}	sand	10^{-6}
6	33-50	sand	10^{-6}	sand	10^{-6}	sand	10^{-4}	sand	10^{-6}
7	50-61	sand	10^{-6}	sand	10^{-6}	sand	10^{-4}	sand	10^{-6}
8	61-79	clay	10^{-9}	clay	10^{-9}	clay	10^{-6}	clay	10^{-9}
9	79-83	sand	10^{-6}	sand	10^{-6}	sand	10^{-4}	sand	10^{-6}

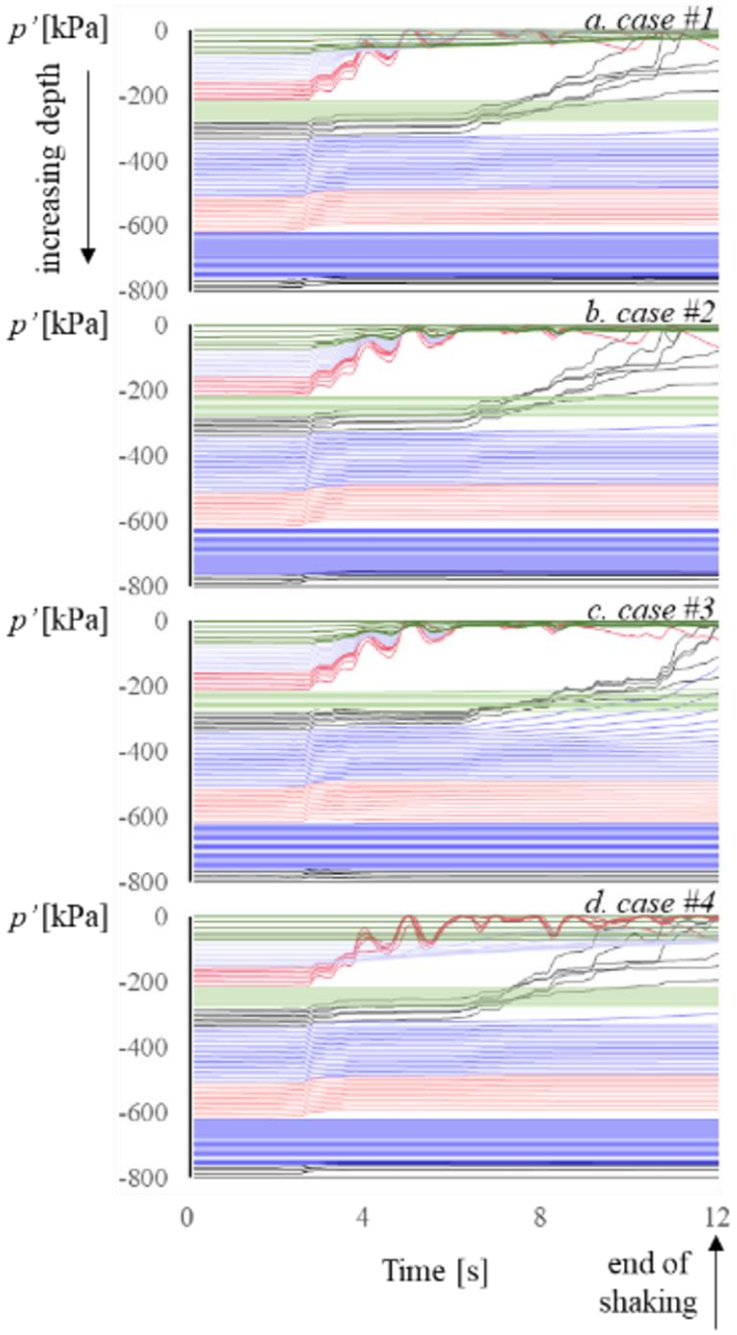

Figure 4.15. Evolution of the mean effective stress *p'* for the four profiles listed in Table 4.4, for 12s of earthquake shaking.

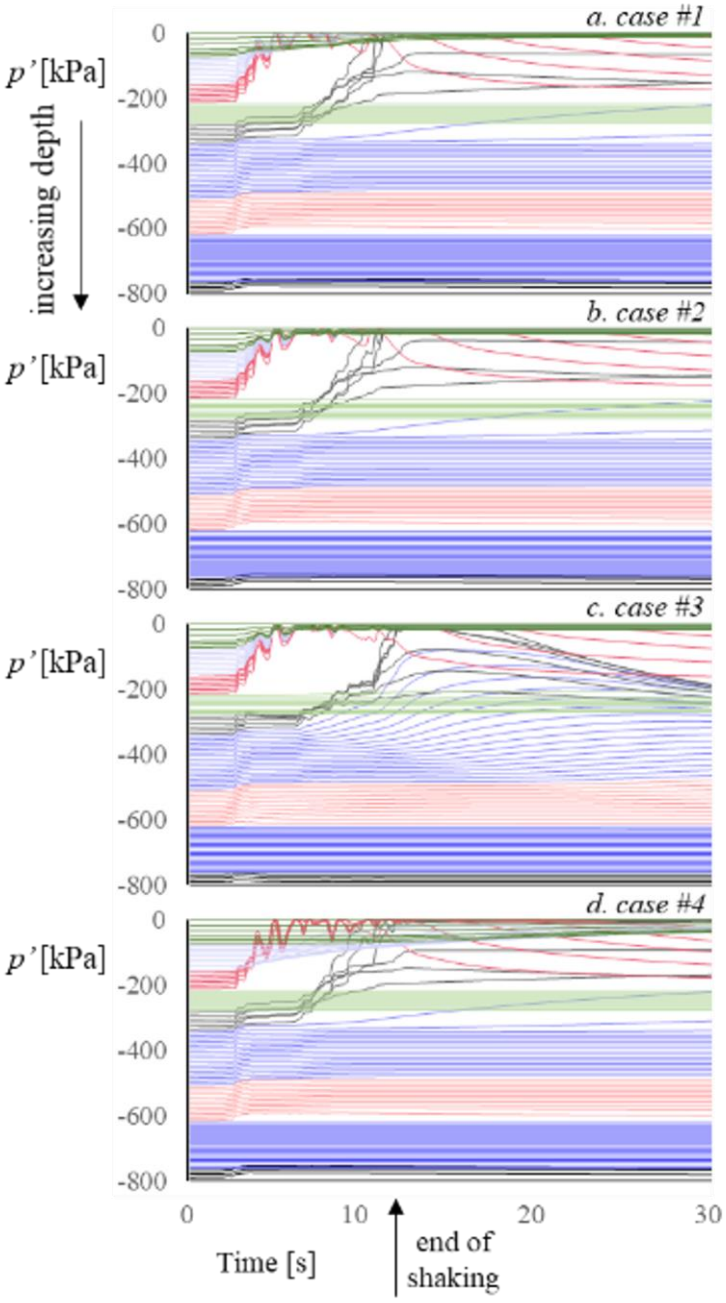

Figure 4.16. Evolution of the mean effective stress *p'* for the four profiles listed in Table 4.4 extended to 100s, for 12s of earthquake shaking.

Chapter 5

Seismic response of S_2 type soil profiles

5.1. Introduction

The prediction of the response spectra of liquefiable soil deposits is not rigorously investigated in the literature (Gingery et al. 2015) and not adequately covered by the international and domestic codes, since constructing in such conditions should be generally avoided according to the code guidelines, unless special measures are taken, such as soil reclamation, piles, etc. However, a number of studies evince that such precautions may not be inflicted, on condition that a surface non liquefiable soil layer will be used to mitigate structure settlements (Ishihara et al. 1993, Acacio et al 2001, Cascone and Bouckovalas 1998, Naesgaard et al. 1998, Dashti et al. 2010, Karamitros et al. 2013, Dimitriadi et al. 2017) Thus, estimating the seismic response in prone to liquefaction sites has recently arouse academic interest, since the evaluation of ground response is usually the first step in the calculation of structural response in soil-structure interaction problems. EC8 indicates that, the antiseismic design in potentially liquefiable soils, requires special studies that should be carried out in order to define the seismic action. Different methodologies to estimate the response spectra at liquefaction sites have been proposed , e. g. Tsiapas and Bouckovalas (2019) suggested computing the soil response spectrum for the native soil properties and for the properties of the liquified soil, using the equivalent linear method, and then applying an interpolation method between

them; Gingery et al. (2015) proposed a model in order to adjust the NGA-estimated (Next Generation Attenuation) acceleration response spectra to account for the effects of liquefaction.

This section concerns the preliminary application of the developed ground response analysis algorithm, aiming at composing elastic response spectra for soil profiles with liquefiable layers (Anthi and Gerolymos, 2021). The present work is an attempt to approach this subject, by executing a large number of seismic analyses to various potentially liquefiable soil profiles, excited with actual seismic records at their base. For each analysis the elastic acceleration response spectrum at the surface will be attained. Similar to previous studies for non-liquifiable soils (e.g. Rey et al. 2002, Pitilakis et al. 2013, Anastasiadis and Riga 2014), processing of the results leads to the recommendation of an idealized ground surface response spectrum in terms of the design spectrum parameters S, T_B and T_C, as per the EC8.

5.2. Methodology description

5.2.1. Selection of soil profiles with liquefiable layers

Ten soil profiles were composed, each one including a potentially liquefiable layer, e. g. a layer of saturated loose sandy soil, and two meters deep clayey zones at the surface and the base of configuration. The varying parameters of the examined idealized soil profiles are: total thickness H, soil type, relative density D_r for sands or undrained shear strength S_u for clays, and permeability k. The liquefiable layer is a D_r =35% sand with k=10^{-3}m/s, for which different thicknesses h_L and distances from surface h_f are examined. Surface and bottom clayey layers are 2m thick, with k=10^{-6} m/s and varying S_u. From all combinations available, certain cases were advisedly selected to create a sample as uniform as possible (using an appropriate sampling algorithm) but remain physically meaningful. The selected profiles are listed in Table 5.1.

5.2.2. Selection of earthquake motions as base excitation

The selection of the recorded earthquake motions that served as base excitations, was made through PEER Ground Motion Database (Pacific Earthquake Engineering Research Center Ground Motion Database, Ancheta et al. 2013), which includes a considerable amount of ground motions recorded worldwide. Selecting the desirable values for certain earthquake

parameters (such as the earthquake magnitude M_w, the region, the fault type, the closest distance to rupture plane R_{rup}, the Joyner-Boore distance to rupture plane R_{JB}, the average shear velocity of top 30m $V_{s,30}$ and others), PEER provides the target spectrum, calculated by employing the NGA – West2 GMMs (Next Generation Attenuation Relationships for Western US Ground Motion Models) (Abrahamson et al. (2014), Campbell and Bozorgnia (2014), Boore et al. (2014), Chiou and Youngs (2014), Idriss (2014)). Consequently, the user can obtain records that match the desired seismological parameters and yield a response spectrum compatible with the target, a process in accordance with the current practice (e.g. Katsanos et al. 2010, Sextos 2014). In the framework of the presented study, the following 9 seismic categories were assigned depending on the earthquake magnitude and the distance from rupture, making all possible combinations among the values: M_w=7.5, 7 and 6.5 and R_{JB}=5 km, 10 km and 15 km. For each seismic category, a list of 7 earthquake motions was selected, with response spectrum compatible with the corresponding spectrum calculated by the NGA – West2 attenuation relationships. Furthermore, there was the requirement that the selected earthquake motions should be recorded on rocky formation with average shear wave velocity $V_{s,30}$> 800 m/s (ground type *A*, according to EC8). Regarding accelerogram's magnitude and distance to rupture, they should be equal or similar with the corresponding parameters of the response spectrum derived via NGA – West2 GMMs attenuation relationships. Figure 5.1 reflects the variety of the selected records in respect of intensity and durance, in a qualitative manner, presenting some representative earthquake motions that were used.

5.2.3. Analysis methodology

As has thoroughly been discussed in the previous, the selected motions should yield a response spectrum compatible with the target spectrum of the corresponding category, derived via the attenuation relationships. In order to achieve this with acceptable engineering accuracy, two different approaches were adopted. Initially, the accelerograms were only scaled to match the target spectrum (scaling is provided by PEER), keeping the scaling factor in a certain, small range close to unity (from 0.7 to 1.4 in most cases and between 0.4 and 2.5 in others) to promote the "physical realism" of earthquake excitations, maintaining compatibility with their frequency content. The second approach was to fully modify the motions through a mathematical procedure (Zafeirakos and Gerolymos, 2013) that performs spectral matching. Figure 5.2 illustrates the target spectra of the 9 seismic categories, along with the spectra calculated with scaling and spectral matching procedure (mean values out of

7 accelerograms). The Earthquake motions were used as rock outcrop motions for the dynamic analyses. Each analysis was conducted under either fully drained conditions or fully undrained, or, considering consolidation during shaking. Therefore, for each one of the two aforementioned approaches (fully modified & only scaled accelerograms), 70 analyses were conducted for each M_w, R_{JB} category (10 liquefiable profiles × 7 base excitations), each one for 3 drainage conditions; 3.780 analyses in total.

As an example of the performed analyses, some characteristic results of the seismic response of a 30 m deep soil profile (profile #4 in Table 5.1), including a 5m liquefiable layer are illustrated in figures 5.3 to 5.6. The configuration presented in Figure 5.3 is excited with the Irpinia, Italy (1980) record on its base, multiplied with a scaling factor equal to 1.18 to approximate the target spectrum of the M_w=7 and R_{JB}=5km seismic category. The surface acceleration time histories under drained, undrained, and consolidation conditions during shaking are given in Figure 5.4, along with the base excitation. The first stage of the response (shaded area in the figure) is quite similar in all three cases, and represents the pre-liquefaction phase. During this part of motion, amplification effects can occur as has been well documented in the literature (Tsiapas and Bouckovalas, 2019) The remaining part of the drained response is way more intense than the weak undrained and consolidation response, that signifies the liquefaction phenomena that took place. Similar remarks arise from the elastic spectra in Figure 5.5, where high frequency components have been amplified by the drained analysis and depressed by the analyses in which excess pore pressure was generated, while the opposite is observed for the low frequency components. Finally, the profile of the maximum values of the excess pore pressure (Figure 5.6) indicates that if fully undrained conditions are assumed, $r_{u,max}$ equals 1 inside the liquefied zone and less than 0.25 outside of it. If water flow phenomena are modelled, the surrounding soil layers seem to be affected by the liquified zone and high values of $r_{u,max}$ are observed until they turn to zero close to the boundaries. It is noted, that in all the analyses the water table is placed at the surface of the soil profile.

5.3. Results

Figures 5.7 and 5.8 depict the ground response analysis results, in terms of the elastic acceleration spectra at the surface, considering all three different drainage conditions (undrained, fully drained, partially drained). Each spectrum is calculated as the mean elastic

response spectrum out of 70 analyses (10 soil profiles × 7 accelerograms). The spectra of the base excitations are also drawn (mean values as were presented in Figure 5.2). Figure 5.7 refers to the scaled base excitations and Figure 5.8 refers to the spectrum matched input motions. To elucidate the effect of drainage conditions on the frequency content of the response spectrum, the spectral accelerations are normalized with respect to the maximum ground acceleration (*PSA* for *T*=0). The following generic observations can be drawn: (i) For fully undrained and partially drained (consolidation) conditions only minor differences are observed; the divergence mainly appears when comparing with the drained response. In most cases, the response accounting for consolidation is delimited by the drained and the undrained response. (ii) When fully drained conditions are assumed the maximum spectral accelerations increase compared to the other drainage conditions. (iii) In the high frequency region of the spectra (denoted in figures with shaded area), drained analyses accelerations are higher compared to undrained and consolidation analyses, since excess pore water pressure build up causes de-amplification of the high frequency acceleration components. However, there is a critical period *T* that appears after the maximum acceleration is observed, at which the drained response degrades more rapidly compared to the undrained (or consolidation) response. Thus, while undrained response exhibits smaller maximum spectral acceleration values compared to the other drainage conditions, it shows greater normalized spectral values for periods greater than T_{cr}. This critical period has a mean value of 0.57s for the spectra of figure 5.7 and 0.51s for those of figure 5.8. Based on the ground response with consolidation, since it is the most representative of the actual field conditions, the normalized mean spectra proceeding from all the seismologic conditions are illustrated in figure 5.9. The response spectra in terms of $S_e\ /a_g$ are presented with grey dotted lines and the mean spectrum with solid black line, where a_g is the design ground acceleration of ground type *A* which is equal to S_e for T = 0 at the mean base spectrum. It is observed that the final spectra are very similar both in shape and amplitudes, regardless of the type of the applied input motion (scaled or spectrum matched).

The elastic response spectra calculated for each M_w, R_{JB} combination, soil profile and base excitation are summarized in the Appendix. The seismic base motions are named as per the PEER Ground Motion Database.

5.4. Proposed elastic response spectrum for ground type S_2

According to EC8, the ground motion at a given point on the surface is represented by an elastic ground acceleration response spectrum $S_e(T)$, which consists of four branches defined by the following expressions:

$$0 \le T \le T_B : S_e(T) = a_g S \left[1 + \frac{T}{T_B}(\eta A_C - 1)\right] \quad (5.1.1)$$

$$T_B \le T \le T_C : S_e(T) = a_g S \eta A_C \quad (5.1.2)$$

$$T_C \le T \le T_D : S_e(T) = a_g S \eta A_C \left[\frac{T_C}{T}\right] \quad (5.1.3)$$

$$T_D \le T \le 4s : S_e(T) = a_g S \eta A_C \left[\frac{T_C T_D}{T^2}\right] \quad (5.1.4)$$

where $S_e(T)$ is the elastic response spectrum, T is the vibration period of a linear single degree of freedom system, A_C is the spectral amplification parameter, equals 2.5, a_g is the design ground acceleration for ground type *A* ($a_g = \gamma_I a_g R$), T_B is the lower limit of the period of the constant spectral acceleration branch, T_C is the upper limit of the period of the constant spectral acceleration branch, T_D is the value defining the beginning of the constant displacement response range of the spectrum, S is the soil factor and η is the damping correction factor (η =1 for 5% viscous damping). The values of T_B, T_C and T_D and of the soil factor S describing the shape of the elastic response spectrum, depend upon the ground type. Specific values are defined for ground types *A, B, C, D* and *E*, whereas for ground type S_2 special studies are required to define the seismic action.

In this framework, the mean spectrum of the average spectra of figure 5.9 (mean spectrum of figure 5.9 solid black lines), along with the corresponding mean spectrum at the base, are described via the four-branch curve of equation 5.1 (Figure 5.10). The grey solid curve represents the elastic spectrum for ground type *A*, the black solid curve the response of profiles with liquefiable soil layers (ground type S_2) and dotted lines are their linearization according to EC8. The parameters that define the shape of the spectrum for ground types *A* and S_2, are described in figure 5.11. The best-fitted values of these parameters, to better approximate the mean response spectra, are listed in the same figure. Both approaches

regarding the type of the input motion (scaled or spectral matched) converged to a similar soil factor S, with a mean value equal to 1.42. Regarding the key periods, the ratios of ground type S_2 spectral periods over the corresponding periods for ground type *A,* e.g. $T_B(S_2)$ / $T_B(A)$ and T_C (S_2) / T_C (A) equal to 1.3 and 2.8 respectively. Thus, if a reference ground type *A* spectrum is defined in terms of A_C, T_B and T_C, then the response spectrum of ground type S_2 could be determined.

It has to be mentioned, that the proposed methodology does not aim at revising or adding to the antiseismic codes, but consist an effort to provide some directions at the level of preliminary design. Thus, the special studies and ground response analysis that are suggested by the codes when dealing with such prone to liquefaction profiles, cannot be replaced by the proposed methodology. Furthermore, the liquefiable soil profiles that were examined formed a limited sample, mainly consisting of soil profiles including a thin liquefiable layer, and thus did not cover all the possible ground conditions that can be encountered at a site. However, it is the author's belief that profiles including a relatively limited liquefiable zone are more likely to be encountered, rather that profiles that are almost totally consisting of liquifiable soil material. Moreover, the elastic spectra resulting from profiles with liquefiable zone of limited thickness, are conceivably more detrimental, which is in accordance with the conservatism principally promoted by the codes.

References

Abrahamson, N. A., Silva, W. J., & Kamai, R. (2014). Summary of the ASK14 ground motion relation for active crustal regions. *Earthquake Spectra*, *30*(3), 1025-1055.

Acacio, A. A., Kobayashi, Y., Towhata, I., Bautista, R. T., & Ishihara, K. (2001). Subsidence of building foundation resting upon liquefied subsoil: case studies and assessment. *Soils and Foundations*, *41*(6), 111-128.

Anastasiadis, A., & Riga, E. (2014). Site classification and spectral amplification for seismic code provisions. In *Earthquake Geotechnical Engineering Design* (pp. 23-72). Springer, Cham.

Ancheta T. D., Darragh R. B., Stewart J. P., Seyhan E., Silva W. J., Chiou B. S.J., Wooddell K. E., Graves R.W., Kottke A. R., Boore D. M., Kishida T. and Donahue J. L. (2013) PEER NGA-West2 Database, PEER Report2013/03, Pacific Earthquake Engineering Research Center, Headquarters at the University of California, Berkeley, May 2013

Anthi, M., & Gerolymos, G., (2021) Site Response Analysis of S_2 Soil Deposits Focusing on the Effects of Liquefaction and Pore-Pressure Dissipation on the Ground Surface Response Spectrum. Bulletin of Earthquake Engineering *(under review)*

Boore, D. M., Stewart, J. P., Seyhan, E., & Atkinson, G. M. (2014). NGA-West2 equations for predicting PGA, PGV, and 5% damped PSA for shallow crustal earthquakes. *Earthquake Spectra*, *30*(3), 1057-1085.

Campbell, K. W., & Bozorgnia, Y. (2014). NGA-West2 ground motion model for the average horizontal components of PGA, PGV, and 5% damped linear acceleration response spectra. *Earthquake Spectra*, *30*(3), 1087-1115.

Cascone, E., & Bouckovalas, G. (1998, September). Seismic bearing capacity of footings on saturated sand with a clay cap. In *Proc., 11th European Conf. on Earthquake Engineering*.

Chiou, B. S. J., & Youngs, R. R. (2014). Update of the Chiou and Youngs NGA model for the average horizontal component of peak ground motion and response spectra. *Earthquake Spectra*, *30*(3), 1117-1153.

Dashti, S., Bray, J. D., Pestana, J. M., Riemer, M., & Wilson, D. (2010). Mechanisms of seismically induced settlement of buildings with shallow foundations on liquefiable soil. *Journal of geotechnical and geoenvironmental engineering*, *136*(1), 151-164.

Dimitriadi, V. E., Bouckovalas, G. D., & Papadimitriou, A. G. (2017). Seismic performance of strip foundations on liquefiable soils with a permeable crust. *Soil Dynamics and Earthquake Engineering*, *100*, 396-409.

Gingery, J. R., Elgamal, A., & Bray, J. D. (2015). Response spectra at liquefaction sites during shallow crustal earthquakes. *Earthquake Spectra*, *31*(4), 2325-2349.

Idriss, I. M. (2014). An NGA-West2 empirical model for estimating the horizontal spectral values generated by shallow crustal earthquakes. Earthquake Spectra, 30(3), 1155-1177.

Ishihara, K., Acacio, A. A., & Towhata, I. (1993). Liquefaction-induced ground damage in Dagupan in the July 16, 1990 Luzon earthquake. *Soils and Foundations*, *33*(1), 133-154.

Karamitros, D. K., Bouckovalas, G. D., & Chaloulos, Y. K. (2013). Insight into the seismic liquefaction performance of shallow foundations. *Journal of Geotechnical and Geoenvironmental Engineering*, *139*(4), 599-607.

Katsanos, E. I., Sextos, A. G., & Manolis, G. D. (2010). Selection of earthquake ground motion records: A state-of-the-art review from a structural engineering perspective. *Soil dynamics and earthquake engineering*, *30*(4), 157-169.

Naesgaard, E., Byrne, P. M., & Huizen, G. V. (1998). Behaviour of Light Structures Founded on Soil "Crust" over Liquefied Ground. In *Geotechnical Earthquake Engineering and Soil Dynamics III* (pp. 422-433). ASCE.

Pitilakis, K., Riga, E., & Anastasiadis, A. (2013). New code site classification, amplification factors and normalized response spectra based on a worldwide ground-motion database. *Bulletin of Earthquake Engineering*, *11*(4), 925-966.

Rey, J., Faccioli, E., & Bommer, J. J. (2002). Derivation of design soil coefficients (S) and response spectral shapes for Eurocode 8 using the European Strong-Motion Database. *Journal of seismology*, *6*(4), 547-555.

Sextos, A. G. (2014). Selection of ground motions for response history analysis. *Encyclopedia of Earthquake Engineering*, 3239-3247.

Tsiapas, Y. Z., & Bouckovalas, G. D. (2019). Equivalent linear computation of response spectra for liquefiable sites: the spectral interpolation method. *Soil Dynamics and Earthquake Engineering*, *116*, 541-551.

Zafeirakos, A., & Gerolymos, N. (2013). On the seismic response of under-designed caisson foundations. *Bulletin of Earthquake Engineering*, *11*(5), 1337-1372.

Figures

Table 5.1. Examined potentially liquefiable soil profiles; parametric investigation regarding the surrounding soil, the liquefiable sandy layer and the top and bottom clayey layers.

	Soil Profile	*# 1*	*# 2*	*# 3*	*# 4*	*# 5*	*# 6*	*# 7*	*# 8*	*# 9*	*# 10*
surrounding soil	Type			sand					clay		
	H (m)	15	20	25	30	35	15	20	25	30	35
	D_r [%]	40	50	60	70	80	-	-	-	-	-
	S_u [kPa]	-	-	-	-	-	40+5z	45+5z	50+5z	55+5z	60+5z
	k [m/s]	10^{-3}	10^{-3}	10^{-4}	10^{-4}	10^{-4}			10^{-6}		
liquefiable layer: D_r=35%, k=10^{-3}m/s	h_L [m]	1.5	5	1.5	5	7	1.5	5	1.5	5	7
	h_f [m]	2	2	7	7	7	2	2	7	7	7
surface clay: h=2m, k=10^{-6}m/s	S_u [kPa]	40	45	50	55	60	40	45	50	55	60
bottom clay: h=2m, k=10^{-6}m/s	S_u [kPa]	105	135	165	195	225	105	135	165	195	225

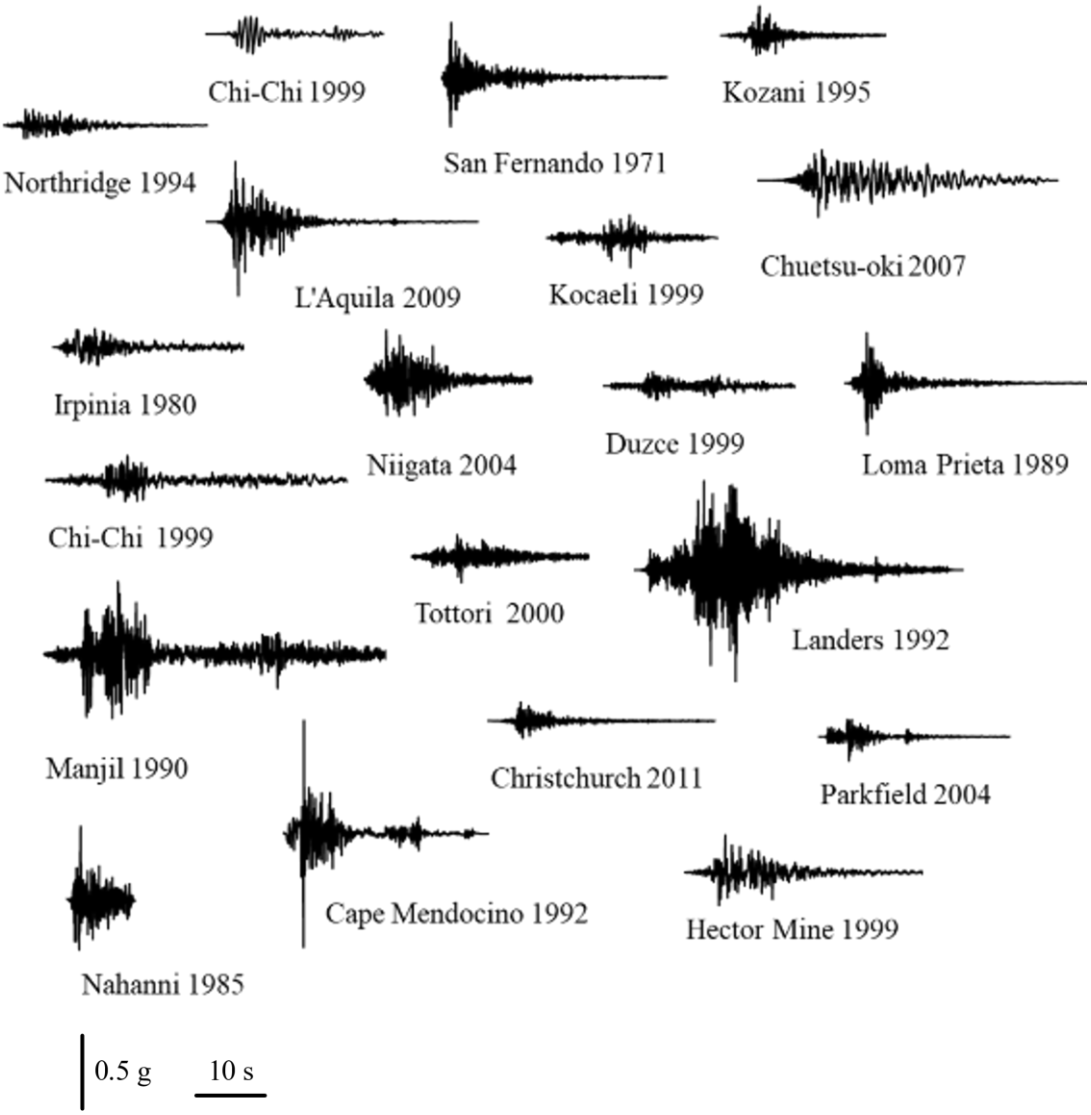

Figure 5.1. Indicative recorded earthquake motions that were used as base excitations (data from Peer Ground Motion Database).

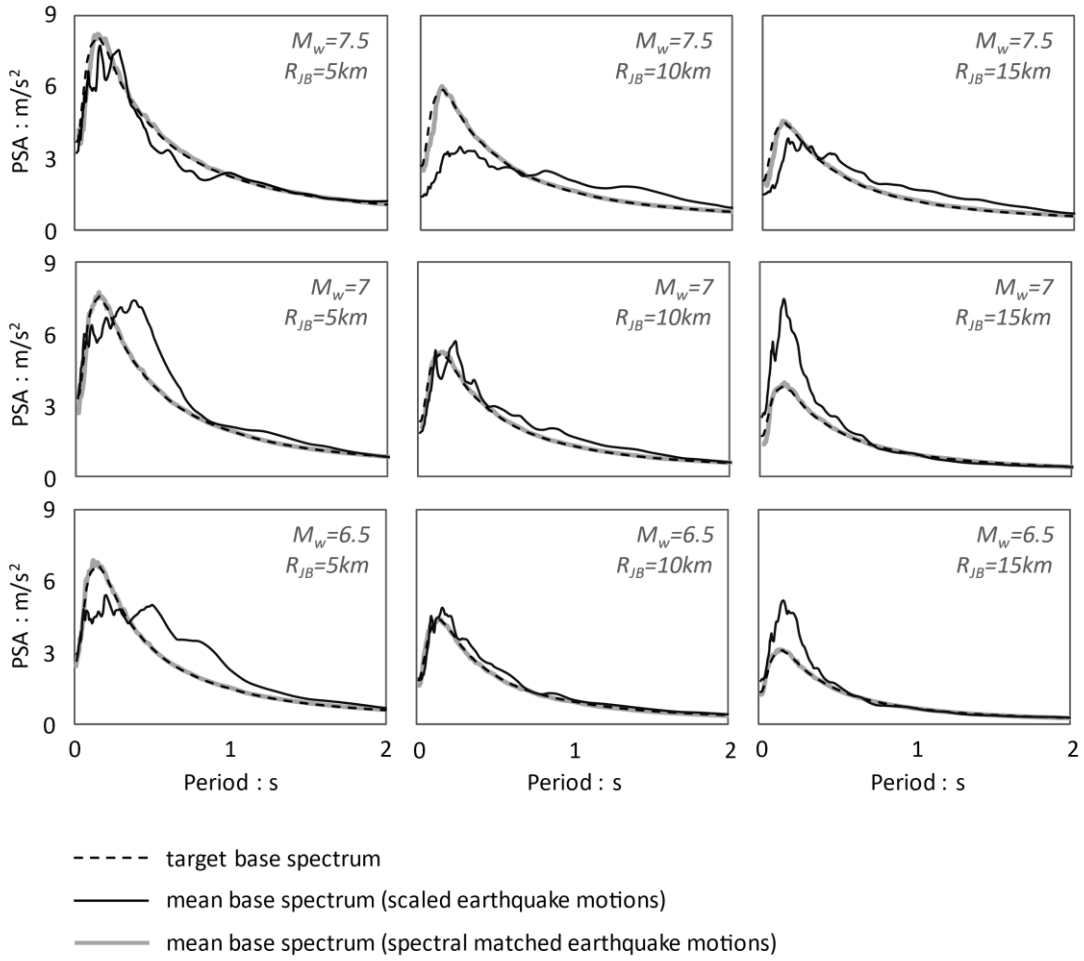

Figure 5.2. Target spectra, derived via the NGA – West2 attenuation relationships, calculated for 9 (M_w, R_{JB}) combinations in comparison with acceleration response spectra (mean values) of the recorded earthquake motions that were used as base excitations at the ground response analyses.

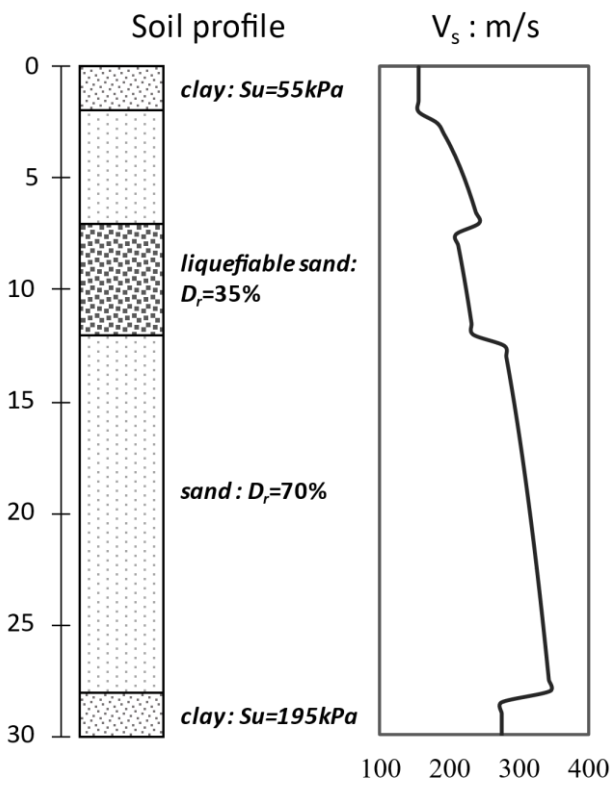

Figure 5.3. Soil profile and V_s distribution with depth used in the example analysis. (profile #4 in Table 5.1).

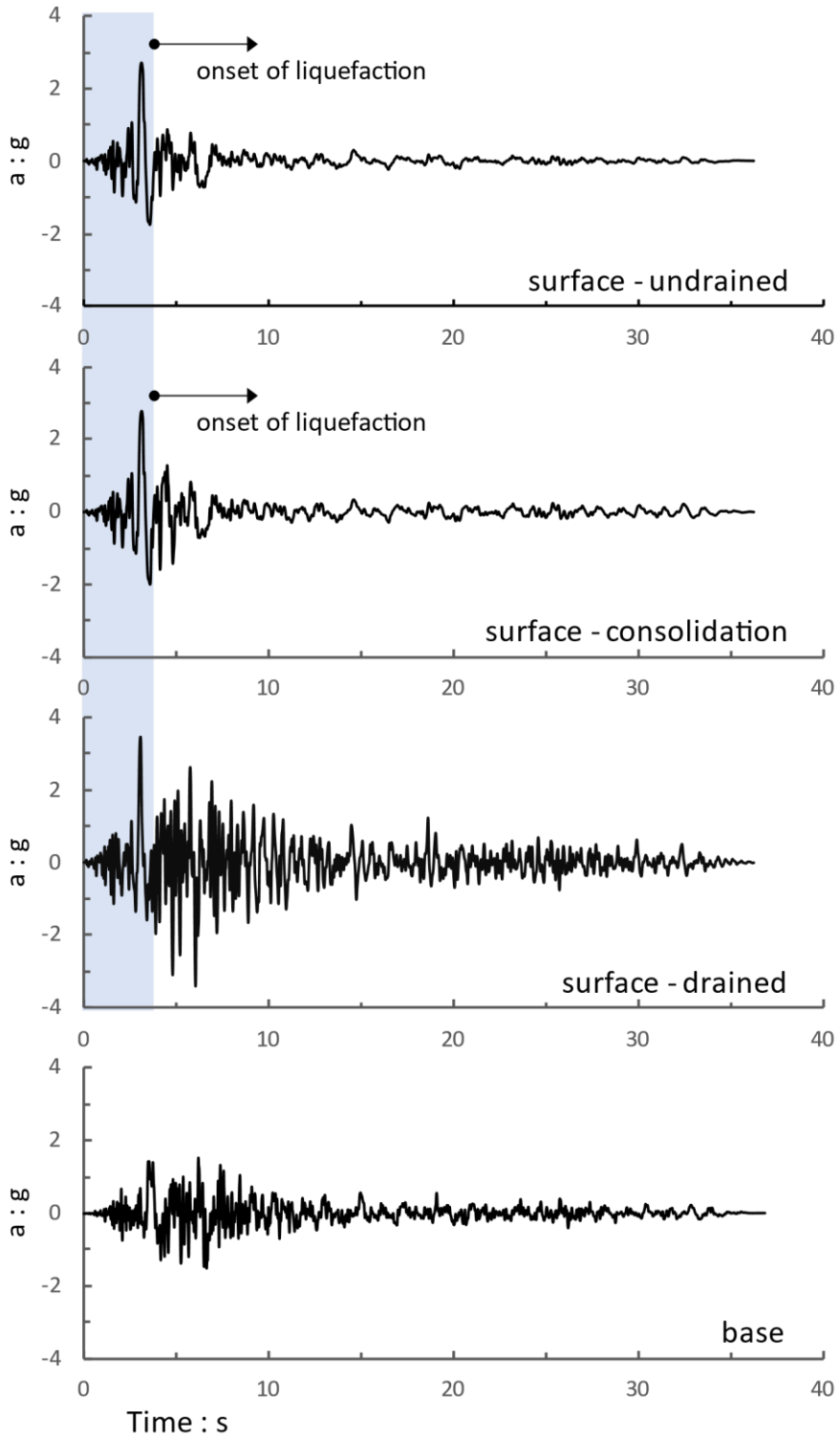

Figure 5.4. Ground response analyses results in terms of the computed acceleration time history, considering drained, undrained and consolidation conditions during shaking. Base motion used in the example analysis: Irpinia Italy 1980, Station name Bagnoli Irpinio, Magnitude 6.9 (scaling factor 1.18).

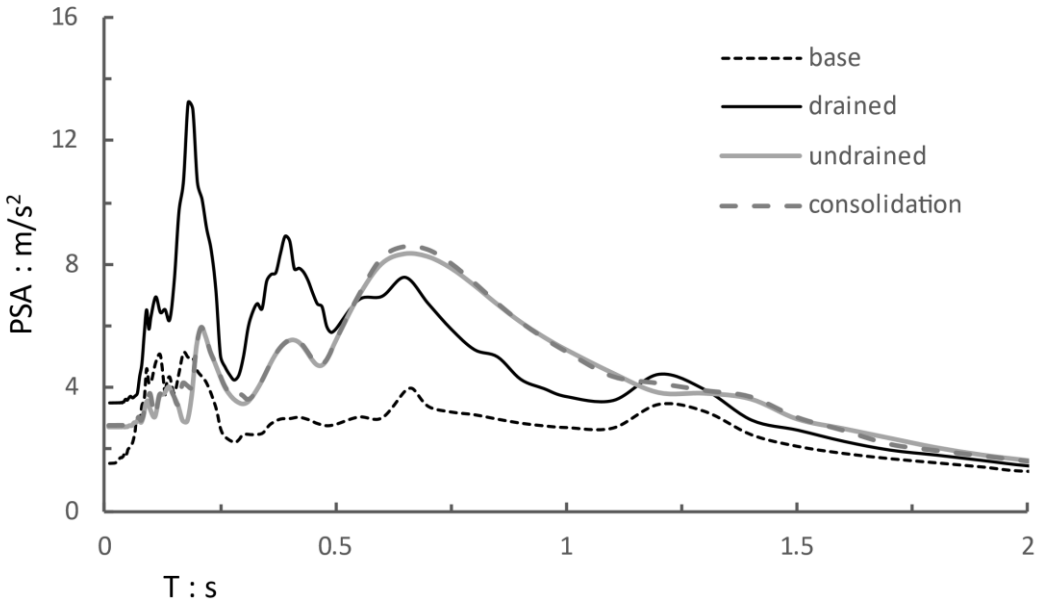

Figure 5.5. Ground surface elastic response spectra predicted by the example analysis considering drained, undrained and consolidation conditions during shaking. Base motion: Irpinia Italy 1980, Station name Bagnoli Irpinio, Magnitude 6.9 (scaling factor 1.18).

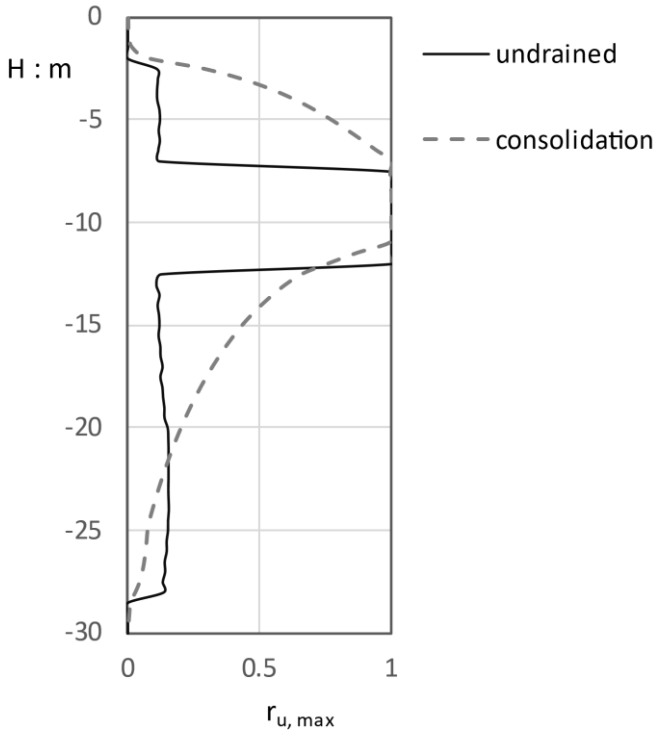

Figure 5.6. Profile of the maximum excess pore water pressure ratio ru_{max} distribution with depth predicted by the example analysis considering undrained and consolidation conditions during shaking.

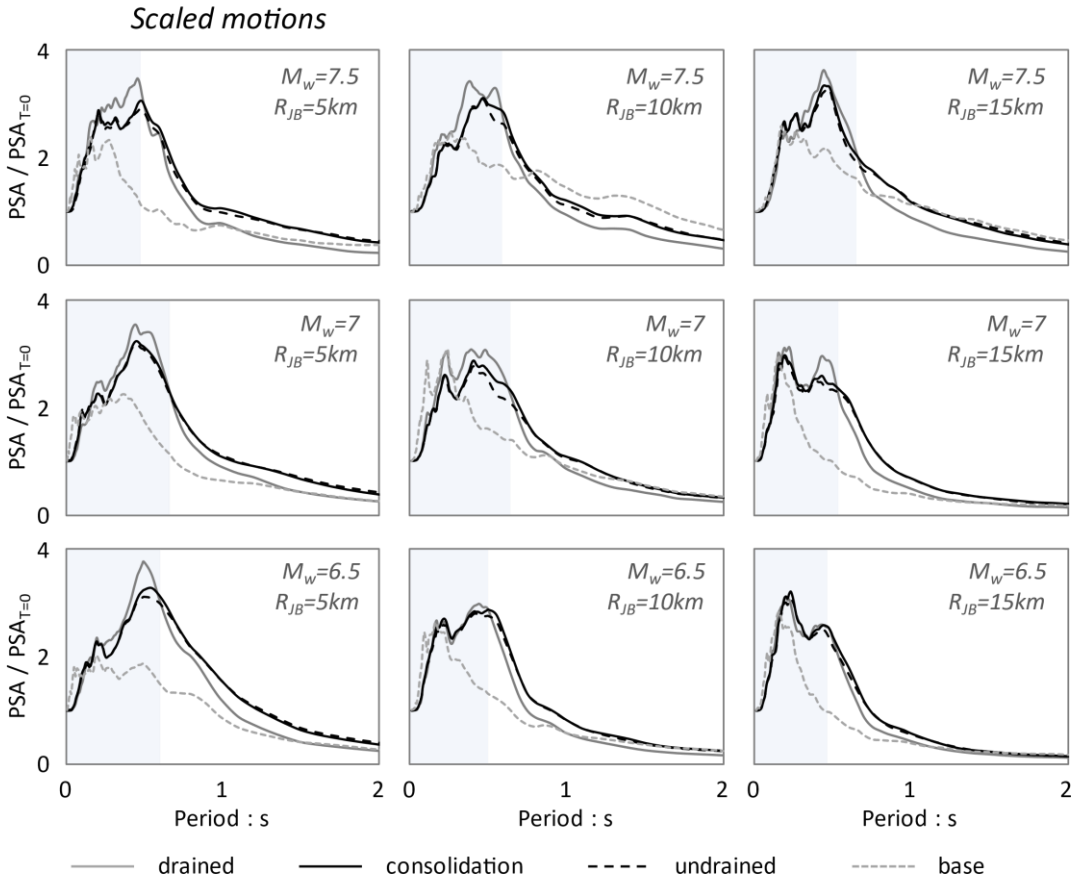

Figure 5.7. Elastic acceleration response spectra at ground surface (average values) for 9 (M_w, R_{JB}) combinations, calculated assuming drained, undrained and consolidation conditions during shaking. Mean spectra at the base (only scaled earthquake motions to approximate the target base spectrum) are also included.

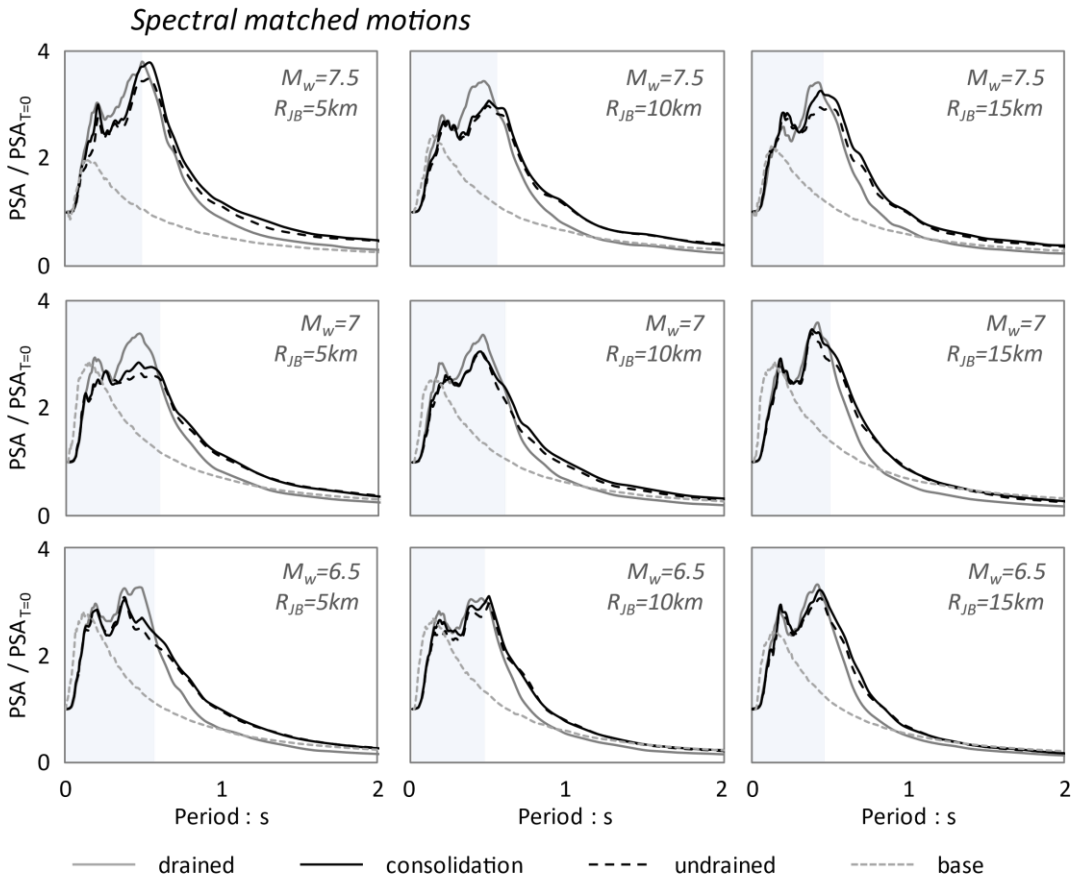

Figure 5.8. Elastic acceleration response spectra at the surface (average values) for 9 (M_w, R_{JB}) combinations calculated assuming drained, undrained and consolidation conditions during shaking. Mean spectra at the base (spectral matched earthquake motions to approximate the target base spectrum) are also included.

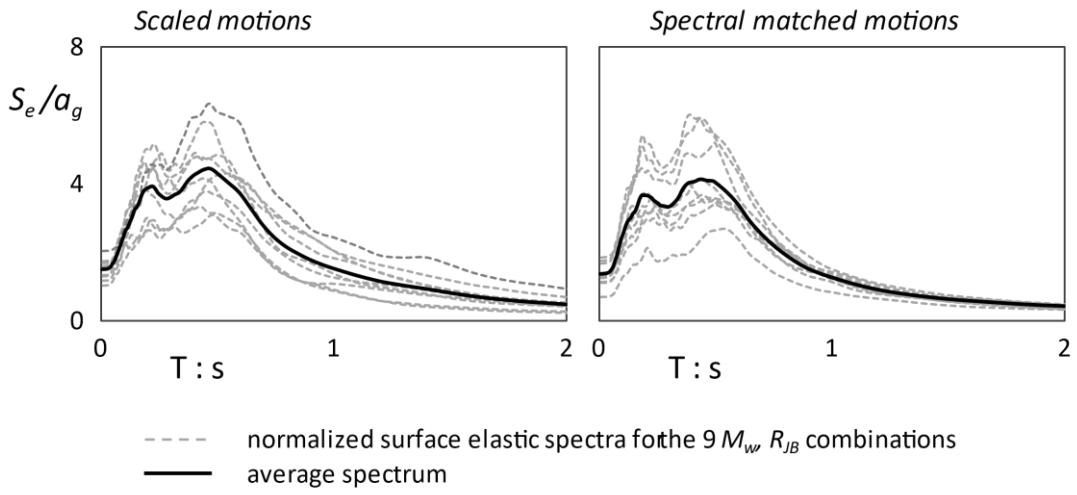

Figure 5.9. Ground surface elastic response spectra (considering consolidation conditions) normalized to a_g, i.e. S_e value for T=0 at the mean base spectrum, along with their average spectrum.

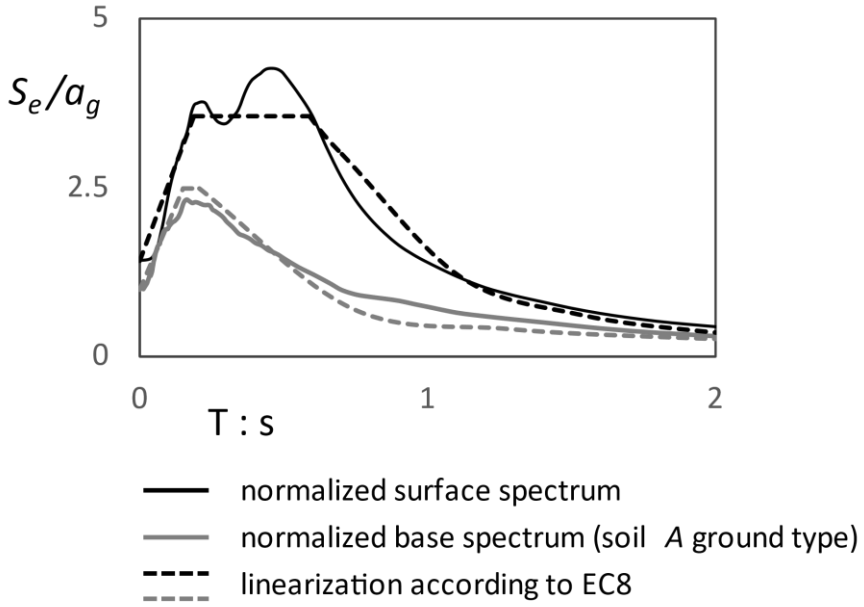

Figure 5.10. Average normalized to a_g surface elastic response spectra in comparison with the corresponding base spectra (ground type *A*). Linearization according to EC8 four-branches elastic spectrum also provided.

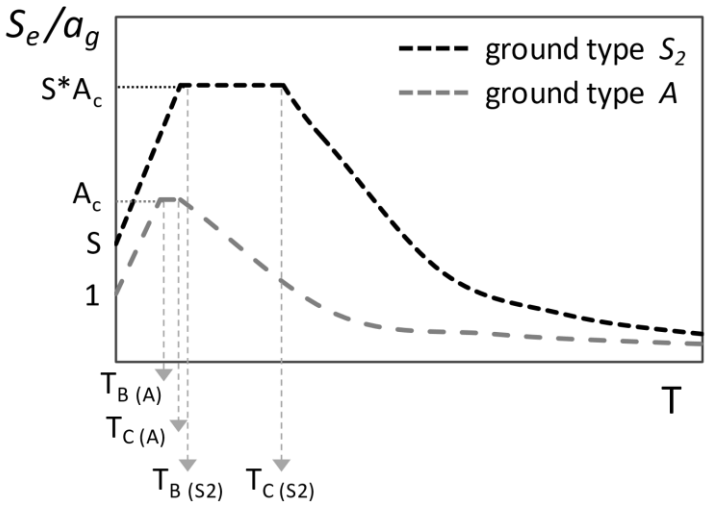

	A_C	S	T_B [s]	T_C [s]
Soil A	2.5	1	0.15	0.21
Soil S_2		1.42	0.19	0.59

Figure 5.11. Selected values of A_c, S, T_B, and T_C to express the response spectrum at ground type S_2 and ground type A according to EC8 four-branches elastic spectrum.

Chapter 6

Numerical modeling of drainages

6.1. Introduction

The occurrence of soil liquefaction under earthquake loading has always been one of the most critical issues in Geotechnical Earthquake Engineering. Thus, in the last decades several techniques have been used to mitigate liquefaction and lateral spreading hazardous effects. One of the most commonly used practice worldwide is the placement of stone columns or gravel piles in the susceptible non cohesive soil and the simultaneous vibrating compaction of the surrounding loose sand. This preventive measure provides benefits through multiple mechanisms. It accelerates drainage by activating radial water flow through the much more permeable, compared to the native ground, drains and thus attenuates the developed excess pore pressures and it improves the overall soil strength and liquefaction resistance by increasing its density. Moreover, the process of placing the gravel drains is usually accompanied by vibrating densification of the surrounding soil. However, in certain cases vibration might be prohibited, if limitations are imposed by near-to-the-field structures. The presence of a relatively stiffer material may also cause redistribution of earthquake induced shear stresses and strains that would have otherwise been received by the ground (Bouckovalas et al. 2011b, Priebe 1989 and Adalier et al. 2003), however this mechanism probably does not have considerable effects due to the replacement ratios commonly used in

practice. Besides, the stiffer material of gravel piles may lead to amplification of the seismic motion that will diminish the positive effects of the redistribution (Bouckovalas et al. 2006, Papadimitriou et al. 2006). An alternative, more recently applied solution, is the placement of prefabricated vertical drains (*PVDs*) made of plastic or metal material, that can be used instead of the traditional gravel piles as they have numerous advantages. They cause limited environmental impact and they are beneficial thanks to their less demanding placement process (Rollins et al. 2004, Harada et al. 2006, Marinucci et al. 2008). Although the performance of the traditional gravel drains may be attenuated by clogging due to thin soil material drifted by the water flow that decreases the permeability, *PVDs* are much more permeable than gravel drains and protected against clogging. Since *PVDs* draw their benefits exclusively from radial flow, developing tools that can calculate the effects in the response that arise exclusively from radial drainage, is important.

Designing a drainage system basically requires the selection of the drain diameter and the drain spacing (drains center-to-center distance) usually aiming at keeping the maximum excess pore water pressure ratio under a specified threshold for the design earthquake; e.g. $r_{u,max} < 0.6$ (Onoue 1988, Japanese Geotechnical Society 1998). To this purpose, Seed & Booker (1977) were pioneers to propose design charts that predict $r_{u,max}$ within the unit cell around a single drain, given the drain characteristics, the soil properties and the characteristics of earthquake shaking, under the assumptions of exclusively axisymmetric flow towards the uniform soil, a constant overall stiffness of the ground and an infinitely permeable, compared to the surrounding soil, drain. Several researchers afterwards proposed modifications and improvements, e.g. Onoue (1988) introduced the dimensionless parameter of drain resistance *L*, that allowed to take into consideration the actual drain permeability and accordingly its potentially decreased effectiveness and the simultaneous horizontal and vertical water flow through the soil. Further refinements were also suggested by Matsubara et al. (1988) and Iai and Koizumi (1986). Bouckovalas et al. (2009, 2011b) revisited Seed and Brooker (1997) design charts by reformulating the mathematical assumption for the generation of pore water pressures under earthquake loading, considering sand fabric evolution effects. The conventional design methodology at a site prone to liquefaction consists in selecting the diameter and drain spacing according to the aforementioned design charts, calculating the developed pore pressure, determining the reduced shear modulus or shear wave velocity for the developed r_u and finally executing site response analysis for the reduced G_0.

The forementioned design charts are user friendly and convenient for practical use, but fail to provide information about the response in terms of lateral deformation and settlements of the drain improved ground. Conversely, numerical modelling can predict the response in more details, at the cost of computational time and complexity. A 3D finite element program (*FEQDrain*) was developed by Pestana et al. (1997) to model the 3D unit cell around a single drain, capable of simulating prefabricated drains. Bouckovalas et al (2011a) used a 3D fully coupled finite differences model under advanced constitutive modelling, to examine the seismic response of a thin sand layer, treated with gravel drains. The case of a sloping ground improved with drains was examined by Seid Karbasi and Byrne (2007) in a 2D unit cell under fully coupled constitutive modelling. Finally, Vytiniotis and Whittle (2013) studied the response in terms of deformations, of slopes improved with *PVDs* in a 2D finite element model under fully coupled constitutive modelling. More recently Howell et al. (2015) used 3D and 2D finite element analysis to evaluate their performance with respect to centrifuge experiments described by Howell et al. (2012) and Howell (2013).

In the present section, the developed numerical algorithm is applied for the simulation of the seismic response of liquefiable sandy sites improved with vertical drains. The differential equation of soil consolidation is reformulated to account not only for the vertical water flow up to the ground surface, but also for the axisymmetric flow of water, through the ground towards the drain. The drain can be simulated as a "perfect drain" of infinitely large permeability compared to the surrounding soil (usually applies to *PVDs*) or simulated according to its actual permeability. The mechanical interaction between the drain material and the surrounding soil in case of stone columns / gravel piles, is possible to be taken into consideration, by increasing the overall strength of the composite gravel pile-surrounding soil material. The comparison between the proposed model and the described conventional methodology for designing a drain system is not included in the present study, but is an author's future scope.

6.2. Three-dimensional axisymmetric flow due to uniform surface load q

The continuity equation for saturated soils, takes the following form as it was established by Lambe and Whitman (1969):

$$k_x \frac{\partial^2 h}{\partial x^2} + k_y \frac{\partial^2 h}{\partial y^2} + k_z \frac{\partial^2 h}{\partial z^2} = \frac{1}{1+e}\frac{\partial e}{\partial t} = -\frac{\partial \varepsilon_{vol}}{\partial t} \quad (6.1)$$

where k_x, k_y, k_z are the invariable coefficients of permeability in x, y, z directions respectively, h is the piezometric head, e is the soil void ratio, ε_{vol} is the volumetric strain and t is time. Eq. (6.1) converted with respect to polar coordinate system, is expressed as follows:

$$k_r \left(\frac{\partial^2 h}{\partial r^2} + \frac{1}{r}\frac{\partial h}{\partial r} + \frac{1}{r^2}\frac{\partial^2 h}{\partial \theta^2}\right) + k_z \frac{\partial^2 h}{\partial z^2} = -\frac{\partial \varepsilon_{vol}}{\partial t} \quad (6.2)$$

and considering axisymmetric water flow:

$$\frac{1}{r^2}\frac{\partial^2 h}{\partial \theta^2} = 0 \quad (6.3)$$

Thus, the differential equation governing the excess pore pressure in the soil specimen $u_{r,z,t}$ is given as follows:

$$\frac{k_r}{\gamma_w}\left(\frac{\partial^2 u}{\partial r^2} + \frac{1}{r}\frac{\partial u}{\partial r}\right) + \frac{k_z}{\gamma_w}\frac{\partial^2 u}{\partial z^2} = -\frac{\partial \varepsilon_{vol}}{\partial t} \quad (6.4)$$

- $\frac{k_r}{\gamma_w}\left(\frac{\partial^2 u}{\partial r^2} + \frac{1}{r}\frac{\partial u}{\partial r}\right)$: horizontal – radial flow
- $\frac{k_z}{\gamma_w}\frac{\partial^2 u}{\partial z^2}$: vertical flow

6.2.1. Isotropic linear elastic soil under purely radial flow

The problem studied herein is the radial water flow that is caused in a saturated soil deposit of isotropic, linear, elastic soil by the imposition of a uniform surficial load *q*, through the soil along a vertical drain with infinitely permeable surface. By abstracting the term that refers to the vertical flow from equation (6.4), continuity equation takes the following form:

$$\frac{k_r}{\gamma_w}\left(\frac{\partial^2 u}{\partial r^2} + \frac{1}{r}\frac{\partial u}{\partial r}\right) = -\frac{\partial \varepsilon_{vol}}{\partial t} \Rightarrow \frac{k_r}{\gamma_w}\left(\frac{\partial^2 p'}{\partial r^2} + \frac{1}{r}\frac{\partial p'}{\partial r}\right) = \frac{\partial \varepsilon_{vol}}{\partial t} \quad (6.5)$$

, where *p'* represents the mean effective stress. In one dimensional contraction of an isotropic, linear, elastic soil:

$$\frac{\partial \varepsilon_{vol}}{\partial t} = \frac{1}{K}\frac{\partial p'}{\partial t} \tag{6.6}$$

, where K stands for the soil bulk modulus.

Thus, combining equations (6.5) and (6.6):

$$\frac{k_r}{\gamma_w}\left(\frac{\partial^2 p'}{\partial r^2} + \frac{1}{r}\frac{\partial p'}{\partial r}\right) = \frac{1}{K}\frac{\partial p'}{\partial t} \Rightarrow \frac{k_r K}{\gamma_w}\left(\frac{\partial^2 p'}{\partial r^2} + \frac{1}{r}\frac{\partial p'}{\partial r}\right) = \frac{\partial p'}{\partial t} \Rightarrow C_r\left(\frac{\partial^2 p'}{\partial r^2} + \frac{1}{r}\frac{\partial p'}{\partial r}\right) = \frac{\partial p'}{\partial t} \tag{6.7}$$

, with $C_r = \frac{k_r K}{\gamma_w}$, so that $C_r = \frac{k_r}{k_v} C_v$. Differential equation (6.7) that governs the radial flow in an isotropic, linear elastic soil can be solved according to the finite differences approached. Figure 6.1 gives a schematic depiction of the discretization of the grid along a soil radius R_e, of a unit cell around a single drain R_d. Symmetry imposes that soil unit cell circumference is a non permeable boundary. Drain circumference is assumed to be fully permeable and thus the surface of the drain is not included in the grid. The examined radius $R = R_e - R_d$ is discretized into M steps of size equal to w, so that $M = R/w$, and the radial distance of each node k from the center, is $r_k = R_e + w(1-k), for\ k = 1{:}\ M+1$. Considering the central difference for the 2nd order radial derivative and backward difference for the 1st order radial and time derivatives of the mean effective stress $p'_{time,radius} = p'_{i,k}$:

- $\left(\frac{\partial^2 p'}{\partial r^2}\right)_{i,k} = \frac{p'_{i,k+1} - 2p'_{i,k} + p'_{i,k-1}}{w^2}$ central difference
- $\left(\frac{\partial p'}{\partial r}\right)_{i,k} = \frac{p'_{i,k} - p'_{i,k-1}}{w}$ backward difference
- $\left(\frac{\partial p'}{\partial t}\right)_{i,k} = \frac{p'_{i,k} - p'_{i-1,k}}{\Delta t}$ backward difference

and by substituting to equation (6.7), we obtain:

$$C_r\left(\frac{p'_{i,k+1} - 2p'_{i,k} + p'_{i,k-1}}{w^2} + \frac{1}{r_k}\frac{p'_{i,k} - p'_{i,k-1}}{w}\right) = \frac{p'_{i,k} - p'_{i-1,k}}{\Delta t} \tag{6.8}$$

Assuming that:

$$\frac{C_r\,\Delta t}{w^2\, r_k} = Q_k \tag{6.9}$$

, we finally have:

$$Q_k r_k p'_{i,k+1} + (-2Q_k r_k + Q_k w - 1)p'_{i,k} + (Q_k r_k - Q_k w)p'_{i,k-1} = -p'_{i-1,k}$$
$$for\ k = 2{:}M \tag{6.10}$$

Initial conditions are the geostatic pressures at the field:

- $p'_{1,k} = p'_0\ \ for\ k = 1{:}M+1$ (6.11)

The boundary conditions are the permeable circumference of the drain for $r = R_d$ and the non-permeable soil circumference for $r = R_e$:

- $p'_{i,M+1} = p'_{1,M+1} + q$ (6.12a)
- $\left(\frac{\partial u}{\partial r}\right)_{i,1} = 0 \Rightarrow \left(\frac{\partial p'}{\partial r}\right)_{i,1} = 0 \Rightarrow \frac{p'_{i,2} - p'_{i,1}}{w} = 0 \Rightarrow p'_{i,2} = p'_{i,1}$ (6.12b)

Thus, at time $t = t_i$, $M+1$ linear equations are solved, in order to calculate the mean effective stresses $p'_{i,k}$. The linear system of equations (6.10) along with the initial conditions of eq. (6.11) and the boundary conditions of eq. (6.12), can be written in matrix form as follows:

$$\begin{array}{c} radius\,k \longrightarrow \\ radius\,k \downarrow \end{array}$$

$$\begin{array}{c} \\ 1 \\ 2 \\ 3 \\ \\ \\ \\ M-1 \\ M \\ M+1 \end{array}
\begin{array}{c} \begin{array}{cccccccccc} 1 & 2 & 3 & 4 & & & M-2 & M-1 & M & M+1 \end{array} \\
\begin{bmatrix}
1 & -1 & 0 & 0 & & & 0 & 0 & 0 & 0 \\
F_2 & G_2 & H_2 & 0 & & & 0 & 0 & 0 & 0 \\
0 & F_3 & G_3 & H_3 & & & 0 & 0 & 0 & 0 \\
 & \cdot & & & \cdot & & & \cdot & & \\
 & \cdot & & & \cdot & & & \cdot & & \\
 & \cdot & & & \cdot & & & \cdot & & \\
0 & 0 & 0 & 0 & & & F_{M-1} & G_{M-1} & H_{M-1} & 0 \\
0 & 0 & 0 & 0 & & & 0 & F_M & G_M & H_M \\
0 & 0 & 0 & 0 & & & 0 & 0 & 0 & 1
\end{bmatrix} \end{array}
\times
\begin{bmatrix} p'_{j,1} \\ p'_{i,2} \\ p'_{i,3} \\ \cdot \\ \cdot \\ \cdot \\ p'_{i,M-1} \\ p'_{i,M} \\ p'_{i,M+1} \end{bmatrix}
=
\begin{bmatrix} 0 \\ -p'_{i-1,2} \\ -p'_{i-1,3} \\ \cdot \\ \cdot \\ \cdot \\ -p'_{i-1,M-1} \\ -p'_{i-1,M} \\ p'_{1,M+1} + q \end{bmatrix}$$

Matrix 6.1

, where $F_k = \frac{k_r\, K\, \Delta t}{\gamma_w\, w^2\, r_k}(r_k - w)$, $G_k = \frac{k_r\, K\, \Delta t}{\gamma_w\, w^2\, r_k}(w - 2r_k) - 1$ and $H_k = \frac{k_r\, K\, \Delta t}{\gamma_w\, w^2}$

6.2.2. Hysteretic damping soil

6.2.2.1. Purely radial flow

Considering the constitutive equation (1.1), and by assuming zero deviatoric strain increment, the volumetric strain derivative can be expressed using the backward difference, as follows:

$$\left(\frac{\partial \varepsilon_{vol}}{\partial t}\right)_{i,k} = \frac{\varepsilon_{vol_{i,k}} - \varepsilon_{vol_{i-1,k}}}{\Delta t} = \frac{d\varepsilon_{vol_{i,k}}}{\Delta t} = \frac{dp'_{i,k}}{A_{i-1,k}\,\Delta t} \tag{6.13}$$

According to equation (6.5) for the purely radial flow, the central difference for the 2nd order radial derivative and the backward difference for the 1st order radial derivative are used:

- $\left(\frac{\partial^2 p'}{\partial r^2}\right)_{i,k} = \frac{p'_{i,k+1} - 2p'_{i,k} + p'_{i,k-1}}{w^2}$ central difference
- $\left(\frac{\partial p'}{\partial r}\right)_{i,k} = \frac{p'_{i,k} - p'_{i,k-1}}{w}$ backward difference

Thus, by substituting to equation (6.5):

$$\frac{k_r}{\gamma_w}\left(\frac{p'_{i,k+1} - 2p'_{i,k} + p'_{i,k-1}}{w^2} + \frac{1}{r_k}\frac{p'_{i,k} - p'_{i,k-1}}{w}\right) = \frac{p'_{i,k} - p'_{i-1,k}}{A_{i-1,k}\,\Delta t} \tag{6.14}$$

Assuming that:

$$\frac{k_r\, A_{i-1,k}\,\Delta t}{\gamma_w\, w^2\, r_k} = Q^*_k \tag{6.15}$$

We finally obtain:

$$Q^*_k r_k p'_{i,k+1} + \left(-2Q^*_k r_k + Q^*_k w - 1\right)p'_{i,k} + \left(Q^*_k r_k - Q^*_k w\right)p'_{i,k-1} = -p'_{i-1,k}$$
$$for\ k = 2{:}\,M \tag{6.16}$$

Initial conditions are the geostatic pressures at the field (equation 6.11) and the boundary conditions are the permeable circumference of the drain for $r = R_d$ and the non-permeable circumference for $r = R_e$ (equations (6.12a) and (6.12b) respectively). Thus, at time $t = t_i$, $M + 1$ linear equations are solved, in order to calculate the mean effective stresses $p'_{i,k}$. The system of linear equations (6.16), (6.11) and (6.12) can be written in matrix form according to Matrix 6.1, by substituting:

$$F_k = F^*_{i-1,k} = \frac{k_r\, A_{i-1,k}\,\Delta t}{\gamma_w\, w^2\, r_k}(r_k - w),\ G_k = G^*_{i-1,k} = \frac{k_r\, A_{i-1,k}\,\Delta t}{\gamma_w\, w^2\, r_k}(w - 2r_k) - 1$$

and $H_k = H^*_{i-1,k} = \frac{k_r A_{i-1,k} \Delta t}{\gamma_w w^2}$.

6.2.2.2 Combined radial and vertical flow

If the case of combined radial and vertical flow through the soil deposit towards the boundaries is examined, according to equation (6.4), the governing equation would be:

$$\frac{k_r}{\gamma_w}\left(\left(\frac{\partial^2(-p')}{\partial r^2}\right)_{i,j,k} + \frac{1}{r_k}\left(\frac{\partial(-p')}{\partial r}\right)_{i,j,k}\right) + \frac{k_z}{\gamma_w}\left(\frac{\partial^2(-\Sigma dp')}{\partial z^2}\right)_{i,j,k} = -\left(\frac{\partial \varepsilon_{vol}}{\partial t}\right)_{i,j,k} \Rightarrow \quad (6.17)$$

, where: $parameter_{i,j,k} = parameter_{time,\ height,\ radius}$. Accordingly to what has been discussed in chapter 3 where purely vertical flow was examined, the soil deposit of total height H is discretized into Z steps of size equal to h, so that $Z = H/h$, and the vertical distance of each node j from the base, is $z_j = h\,(j-1), for\ j = 1{:}\,Z+1$. Differential equation (6.17) is solved according to the finite differences approach. Two different techniques are employed; the implicit and the explicit method.

Implicit method

Considering the central difference for the 2nd order radial derivative, the backward difference for the 1st order radial derivative, the central difference for the 2nd order height derivative and the backward difference for the 1st order time derivative:

- $\left(\frac{\partial^2(-p')}{\partial r^2}\right)_{i,j,k} = -\left(\frac{\partial^2 p'}{\partial r^2}\right)_{i,j,k} = -\frac{p'_{i,j,k+1} - 2p'_{i,j,k} + p'_{i,j,k-1}}{w^2}$ central difference
- $\left(\frac{\partial(-p')}{\partial r}\right)_{i,j,k} = -\left(\frac{\partial p'}{\partial r}\right)_{i,j,k} = -\frac{p'_{i,j,k} - p'_{i,j,k-1}}{w}$ backward difference
- $\left(\frac{\partial^2(-\Sigma dp')}{\partial z^2}\right)_{i,j,k} = -\left(\frac{\partial^2(\Sigma dp')}{\partial z^2}\right)_{i,j,k} = -\frac{\Sigma dp'_{i,j+1,k} - 2\Sigma dp'_{i,j,k} + \Sigma dp'_{i,j-1,k}}{h^2} =$
  $-\left(\frac{p'_{i,j+1,k} - 2p'_{i,j,k} + p'_{i,j-1,k}}{h^2} + \frac{-p'_{0,j+1,k} + 2p'_{0,j,k} - p'_{0,j-1,k}}{h^2}\right)$ central difference
- $\left(\frac{\partial \varepsilon_{vol}}{\partial t}\right)_{i,j,k} = \frac{\varepsilon vol_{i,j,k} - \varepsilon vol_{i-1,j,k}}{\Delta t}$ backward difference

and by substituting to equation (6.17), we obtain:

$$\frac{k_r}{\gamma_w}\left(\frac{p'_{i,j,k+1} - 2p'_{i,j,k} + p'_{i,j,k-1}}{w^2} + \frac{1}{r_k}\frac{p'_{i,j,k} - p'_{i,j,k-1}}{w}\right) + \frac{k_z}{\gamma_w}\left(\frac{p'_{i,j+1,k} - 2p'_{i,j,k} + p'_{i,j-1,k}}{h^2} + \frac{-p'_{0,j+1,k} + 2p'_{0,j,k} - p'_{0,j-1,k}}{h^2}\right) = \frac{\varepsilon vol_{i,j,k} - \varepsilon vol_{i-1,j,k}}{\Delta t} \quad (6.18)$$

Considering the constitutive equation (1.1), and by assuming zero deviatoric strain increment, the volumetric strain derivative can be expressed using the backward difference, as follows:

$$\frac{\varepsilon_{vol_{i,j,k}}-\varepsilon_{vol_{i-1,j,k}}}{\Delta t}=\frac{d\varepsilon_{vol_{i,j,k}}}{\Delta t}=\frac{dp'_{i,j,k}}{A_{i-1,j,k}\Delta t}=\frac{p'_{i,j,k}-p'_{i-1,j,k}}{A_{i-1,j,k}\,\Delta t} \tag{6.19}$$

Thus, assuming that $\frac{k_r\,A_{i-1,j,k}\,\Delta t}{\gamma_w\,w^2\,r_k}=F_{r\,i-1,j,k}$ and $\frac{k_z\,A_{i-1,j,k}\,\Delta t}{\gamma_w\,h^2}=F_{z\,i-1,j,k}$ and by substituting to equation (6.18), we finally obtain:

$$F_{r\,i-1,j,k}\left[r_k\left(p'_{i,j,k+1}-2p'_{i,j,k}+p'_{i,j,k-1}\right)+w\left(p'_{i,j,k}-p'_{i,j,k-1}\right)\right]+F_{z\,i-1,j,k}\left(p'_{i,j+1,k}-2p'_{i,j,k}+p'_{i,j-1,k}\right)+F_{z\,i-1,j,k}\left(-p'_{0,j+1,k}+2p'_{0,j,k}-p'_{0,j-1,k}\right)=p'_{i,j,k}-p'_{i-1,j,k} \tag{6.20}$$

Assuming that:

- $\Pi_{1\,i-1,j,k}=F_{r\,i-1,j,k}\,r_k$
- $\Pi_{2\,i-1,j,k}=-2F_{r\,i-1,j,k}\,r_k+F_{r\,i-1,j,k}\,w-2F_{z\,i-1,j,k}-1$
- $\Pi_{3\,i-1,j,k}=F_{r\,i-1,j,k}\,(r_k-w)$
- $\Pi_{4\,i-1,j,k}=\Pi_{5\,i-1,j,k}=F_{z\,i-1,j,k}$
- $G_{i-1,j,k}=-p_{i-1,j,k}+F_{z\,i-1,j,k}\left(p_{0,j+1,k}-2p_{0,j,k}+p_{0,j-1,k}\right)$

, equation (6.20) can be written in the following form:

$$\Pi_{1\,i-1,j,k}\,p'_{i,j,k+1}+\Pi_{2\,i-1,j,k}\,p'_{i,j,k}+\Pi_{3\,i-1,j,k}\,p'_{i,j,k-1}+\Pi_{4\,i-1,j,k}\,p'_{i,j+1,k}+\Pi_{5\,i-1,j,k}\,p'_{i,j-1,k}=G_{i-1,j,k}\qquad for\ k=2{:}M\ and\ j=2{:}Z \tag{6.21}$$

Thus, at time $t=t_i$ we have $(Z-1)\times(M-1)=ZM-Z-M+1$ linear equations deriving from equation (6.21) and $(Z+1)\times(M+1)=ZM+Z+M+1$ unknown parameters; the stresses $p'_{i,j,k}\ for\ k=1{:}M+1\ and\ j=1{:}Z+1.$ Thus, $2Z+2M$ equations are required at each time step *dt* that will be provided by the boundary conditions.

The boundary conditions are:

- Permeable base ($M+1$ equations): $p'_{i,1,k}=p'_{0,1,k}+q\ \ for\ k=1{:}M+1$ (6.22a)
- Free surface ($M+1$ equations): $p'_{i,Z+1,k}=p'_{0,Z+1,k}+q\ \ for\ k=1{:}M+1$ (6.22b)
- Drain circumference – permeable boundary ($Z+1$ equations):

$$p'_{i,j,M+1} = p'_{0,j,M+1} + q \quad for\ j = 1{:}\,Z+1 \tag{6.22c}$$

- Soil unit cell circumference – impermeable boundary ($Z+1$ equations):

$$\left(\frac{\partial u}{\partial r}\right)_{i,j,1} = 0 \Rightarrow p'_{i,j,1} = p'_{i,j,2} \quad for\ j = 1{:}\,Z+1 \tag{6.22d}$$

In total, the boundary conditions are $2M + 2Z + 4$ equations. The additional 4 equations, correspond to the 4 points of the grid j, k that a vertical and a horizontal boundary meet and thus two boundary conditions co-exist. These points are:

- Drain circumference R_d – soil surface: $(j,k) = (Z+1, M+1)$
- Drain circumference R_d – soil base: $(j,k) = (1, M+1)$
- Unit cell circumference R_e – soil surface: $(j,k) = (Z+1,1)$
- Unit cell circumference R_e – soil base: $(j,k) = (1,1)$

These 4 equations came up because these points have been concluded in both horizontal and vertical boundaries. If two co-existing boundary conditions are different, the permeable boundary condition is chosen; in this case the $(Z+1,1)$ point where the free surface meets the impermeable boundary of R_e circumference and the $(1,1)$ point where the permeable base meets the R_e circumference.

The initial conditions are the geostatic pressures at the field:

- $p'_{1,j,k} = p'_{0,j,k} \quad for\ k = 1{:}\,M+1 \ \ and\ j = 1{:}\,Z+1$ (6.23)

The linear system of equations (6.21), along with the boundary conditions of equations (6.22) and the initial conditions of equations (6.23), can be written in the following matrix form:

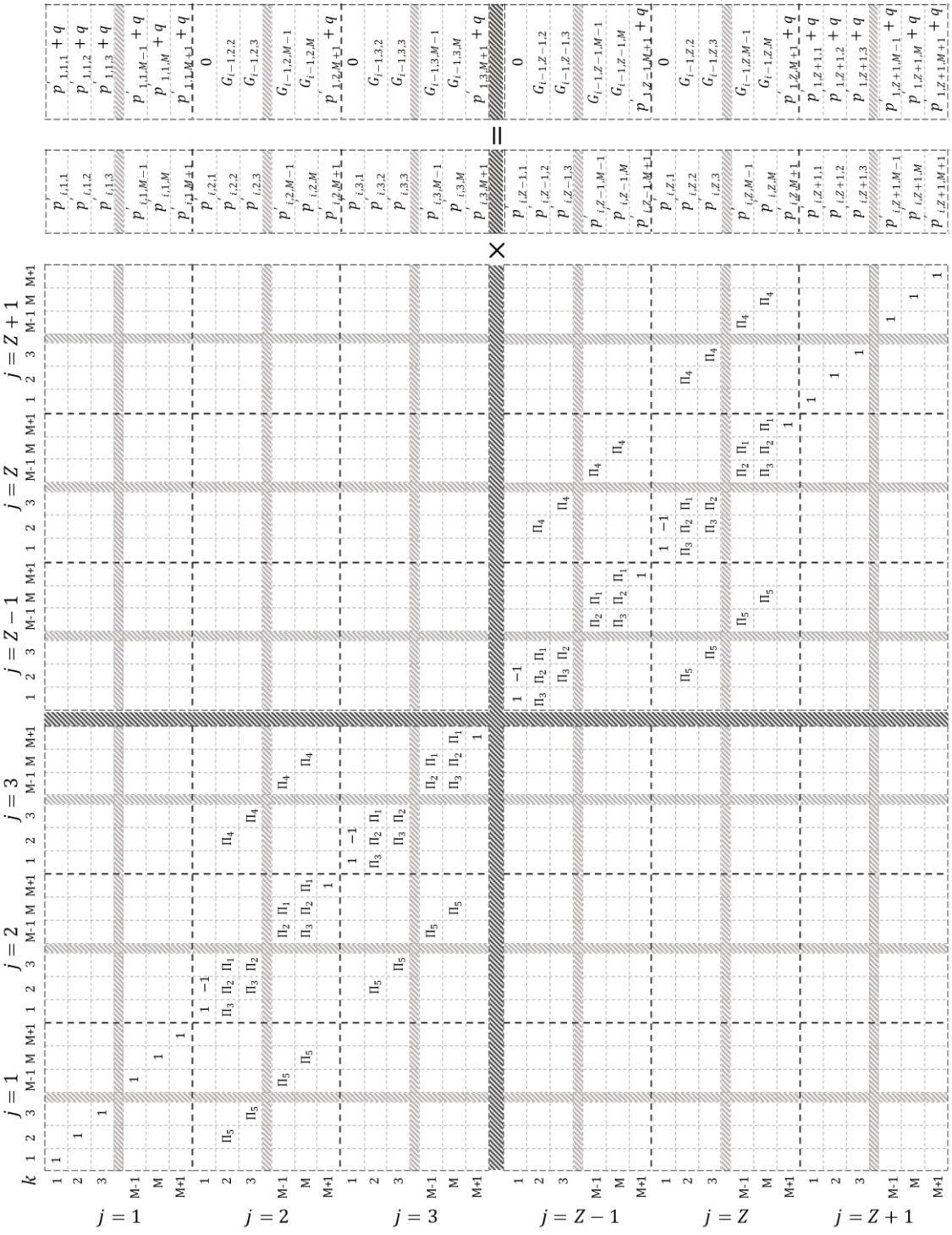

Matrix 6.2

Explicit method

The differential equation (6.17) is solved according to the following: the central difference is used for the 2nd order radial derivative, the backward difference for the 1st order radial

derivative, the central difference for the 2nd order height derivative and the forward difference (*backward difference was used in the implicit method*) for the 1st order time derivative:

- $\left(\frac{\partial^2(-p')}{\partial r^2}\right)_{i,j,k} = -\left(\frac{\partial^2 p'}{\partial r^2}\right)_{i,j,k} = -\frac{p'_{i,j,k+1}-2p'_{i,j,k}+p'_{i,j,k-1}}{w^2}$ central difference
- $\left(\frac{\partial(-p')}{\partial r}\right)_{i,j,k} = -\left(\frac{\partial p'}{\partial r}\right)_{i,j,k} = -\frac{p'_{i,j,k}-p'_{i,j,k-1}}{w}$ backward difference
- $\left(\frac{\partial^2(-\Sigma dp')}{\partial z^2}\right)_{i,j,k} = -\frac{\Sigma dp'_{i,j+1,k}-2\Sigma dp'_{i,j,k}+\Sigma dp'_{i,j-1,k}}{h^2} = -\left(\frac{p'_{i,j+1,k}-2p'_{i,j,k}+p'_{i,j-1,k}}{h^2} + \frac{-p'_{0,j+1,k}+2p'_{0,j,k}-p'_{0,j-1,k}}{h^2}\right) =$ central difference
- $\left(\frac{\partial \varepsilon_{vol}}{\partial t}\right)_{i,j,k} = \frac{\varepsilon_{vol_{i+1,j,k}}-\varepsilon_{vol_{i,j,k}}}{\Delta t}$ forward difference

By substituting to equation (6.17):

$$\frac{k_r}{\gamma_w}\left(\frac{p'_{i,j,k+1}-2p'_{i,j,k}+p'_{i,j,k-1}}{w^2}+\frac{1}{r_k}\frac{p'_{i,j,k}-p'_{i,j,k-1}}{w}\right)+\frac{k_z}{\gamma_w}\left(\frac{p'_{i,j+1,k}-2p'_{i,j,k}+p'_{i,j-1,k}}{h^2}+\frac{-p'_{0,j+1,k}+2p'_{0,j,k}-p'_{0,j-1,k}}{h^2}\right)=\frac{\varepsilon_{vol_{i+1,j,k}}-\varepsilon_{vol_{i,j,k}}}{\Delta t} \quad (6.24)$$

The volumetric strain derivative from constitutive equation (1.1), assuming zero deviatoric strain increment, can be expressed as:

$$\frac{\varepsilon_{vol_{i+1,j,k}}-\varepsilon_{vol_{i,j,k}}}{\Delta t}=\frac{d\varepsilon_{vol_{i+1,j,k}}}{\Delta t}=\frac{dp'_{i+1,j,k}}{A_{i,j,k}\Delta t}=\frac{p'_{i+1,j,k}-p'_{i,j,k}}{A_{i,j,k}\,\Delta t} \quad (6.25)$$

Thus, assuming that $\frac{k_r\,A_{i,j,k}\,\Delta t}{\gamma_w\,w^2\,r_k}=F_{r\,i,j,k}$ and $\frac{k_z\,A_{i,j,k}\,\Delta t}{\gamma_w\,h^2}=F_{z\,i,j,k}$, we finally obtain:

$$F_{r\,i,j,k}\left[r_k\left(p'_{i,j,k+1}-2p'_{i,j,k}+p'_{i,j,k-1}\right)+w\left(p'_{i,j,k}-p'_{i,j,k-1}\right)\right]+F_{z\,i,j,k}\left(p'_{i,j+1,k}-2p'_{i,j,k}+p'_{i,j-1,k}\right)+F_{z\,i,j,k}\left(-p'_{0,j+1,k}+2p'_{0,j,k}-p'_{0,j-1,k}\right)=p'_{i+1,j,k}-p'_{i,j,k}\Rightarrow$$

$$\begin{aligned}p'_{i+1,j,k} = {} & F_{r\,i,j,k}\,r_k\,p'_{i,j,k+1}+\left(-2F_{r\,i,j,k}\,r_k+F_{r\,i,j,k}\,w-2F_{z\,i,j,k}+1\right)p'_{i,j,k}\\ & +\left(F_{r\,i,j,k}\,r_k-F_{r\,i,j,k}\,w\right)p'_{i,j,k-1}+F_{z\,i,j,k}\left(p'_{i,j+1,k}+p'_{i,j-1,k}\right)\\ & -F_{z\,i,j,k}\left(p'_{0,j+1,k}-2p'_{0,j,k}+p'_{0,j-1,k}\right)\end{aligned}$$

$$for\ j=2:Z\ \ and\ \ k=2:M \quad (6.26)$$

The boundary and initial conditions are the same with those that were valid for the implicit method, i.e. equations (6.22) and (6.23) respectively.

6.2.2.3 Modelling the finite drain permeability

According to what has been discussed in this chapter so far, a unit cell was examined around a single drain, with the drain - soil interface being modelled as a permeable boundary. Thus, a drain of infinite permeability was implied ("perfect drain"). In order to model the actual, finite drain permeability, the following reformulations have to be made. The examined radius which in this case is $R = R_e$ is discretized in M steps of size equal to w, so that $M = R/w$, and the radial distance of each node k from the center, is $r_k = R_e + w(1-k), for\ k = 1{:}\,M+1$. Two different areas are identified along a radius r_k:

- $for\ k = 1{:}\frac{R_e - R_d}{w} \Rightarrow r_k = R_e{:}\,R_d + w$
- $for\ k = \frac{R_e - R_d}{w} + 1{:}\,M+1 \Rightarrow r_k = R_d{:}\,0$

For $r_k = R_e{:}\,R_d + w$, the vertical and horizontal coefficients of permeability involved in the calculations equal to the soil coefficients, $k_z = k_{z,soil}$ & $k_h = k_{h,soil}$, while for $r_k = R_d{:}\,0$, drain permeabilities are considered: $k_z = k_{z,drain}$ & $k_h = k_{h,drain}$. The new boundary condition is, by symmetry, the impermeable center of the drain, at $r_k = 0$.

$$\left(\frac{\partial_u}{\partial_r}\right)_{i,j,M+1} = 0 \Rightarrow p'_{i,j,M+1} = p'_{i,j,M} \quad for\ j = 2{:}\,Z \tag{6.27}$$

, while the boundary condition at the soil circumference remains unchanged (equation 6.22d).

6.3. Seismic response of a site improved with drains

6.3.1. Numerical modelling

The problem examined herein, is the prediction of the seismic response of a site improved with vertical drains, under combined vertical and axisymmetric horizontal water flow. The one dimensional, vertical, shear wave propagation, that was expressed according to the diff. equation (3.12), is solved in conjunction with the consolidation equation (6.4). The last is solved according to the finite difference technique, employing the implicit and the explicit method. In what follows, the implicit method is presented.

Implicit method

Considering the central difference for the 2nd order radial derivative, the backward difference for the 1st order radial derivative, the central difference for the 2nd order height derivative and the backward difference for the 1st order time derivative:

- $\left(\frac{\partial^2(-p')}{\partial r^2}\right)_{i,j,k} = -\left(\frac{\partial^2 p'}{\partial r^2}\right)_{i,j,k} = -\frac{p'_{i,j,k+1}-2p'_{i,j,k}+p'_{i,j,k-1}}{w^2}$ central difference
- $\left(\frac{\partial(-p')}{\partial r}\right)_{i,j,k} = -\left(\frac{\partial p'}{\partial r}\right)_{i,j,k} = -\frac{p'_{i,j,k}-p'_{i,j,k-1}}{w}$ backward difference
- $\left(\frac{\partial^2(-\Sigma dp')}{\partial z^2}\right)_{i,j,k} = -\frac{\Sigma dp'_{i,j+1,k}-2\Sigma dp'_{i,j,k}+\Sigma dp'_{i,j-1,k}}{h^2} = -\left(\frac{p'_{i,j+1,k}-2p'_{i,j,k}+p'_{i,j-1,k}}{h^2} + \frac{-p'_{0,j+1,k}+2p'_{0,j,k}-p'_{0,j-1,k}}{h^2}\right)$ central difference
- $\left(\frac{\partial \varepsilon_{vol}}{\partial t}\right)_{i,j,k} = \frac{\varepsilon_{vol_{i,j,k}}-\varepsilon_{vol_{i-1,j,k}}}{\Delta t}$ backward difference

The volumetric strain time derivative is expressed according to the constitutive equation (1.1):

$$\left(\frac{\partial \varepsilon_{vol}}{\partial t}\right)_{i,j,k} = \frac{\varepsilon_{vol_{ij,k}}-\varepsilon_{vol_{i-1,j,k}}}{\Delta t} = \frac{d\varepsilon_{vol_{i,j,k}}}{\Delta t} = \frac{dp'_{i,j,k}-B_{i-1,j}d\varepsilon_{q_{i,j}}}{A_{i-1,j}\,\Delta t} = \frac{p_{i,j,k}-p'_{i-1,j,k}-B_{i-1,j}d\varepsilon_{q_{i,j}}}{A_{i-1,j}\,\Delta t}$$

Thus, by substituting to equation (6.17):

$$\frac{k_r}{\gamma_w}\left(\frac{p'_{i,j,k+1}-2p'_{i,j,k}+p'_{i,j,k-1}}{w^2}+\frac{1}{r_k}\frac{p'_{i,j,k}-p'_{i,j,k-1}}{w}\right)+\frac{k_z}{\gamma_w}\left(\frac{p'_{i,j+1,k}-2p'_{i,j,k}+p'_{i,j-1,k}}{h^2}+\frac{-p'_{0,j+1,k}+2p'_{0,j,k}-p'_{0,j-1,k}}{h^2}\right)=\frac{p'_{i,j,k}-p'_{i-1,j,k}-B_{i-1,j}d\varepsilon_{q_{i,j}}}{A_{i-1,j}\,\Delta t} \quad (6.28)$$

and assuming that $\frac{k_r\,A_{i-1,j}\,\Delta t}{\gamma_w\,w^2\,r_k} = F_{r_{i-1,j,k}}$ and $\frac{k_z\,A_{i,-1j}\,\Delta t}{\gamma_w\,h^2} = F_{z_{i-1,j,k}}$, we obtain:

$$F_{r_{i-1,j,k}}\left[r_k\left(p'_{i,j,k+1}-2p'_{i,j,k}+p'_{i,j,k-1}\right)+w\left(p'_{i,j,k}-p'_{i,j,k-1}\right)\right]+F_{z_{i-1,j,k}}\left(p'_{i,j+1,k}-2p'_{i,j,k}+p'_{i,j-1,k}\right)+F_{z_{i-1,j,k}}\left(-p'_{0,j+1,k}+2p'_{0,j,k}-p'_{0,j-1,k}\right)-p'_{i,j,k}=-p'_{i-1,j,k}-B_{i-1,j}d\varepsilon_{q_{i,j}} \Rightarrow \Pi_{1_{i-1,j,k}}p'_{i,j,k+1}+\Pi_{2_{i-1,j,k}}p'_{i,j,k}+\Pi_{3_{i-1,j,k}}p'_{i,j,k-1}+\Pi_{4_{i-1,j,k}}p'_{i,j+1,k}+\Pi_{5_{i-1,j,k}}p'_{i,j-1,k}=-p'_{i-1,j,k}-B_{i-1,j}d\varepsilon_{q_{i,j}}+F_{z_{i-1,j,k}}\left(p'_{0,j+1,k}-2p'_{0,j,k}+p'_{0,j-1,k}\right)\ for\ k=2:M\ and\ j=2:Z \quad (6.29)$$

Thus, at time $t = t_i$, $(Z-1)\times(M-1) = ZM - Z - M + 1$ linear equations arise. The boundary conditions are:

- Permeable base ($M+1$ equations): $p'_{i,1,k} = p'_{0,1,k}\ \ for\ k = 1:M+1$ (6.30a)

- Free surface ($M+1$ equations): $p'_{i,Z+1,k} = p'_{0,Z+1,k} \quad for\ k = 1{:}\,M+1$ (6.30b)
- Drain circumference – permeable boundary ($Z+1$ equations):

$$p'_{i,j,M+1} = p'_{0,j,M+1} \quad for\ j = 1{:}\,Z+1 \tag{6.30c}$$

- Soil unit cell circumference – impermeable boundary ($Z+1$ equations):

$$\left(\frac{\partial u}{\partial r}\right)_{i,j,1} = 0 \Rightarrow p'_{i,j,1} = p'_{i,j,2} \quad for\ j = 1{:}\,Z+1 \tag{6.30d}$$

In case that the finite drain permeability is modelled, instead of equation (6.30c), the boundary condition would be the impermeable center of the drain, at $r_k = 0$, expressed by equation (6.27). Accordingly, when a non-permeable base rock is examined the boundary condition at the base would be expressed according to equation (3.25). The problem initial conditions are the geostatic pressures at the field (equation 6.23). The linear system of equation (6.29), along with the boundary conditions of equations (6.30) and the initial conditions of equations (6.23), can be written in matrix form according to matrix 6.2, by substituting:

$G_{i-1,j,k} = -p'_{i-1,j,k} - B_{i-1,j} d\varepsilon_{q_{i,j}} + F_{z_{i-1,j,k}} \left(p'_{0,j+1,k} - 2p'_{0,j,k} + p'_{0,j-1,k}\right)$ and $q = 0$.

6.3.2 Condensing the radial degree of freedom

According to the presented methodology, at the end of each time step *dt*, the mean effective stresses $p' = p'_{i,j,k}$, are calculated at every node j,k of the grid. However, the shear wave propagation is executed in the (one dimensional) vertical axis. Thus, wave propagation is calculated according to a characteristic, mean value of the mean effective stress $p'^{*} = p'^{*}(t,z)$ along an examined radius of the model. This value corresponds to the geometric mean value of the mean effective stresses along a radius and is calculated according to the following equation:

$$p'^{*}_{i,j} = \left. \sum_{=1}^{M+1} \left(\frac{r_k}{R_e}\right)^2 p'_{i,j,k} \right/ \sum_{=1}^{M+1} \left(\frac{r_k}{R_e}\right)^2 \tag{6.31}$$

A schematic depiction of the discretization of the grid, according to the presented methodology, of a unit cell R_e and height *H*, improved with a drain R_d is given in Figure 6.2. In sum, within each time step *dt*, a linear system of $(Z+1)\cdot(M+1)$ equations is solved and the mean effective stresses $p'_{i,j,k}$, at every point of the grid (along each model column and

radius), are calculated. The geometrical mean values of the mean effective stresses ${p'}^*_{i,j}$ along each radius are estimated. These mean values of stresses are used in order to execute to one dimensional vertical shear wave propagation. The horizontal displacements and shear stains that arise, are fed back into the equations of consolidation to estimate the mean effective stress $p'_{i+1,j,k}$ of the next time step and so on.

6.3.2. Soil -drainage mechanical interaction

When a site is improved with gravel columns, the presence of a material different from the native soil affects the response under the seismic loading. In the present study, the mechanical interaction between the native ground and the gravel pile is taken into consideration by analyzing the soil-drain system, as an equivalent single–phase material. The equivalent shear modulus of the soil - gravel pile system, is formulated under the assumption of equal shear stresses in the gravel pile and the surrounding soil (Baez and Martin 1993), as follows:

$$G_{system} = (1 - a_s)G_{soil} + a_s G_{drain} \tag{6.32}$$

, where $a_s = \left(\frac{R_d}{R_e}\right)^2$ is the soil replacement ratio.

An alternative approach, would be to express the equivalent shear modulus of the system according to the assumption of equal shear strains between the gravel pile and the surrounding soil (Bouckovalas et al. 2006). The equivalent shear modulus of the system would then be calculated by the following relation:

$${G_{system}}^{-1} = (1 - a_s){G_{soil}}^{-1} + a_s {G_{drain}}^{-1} \tag{6.33}$$

The investigation of the effect on the performance of the algorithm of the alternative equations (6.32) and (6.33) through comparison with detailed numerical analyses, is beyond the scope of the thesis but is a topic for author's future research.

6.4. Numerical algorithm validation

The proposed numerical algorithm is validated against a set of non-linear, dynamic, three dimensional, numerical analyses that were carried out in the finite differences program FLAC3D (Itasca, 2006), by Tsiapas and Tsioulou (2009) and by Bouckovalas et al. (2011a). A thin liquefiable sand layer of D_r=60%, improved with vertical drains with radius R_d=0.5m and a center-to-center distance (2 R_e) equal to 2.8m, was examined. The sand was encased between clayey layers, in order to establish purely horizontal flow towards the drains. The constitutive model that was employed for the numerical analyses was the bounding surface plasticity model *NTUA-SAND* by Andrianopoulos et al. (2010).

A draft of the model that was analyzed by the proposed algorithm is drawn in Figure 6.3. The water table was placed at the surface of the model. In accordance with the numerical analyses (Tsiapas and Tsioulou (2009) and Bouckovalas et al. (2011a)) at which the vertical effective stress in the middle of the sand layer was equal to σ'_0=100kPa, a mean effective stress equal to p'_0=66.6kPa was applied at the same depth. Clay layers were assumed to be elastic, with the material properties listed in Figure 6.3. The mechanical drain - soil interaction (Equations 6.32 & 6.33) was not taken into account and the drain – soil interface was analyzed as a permeable surface (drain of infinitely large permeability). The model was excited with a sinusoidal acceleration time history of 12 uniform loading cycles on its base, with maximum acceleration a_{max}=0.08 g and period T=0.2s. Five values of sand permeability k were examined and for each one of them the evolution with time of the excess pore water pressure at the center of the sand layer was attained.

The calibration of Ta-Ger model was based in the undrained response of the sand and was attained by analyzing the configuration of Figure 6.3, considering zero permeability for the sand. According to Bouckovalas et al. (2011a), initial liquefaction was achieved after N_{cycle}=5-6 uniform loading cycles. The approximation of the numerical response by the model is depicted in Figure 6.4. The undrained cyclic response in *DSS* element test predicted by the calibrated model is depicted in Figures 6.5 and 6.6, under constant stress amplitude τ_{max}=8kPa and τ_{max}=16kPa respectively. The calibration concerned the specified sand with D_r=60%, under initial mean effective stress p_0'=66.6 kPa. In accordance with what has been discussed in the relevant section, the response observed in the laboratory is reproduced by the calibrated model. Specifically, the first undrained loading cycles of constant stress amplitude are

associated with a rapid decrease of effective stress, followed by a decrease in the rate of stress reduction, until a critical threshold is reached where the reduction accelerates again, to finally achieve liquefaction. This behavior is more obvious in the moderate stress element test, where a large number of cycles is required to cause liquefaction (Figure 6.5). The evolution of the undrained component of n, n_u (Equation 2.7), that controls the changes in the rate of p' reduction ($n_0 \rightarrow n_{peak} \rightarrow n_f$) is also illustrated in the same figures against the mean effective stress and the cumulative deviatoric strain.

The convergence between 3D numerical analyses and model predictions is presented in Figure 6.7, for the 5 examined sand permeabilities: k= 5 10^{-6}, 10^{-5}, 2 10^{-5}, 5 10^{-5} and 10^{-4} m/s. The undrained response is also included in the figure. The approximation of the Bouckovalas et al. (2011a) curves is adequate in terms of the maximum value of r_u, while the same trend is observed in both approximations; i.e. the maximum value is obtained at an early stage of loading and consequently excess pore water pressure decreases, even though the applied external loading continues. The driving mechanism behind this response is rigorously described in Bouckovalas et al. (2011b).

The numerically predicted excess pore pressure time histories of Figure 6.7 refer to the mid-distance between the drains, i.e. for $r = R_e$. However, because of limitations imposed by the proposed model, in order to maintain consistency, curves calculated by the model refer to the characteristic mean value of r_u across a soil radius (according to equation 6.31). However, the deviation between this mean value and the maximum value observed at the soil circumference $r = R_e$ is not substantial, as is pointed out in Figure 6.8. Figure 6.8 illustrates the distributions of the maximum value of r_u across a soil radius around the drain, predicted by the proposed model. As expected, $r_{u,max}$ attains its maximum value at the soil circumference and decreases close to the drain, until it becomes zero at the circumference of the drain, $r = R_d$. It is reminded, that the drain is modelled as infinitely permeable. While Figures 6.7 and 6.8 represent the response in the mid-depth of the sand layer, the range of mean effective stresses evolution within the sand layer, is illustrated in Figure 6.9. The observed trend is that the range decreases as the maximum attained r_u decreases and that the response in the center of the layer (red line) approaches the upper limit of the range. In all cases, the upper limit represents the sand area close to the interface with the base clayey layer and the bottom limit the sand close to the top clayey layer. Initially geostatic conditions are almost restored by 3s, for permeabilities greater than 2 10^{-5} m/s. Finally, the variations of the mean effective stress

are elaborately captured by Figures 6.10 and 6.11. After the rapid decrease of *p'* observed during the first loading cycles, the reduction decreases until a critical point where horizontal drainage dominates the response and *p'* begins to recover. In the same figure, the diagram of the exponents *n*, n_u and n_d against Σde_q is given. One can observe that as the amount of *p'* reduction gets more limited the cumulative deviatoric strain at the end of shaking decreases, a performance within expectations. Calibrated parameters n_u, n_d and *n* were calculated according to the following:

$$n_u \rightarrow according\ to\ eq.[2.7]\ for\colon\ n_0 = 0.4, n_{peak} = 4, n_f = 0.2, b = 120, g = 150$$

$$n_d \rightarrow according\ to\ eq.[2.7]\ for\colon\ n_0 = 0.4, n_{peak} = 35, n_f = 35, b = 31, g = 0$$

$$n \rightarrow according\ to\ eq.[2.6]\ for\colon\ A = 200$$

It is noted that for the scope of the presented analyses, the drained component of *n*, n_d, has attained its initial form (Tasiopoulou and Gerolymos, 2016).

6.5 Applications

6.5.1 Uniform sandy soil profile under sinusoidal base excitation

In what follows, an application of the developed model is presented, that concerns a soil profile with total height *H*=15m, of uniform sand with D_r=50%, under a sinusoidal base excitation of 15 uniform loading cycles. The objective of the application is to examine model predictions of the mitigation of the maximum r_u, provided by the horizontal drainage through soil drains. The following cases are examined: (i) fully undrained conditions, (ii) vertical water flow during earthquake shaking; base rock is considered permeable and (iii) simultaneous vertical and horizontal flow during shaking, using a drain of diameter $2R_d$, spacing $2R_e$ and height *h*=15m, for R_d / R_e= 0.1, (iv) R_d / R_e= 0.2, (v) R_d / R_e= 0.3 and (vi) R_d / R_e= 0.4. Three cases of R_e are examined; (i) R_e =1m, (ii) R_e =2m and (iii) R_e =4m and for each one of them, five values of sand permeability are examined; (i) from *k*=2 10^{-5}m/s to *k*=2 10^{-6}m/s, (ii) from *k*=2 10^{-4}m/s to *k*=2 10^{-5}m/s and (iii) from *k*=2 10^{-3}m/s to *k*=2 10^{-4}m/s respectively. The results are depicted in Figures 6.12 to 6.14 in terms of maximum r_u distributions with depth. The r_u values correspond to the geometrical mean value of r_u along a soil radius and were calculated according to the equation 6.10.

Overall, the following observations can be made; (i) the distributions of Figures 6.12 and 6.13, evince that the effect of solely vertical flow in comparison to the fully undrained response, is negligible in the specified cases (the permeabilities examined are relatively small) and is apparent only at the base of the soil profile, close to the permeable rock. Exclusively vertical flow has prominent results in the r_u mitigation, for sand permeabilities k=2 10^{-4}m/s or larger (Figure 6.14). (ii) The shape of the maximum r_u distributions in the case of exclusively vertical flow of Figure 6.14, denotes that the "bulge" of maximum values has been lightly shifted to more shallow depths compared to the undrained response and in some cases values of $r_{u,max}$ exceed the corresponding undrained values, as we move along to the surface. Furthermore, the part of the curve that corresponds to depths bigger that the depth where the maximum $r_{u,max}$ is observed is steeper compared to the close to the surface part of the curve. This response is most likely attributed to the fact that the elastic shear and therefore the bulk modulus are increasing with depth (according to Equation 2.2 for the small strains bulk modulus) which leads to quicker water flow and more rapidly pore pressure dissipation at greater depths. (iii) In general, the effects on mitigating liquefaction depend on the radius of the drain, the drain spacing and the permeability of the sand. For the greatest of the permeabilities examined in each figure (k=2 10^{-5}m/s, k=2 10^{-4}m/s and k=2 10^{-3}m/s in Figures 6.12, 6.13 and 6.14 respectively) all the studied replacement ratios are sufficient to maintain the maximum pore pressures in very modest values. Maximum r_u distributions gradually increase as the sand permeability decreases, and the response almost coincides with the undrained response for the cases of Figures 6.12 and 6.13, for the lowest of the examined permeabilities.

It is noted that, in the presented analyses no mechanical interaction between soil and drain was considered and the drain was modelled as a "perfect drain", i.e. drain with fully permeable surface. The constitutive model calibration was selected according to what has been discussed in chapter 2, based on Ishibashi and Zhang (1993) $G{:}\gamma$, $\xi{:}\gamma$ curves for the drained response and Idriss (1995) *MSF* curve for the undrained response. Parameter A of equation 2.7 was set equal to 50.

6.5.2 The Port Island array in the 1995 Kobe earthquake, improved with vertical drains

In this section, the case of the Port Island array in the 1995 Kobe earthquake improved with vertical drains to mitigate liquefaction effects, is studied. The soil profile of Table 4.1, enhanced with a 16m deep drain is analyzed and a drain diameter and drain spacing are selected, aiming to keep the peak excess pore-water pressures below a specified threshold, for the specified earthquake motion. In order to achieve a maximum excess pore water pressure $r_{u\,max} < 0.5$, a R_d =1m and a R_e =1.5m are required, according to the analysis. The required coverage ratio R_d/R_e=0.67 seems to be exceptionally large, however it is reminded that the surficial 19m of the profile consist of a very loose sand of D_r=30% approximately, subjected to a very intense excitation. In view of that, gravel piles accompanied by vibratory compaction of the surrounding loose sand deposits, would be necessary in order to reduce to required replacement ratio. It has to be mentioned, that the foresaid analysis was conducted without taking into consideration the mechanical interaction between the surrounding soil and the stiffer soil material of the drain (Equations 6.32 & 6.33), in order to examine the benefits of the radial drainage exclusively. Finally, it is noted that as in the case of a previous section where the original Port Island profile was examined, the calibration (methodology and parameter values) was maintained as it was initially presented in chapter 2 of the dissertation, adopting the stratification and V_p, V_s and *SPT* distributions abstracted from the literature.

The results of the improved analyzed profile compared to the original one, are presented in Figures 6.15 to 6.17. The distributions with depth of Figure 6.15 evince that the abatement of the maximum pore pressure from soil surface to -16m results in limited shear strains and horizontal displacements at the same depths, while the accelerations and shear strains distributions are not widely affected. The surface accelerations time histories of the improved and the original profile are given in Figure 6.16. The first part of the response (shadowed area at the figure) is almost identical in both cases examined and represents the pre-liquefaction part of the response. During this part, as has been previously discussed, soil amplification phenomena can be observed, as has been documented in the literature (Tsiapas and Bouckovalas, 2019). The rest part of the response, is way more intense in the case of the drain improved profile compared to the "weak" original response, a fact that signalizes the liquefaction phenomena that tool place. Similar remarks can be made for the elastic response spectra at the surface of Figure 6.17, where the high frequency components have been

amplified and the low frequencies have been suppressed by the drain improved profile, while the opposite behavior is observed for the original profile.

References

Adalier, K., Elgamal, A., Meneses, J., & Baez, J. I. (2003). Stone columns as liquefaction countermeasure in non-plastic silty soils. *Soil Dynamics and Earthquake Engineering*, *23*(7), 571-584.

Andrianopoulos, K. I., Papadimitriou, A. G., & Bouckovalas, G. D. (2010). Explicit integration of bounding surface model for the analysis of earthquake soil liquefaction. *International Journal for Numerical and Analytical Methods in Geomechanics*, *34*(15), 1586-1614.

Baez J, Martin G. (1993, May). Advances in the design of vibro systems for the improvement of liquefaction resistance. In *Symposium Ground Improvement* (pp. 1-16).

Bouckovalas, G., Dimitriadi, V., Tsiapas, Y., & Tsioulou, A. (2011a, January). Numerical simulation of drain performance in liquefiable soils. In *Proceedings of the 5th International Conference on Earthquake Geotechnical Engineering, Santiago, Chile* (pp. 10-13).

Bouckovalas, G. D., Papadimitriou, A. G., Kondis, A., & Bakas, G. J. (2006, September). Equivalent-uniform soil model for the seismic response analysis of sites improved with inclusions. In *Proc., 6th European Conf. on Numerical Methods in Geotechnical Engineering* (pp. 801-807).

Bouckovalas, G. D., Papadimitriou, A. G., & Niarchos, D. (2009). Gravel drains for the remediation of liquefiable sites: the Seed & Booker (1977) approach revisited. In *Proceedings of International Conference on Performance-Based Design in Earthquake, IS-Tokyo*.

Bouckovalas, G. D., Papadimitriou, A. G., Niarchos, D. G., & Tsiapas, Y. Z. (2011b). Sand fabric evolution effects on drain design for liquefaction mitigation. *Soil Dynamics and Earthquake Engineering*, *31*(10), 1426-1439.

Harada, N., Towhata, I., Takatsu, T., Tsunoda, S., & Sesov, V. (2006). Development of new drain method for protection of existing pile foundations from liquefaction effects. *Soil Dynamics and Earthquake Engineering*, *26*(2-4), 297-312.

Howell, R. L. (2013). The performance of lateral spread sites treated with prefabricated vertical drains: Physical and numerical models.

Howell, R., Rathje, E. M., & Boulanger, R. W. (2015). Evaluation of simulation models of lateral spread sites treated with prefabricated vertical drains. *Journal of Geotechnical and Geoenvironmental Engineering*, *141*(1), 04014076.

Howell, R., Rathje, E. M., Kamai, R., & Boulanger, R. (2012). Centrifuge modeling of prefabricated vertical drains for liquefaction remediation. *Journal of geotechnical and geoenvironmental engineering*, *138*(3), 262-271.

Iai S, Koizumi K. Estimation of earthquake induced excess pore pressure for gravel drains. In: Proceedings of the 7th Japan Earthquake Symposium; 1986, p. 679–84.

Japanese Geotechnical Society. (1998). Remedial measures against soil liquefaction, Balkema, Rotterdam, Netherlands.

Lambe, T. W., and Whitman, R. V. (1969). Soil mechanics. John Wiley and Sons, Inc., New York, N.Y.

Marinucci, A., Rathje, E., Kano, S., Kamai, R., Conlee, C., Howell, R., ... & Gallagher, P. (2008). Centrifuge testing of prefabricated vertical drains for liquefaction remediation. In *Geotechnical earthquake engineering and soil dynamics IV* (pp. 1-10).

Matsubara, K., Mihara, M., & Tsujita, M. (1988). Analysis of gravel drain against liquefaction and its application to design. In *Proceedings, 9th World Conference on Earthquake Engineering* (Vol. 3, pp. 249-254).

Onoue, A. (1988). Diagrams considering well resistance for designing spacing ratio of gravel drains. Soils Found., 28(3), 160–168.

Papadimitriou, A. G., Bouckovalas, G. D., Vytiniotis, A. C., & Bakas, G. J. (2006, September). Equivalence between 2D and 3D numerical simulations of the seismic response of improved sites. In *6th European Conference on Numerical Methods in Geotechnical Engineering, Graz* (pp. 6-8).

Pestana, J. M., Hunt, C. E., & Goughnour, R. R. (1997). *FEQDrain: A finite element computer program for the analysis of the earthquake generation and dissipation of pore water pressure in layered sand deposits with vertical drains*. Earthquake Engineering Research Center, University of California.

Priebe, H. J. (1991). The prevention of liquefaction by vibro replacement. In *International conference on earthquake resistant construction and design* (pp. 211-219).

Rollins, K., Anderson, J. K., Goughnour, R. R., & McCain, A. K. (2004, August). Liquefaction hazard mitigation using vertical composite drains. In *The 13th World Conference on Earthquake Engineering. Vancouver BC, Canada*.

Seed, H. B., and Booker, J. R. (1977). Stabilization of potentially liquefiable sand deposits. J. Geotech. Engrg. Div., 103(7), 757–768.

Seid-Karbasi, M., & Byrne, P. M. (2007). Seismic liquefaction, lateral spreading, and flow slides: a numerical investigation into void redistribution. *Canadian Geotechnical Journal*, *44*(7), 873-890.

Tasiopoulou, P., & Gerolymos, N. (2016). Constitutive modeling of sand: Formulation of a new plasticity approach. *Soil Dynamics and Earthquake Engineering*, *82*, 205-221.

Tsiapas, Y. Z., & Bouckovalas, G. D. (2019). Equivalent linear computation of response spectra for liquefiable sites: the spectral interpolation method. *Soil Dynamics and Earthquake Engineering*, *116*, 541-551.

Tsiapas, I., & Tsioulou, A. (2009). *Revised design of drains for seismic liquefaction mitigation* (Doctoral dissertation, Diploma Thesis, School of Civil Engineering, National Technical University of Athens).

Vytiniotis, A., & Whittle, A. J. (2013). Effectiveness of PV drains for mitigating earthquake-induced deformations in sandy slopes. In *Geo-Congress 2013: Stability and Performance of Slopes and Embankments III* (pp. 908-917).

Figures

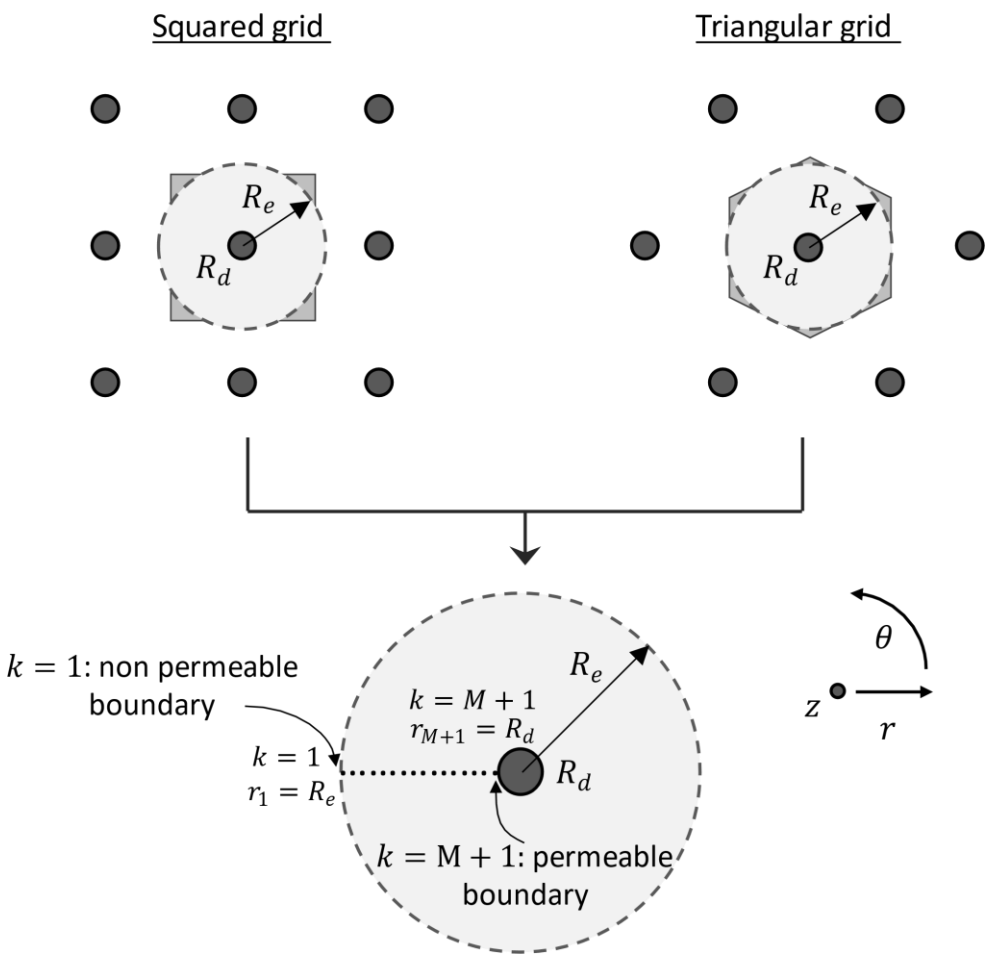

Figure 6.1. Squared and triangular configuration of vertical drains of radius R_d .Schematic depiction of the discretization and boundary conditions (drain of infinite permeability) across a soil radius R_e, according to the proposed algorithm.

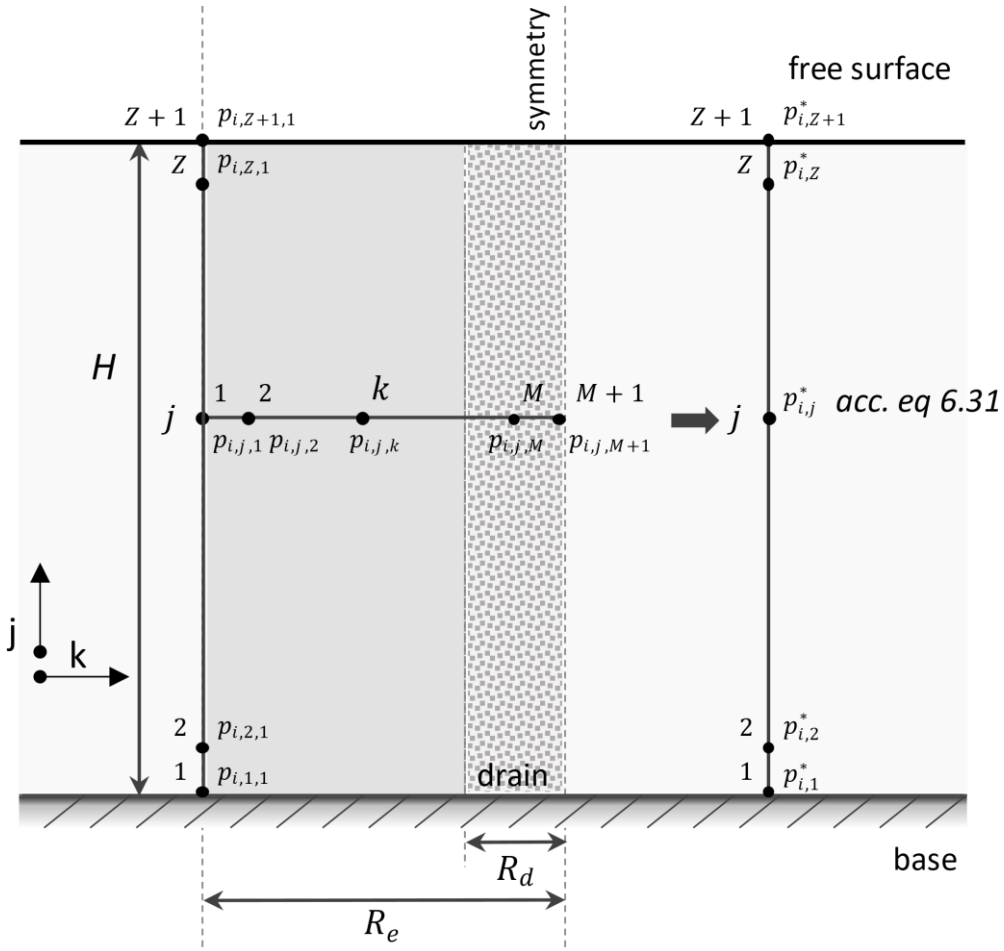

Figure 6.2. Schematic depiction of the discretization along the vertical and the horizontal axis (considering the actual finite permeability of the drain) according to the proposed algorithm.

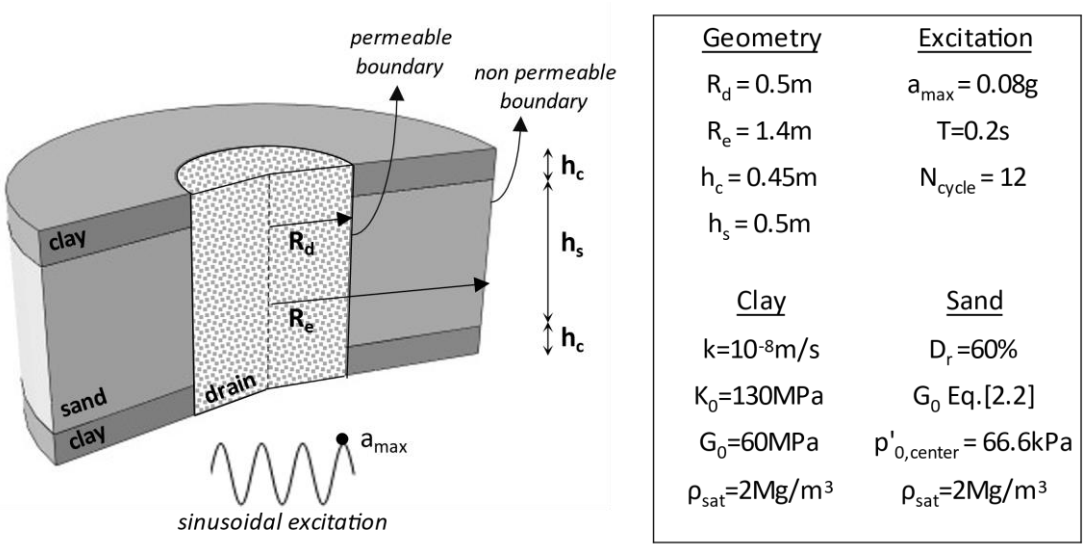

Figure 6.3. Schematic depiction of the configuration of drain improved liquefiable sand encased between two impermeable clay layers, that was analyzed in order to validate the proposed algorithm against 3D numerical analyses with FLAC 3D Itasca (Bouckovalas et al. 2011a).

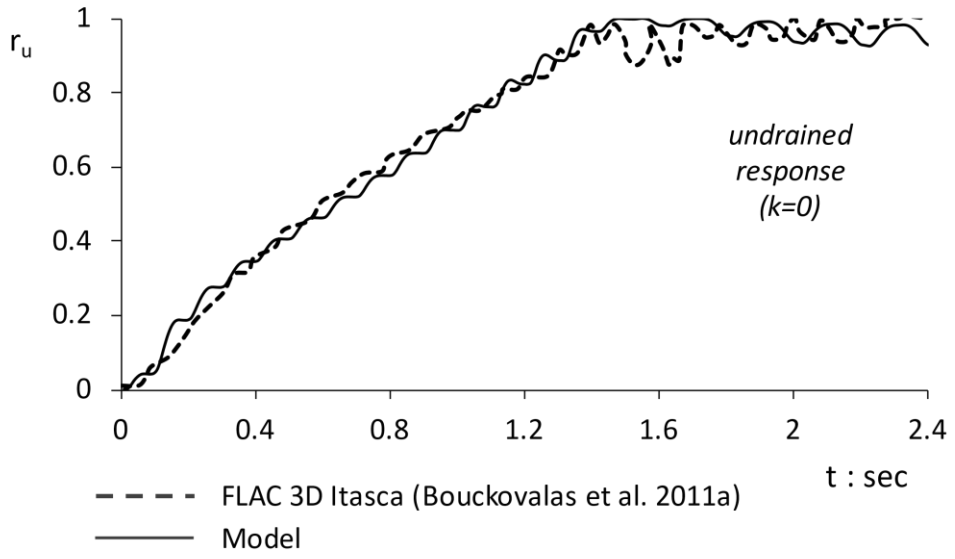

Figure 6.4. Excess pore water pressure time history of the undrained response of the configuration presented in Figure 6.3, in the middle of the sand layer.

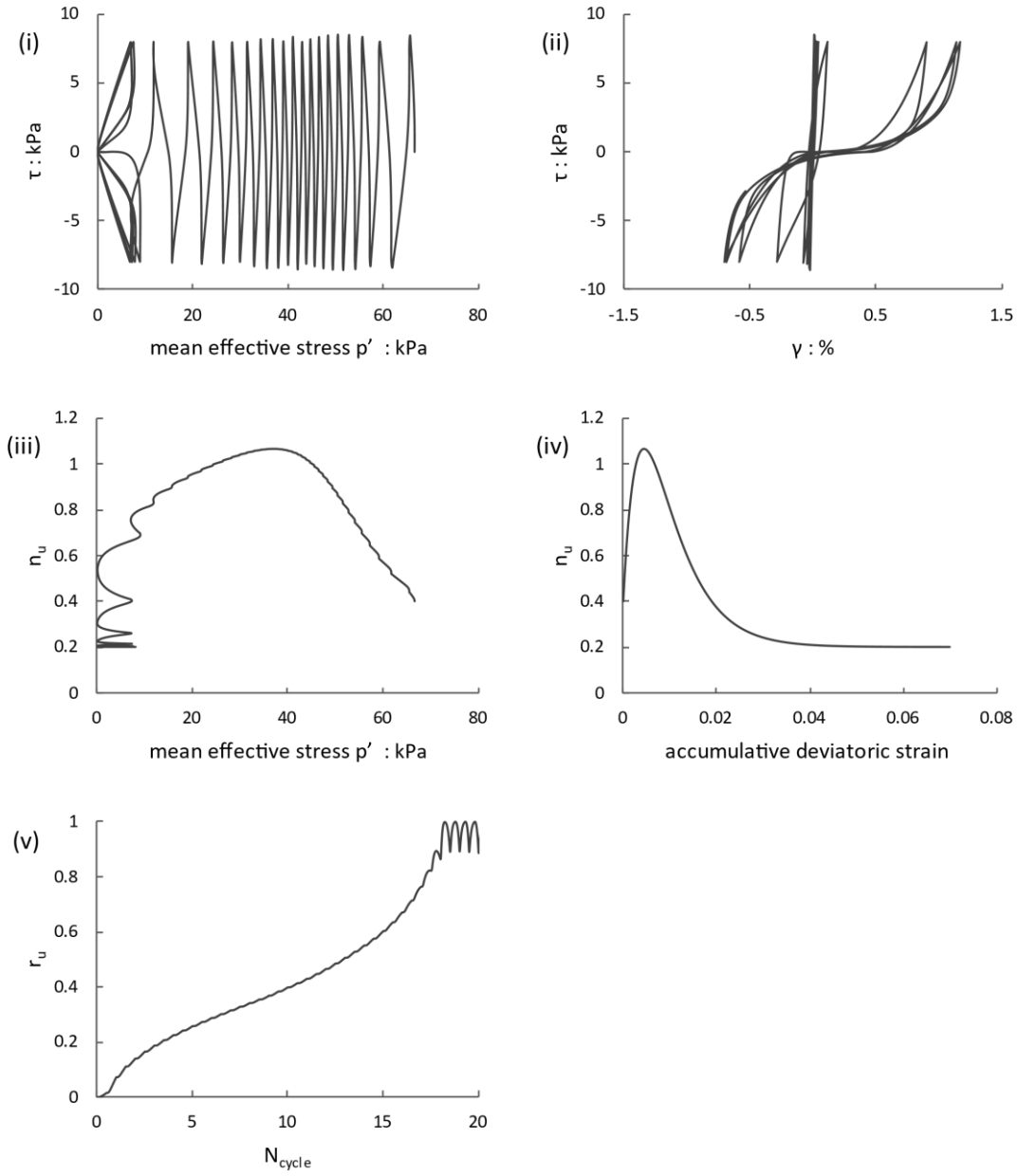

Figure 6.5. Computed undrained cyclic *DSS* response of a sand specimen with D_{r0}=60% and p'_0=66.6kPa, under maximum imposed shear stress τ_{max}=8kPa. The response is illustrated in terms of: (i) mean effective stress – shear stress, (ii) shear strain – shear stress, (iii) mean effective stress – exponent n_u, (iv) cumulative deviatoric strain - exponent n_u and (v) sinucoidal loading cycles – excess pore pressure. The calibration of the model has been based on matching the response with the undrained response of the sand in the 3D f.d. analyses with FLAC 3D Itasca (Bouckovalas et al. 2011a).

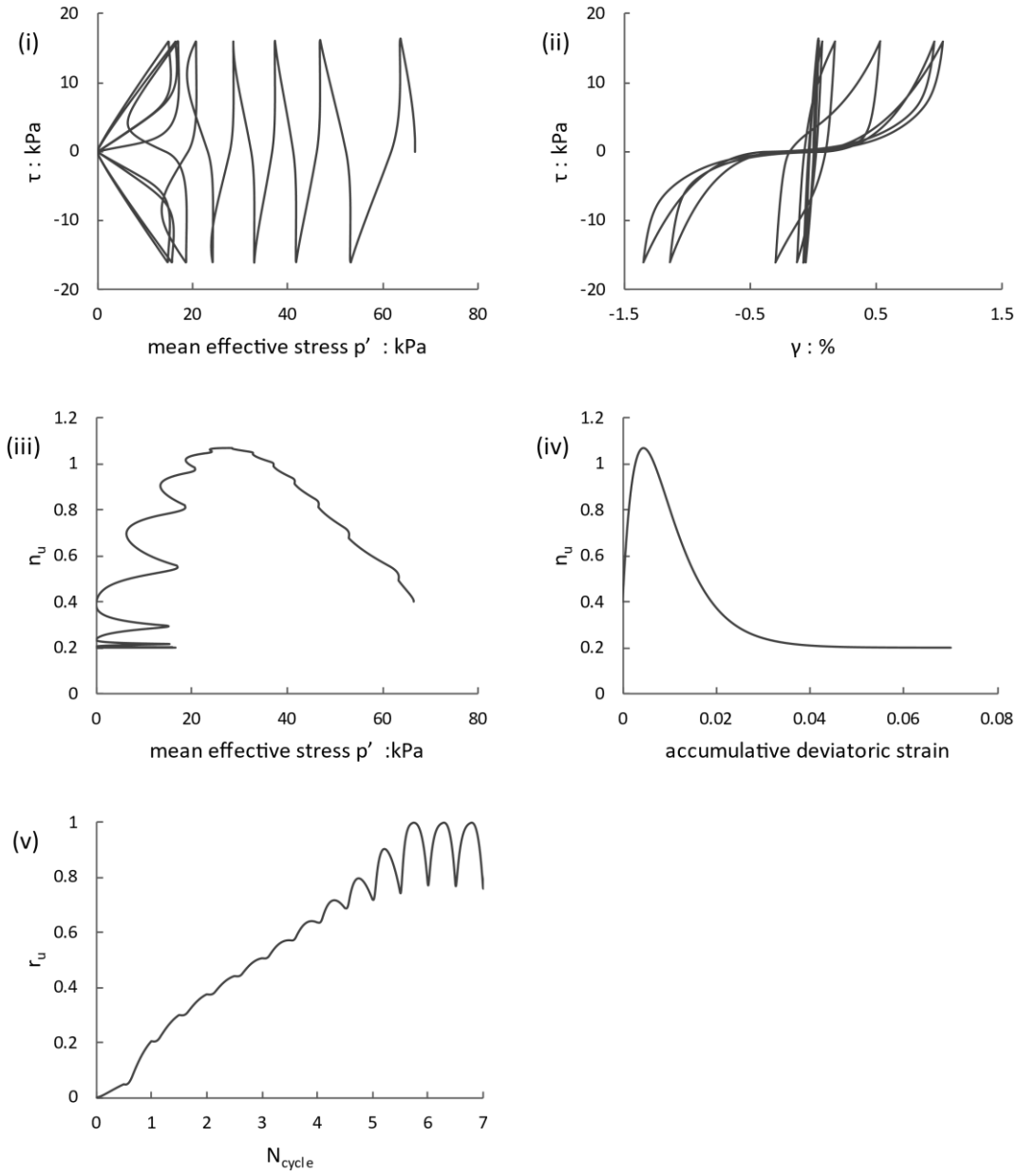

Figure 6.6. Computed undrained cyclic *DSS* response of a sand specimen with D_{r0}=60% and p'_0=66.6kPa, under maximum imposed shear stress τ_{max}=16kPa. The response is illustrated in terms of: (i) mean effective stress – shear stress, (ii) shear strain – shear stress, (iii) mean effective stress – exponent n_u, (iv) cumulative deviatoric strain - exponent n_u and (v) sinucoidal loading cycles – excess pore pressure. The calibration of the model has been based on matching the response with the undrained response of the sand in the 3D f.d. analyses with FLAC 3D Itasca (Bouckovalas et al. 2011a).

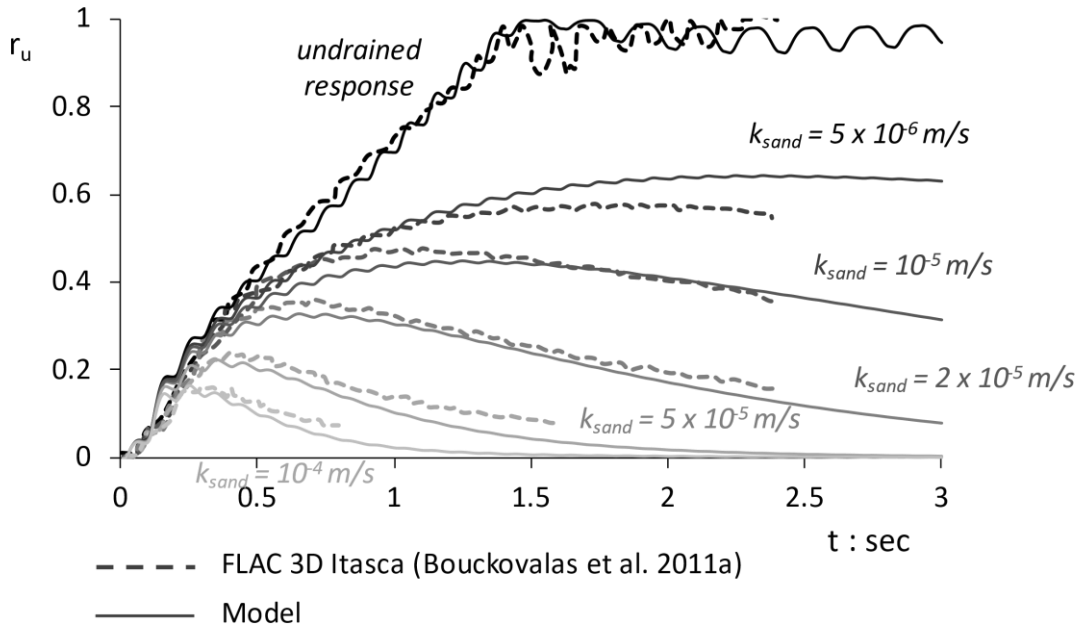

Figure 6.7. Validation of the proposed algorithm based on 3D f.d. analyses in FLAC 3D Itasca (Bouckovalas et al. 2011a), in terms of the evolution with time of the excess pore water pressure in the center of a thin sand layer set between clayey layers, with vertical drain of R_d=0.5m and R_e=1.4m for sand permeability k: (i) 5 10^{-6} m/s, (ii) 10^{-5} m/s, (iii) 2 10^{-5} m/s, (iv) 5 10^{-5} m/s and (v) 10^{-4} m/s. Curves refer to the geometric mean value of r_u across a soil radius (equation 26).

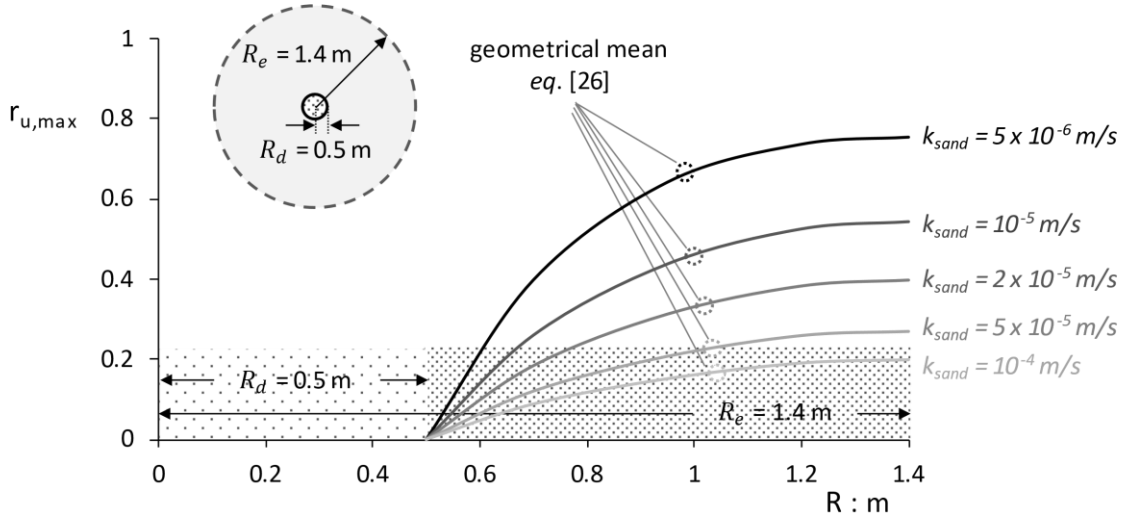

Figure 6.8. Distribution of the maximum excess pore water pressure along the soil radius R_e=1.4m and drain radius R_d=0.5m for sand permeability k: (i) 5 10^{-6} m/s, (ii) 10^{-5} m/s, (iii) 2 10^{-5} m/s, (iv) 5 10^{-5} m/s and (v) 10^{-4} m/s. The geometric mean value of r_u along the radius according to equation [26], that is used to execute the one dimensional vertical wave propagation, is also depicted.

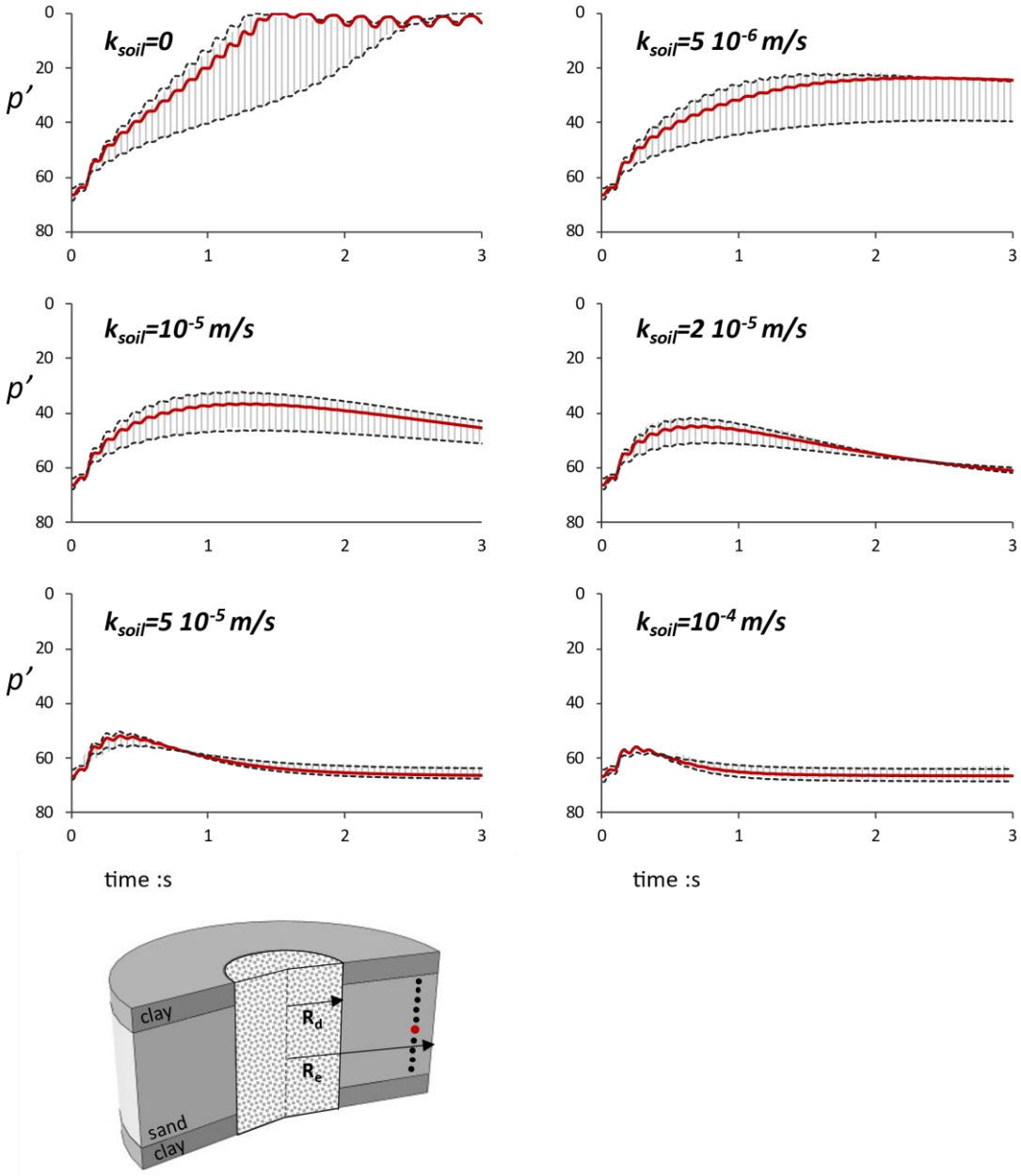

Figure 6.9. Evolution with time of the mean effective stress of the sand (the red line represents the center of the sand layer and the shaded area is the range of values within the layer) for soil radius R_e=1.4m and drain radius R_d=0.5m, for sand permeability k: (i) 5 10^{-6} m/s, (ii) 10^{-5} m/s, (iii) 2 10^{-5} m/s, (iv) 5 10^{-5} m/s and (v) 10^{-4} m/s.

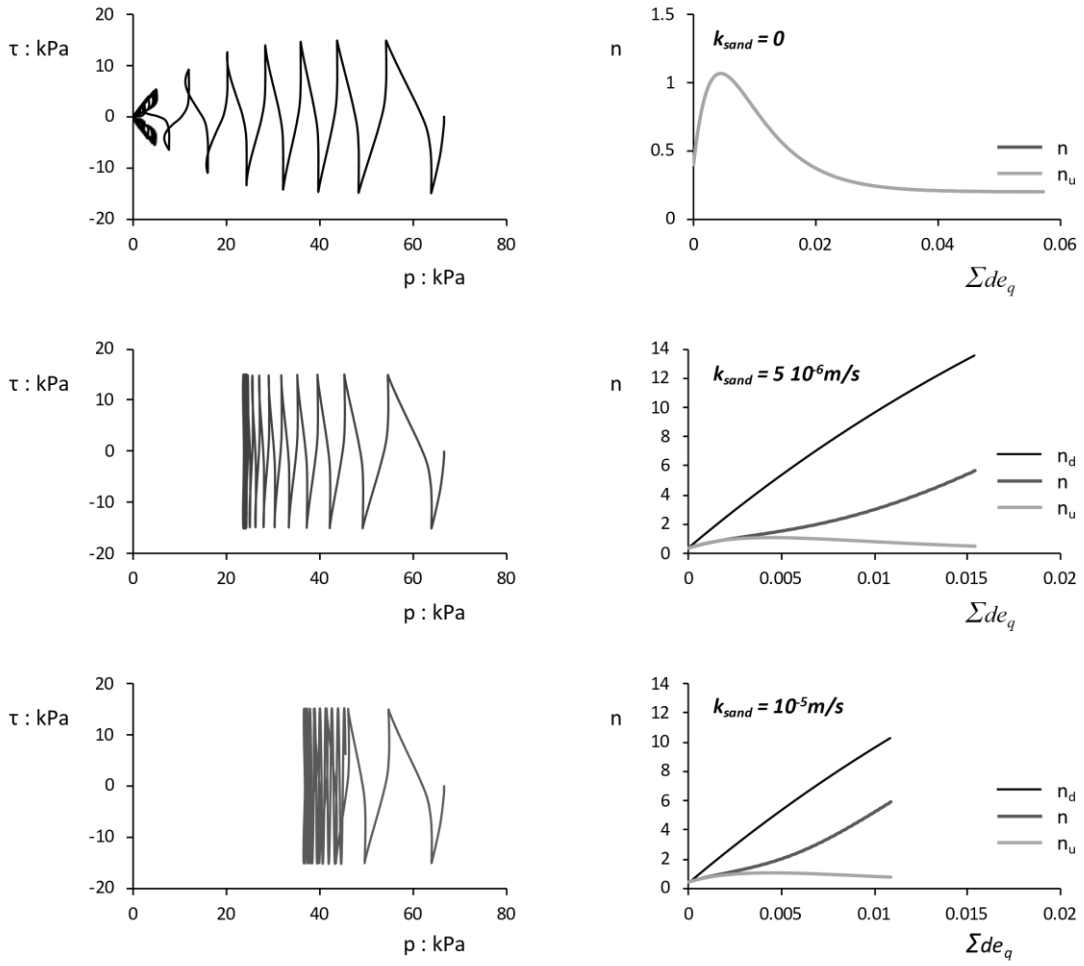

Figure 6.10. Sand response in terms of the evolution of the mean effective stress with the shear stress and the evolution of the exponent n and its components n_u and n_d with the cumulative deviatoric strain, for sand permeability k: (i) 0, (ii) 5 10^{-6} m/s and (iii) 10^{-5} m/s. (iii) 2 10^{-5} m/s, (iv) 5 10^{-5} m/s and (v) 10^{-4} m/s.

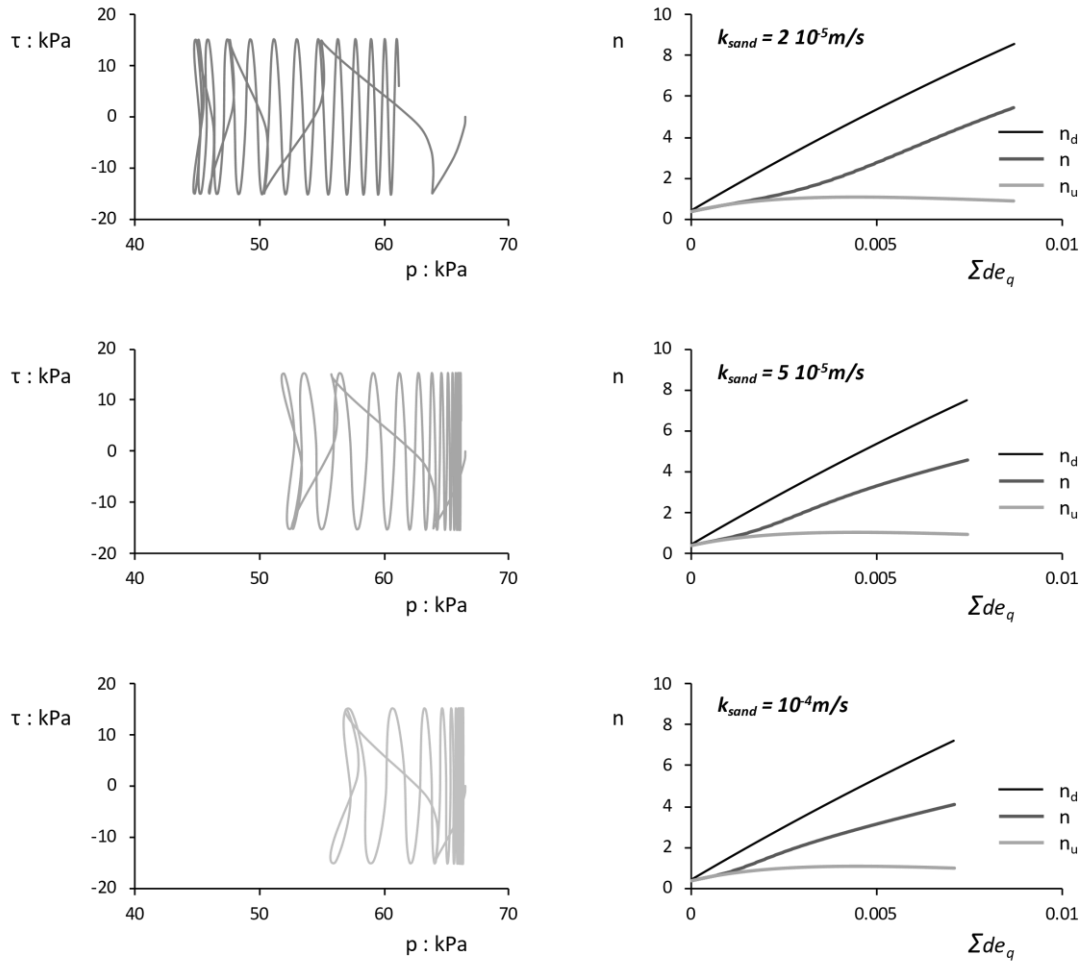

Figure 6.11. Sand response in terms of the evolution of the mean effective stress with the shear stress and the evolution of the exponent n and its components n_u and n_d with the cumulative deviatoric strain, for sand permeability k: (i) 2 10^{-5} m/s, (ii) 5 10^{-5} m/s and (iii) 10^{-4} m/s.

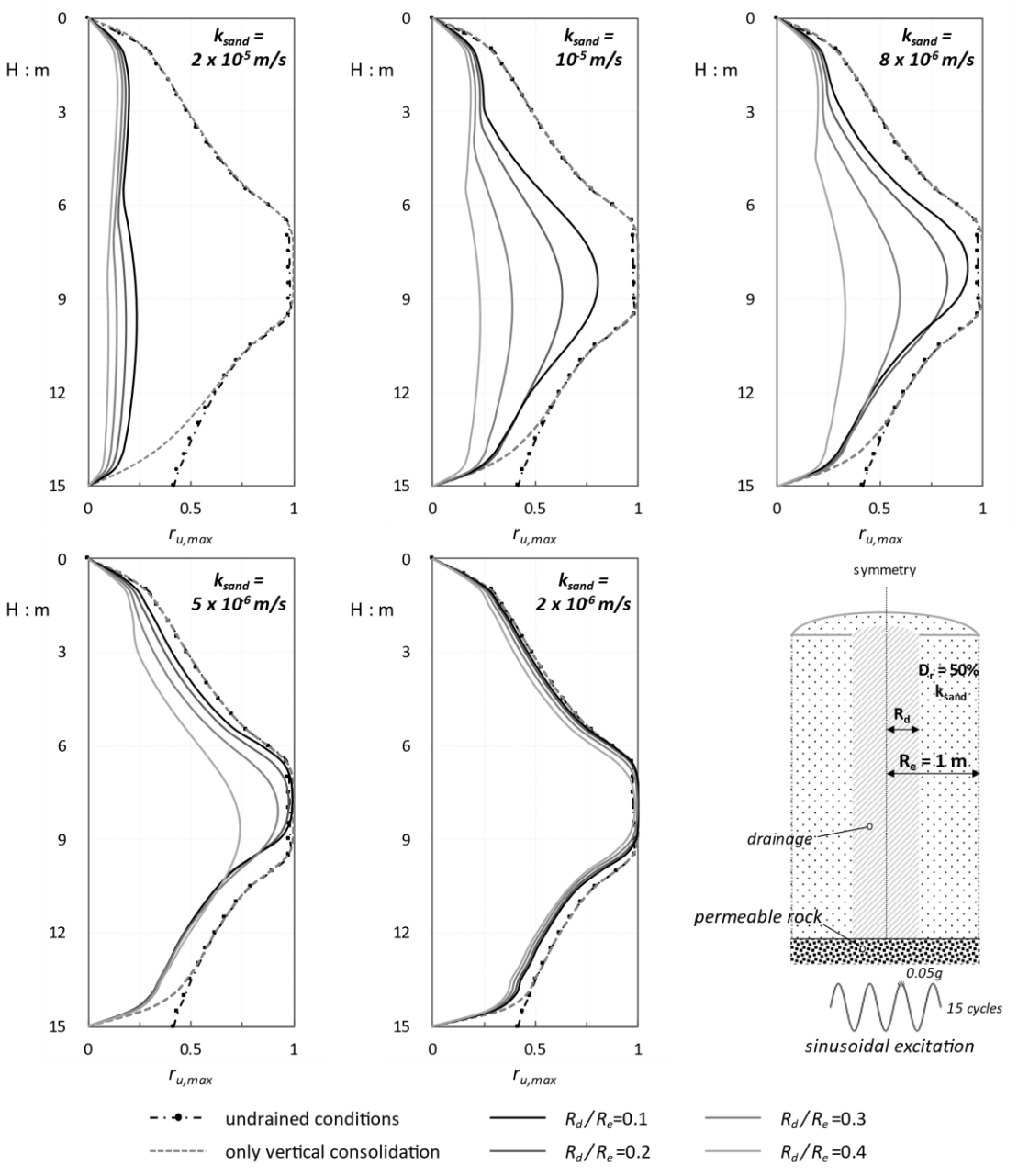

Figure 6.12. Model predictions of the distributions with depth of the maximum excess pore water pressure $r_{u,max}$ considering: (i) undrained conditions, (ii) vertical flow, (iii) combined vertical and horizontal flow with R_d/R_e=0.1, (iv) R_d/R_e=0.2, (v) R_d/R_e=0.3 and (vi) R_d/R_e =0.4, where R_d is the drain radius and R_e=1m the radius of the surrounding soil, for a uniform sand column of H=15m and D_r=50%, under sinusoidal excitation.

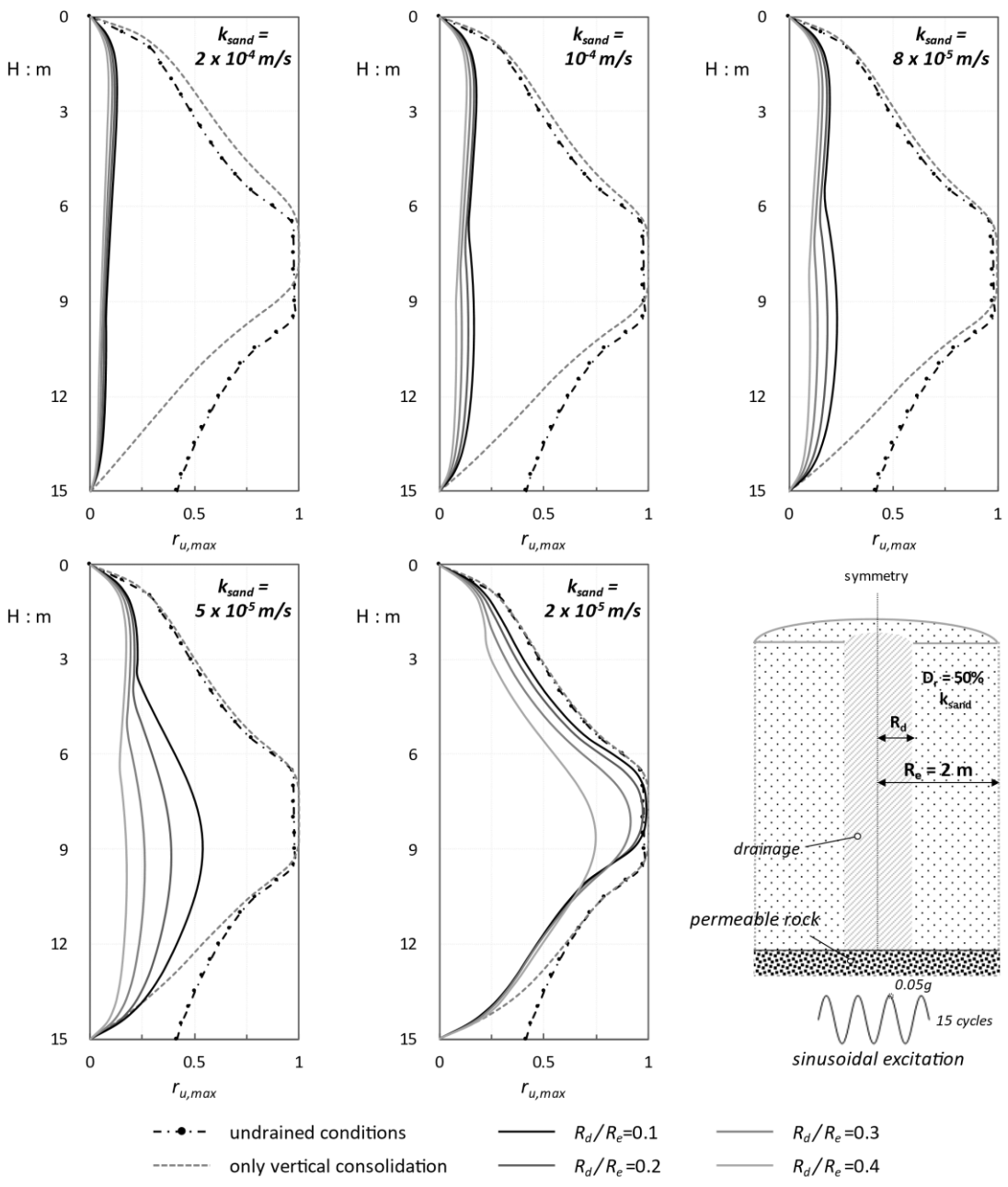

Figure 6.13. Model predictions of the distributions with depth of the maximum excess pore water pressure $r_{u,max}$ considering: (i) undrained conditions, (ii) vertical flow, (iii) combined vertical and horizontal flow with R_d/R_e=0.1, (iv) R_d/R_e=0.2, (v) R_d/R_e=0.3 and (vi) R_d/R_e =0.4, where R_d is the drain radius and R_e=2m the radius of the surrounding soil, for a uniform sand column of H=15m and D_r=50%, under sinusoidal excitation.

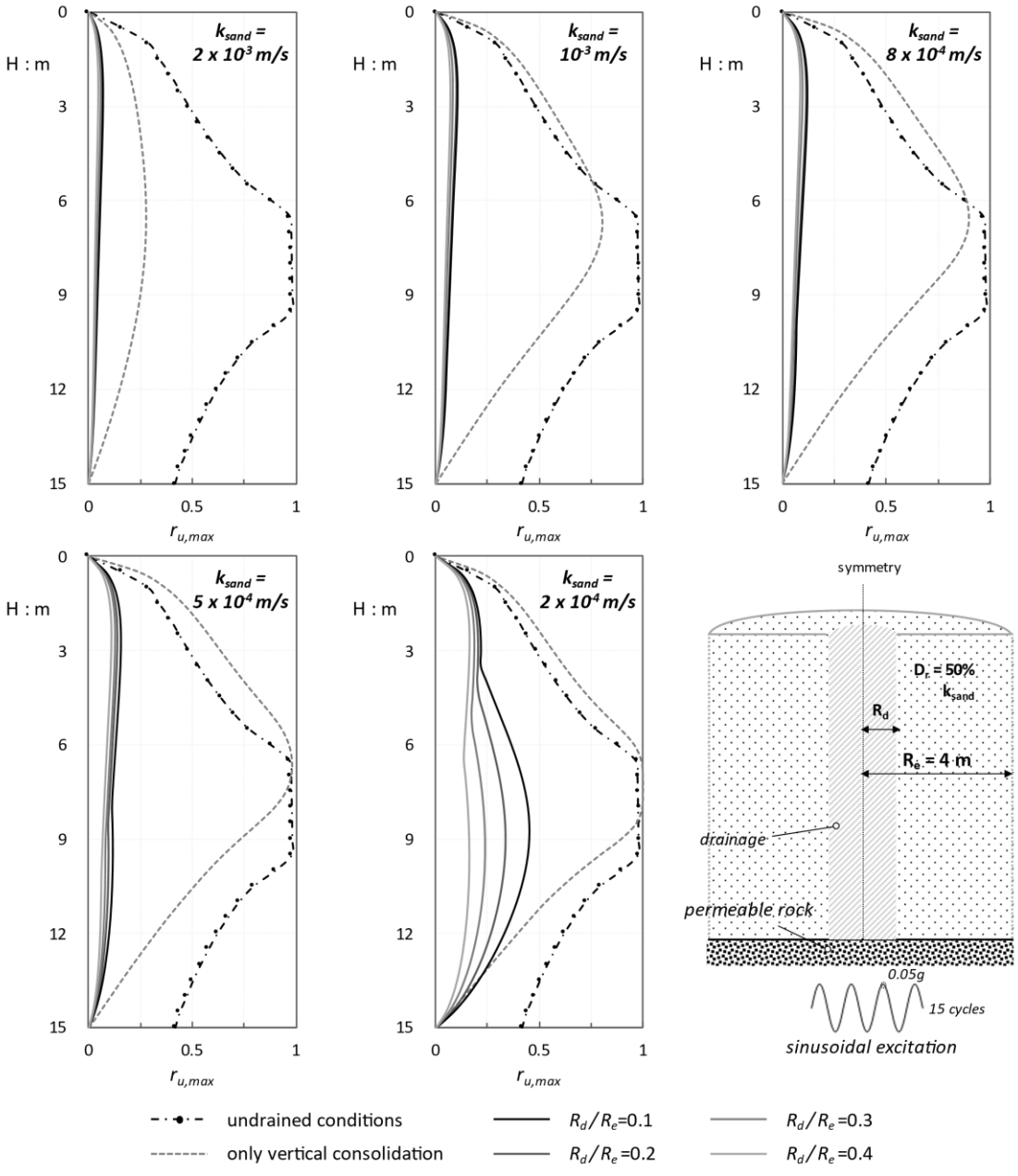

Figure 6.14. Model predictions of the distributions with depth of the maximum excess pore water pressure $r_{u,max}$ considering: (i) undrained conditions, (ii) vertical flow, (iii) combined vertical and horizontal flow with R_d/R_e=0.1, (iv) R_d/R_e=0.2, (v) R_d/R_e=0.3 and (vi) R_d/R_e =0.4, where R_d is the drain radius and R_e=4m the radius of the surrounding soil, for a uniform sand column of H=15m and D_r=50%, under sinusoidal excitation.

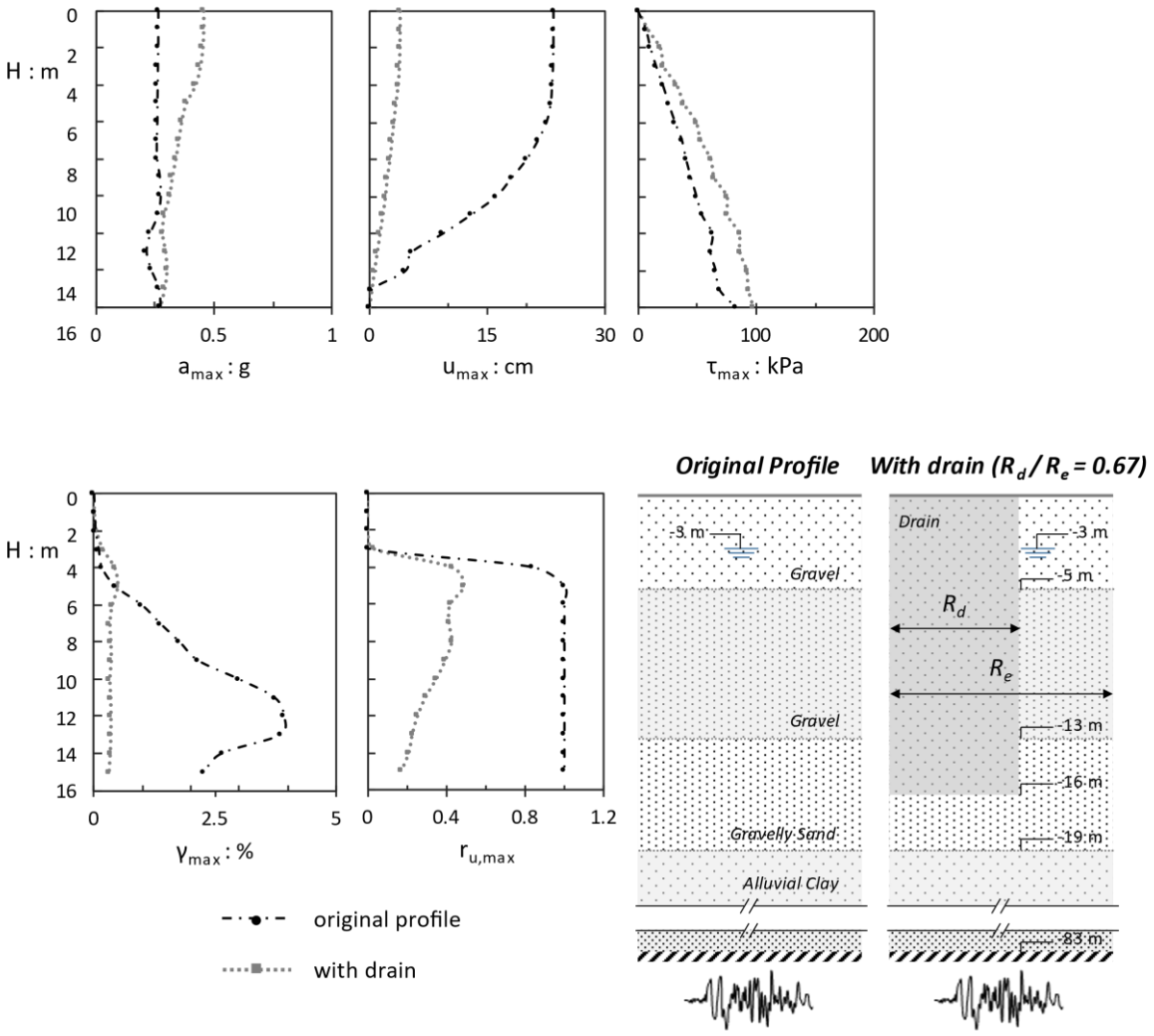

Figure 6.15. Distributions with depth of the maximum: (i) acceleration, (ii) horizontal displacement relative to the displacement at -16m, (iii) shear stress, (iv) shear strain and (v) excess pore water pressure, for the soil profile of Table 1 and for the same profile enhanced with a vertical drain up to -16m, with R_d =1m and R_e =1.5m (base excitation: NS component of the Kobe Port Island, 1995 record).

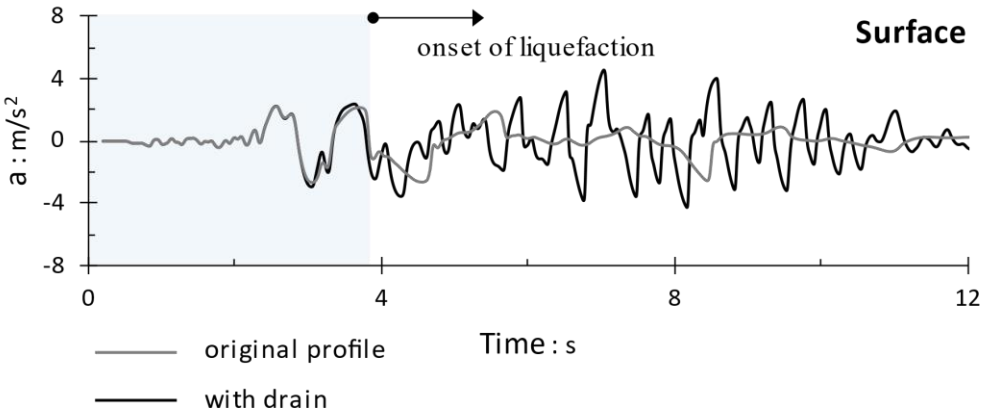

Figure 6.16. Acceleration time history at the surface of the soil profile of Table 1 and for the same profile enhanced with a vertical drain up to -16m, with R_d =1m and R_e =1.5m (base excitation: NS component of the Kobe Port Island, 1995 record).

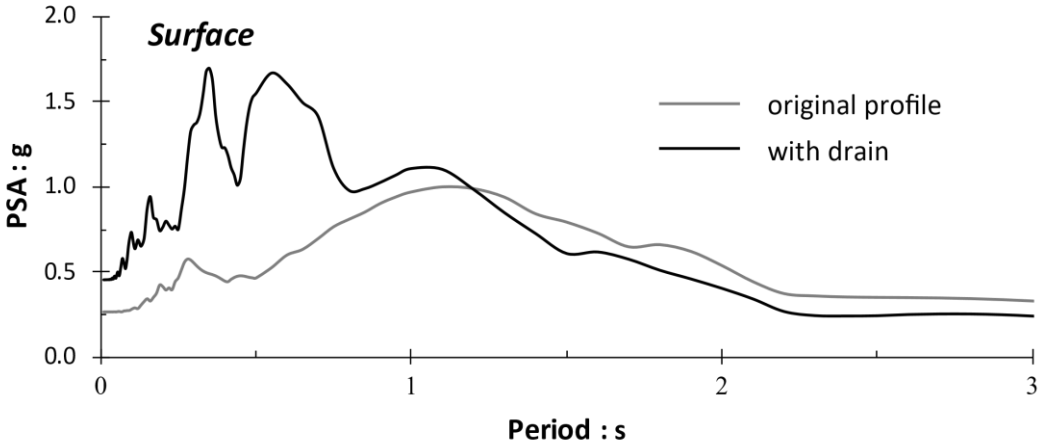

Figure 6.17. Elastic acceleration response spectrum at the surface of the soil profile of Table 1 and for the same profile enhanced with a vertical drain up to -16m, with R_d =1m and R_e =1.5m (base excitation: NS component of the Kobe Port Island, 1995 record).

Chapter 7

Conclusions

A plasticity-based model was developed for site response analysis of horizontally layered soil deposits. The model is a *p*-*q* version of Ta-Ger constitutive law for sand (Tasiopoulou and Gerolymos 2016a, b) after modifications to allow for flexibility in reproducing the response in both drained and undrained load conditions without re-adjusting the values of the parameters. The calibration was based on matching the response in terms of the liquefaction resistance ratio and experimental shear modulus and damping ratio curves available in the literature. It was shown that the calibrated model reproduced the macroscopic response in terms of the aforementioned design curves with sufficient engineering accuracy, while at the same time maintained its capability to yield physically meaningful results at the stress-strain level, consistent with the observed response.

The model was then implemented into a finite difference computer code to perform 1D nonlinear site response analysis. The accuracy of the model's prediction was tested against analytical solutions of the amplification function for non homogenous shear wave velocity profiles as derived by Gazetas, 1982. It was observed that as soil inhomogeneity increases, the deviation between model predictions and analytical results escalates.

The capability of the model in simulating the seismic response of horizontally layered deposits was then validated against two centrifuge experiments and through comparison with several ground response analysis techniques (Hashash et al., 2015) The tests involved a 26 m thick profile of dry stiff Nevada sand with D_r = 60%, subjected to two levels of seismic excitation at its base. The computed response was reasonably compared to the measured one, though the

accuracy of the prediction was compromised by the divergence between the original input motion and that actually imposed as base excitation.

Integrating the one dimensional consolidation equation into the developed computer code, the dissipation through soil grains of the excess pore water pressure, that is generated due to cyclic loading of sand, is taken into account. Its numerical solution with the finite difference method was tested against Terzaghi's analytical solution. The accuracy of model predictions in simulating the seismic response of saturated soil was validated against the case history of Port island vertical array records, in 1995 Kobe earthquake (Iwasaki 1995 & 1996). The convergence was tested against acceleration time histories at 0m, -16m, -32m and -83m and surface spectrum, calculated under undrained conditions and considering vertical consolidation during shaking, and proved sufficient for engineering accuracy, except for that at − 16 m where the model considerably underpredicted the measurements. Field investigations (Iwasaki, 1995) along with previous simulations of the seismic response of the site (Yamazaki et al. 1995, Elgamal et al. 1997) indicated that liquefaction must have occurred at the gravelly sand layer above the shallow alluvial clay and the sandy layer below it. This was confirmed by the present analysis, where pore water pressure generation took place at the specific layers. Thus, it can be inferred that the developed model was satisfactory in reproducing the observed response. Although the predicted undrained site response was quite similar with the one calculated considering consolidation conditions, in the last case the surface gravelly layers seemed to be affected by the vertical water flow that took place, since high values of the $r_{u,max}$ were observed at these surficial layers.

Consequently, the model was applied to estimate the elastic response spectra at the surface of soil profiles with liquefiable layers. The methodology concerned the ground response analysis of diverse soil profiles, all including a liquefiable zone, excited with a suite of earthquake motions at their base, recorded on rocky formations of ground type *A*. The normalized mean surface response spectrum was linearized to a four-brunch curve, as per the EC8 approach. Specific values for the key parameters that define the shape of the design spectrum were suggested for ground types S_2 and *A*. Although this work is a preliminary application, it is believed that the presented approach, fleshed out with a bigger and more representative ensemble of soil profiles and base excitations, can form the basis to develop a veridical methodology for estimating the design ground surface response spectrum for soil deposits with potentially liquefiable layers.

Finally, the developed numerical algorithm is applied for the simulation of the seismic response of liquefiable sandy sites improved with vertical drains, by reformulating the soil consolidation differential equation to account for the horizontal axisymmetric water flow. Model validation against 3D numerical analysis in FLAC3D (Tsiapas & Tsioulou, 2009 and Bouckovalas et al., 2011) proved that, given that Ta-Ger model is appropriately calibrated against the undrained response of the system, the effect of the sand coefficient of permeability in the seismic response in terms of the excess pore water pressure evolution with time, is adequately reproduced by the model, qualitatively and quantitatively. A set of parametric analyses in a sandy soil profile of uniform D_r, indicated that the effects on mitigating liquefaction generally depend on the radius of the drain, the drain spacing and the permeability of the sand. In order to demonstrate the performance of the algorithm, the seismic response of the Port Island array improved with vertical drain up to 16m deep, is examined. A replacement ratio a/b =0.67 is required in order to maintain the maximum value of excess pore pressure $r_{u,max}$ below 0.5, along the top 16m. The expected attenuation of the shear strains and horizontal displacements at the same depths as well as the more intense accelerogram at the surface compared to the original profile response, are well reproduced by the model.

References

Bouckovalas, G., Dimitriadi, V., Tsiapas, Y., & Tsioulou, A. (2011, January). Numerical simulation of drain performance in liquefiable soils. In *Proceedings of the 5th International Conference on Earthquake Geotechnical Engineering, Santiago, Chile* (pp. 10-13).

Elgamal, A. W., Zeghal, M., & Parra, E. (1997). Identification and modeling of earthquake ground response. In *Earthquake Geotechnical Engineering* (pp. 1369-1406).

Gazetas, G. (1982). Vibrational characteristics of soil deposits with variable wave velocity. *International journal for numerical and analytical methods in Geomechanics*, *6*(1), 1-20.

Hashash, Y. M., Dashti, S., Romero, M. I., Ghayoomi, M., & Musgrove, M. (2015). Evaluation of 1-D seismic site response modeling of sand using centrifuge experiments. *Soil Dynamics and Earthquake Engineering*, *78*, 19-31.

Iwasaki, Y. (1995). Geological and geotechnical characteristics of Kobe area and strong ground motion records by 1995 Kobe earthquake. *Tsuchi to kiso*, *43*(6), 15-20.

Iwasaki, Y., & Tai, M. (1996). Strong motion records at Kobe port island. *Soils and foundations*, *36*(Special), 29-40.

Tasiopoulou, P., & Gerolymos, N. (2016a). Constitutive modeling of sand: Formulation of a new plasticity approach. *Soil Dynamics and Earthquake Engineering*, *82*, 205-221.

Tasiopoulou, P., & Gerolymos, N. (2016b). Constitutive modelling of sand: a progressive calibration procedure accounting for intrinsic and stress-induced anisotropy. *Géotechnique*, *66*(9), 754-770.

Tsiapas, I., & Tsioulou, A. (2009). *Revised design of drains for seismic liquefaction mitigation.* (Doctoral dissertation, Diploma Thesis, School of Civil Engineering, National Technical University of Athens).

Yamazaki, F., Ansary, M. A., & Towhata, I. (1995). Application of a dynamic effective stress model at a reclaimed site during the Great Hanshin earthquake, 1995. *Earthquake Geotechnical Engineering, IS TOKYO*, *95*, 591-597.

Acknowledgment

This research is co-financed by Greece and the European Union (European Social Fund-ESF) through the Operational Programme «Human Resources Development, Education and Lifelong Learning» in the context of the project “Strengthening Human Resources Research Potential via Doctorate Research – 2nd Cycle” (MIS-5000432), implemented by the State Scholarships Foundation (IKY).

Appendix

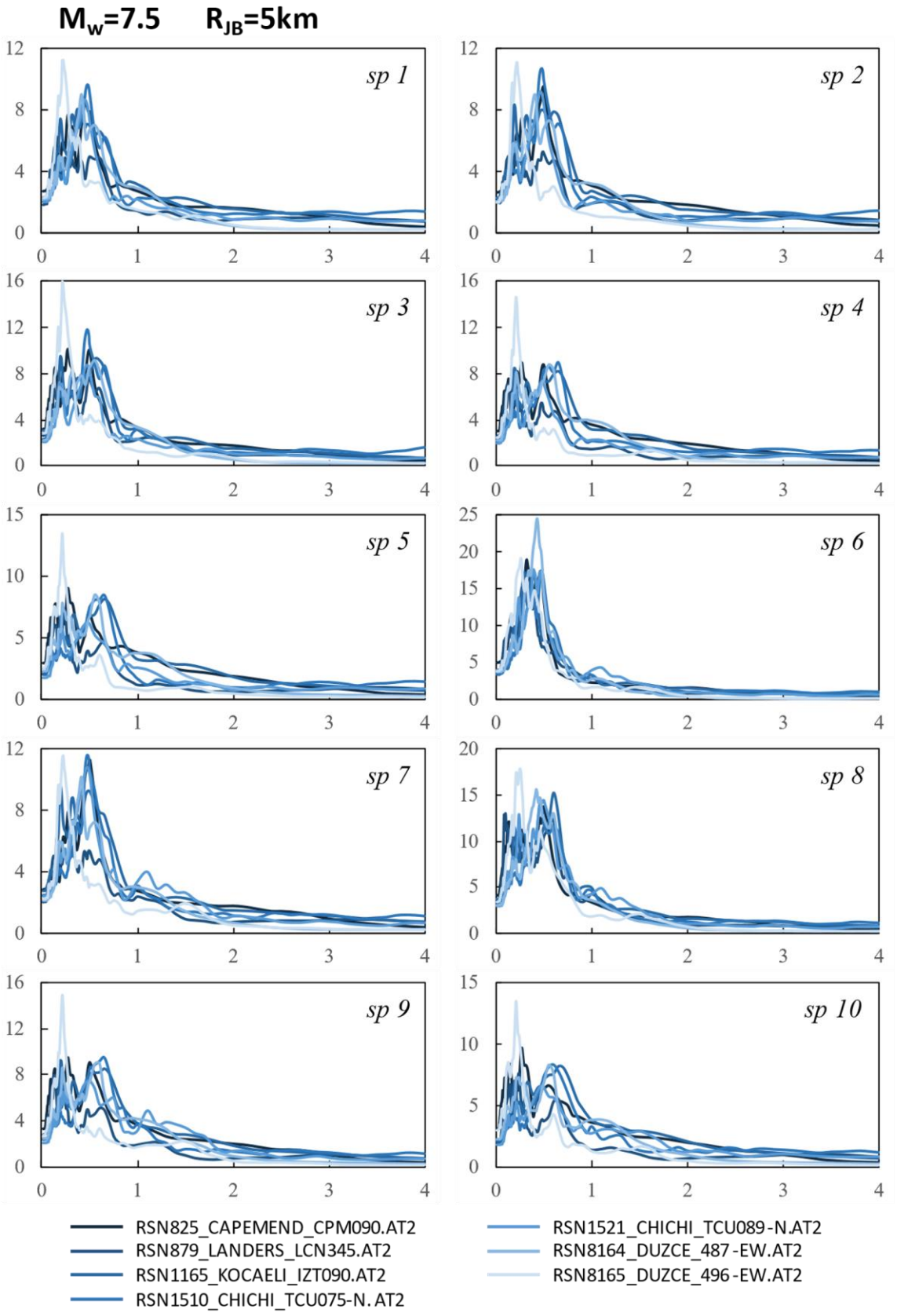

Figure B1. Elastic response spectra at the surface of the 10 soil profiles of Table 5.1, for the seismic category M_w=7.5 and R_{JB}=5km, calculated according to the proposed methodology.

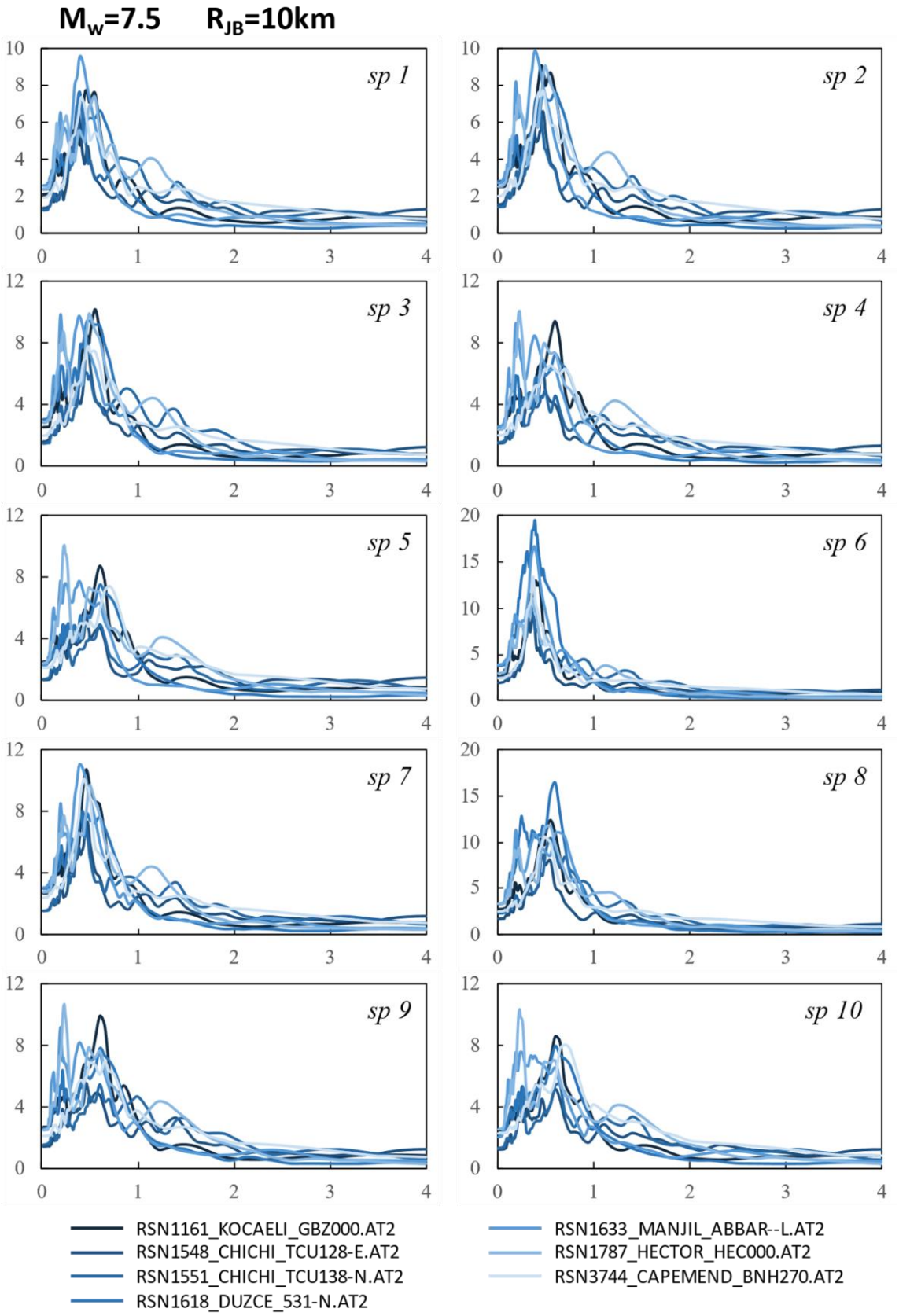

Figure B2. Elastic response spectra at the surface of the 10 soil profiles of Table 5.1, for the seismic category M_w=7.5 and R_{JB}=10km, calculated according to the proposed methodology.

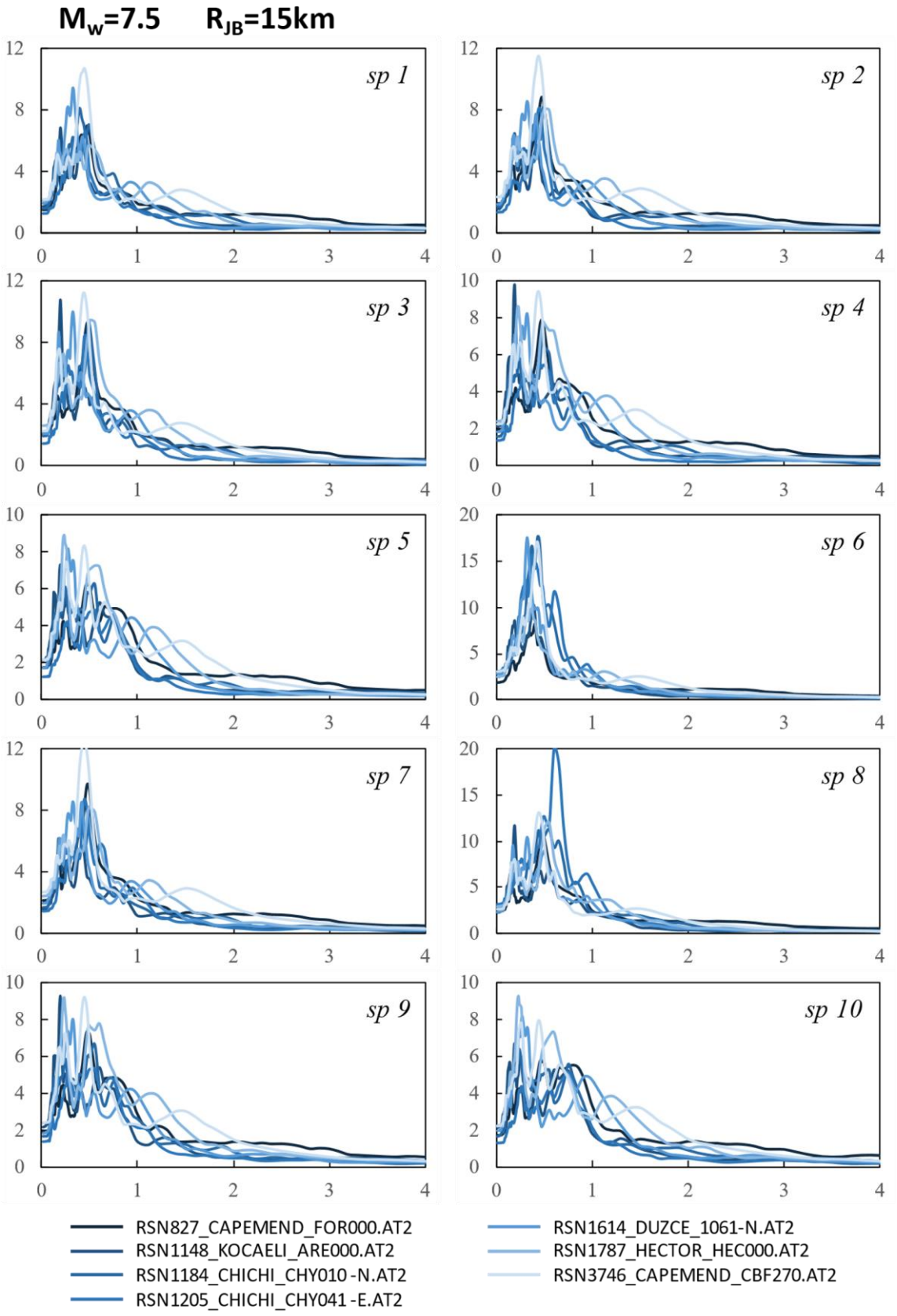

Figure B3. Elastic response spectra at the surface of the 10 soil profiles of Table 5.1, for the seismic category M_w=7.5 and R_{JB}=15km, calculated according to the proposed methodology.

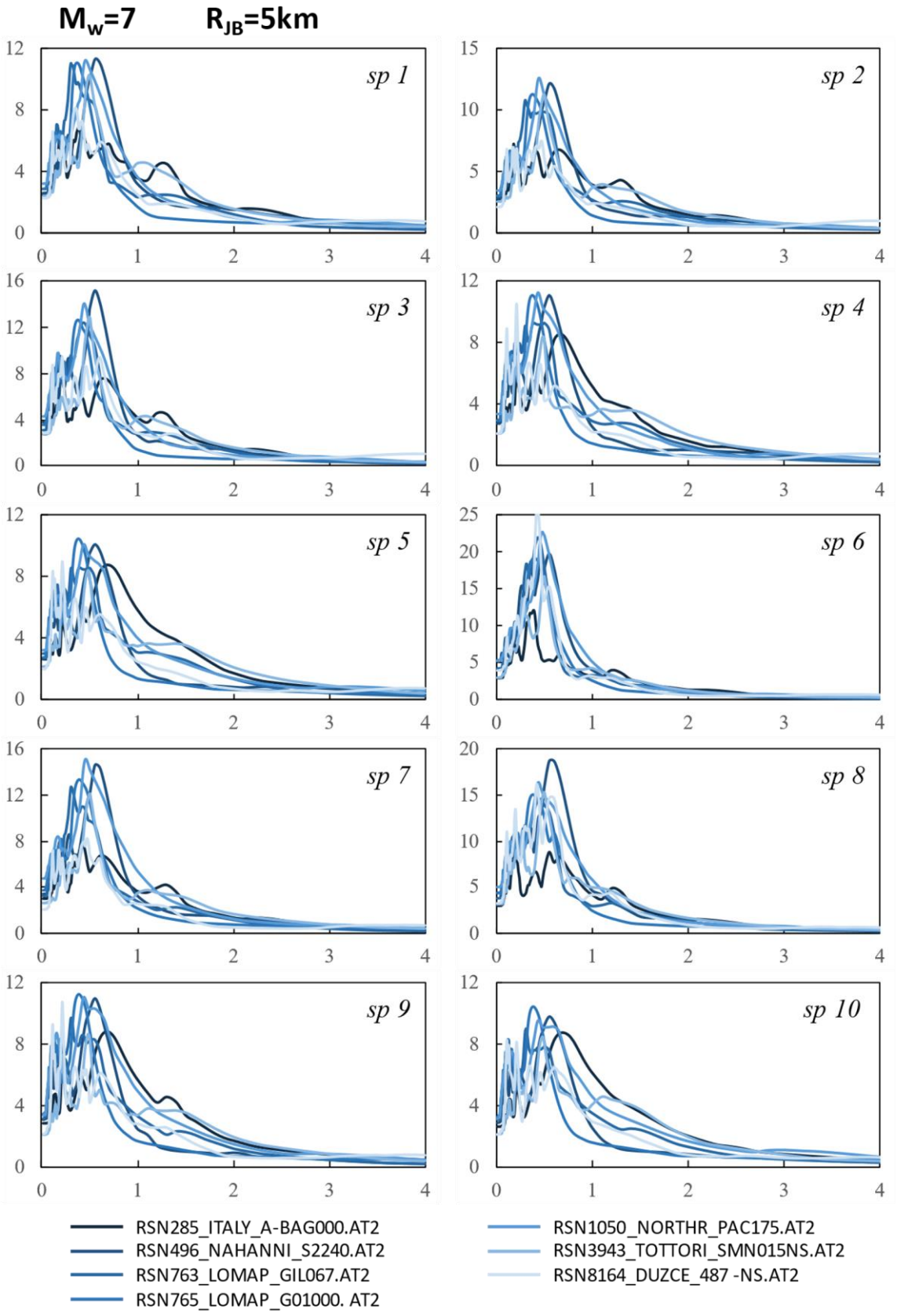

Figure B4. Elastic response spectra at the surface of the 10 soil profiles of Table 5.1, for the seismic category M_w=7 and R_{JB}=5km, calculated according to the proposed methodology.

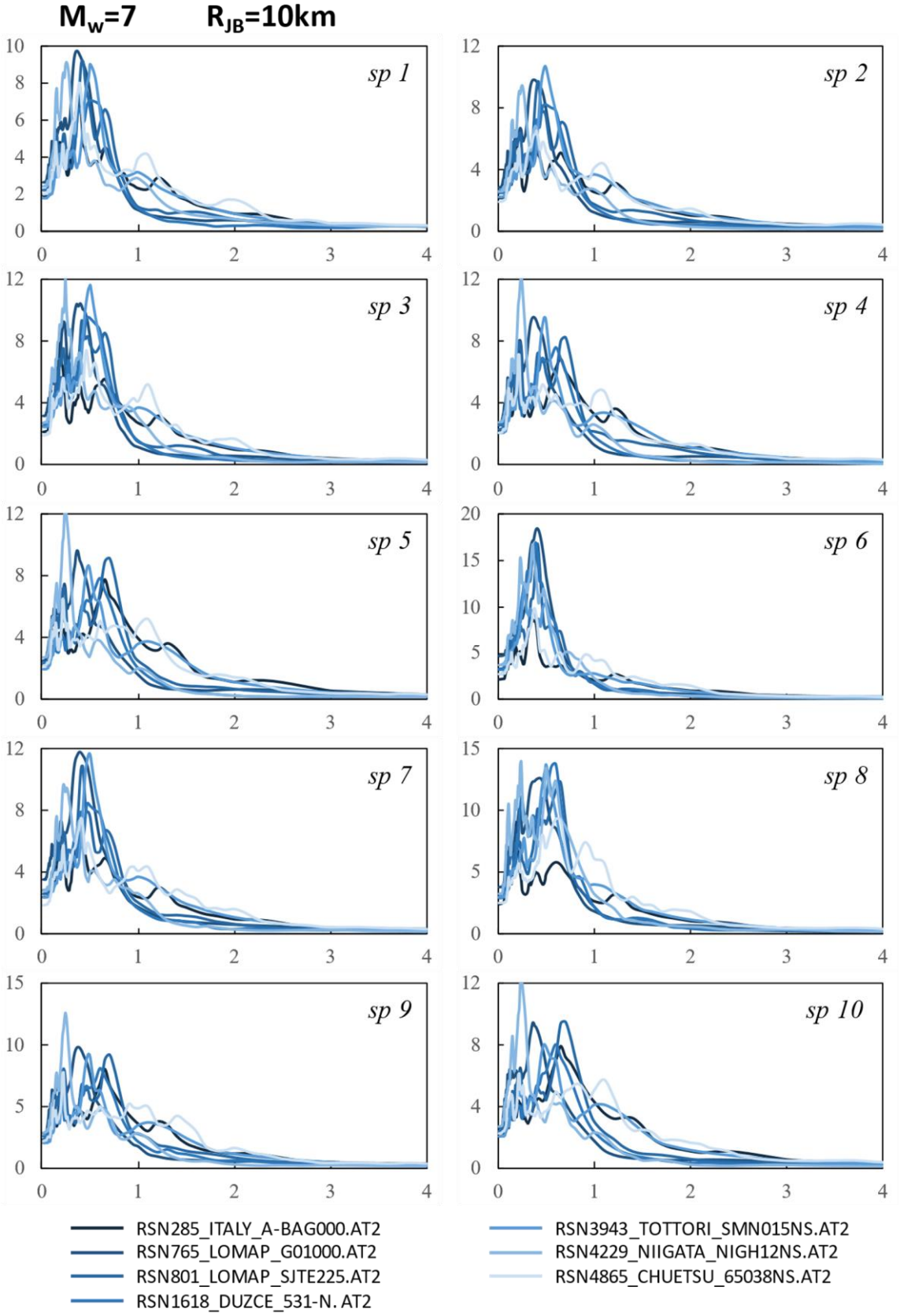

Figure B5. Elastic response spectra at the surface of the 10 soil profiles of Table 5.1, for the seismic category M_w=7 and R_{JB}=10km, calculated according to the proposed methodology.

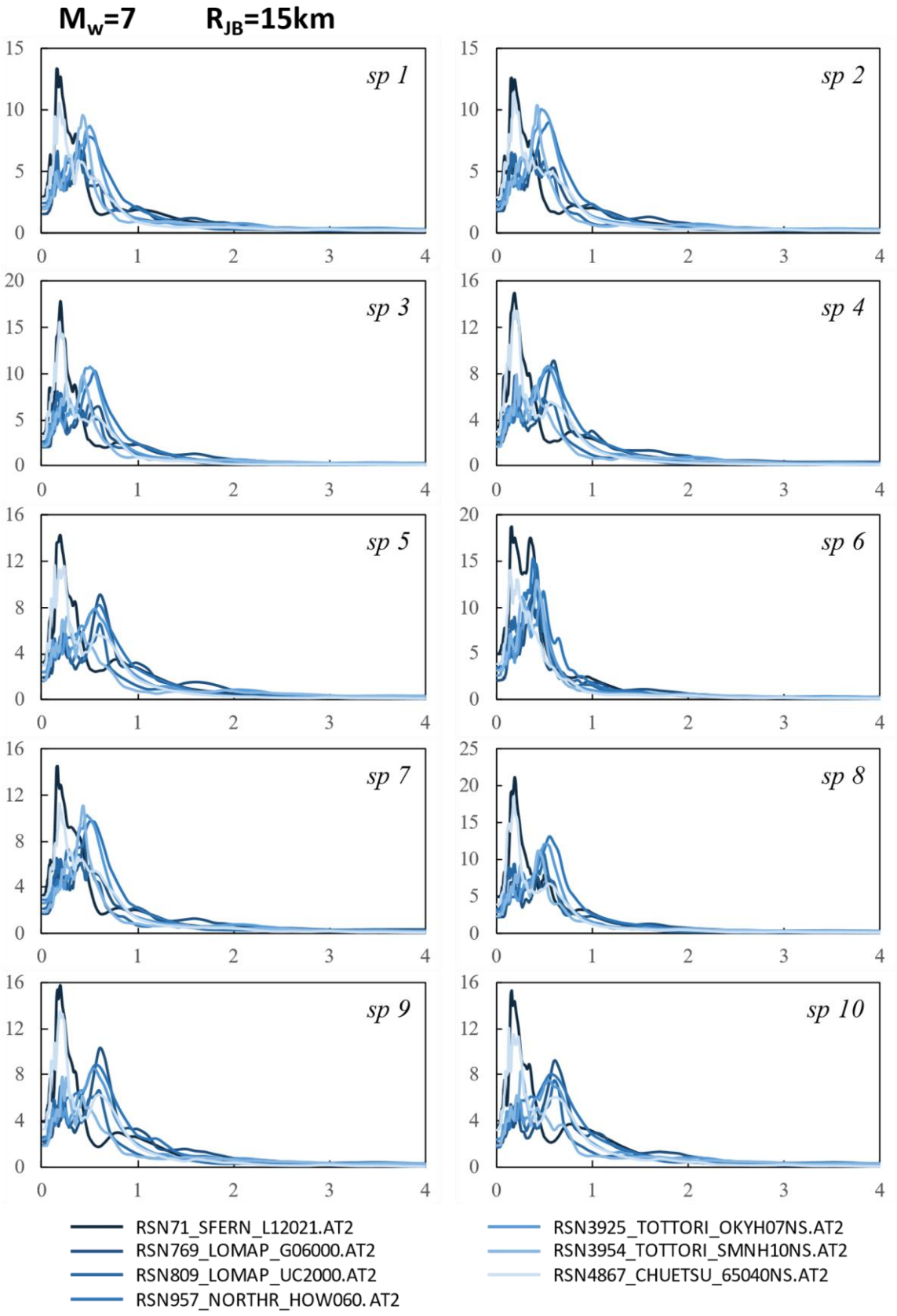

Figure B6. Elastic response spectra at the surface of the 10 soil profiles of Table 5.1, for the seismic category M_w=7 and R_{JB}=15km, calculated according to the proposed methodology.

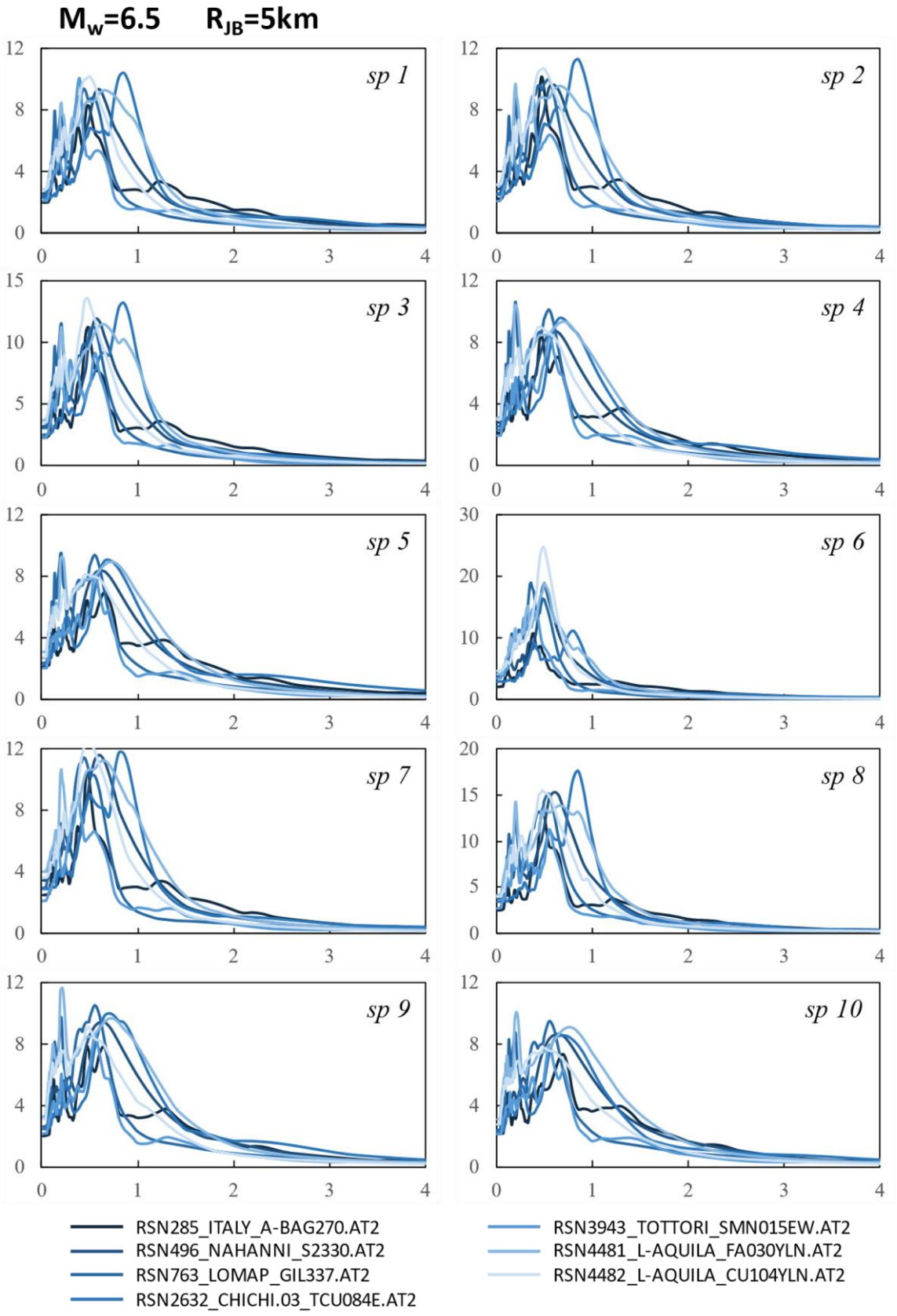

Figure B7. Elastic response spectra at the surface of the 10 soil profiles of Table 5.1, for the seismic category M_w=6.5 and R_{JB}=5km, calculated according to the proposed methodology.

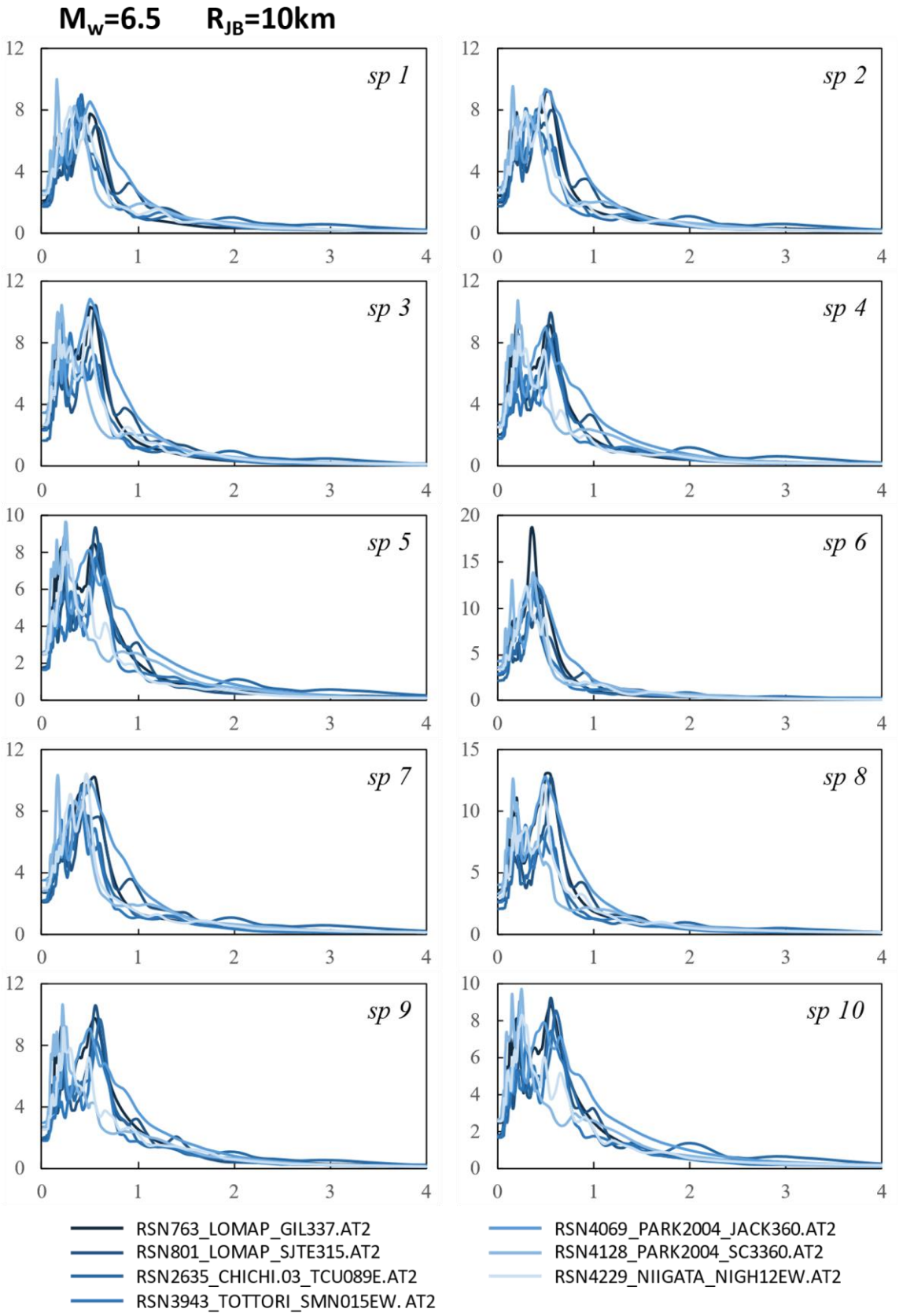

Figure B8. Elastic response spectra at the surface of the 10 soil profiles of Table 5.1, for the seismic category M_w=6.5 and R_{JB}=10km, calculated according to the proposed methodology.

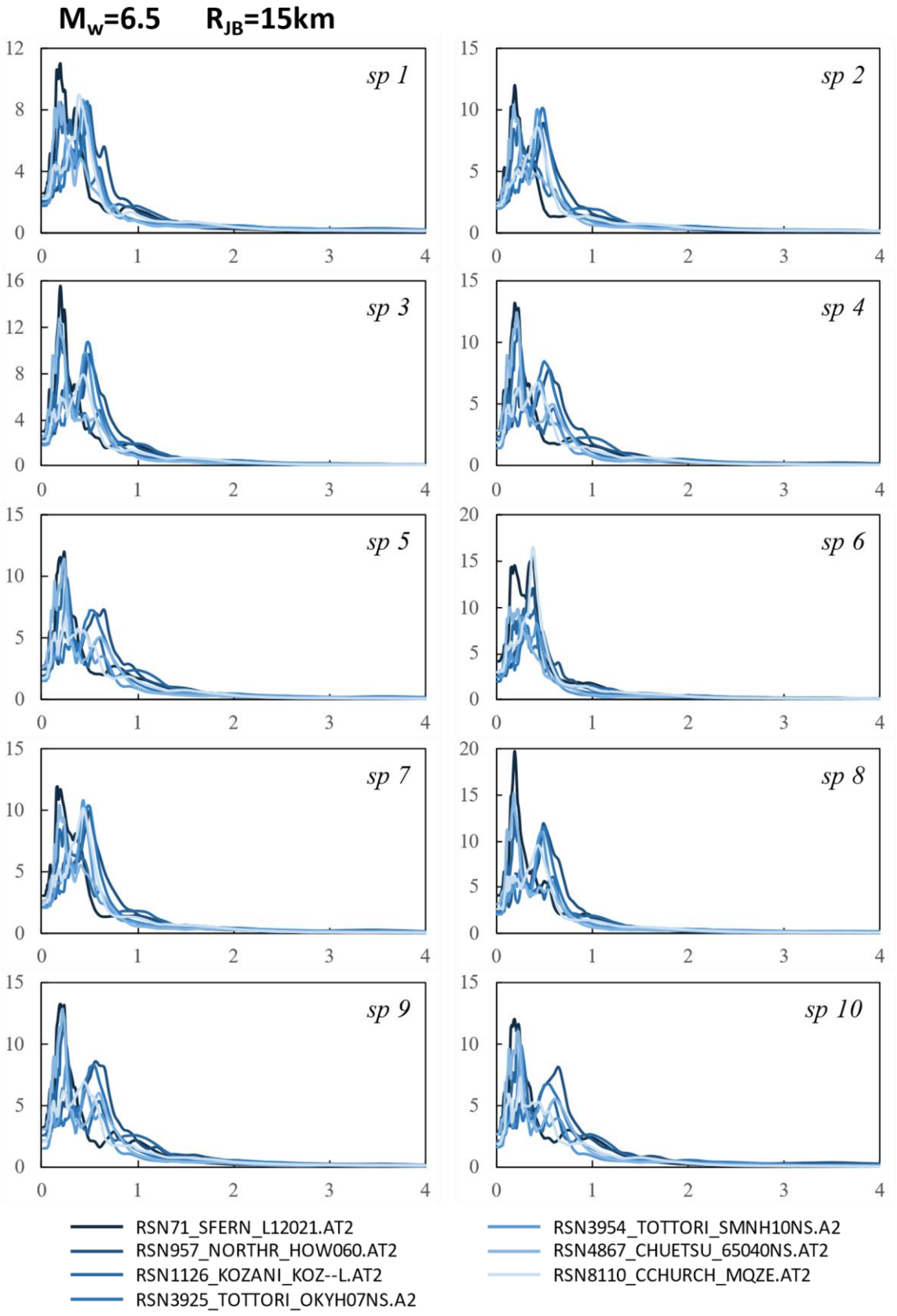

Figure B9. Elastic response spectra at the surface of the 10 soil profiles of Table 5.1, for the seismic category M_w=6.5 and R_{JB}=15km, calculated according to the proposed methodology.